UC San Diego

UC San Diego Electronic Theses and Dissertations

Title

Characterizing Erosion and Redeposition of Aluminum in DIII-D Divertor Plasmas

Permalink

https://escholarship.org/uc/item/2vv5m4wh

Author

Chrobak, Christopher Peter

Publication Date

2018

Peer reviewed|Thesis/dissertation

eScholarship.org Powered by the California Digital Library
University of California

UNIVERSITY OF CALIFORNIA, SAN DIEGO

Characterizing Erosion and Redeposition of Aluminum in DIII-D Divertor Plasmas

A dissertation submitted in partial satisfaction of the
requirements for the degree Doctor of Philosophy

in

Engineering Sciences (Engineering Physics)

by

Christopher Peter Chrobak

Committee in charge:

George R. Tynan, Chair
Farhat N. Beg
Ping Liu
Rick A. Moyer
Kevin B. Quest

2018

Copyright

Christopher Peter Chrobak, 2018

All rights reserved

This Dissertation of Christopher Peter Chrobak is approved, and it is acceptable in quality and form for publication on microfilm and electronically:

_____

_____

_____

_____

_____
Chair

University of California, San Diego

2018

DEDICATION

To Alexis, Mabel, and Sage

TABLE OF CONTENTS

LIST OF FIGURES

LIST OF TABLES

ACKNOWLEDGEMENTS

Many huge thanks and credit to my family and friends, for believing in me and not letting me give up. Without their support, I would never have made it this far. I am indebted to my advisor George Tynan for challenging me to be a better scientist, presenter, and communicator. His guidance was crucial in converting a seemingly endless supply of curiosity into a focused and productive investigation. Thanks also to my unofficial advisor Peter Stangeby for the initial inspiration, many thoughtful discussions, and comprehensive revisions of each of my publications. Thanks to Clement Wong, Jeff Brooks and Dennis Whyte for the early work that laid the groundwork for these and many other plasma-material interaction experiments on the DiMES facility in DIII-D. Thanks to all my co-authors for their help planning, supporting and executing these experiments. Thanks to Dean Buchenauer and Berenice Mills for their help preparing and producing the physical samples. Thanks to the efforts of Bill Wampler and Graham Wright for providing world class post-mortem surface analysis data. Thanks also to Charles Skinner for his collaboration and detailed surface composition measurements. Thanks to Jon Watkins and Charlie Lasnier for providing ion and heat flux measurements. Thanks to Adam Mclean and Neil Brooks for their spectroscopic expertise which was instrumental in these experiments. Thanks to Eric Hollmann, Rui Ding, David Elder, and Jerome Guterl for their discussions and lessons on modeling sputtering, ionization, and emission processes. Thanks to Russ Doerner for his advice and insightful discussions, and to the rest of the staff at the UCSD PISCES facility for helping with my early investigations into aluminum erosion and spectroscopy. Thanks to my managers Arnie Kellman, Pete Taylor, and Kurt Holtrop for giving me the flexibility to pursue this degree in parallel with my

career. Lastly, and most importantly I want to acknowledge the often super-human efforts of the entire DIII-D team – the technicians, scientists and engineers that design, build and operate the machine that is the DIII-D National Fusion Facility – without which the work presented in this dissertation could not be accomplished.

Chapters 4 and 6, in part, have been published in: C. P. Chrobak, P. C. Stangeby, A. W. Leonard, D. L. Rudakov, C. P. C. Wong, A. G. McLean, G. M. Wright, D. A. Buchenauer, J. G. Watkins, W. R. Wampler, J. D. Elder, R. P. Doerner, D. Nishijima and G. R. Tynan 2015 Measurements of Gross Erosion of Al in the DIII-D Divertor J. Nucl. Mater. 463 810–3.

Chapter 5, in part, has been submitted for publication and material may appear in Nuclear Fusion, 2018 under C. P. Chrobak, P.C. Stangeby, E. Hollmann, D.L. Rudakov, T. Abrams, R. Ding, J.D. Elder, J. Guterl, E. Hinson, H.Y. Guo, D.M. Thomas, C. H. Skinner, A.G. McLean, W.R. Wampler, D.A. Buchenauer, R.P. Doerner, G.R. Tynan, "Measurement and Modeling of Al Erosion and Ionization in the DIII-D Divertor Including Magnetic Pre-Sheath Effects."

Chapter 7, in part, has been published in C. P. Chrobak, R. P. Doerner, P. c. Stangeby, W. R. Wampler, D. L. Rudakov, G. M. Wright, T. Abrams, R. Ding, J. D. Elder, J. Guterl, H. Y. Guo, C. Lasnier, D. M. Thomas, A. W. Leonard, D. A. Buchenauer, A. G. McLean, J. G. Watkins and G. R. Tynan 2017 Characterizing Low-Z Erosion and Deposition in the DIII-D Divertor Using Aluminum Nucl. Mater. Energy 12 441–6.

Chapters 3, of this dissertation includes text and data which describe experimental conditions and were published in part in each of the aforementioned papers. The dissertation author was the primary investigator in each of these aforementioned published or submitted papers.

VITA

2018 Ph.D., Engineering Sciences (Engineering Physics), University of California, San Diego

2006 B.S, M.S. Nuclear Engineering and Engineering Physics, University of Wisconsin Madison

PUBLICATIONS

"Measurement and Modeling of Al Erosion and Ionization in the DIII-D Divertor Including Magnetic Pre-sheath Effects," *Submitted to Nucl. Fusion, Jan. 2018.*

"Characterizing Low-Z erosion and deposition in the DIII-D divertor using aluminum," *Nucl. Mater. Energy*, vol. 12, pp. 441–446, Aug. 2017.

"Measurements of gross erosion of Al in the DIII-D divertor," *J. Nucl. Mater.*, vol. 463, no. 0, pp. 810–813, Aug. 2015.

"Restoring transmission of irradiated image fiber bundles," *Rev. Sci. Instrum.*, vol. 83, no. 10, p. 10E514, Oct. 2012.

CO-AUTHORED PUBLICATIONS

Contributed as Co-Author to 27 publications, including:

K. Holtrop *et al.*, "The Design and Use of Tungsten Coated TZM Molybdenum Tile Inserts in the DIII-D Tokamak Divertor," *Fusion Sci. Technol.*, vol. 72, no. 4, pp. 1–6, Aug. 2017.

R. P. Doerner *et al.*, "Investigation of He–W interactions using DiMES on DIII-D," *Phys. Scr.*, vol. T167, no. T167, p. 14054, Feb. 2016.

D. L. Rudakov *et al.*, "Control of high-Z PFC erosion by local gas injection in DIII-D," *J. Nucl. Mater.*, vol. 463, pp. 605–610, Aug. 2015.

G. L. Jackson *et al.*, "Effect of lithium in the DIII-D SOL and plasma-facing surfaces," *J. Nucl. Mater.*, vol. 463, pp. 1160–1164, Aug. 2015.

A. Litnovsky *et al.*, "Impact of Thermo-Oxidative Wall Conditioning on the Performance of Diagnostic Mirrors for ITER," *Fusion Sci. Technol.*, vol. 62, no. 1, pp. 97–103, Aug. 2012.

I. V. Fomenkov *et al.*, "Laser-produced plasma source system development," in *Proceedings of SPIE*, vol. 6517, no. PART 2, p. 65173J, 2007.

J. P. Allain *et al.*, "Erosion and degradation of EUV lithography collector mirrors under particle bombardment," in *Proceedings of SPIE*, vol. 5751, no. II, p. 1110, 2005.

PRESENTATIONS

"Erosion and Deposition of Al in DIII-D Divertor He and D Plasmas" Poster session presented at: 22nd International Conference on Plasma Surface Interactions, 2016; Rome, Italy.

"DIII-D First Wall Metal Impurity Migration Trends", Poster session presented at: 58th Annual meeting of the APS Division of Plasma Physics, 2016; San Jose, CA.

"Measurements of gross erosion of Al in the DIII-D divertor," Poster session presented at: 21st International Conference on Plasma Surface Interactions, 2014; Kanazawa, Japan.

"Survey and Cleaning of Metal Contamination in Graphite Armor Tiles in DIII-D," Poster session presented at: 54th Annual Meeting of the APS Division of Plasma Physics, 2012; Providence, RI.

PATENTS

"Systems and Methods For Collector Mirror temperature Control Using Direct Contact Heat Transfer," US 7641349 B1, 2010.

"Systems and Methods For Collector Mirror temperature Control Using Direct Contact Heat Transfer," US 7641349 B1, 2010.

FIELDS OF STUDY

Major Field: Engineering Sciences (Engineering Physics)
Studies in Plasma-Material Interactions and Radiation Damage in Materials
Professor George R. Tynan

ABSTRACT OF THE DISSERTATION

Characterizing Erosion and Redeposition of Aluminum in DIII-D Divertor Plasmas

by

Christopher Peter Chrobak

Doctor of Philosophy in Engineering Sciences (Engineering Physics)

University of California, San Diego, 2018

Professor George R. Tynan, Chair

Understanding the erosion and redeposition behavior of tokamak plasma facing materials is important to ensure component lifetime. The goal of this thesis was to characterize the erosion and redeposition of aluminum (Al) when exposed to a tokamak divertor plasma. Al was chosen for its similarities to beryllium (Be), which is intended for use as the first wall material in ITER but is toxic and restricted in DIII-D and most other tokamaks. The Divertor Material Evaluation Station (DiMES) was used to expose a set of Al-coated samples to low-density L-mode plasma discharges in the DIII-D divertor. Different plasma conditions were used for each sample (including He and D plasmas), and samples with both ideal (smooth) and practical (rough) surfaces were exposed. Measurements of quantitative emission spectroscopy and film thickness change were compared to simulations of sputtering, ionization, and redeposition of Al to determine the gross erosion rate, redeposition fraction, and spectroscopic emission efficiency.

We present the first quantitative spectroscopic measurements of neutral emission anisotropy due to sputtering erosion in a tokamak divertor plasma. We present an ionization-emission model that reproduced the anisotropy by assuming full angular

sputtering yield distributions predicted by grazing angle sputtering simulations and ion beam sputtering measurements. Grazing angle ions were expected due to the disappearance of the classical Debye sheath in favor of a thicker magnetic pre-sheath (MPS) at small magnetic field surface inclination angles. The direction of presumed sputtering anisotropy and E×B drift of ions within the MPS was consistent with the direction of deposition patterns found on the samples and within individual pores of the rough surfaces. A model of the erosion-redeposition cycle including re-erosion and material mixing reproduced observed film thickness change measurements. The characteristic Al redeposition length was on the order of its ionization length, 1-3mm at the $1\times10^{13}cm^{-3}$ plasma densities analyzed. Total redeposition fractions ranged from 30% to 76%, increasing with higher plasma temperature due to the higher sheath electric field strength. On rough surfaces on the order of 50% of redepositing material was retained in hidden or shadowed regions, while on smooth surfaces this effect was negligible.

Chapter 1
Introduction

1.1 The promise and challenge of fusion as an energy source

For decades, fusion has been touted as the holy grail source of clean energy. Fusion promises to be an advanced nuclear power technology that has a virtually limitless fuel supply and produces energy without generating pollution, carbon emissions, or any long-lived nuclear waste. After all, it is fusion energy that has been powering the sun for billions of years, providing the heat and light that fundamentally sustains all life on Earth. However, modern industrial civilization requires a reliable, controllable, and plentiful source of energy to provide heat and electricity on demand to a growing population. The increasing energy demands of the world's growing civilization continue to require greater generating capacity, straining existing reserves of fuels and compromising the stability of global climate. In order to continue the current pace of growth, future generations will need a strategy to produce increasingly more energy generating capacity while at the same time finding a replacement for the cheap and reliable fossil fuels that have provided the backbone to the existing energy infrastructure. Nuclear fusion energy, once realized, can rewrite the energy strategy playbook.

An enormous amount of energy is released in the fusion reaction, tens of millions of times more energy per reaction than in the most intense chemical reactions. The challenge is that the energy required to produce the reaction is also enormous. The first demonstration of the raw power of nuclear fusion, the notorious and terrifying hydrogen bomb, required a nuclear explosion to trigger the reaction that released more energy in

a single instant than a large power plant can produce in a year. Fusion between two light atoms occurs when their nuclei collide with enough energy to overcome their mutual repulsive force and get close enough to fuse into a new nucleus. Generating such energetic and frequent collisions between atoms requires that the fuel is heated to extreme temperatures – even hotter than the core of the sun – between 100 and 200 million degrees C. At these temperatures, all matter is a fully ionized plasma. Since the cold war, a worldwide community of scientists and engineers have been researching and collaborating on methods to control plasmas and heat them to thermonuclear fusion temperatures for the benefit of humankind.

A universal figure of merit for fusion device performance is known as the Lawson criterion, defined as the minimum product of electron density and energy confinement time required for a fusion reaction to reach ignition, or be self-sustaining. A more useful extension of this metric is the triple product, which includes electron temperature, and is thus expressed in terms of the product of plasma pressure and energy confinement time. In order to achieve a burning plasma, the triple product needs to be such that the energy of the alpha particles generated by the fusion reaction are able to balance the energy escaping the plasma. The minimum value for this depends on the specific fusion reaction, since each reaction has a different energy input and output. The most accessible fusion reaction by far is D-T fusion, but other possible contenders are D-D (typically used for research), and D-He3. The nuclear equations for each reaction are listed below. The triple product required for burning plasma for each reaction is compared in Figure 1-1. The nuclear equations of these reactions, including reactants, products, and energy released are as follows [1]:

D-T Fusion: $${}_1^2D + {}_1^3T \longrightarrow {}_2^4He\ (3.5\ MeV) + n\ (14.1\ MeV)$$

D-D Fusion: $${}_1^2D + {}_1^2D \longrightarrow \begin{cases} {}_1^3T\ (1.0\ MeV) + p\ (3\ MeV) \\ {}_2^3He\ (0.82\ MeV) + n\ (2.45\ MeV) \end{cases}$$

D-Helium 3 Fusion: $${}_1^2D + {}_2^3He \longrightarrow {}_2^4He\ (3.6\ MeV) + p\ (14.7\ MeV)$$

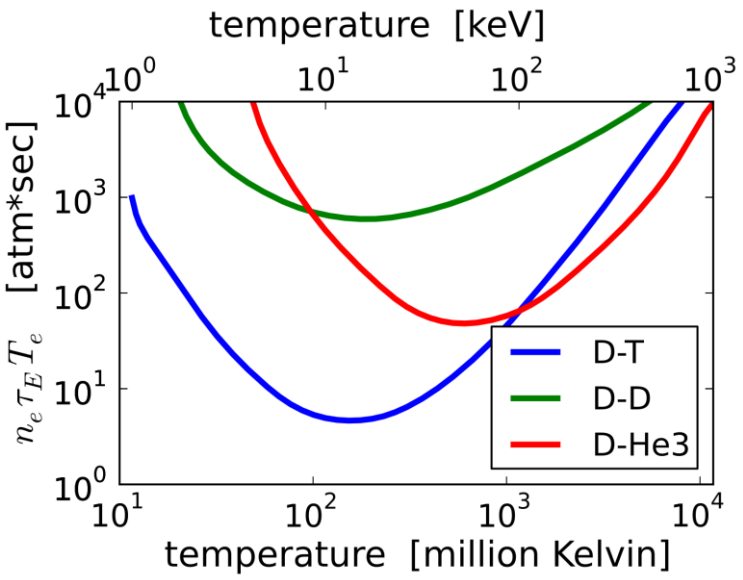

Figure 1-1. Triple product for fusion energy break-even (Q=1) required for three common fusion reactions [2]

Two distinct methods of confining the extreme temperature plasma for achieving fusion have emerged: 1) Inertial confinement which uses high intensity lasers to implode pellets of fusion fuel to such extreme temperatures and densities that thermonuclear ignition occurs rapidly before the fuel has a chance to disperse; and 2) Magnetic confinement, which exploits the electrically conductive nature of a plasma to stabilize and compress it using strong magnetic fields, while heating it with electromagnetic waves. However, to date no scheme has emerged as proven to release more energy than required to generate the reaction in the first place. To date, the most successful of the confinement technologies, and the most promising from the standpoint of designing a power generating nuclear fusion reactor, is arguably the tokamak.

1.2 The Tokamak

In the early history of researching plasma magnetic confinement schemes, the tokamak emerged as a front runner with longer confinement times and higher maximum core plasma temperatures. The tokamak uses closed loops of magnetic fields to confine, compress, and stabilize a ring of current-carrying plasma as it is heated to fusion generating temperatures. The tokamak magnetic configuration is achieved through the use of nested electromagnets wrapped around a toroidal loop of current-carrying plasma, as shown conceptually in Figure 1-2. The tokamak operates by striking an ultra-high purity deuterium (and tritium) plasma inside of a torus shaped vacuum chamber. A strong current is induced in this ring of plasma by ramping current through a central solenoidal coil, akin to the primary and secondary windings of a conventional power transformer. The plasma current generates a poloidal magnetic field and a pinch instability that tends to compress the plasma, while an externally applied strong toroidal magnetic field provides support to stabilize the plasma against the instability. The result is a helical field structure that confines the plasma and allows it to be heated without contacting the wall. External shaping coils are used to maintain control of the plasma position and shape so that it does not contact the wall of the vacuum vessel.

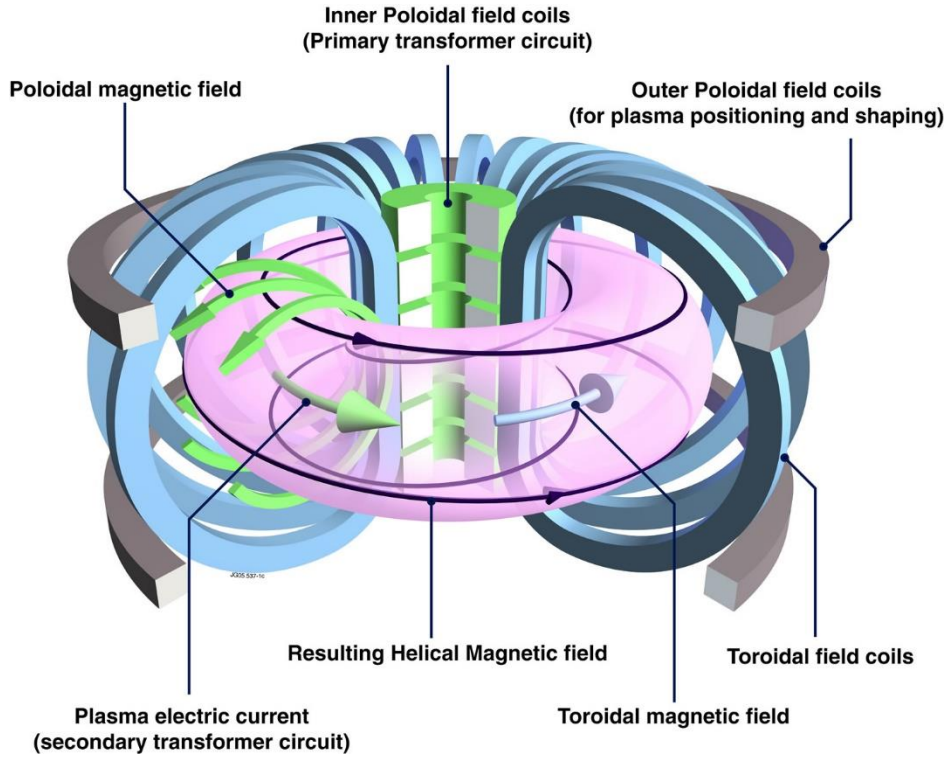

Figure 1-2. The fundamental concept of a Tokamak, using nested electromagnetic control coils to create a ring of plasma with an internal helical magnetic field structure [3].

Over the past decades, advancement of the tokamak concept has led to numerous innovations and improvements in stability, heating efficiency, and pulse length. One of these innovations is a so-called divertor magnetic configuration gives the tokamak its ability to control plasma density and exhaust helium 'ash'. An example of the typical divertor magnetic configuration is shown in poloidal cross-section in Figure 1-3, with detailed inset regions relevant to plasma-material interactions at the "edge region" near the first wall and the "divertor region" near the divertor targets. Given the toroidal symmetry of the tokamak, the magnetic flux surfaces represent poloidal projections of helical magnetic field lines. Magnetic flux surfaces inside the plasma core region are closed, that is the field lines never leave the core. The last closed flux surface, also called the separatrix, defines the edge of the confined plasma and the start of the so-called

scrape-off-layer where field lines intersect the first wall. In the divertor region, additional poloidal field shaping coils are employed to create a null in the poloidal field called the X-point, enabling the last closed flux surface to intersect with a target called the divertor at the so-called inner and outer strike-points. The divertor is a region of the wall which is specially designed and instrumented to withstand high heat and particle fluxes escaping along the last closed flux surface.

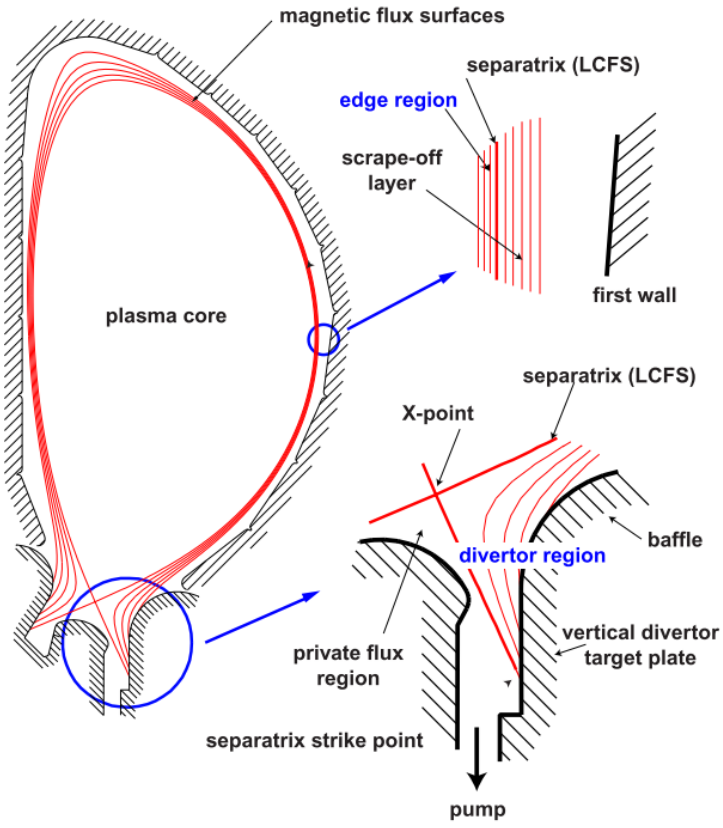

Figure 1-3. Reproduced with permission from [4] Poloidal cross-section of a tokamak plasma, showing magnetic flux surfaces of a single magnetic null divertor configuration. Detail of the divertor and limiter regions is shown.

One important next step device on the roadmap to a fusion reactor is achieving and sustaining a burning plasma, that is a plasma whose temperature is self-sustained by its own fusion reactions. The international tokamak community has chosen to build a large volume, long pulse superconducting tokamak called ITER to achieve this very goal.

The ability of the tokamak plasma to confine and insulate high plasma temperatures, and therefore the fusion power production, scales with plasma volume and toroidal magnetic field strength. A model depiction of the ITER tokamak is shown in Figure 1-4. In the same figure we show the DIII-D tokamak, presently the largest operating tokamak in the United States, in relative scale standing alongside ITER.

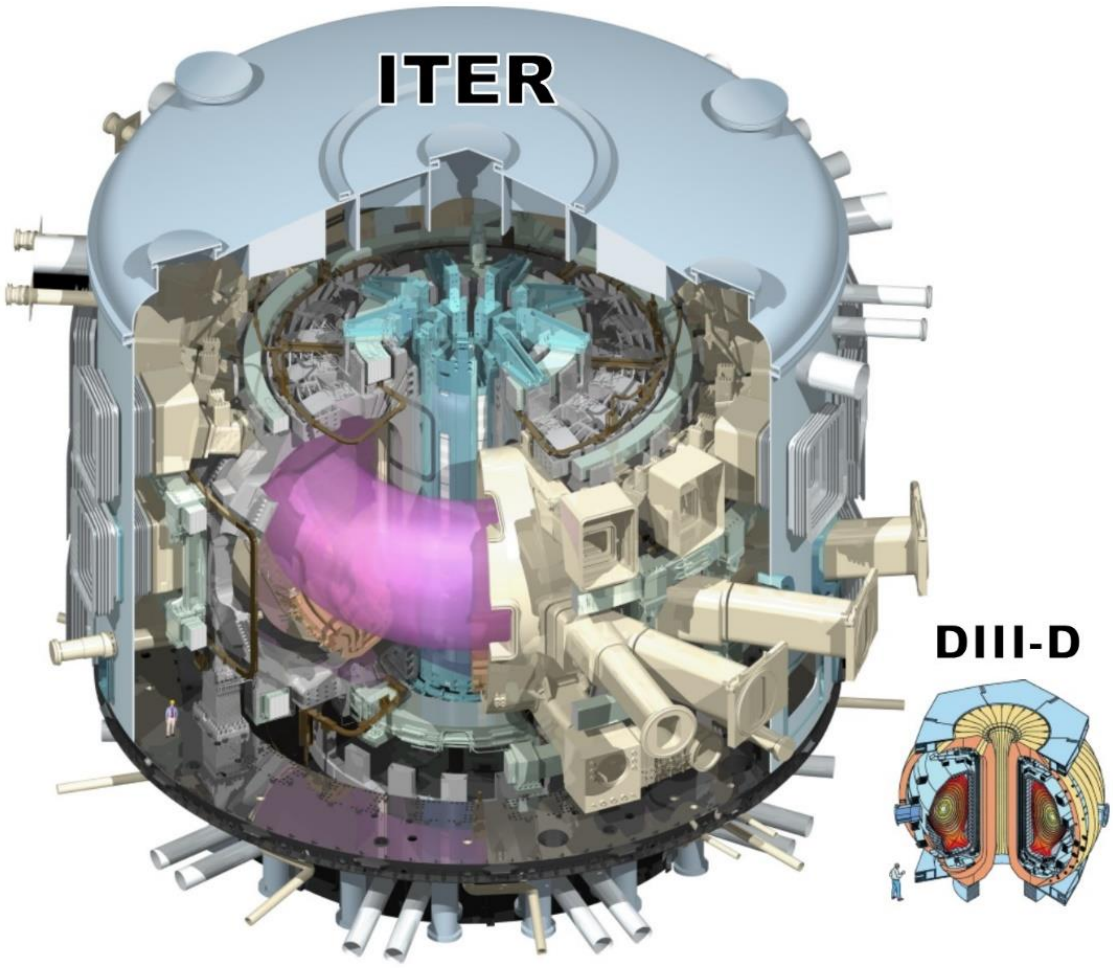

Figure 1-4. Illustrations of the ITER [5] and DIII-D [6] tokamaks side by side and approximately to scale, showing internal components, structures, and people for scale reference.

The plasma-facing components (PFCs) in the divertor have to withstand some of the highest heat fluxes of any industrial material, and thus are often built of high

temperature capable materials such as tungsten or carbon (i.e. graphite, carbon-fiber). The rest of the wall, on the other hand, can operate at comparatively lower temperatures but needs to survive high nuclear heat loads (from the generated neutrons) and energetic particles (from the ions and neutrals that escape the confined plasma). The plasma-facing components (PFCs) in the DIII-D tokamak are made from graphite, a material capable of high temperatures and resilient to thermal shock. The first wall design choice for ITER, the international tokamak community's next step experimental device, uses a main chamber wall of beryllium (Be) with a divertor of tungsten (W).

1.3 Plasma Facing Component Requirements

There are four main engineering requirements that the tokamak plasma-facing material must meet: 1) capable of handling high heat flux, 2) withstand complex plasma-material interactions, 3) have extremely low fuel retention properties, and 4) be resistant to neutron damage and activation. These requirements are not unique to the tokamak. In fact, any device attempting to confine a thermonuclear plasma for any considerable amount of time will require a solution to the same plasma facing material challenges.

Excessive heat flux, or power deposition, can damage or degrade the plasma facing component by melting, cracking (thermal shock or cyclic loading), or annealing (recrystallizing) the material. Heat flux is most intense near the divertor region, where high fluxes of energetic particles can deposit their heat in a narrow band. This heat flux increases with increased input power to the plasma, but also scales linearly with plasma current, magnitude of the poloidal field, and inversely with plasma density [7]. There are primarily three methods employed to reduce heat flux to the divertor target surfaces when operating the tokamak: 1) aligning the target surfaces with the magnetic field in

such a way as to decrease the perpendicular heat flux to the surface, 2) operating at higher densities such that the plasma near the target surfaces enters a low temperature (few eV), highly radiative regime through a process known as detachment [8], and 3) operating with increased expansion of the magnetic flux surfaces such that the width of the strike region is expanded [9]. Each method has its drawbacks: 1) alignment is limited by requisite gaps between components where leading edges can form, 2) detachment tends also to decrease core plasma temperatures, and 3) flux expansion requires higher poloidal field shaping currents and larger vessel and toroidal field volume (therefore higher cost).

Plasma-material interactions can damage component surfaces through a number of different particle-surface interaction events. These include: 1) sputtering, or the ballistic removal of surface atoms by incident ions and neutrals, 2) implantation, the forced inclusion of an atom from the plasma into the near surface layer of the material which can lead to compositional or microstructural changes in the surface, 3) plasma deposition, or the formation of amorphous layers of mixed materials on top of the plasma facing component, often composed of material eroded from other parts of the machine. In addition to being damaged by the bombarding energetic ions and neutral atoms, the release of these materials into the plasma creates impurity ions that can transport to the plasma core and create energy losses through radiation [10].

Fuel retention is the third challenge, and potentially one of the most concerning for the viability of fusion power reactor. Fuel retention is the trapping of tritium fuel in the plasma facing component, either by direct implantation, diffusion, or co-deposition with other depositing species. In a tritium burning tokamak, limits of in-vessel fuel retention is are likely to be exceeded before component erosion wear or neutron damage lifetimes

are met. In ITER, the administrative limit for in-vessel tritium retention has been set to 700 grams. Based on estimates of erosion and co-deposition with beryllium, the tritium retention limit is expected to be reached in the range of 10^6 seconds (280 hours) of plasmas operations or about 2500 discharges, as shown in Figure 1-5. These are conservative estimates based on erosion of the wall, and not including tritium release by heating or subsequent re-erosion of the deposits.

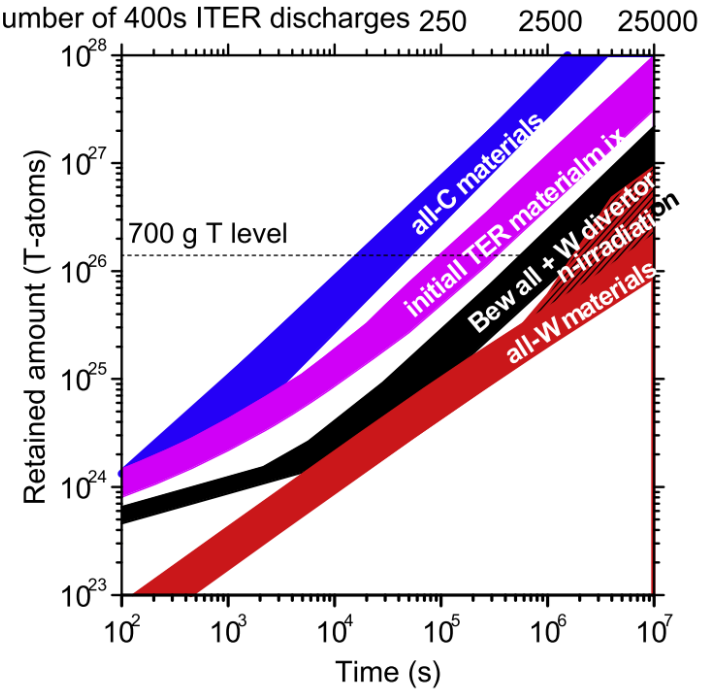

Figure 1-5. Reproduced with permission from [11]. Tritium inventory in ITER for different wall material configuration options. The assessment includes erosion from the main wall and divertor.

The fourth, and probably longest term problem on the horizon is neutron damage and activation. When using D-T fuel mix, the 14 MeV neutron emitted in the reaction must pass through the first wall and structural materials before reaching the blanket, which serves as a primary heat exchanger, a radiation shield and tritium fuel breeding module. Bombardment of materials with these energetic neutrons produces clusters of atomic defects and formation of He bubbles throughout the bulk of the material. These defects

can lead to material embrittlement [12] and increased retention of diffusing tritium [13], exacerbating the already difficult heat and particle load challenges faced by the PFCs. The other challenge, neutron activation, imposes a restriction to the elements that a reactor can be made from such that the materials constructing the reactor itself do not transmute into long-lived hazardous radioactive waste.

Present day tokamaks operate at very low duty cycle compared to a power generating fusion reactor, and thus have not had component lifetimes limited by the rate of erosion wear. While detachment or advanced divertor configurations may be used to reduce particle or heat flux and erosion rates in the divertor, the main wall faces a major source of erosion that cannot be easily reduced: high energy charge exchange neutrals. Shown in Table 1-1 are crude estimates of the annual gross erosion rate of the first wall of current and future reactors based on sputtering by charge-exchange neutrals [14]. The erosion estimates are scaled proportional to the annual energy load (E_{load}) and total annual plasma time (τ_{annual}) expected at the wall. Progressing from present fusion devices to future reactors, the gross erosion rates will increase by about 5 orders of magnitude. This brings to the forefront the problem of material redeposition and buildup in the divertor, as the sheer quantities of eroded 'slag' to be managed become huge. Even estimates for an all-tungsten PFC DEMO reactor, erosion due to just charge exchange neutral particle impact on the wall alone would be ~7,900 kg/yr, with this material migrating to regions of net deposition i.e. the divertor. For ITER, with an annual duty cycle of ~3%, beryllium erosion rates are estimated to be in the 77 kg/year range.

Table 1-1. Erosion estimates for different hypothetical wall materials in current and future tokamaks [14].

Device	P_{heat} (MW)	τ_{annual} (s/yr)	Annual E_{load} (MJ)	Beryllium net wall erosion rate (kg/yr)	Boron net wall erosion rate (kg/yr)	Carbon net wall erosion rate (kg/yr)	Tungsten net wall erosion rate (kg/yr)
DIII-D	20	10^4	0.2	0.13	0.11	0.08	0.16
JT 60SA	34	10^4	0.34	0.22	0.19	0.15	0.27
EAST	24	10^5	2.4	1.6	1.2	0.82	1.8
ITER	100	10^6	100	77	6.4	44	92
FDF	100	10^7	1000	610	500	340	740
DEMO Reactor	400	$2.5x10^7$	10000	6500	5300	3700	7900

1.4 Motivation Behind This Dissertation

The lifetime of fusion reactor plasma facing components (PFCs) can be limited by a number of different and often competing factors. Erosion by sputtering can wear through components reducing their thickness, strength, and integrity. The most intense erosion rates are expected at limiter and divertor regions, where ion flux and plasma temperatures are the highest. As the eroded material becomes ionized it can be promptly redeposited (possibly reducing the erosion rate [15]), transported to net deposition regions where it can accumulate and cause detrimental buildup on plasma-facing surfaces or diagnostics [16–18], or accumulate as impurities in the core reducing burning plasma performance [19]. The current design choice for ITER uses W for divertor targets due to its low sputtering rate, with Be for the first wall and limiter surfaces. It is expected that the ITER main wall and limiter PFCs will be in a net erosion state with much of the net eroded material migrating to the divertor targets , where it would undergo

deposition and re-erosion and accumulate on shadowed or scrape-off-layer (SOL) surfaces [20–24]. This type of material accumulation leads to retention of tritium fuel by co-deposition [11,25], which is a serious concern for fuel self-sufficiency of any fusion power reactor [26,27] and poses an increased radiological safety risk.

Experiments in recent years have addressed different aspects of the material erosion migration problem for low-Z first wall materials. Measurements of the erosion rates on mid-plane limiter surfaces have been conducted on EAST and JET (C in EAST [28,29], Be in JET [30–32]), confirming the overall net positive erosion expectation. Isotopic tracer studies conducted in DIII-D have shown that about half of the C impurities injected as ^{13}C-methane into the edge plasma transport and deposit in the near SOL outside of the inner and outer divertor strike points [14,33,34]. However, the other half of the injected ^{13}C appears to have been deposited short-range, on the main wall or in the secondary divertor region. The idea that the wall is a source of sputtered impurity which all ends up in the divertor sink is too simplistic: parts of the wall are in a state of net erosion while other parts are in a state of net deposition from wall sources elsewhere. Additionally, within the region immediately surrounding the strike points there are net erosion and net deposition zones that change with varying strike point location and plasma confinement mode [35]. Experimental measurements of Be erosion in the divertor region is limited as there currently is no tokamak facility capable of making controlled and characterized measurements of Be erosion and deposition in a divertor target region. ITER plans to use an unbalanced double null configuration with a secondary divertor at the top clad with toroidally shaped Be targets where potentially high rates of localized erosion and deposition may occur [36]. It is not obvious whether the eroded Be will migrate to the primary (lower) divertor or redeposit locally in the secondary (upper) divertor. Current

estimates of the ITER wall lifetime in these regions relies on extrapolation from and modeling of the JET ITER-like Wall (ILW) whole-machine migration results [37–39]. Benchmarking existing models of erosion and deposition requires controlled and well characterized erosion source and background plasma.

Motivated by these considerations, we have made controlled erosion measurements of Al in the divertor region of three different attached L-mode plasmas in DIII-D using the DiMES facility [40]. We chose to employ the material Al as a proxy for Be, the use of which is restricted in DIII-D and many other facilities due to its toxicity. Al is a practical material to use for this research because it is easily discernible from the background PFC materials in DIII-D (namely C and B), has a low vapor pressure (compared to Li or Mg) and high melting point (compared to Li). In addition, Al has a strong spectroscopic emission signature for both neutral (Al-I) and ionized (Al-II) emission enabling measurement of its erosion with relatively short exposure times. Al also shares similar surface binding energy, and oxide and hydride chemistry with Be [41]. Al is a potentially informative low-Z material for this study because it shares some properties representative of a low-Z material in that it is sputtered primarily by the main ions (rather than by impurity ions) at relatively low plasma temperatures (~15eV) and has a long ionization length compared to its gyro-radius ($\langle\lambda_i\rangle/r_{gyro} \sim 2.5$). It has a ratio of the ionization length to gyro-radius that is lower than Be, Li, or C, but still long enough that prompt redeposition without the presence of the sheath electric field ought not to be dominant. Al atoms are sputtered with relatively high velocities and can penetrate into the plasma with an ionization mean free path (MFP) in the divertor of the order of the Chodura sheath scale length (1-2mm). This is important, as it means the redeposition of Al should be sensitive to the sheath structure, e.g. the sheath potential and density

gradients. In all erosion models, the sheath determines the incident ion energies, and the rate of material redeposition. The sheath electric field gradient is one of the primary forces that accelerates ions back toward the surface, driving erosion but also redeposition of sputtered material. On the other hand, the exponential decay of the electron density toward the surface extends the ionization front away from the surface and reduces the likelihood of redeposition.

Chapter 2
Background and Literature Review

2.1 The Plasma Sheath

Plasma-material interactions occur at the boundary between a solid surface and a plasma, two states of matter that span orders of magnitude in scales of temperature, density, and energy. Plasmas in general are charge neutral, such that the density of ions n_i is equal to the density of electrons n_e and no net electric fields exist. However, in the region of the plasma near an absorbing surface like a wall, a layer of net space charge arises spontaneously due to differences in the electron and ion thermal speeds. Electrons have a much higher thermal velocity compared to the ions, so that they reach the wall before the ions and charge it to a negative wall potential. This sets up an electric field that accelerates ions toward the surface and creates a very thin region of net positive space charge density ($n_e < n_i$) called the Debye sheath (DS). The characteristic length of the charge imbalance is equal to the plasma screening length, or Debye length $\lambda_{Debye} = \sqrt{\varepsilon_0 k T_e / e^2 n}$. The DS is also characterized by the so-called Bohm criterion [42], which says that the ion velocity at the sheath entrance v_{se} must be equal to or greater than the plasma acoustic speed:

$$v_{se} \geq c_s = \sqrt{k_B T_e / e m_i} \tag{2.1}$$

In tokamak edge plasmas, a strong magnetic field exists that is usually inclined at a small angle with respect to the wall. The gyro-motion effect of the ions and electrons in the inclined magnetic field results in the formation of an additional sheath region called

the magnetic pre-sheath (MPS), also known as the Chodura sheath (CS), as shown in Figure 2-1. The MPS is a region of quasi-neutrality with significant E-field directed perpendicular to the surface with thickness on the order of the ion gyro-radius (~mm).

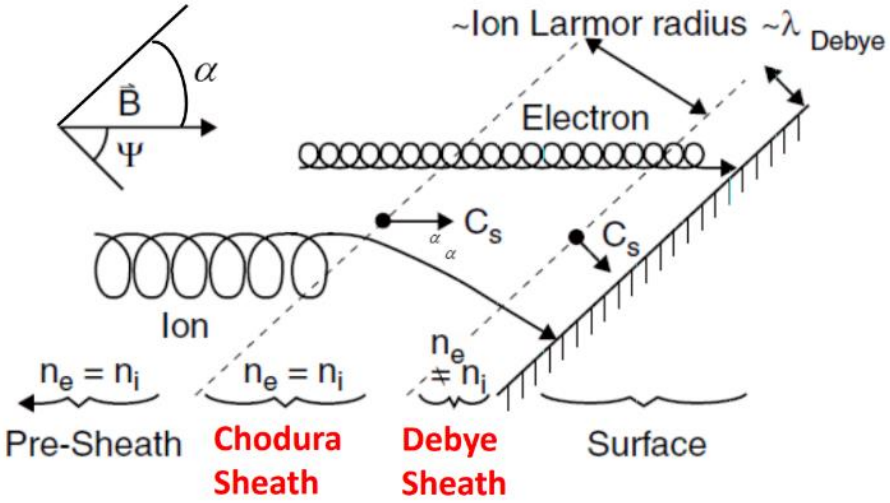

Figure 2-1. Schematic of the plasma sheath in an oblique magnetic field [42]

Particles enter the MPS along magnetic field lines from the so-called collisional pre-sheath (CPS) that connects to the neutral plasma. The CPS has length scales on the order of the ion-neutral collisional mean free path (cm to m), and extends along magnetic field lines into the so-called scrape-off layer (SOL) of the plasma. In this region, ions sourced from the plasma are driven toward the wall, which can be treated as an ideal sink. The plasma flows rapidly along field lines toward the walls, where the maximum flow speed parallel to the field at the exit of this region is sonic ($v_{\parallel} = c_s$). This so-called Chodura criterion is used by fluid models [43–45] to constrain the boundary between CPS and sheath edge, thus defining the velocity at the MPS edge (MPSE) as $v_{MPSE} = \sqrt{T_e/m_i}$.

A description of the MPS was first produced by Chodura [43] using a particle-in-cell simulation and fluid model. The model was constrained by the boundary conditions Chodura criterion at the MPSE and the Bohm criterion at the DS. The other constraint in

the models is that the total potential drop across the combined DS and MPS is limited to $\sim 3kT_e$, the same as for a non-magnetized sheath, and is nearly independent of the field inclination angle. Chodura determined the thickness of the MPS to be equal to $\lambda_{mps} = \sqrt{6}\rho_{ion}\sin(\alpha)$, where $\rho_{ion} = {m_i c_s}/{eB}$ is the ion gyro radius. The normalized electric potential in across the MPS is given as $e\Delta\phi_{CS}/kT_e = \ln(\sin\alpha)$, where α is the angle between the magnetic field and surface plane. The potential drop breaks down as the angle approaches tangency with the surface, since as $\alpha \longrightarrow 0$, $\Delta\phi_{CS} \longrightarrow \infty$.

Recently fluid models [45] and kinetic simulations [46] of the magnetized sheath structure extend the Chodura sheath model to include magnetic field pitch angles (angle with respect to the surface plane) of smaller than ~5 degrees. At a floating wall, the total potential drop across the MPS and DS is shown to be:

$$e\Delta\phi_{floating}/kT_e = 0.5\ln\left(\left[\frac{2\pi m_e}{m_i}\right]\left[1+\frac{T_i}{T_e}\right]\right) \quad (2.2)$$

Thus, at small α, when the potential drop across the MPS equals this total the Debye sheath (DS) essentially ceases to exist and the entire sheath is defined by the MPS. The critical angle α^* between the magnetic field and surface plane of:

$$\alpha^* = \arcsin\left(\sqrt{2\pi(m_e/M_i)\cdot(1+T_i/T_e)}\right) \quad (2.3)$$

Which is roughly 3-5 degrees in DIII-D plasmas. Shown here in Figure 2-2, are the electron density and normalized sheath potential versus distance from the wall over a parametric scan of the magnetic field, as calculated using the kinetic particle-in-cell model in [46].

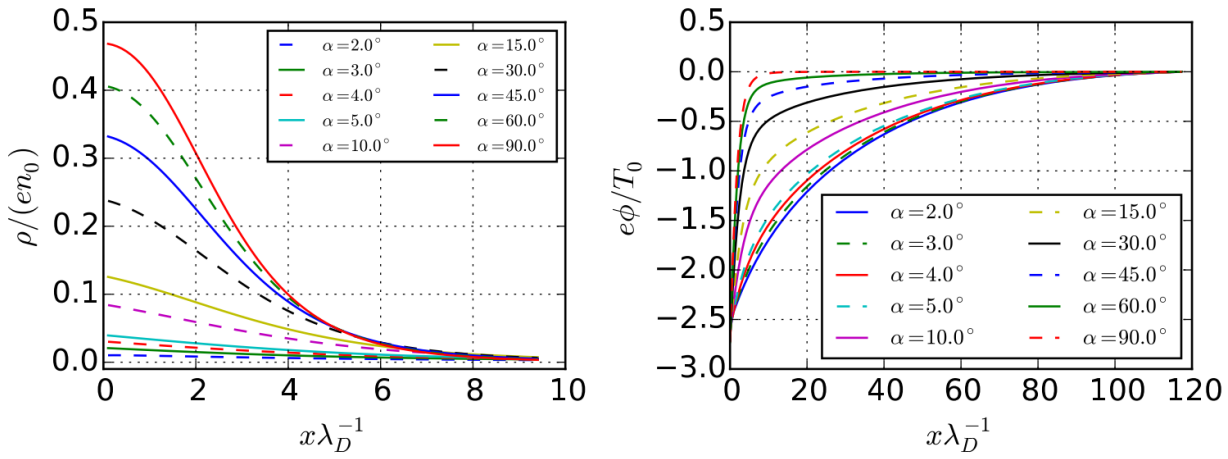

(a) (b)

Figure 2-2. Reproduced with permission from [46]. Spatial profiles of the space charge density within a few Debye lengths of the surface (a) an the electric potential out to 120 Debye lengths (b) for a collisionless case with deuterium ions.

Based on these models, convenient expressions for estimating the sheath density gradients for different magnetic field incidence angles and plasma temperatures have been made by Borodkina [42,43]. The relevant expressions for the MPS structure are summarized in the following equations:

$$n_e = n_{e0}\exp(\psi) \tag{2.4}$$

$$\psi(z) = \psi_w \exp(-2z/L_{MPS}) \tag{2.5}$$

$$\psi_w = \frac{1}{2}\ln\left(2\pi\frac{m_e}{M_i}\frac{T_e+T_i}{T_e}\right) \tag{2.6}$$

$$L_{MPS} = k\rho_i\cos(\alpha) \tag{2.7}$$

In these expressions, electron density n_e in the sheath region follows the Boltzmann relation (Eq. 2.4), , where ψ is the dimensionless potential in the sheath, $\psi = e\phi/kT$. The floating potential at the wall, ψ_w, was shown by [39] to be approximately independent

of magnetic field angle and equal to the standard potential for non-magnetized plasmas (Eq. 2.6). $\mathrm{L_{MPS}}$ is the characteristic length of the magnetic pre-sheath (Eq. 2.7), and z is measured perpendicular to the solid surface. The length $\mathrm{L_{MPS}}$ is assumed to be specified by a numerical factor k, which is the multiplier of the larmor radius ρ_i of a main-ion at the plasma sound speed $c_s = \sqrt{(T_e + T_i)/m_i}$, projected through the magnetic field pitch angle α. This corresponds to Chodura's finding that $\mathrm{L_{MPS}} \sim \mathrm{several} \times \rho_\mathrm{i} \cos(\alpha)$ [43].

There have been relatively few experimental studies aimed at characterizing the magnetic pre-sheath, and none have been made in tokamak plasmas. In cylindrical laboratory plasma devices, emissive probe measurements were used to measure the MPS potentials with different applied magnetic field in [47] and with different ion-neutral collisionality in [48]. Recently, measurements of the 2D velocity profiles in low density Ar plasmas were made with magnetic field angle of 16-60° with respect to surface normal by Siddiqui et al. [49,50]. The measurements agree well with a 1D fluid model similar to that presented by Riemann [44,51] and Ahedo [52], although some disagreement starts to appear in the velocity measurements near the surface at the larger field angles. $\vec{E} \times \vec{B}$ flows as large as 40% of the plasma sound speed c_s were measured. The ion-neutral collision length is significantly shorter in these laboratory plasmas than in the attached low density tokamak plasmas, and as a result the magnetic pre-sheath becomes more collisional and the effect of charge-exchange neutrals impacting the wall becomes significant. In the laboratory measurements of MPS flows and potentials, better agreement between the Chodura and Riemann fluid models was found at low neutral pressures (low ion-neutral collisionality). Measurements also deviated more from the Chodura fluid model at field angles greater than 60° with respect to the surface normal.

2.2 Basic Plasma Material Interactions

At the interface between a plasma and a solid material, there arises a transition layer called a sheath where a space charge and electric field develops that accelerates ions toward the surface. When energetic charged and neutral particles from the plasma strike a material surface, material modifications occur within the range of ion-solid interaction (a very shallow depth of just the first few atomic monolayers of material). A schematic depiction of the plasma-material interaction environment is shown in Figure 2-3. Ions striking the surface can implant below the surface, and create a damage cascade that may eject, or sputter, material back into the plasma. With the abundance of energetic ions and electrons present near the surface, molecules readily dissociate and recombine, leading to a rich surface chemical interactions. Formation of volatile compounds on the surface can remove material (a process known as chemical erosion), while chemisorption of plasma-modified compounds can lead to hard deposits of mixed materials. Atoms removed from the surface enter the plasma and become ionized and can be accelerated back toward the surface, leading to self-sputtering and re-deposition. In this section we will introduce the basic plasma-material interaction processes that occur within this region.

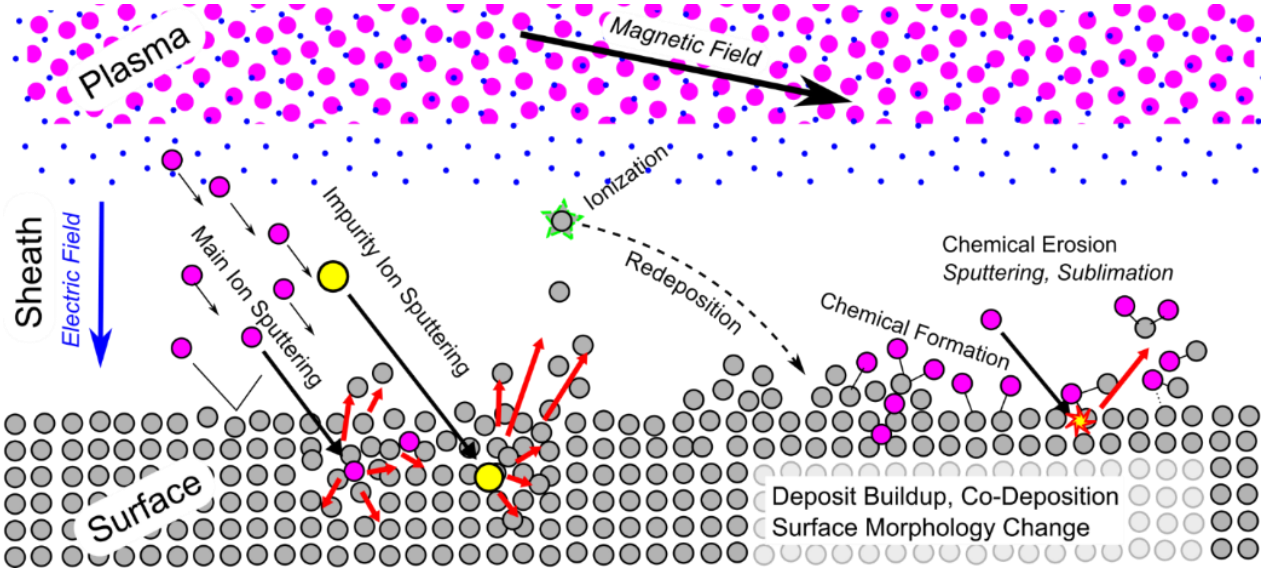

Figure 2-3. Schematic summary of the typical plasma-material interaction processes, adapted from [53].

2.2.1 **Physical Sputtering**

The process of physical sputtering is the removal of atoms from the surface of a material as a result of energetic particle impact. Physical sputtering can occur for any material, and can involve any incident ions or neutrals with sufficient energy. Sputtering occurs when an ion impact deposits enough energy into a surface through atomic collisions such that the ensuing collision cascade creates recoils that collide with surface atoms from within the material. When the surface atom receives enough energy from the cascade to overcome its surface binding energy, it is ejected or sputtered from the material. In each atomic collision, the energy transferred between the incident particle of energy E and a stationary target atom is determined from elastic collision theory:

$$E = \gamma E_0(\cos\theta)^2 = \frac{4m_1m_2}{(m_1+m_2)^2}E_0(\cos\theta)^2 \quad (2.8)$$

Where E_0 denotes the initial projectile energy, and m_1 and m_2 are the projectile and target masses, respectively. θ is the scattering angle. The maximum energy transfer factor $\gamma = 4m_1m_2/(m_1 + m_2)^2$ for projectile mass m_1 and target atom mass m_2 [42].

Physical sputtering will occur only if the energy transferred to a surface atom exceeds the surface binding energy. When calculating the energy transfer through the collision cascade, models generally assume one of two different types of sputtering collision cascades as schematically depicted in Figure 2-4. For higher energy or heavier incident particles, sputtering results from many collisions within a large collision cascade as in Figure 2-4 (a) because of the larger amount of energy transferrable to the primary knock-on atom (PKA). The ensuing collision cascade results in a nearly isotropic distribution of sputtered atom energies and directions from the surface. For some low energy or light ion sputtering processes, a significant fraction of sputtered atoms can be ejected by direct collision with a recoiling projectile as in Figure 2-4 (b). In this case, the sputtered atoms can carry some of the incident particle's momentum which can lead to higher sputtered energies and non-uniform directional distributions.

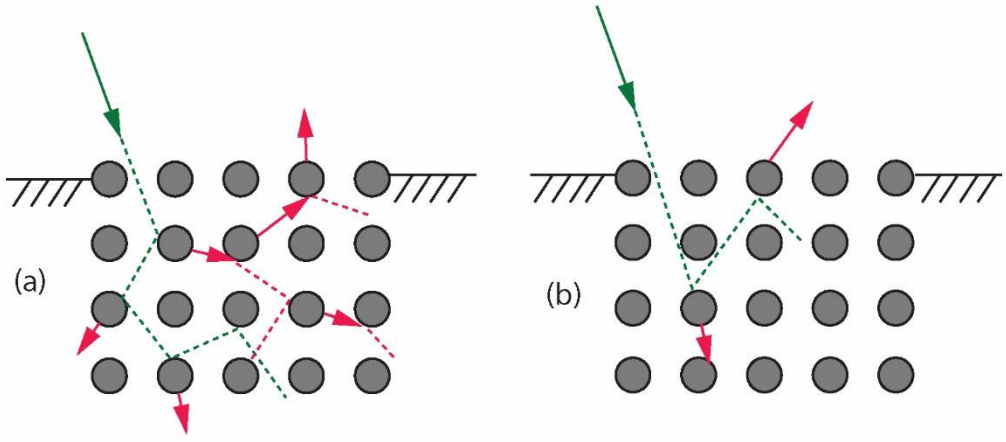

Figure 2-4. Comparison of the sub-surface collision cascades. A linear cascade for heavy or high energy ions (a) and single knock-on recoil cascade for light or low energy ion sputtering (b). Adapted from [54] .

The efficiency of the process, known as the sputtering yield, is described in terms of the number of ejected atoms per incident particle. A widely used analytical formula for calculating sputtering yields was introduced in 1984 by Bohdansky [55] and later revised by Garcia-Rosales, Eckstein and Roth [56]. This formula is based on analytic sputtering theory and describes the sputtering yield as a function of the energy E of a projectile impacting a surface at normal incidence. The formula is expressed in the following four equations for incident particle with energy E_0, atomic number Z_1 and mass M_1, and target with atomic number Z_2 and mass M_2:

$$Y(E) \sim Q s_n(\varepsilon) \left[1 - \left(\frac{E_{th}}{E}\right)^{2/3}\right]\left[1 - \frac{E_{th}}{E}\right]^2 \quad (2.9)$$

$$s_n^{KrC}(\varepsilon) = \frac{0.5 \ln(1 + 1.2288\varepsilon)}{\varepsilon + 0.1728\sqrt{\varepsilon} + 0.008\varepsilon^{0.1504}} \quad (2.10)$$

$$\varepsilon = E_0 \frac{M_2}{M_1 + M_2} \frac{a_L}{Z_1 Z_2 e^2} \quad (2.11)$$

$$a_L = 0.4685\left(Z_1^{2/3} + Z_2^{2/3}\right)^{-1/2} \text{Å} \quad (2.12)$$

Where $Y(E)$ is the energy dependence of the normal incidence sputtering yield, E_{th} is an empirical target-dependent sputtering energy threshold, Q is a modification parameter dependent on the type of sputtering (such as light ion sputtering or near threshold sputtering) on. s_n^{KrC} is the nuclear stopping cross-section based on the Kr-C potential [57] for the ion-target combination, ε is the reduced energy, and a_L is the Lindhard screening length.

Another factor that influences the sputtering yield is the incidence angle between the impacting ion and the surface. Generally, the sputtering yield increases from normal incidence up to ~55-85 degrees, then decreases as incident particle reflection dominates at glancing angles. An empirical formulation of the angular dependence of sputtering by Yamamura [58] is listed below:

$$\frac{Y(\theta)}{Y_0} = \left(\frac{1}{\cos(\theta)}\right)^f \exp\left[-\Sigma\left(\frac{1}{cos(\theta)} - 1\right)\right] \quad (2.13)$$

Where f and Σ are adjustable parameters determined from least-squared fit to experimental data and Y_0 is the normal incidence sputtering yield. As the total sputtering yield increases with incidence angle, the angular distribution of sputtered material also becomes less isotropic, developing a preferred angle of emission in line with the primary knock on atom recoil trajectory [59].

There are many other factors that can affect the sputtering yield of materials in practical situations that are difficult to capture with sputtering theory. Mixed material effects, surface morphology, flux and temperature dependence are a few of these factors. Experimental measurements of sputtering are often made using ion beams to bombard different materials, measuring the total yield by weight loss, film thickness change, material collected on a catcher plate, or quantitative spectroscopy. A compilation of experimentally measured sputtering yields is available in [60]. Experimental measurements of the yield can often be challenging, especially near the threshold since the surface sensitivity of the process lends itself to many confounding variables such as dynamic evolution of surface roughness, surface contamination, and alignment effects.

The stochastic process of sputtering also lends itself well to computer simulations. Since the sputtering process is stochastic, involving many atomic collisions, numerical simulation is often used for estimating sputtering properties of materials. One of the most widely used sputtering modeling codes is SDTRIM.SP [61], also known as TRIM, or TRIM.SP. SDTRIM.SP is a binary collision approximation (BCA) modeling code, i.e. it assumes collisions between atoms can be approximated as described above by elastic binary collisions, and that the energy loss to electrons can be handled separately as an inelastic, friction-like energy loss. It assumes amorphous target structure and determines the path of the primary particle and its recoils inside of the target.

Some example sputtering yields calculated by SDTRIM.SP are shown in Figure 2-5. Total sputtering yield versus energy for normal incidence Helium ions on Al, C, W, and Be are shown in Figure 2-5 (a). Tungsten (W) has the lowest sputtering yield and highest threshold for sputtering owing to its high mass and low collisional energy transfer per collision with He ions. The SDTRIM.SP example calculation of the angular dependence of D ion sputtering of Be and Al are shown in Figure 2-5 (b), shown relative to the normal incidence sputtering yield. The relative angular sputtering enhancement is greater for higher incident energies, shown here comparing 100eV to 200eV incident energy D atoms.

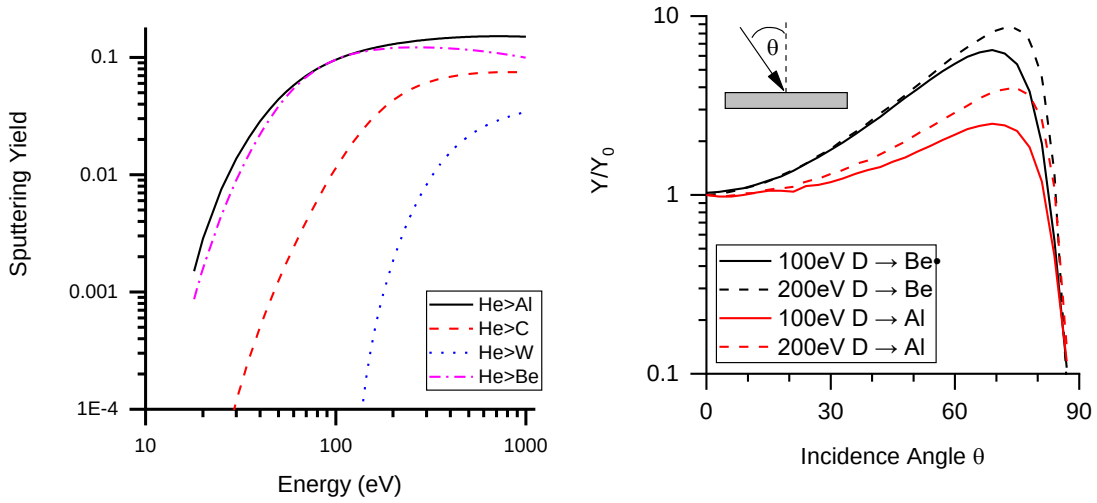

Figure 2-5. Sputtering yields for He ions incident on various elements of interest, calculated using SDTRIM.SP 5.07 [61].

2.2.1.1 Energy of sputtered particles

For sputtering caused by a thermalized cascade of sub-surface collisions, the energy of the sputtered neutrals is often well approximated by a Thompson distribution [62], truncated at a maximum energy based on the impacting energy. The truncated Thompson energy distribution is given as

$$f(E) \propto \left[\frac{E}{(E+E_B)^3}\right]\left\{1-\left[\frac{E+E_B}{E_{max}}\right]^{\frac{1}{2}}\right\} \qquad (2.14)$$

where E_B is the surface binding energy (3.4eV for Al), and E_{max} is the maximum ejected energy at which the distribution is truncated. We know from binary collision theory that the maximum elastic energy transfer between a projectile particle of mass M_1 and target mass M_2 is $\gamma = 4M_1M_2/(M_1+M_2)^2$. For an atom ejected by a recoiling light projectile ion $(M_1/M_2 < 0.2)$, the maximum energy for the ejected particle is thus $E_{max} = \gamma(1-\gamma)E_{impact} - E_B$. For heavier projectile ions $(M_1/M_2 > 0.2)$, the value of maximum sputtered

energy $E_{max} = 8(M_1/M_2)^{0.4}E_{impact} - E_B$. From this distribution, one finds that the for most ion-target combinations the most probable sputtered energy is roughly equal to half the surface binding energy while the average sputtered energy can be significantly higher, up to ~ $\gamma E_{impact}/2$. For sputtering by low energy or light ions, the energy distribution can be quite different than the Thompson due to surface atoms being sputtered by the direct recoil of the incident ion. Different analytical formulations of the energy distributions in these cases have been proposed by [54,63].

As the total yield increases, so does the average sputtered energy. The energy distribution of sputtered atoms emitted at the preferred angle of emission deviates from the Thompson distribution due to a larger fraction of the ejected particles carrying more energy and momentum of the incident particle. Recent experimental measurements by Goehlic, et al [64,65] have measured how the sputtered energy distribution depends on the incidence angle of sputtering ions. The experiments used laser induced fluorescence to measure the energy distribution of Al atoms sputtered from atomically smooth, evaporated thin films at different angles by low-fluence Ar and Xe ion beams. The measured energy distributions were well reproduced using the TRIM.SP modeling code [61,66], which is able to separate the distribution into superimposed components and show that the high energy tail was due to direct recoil of atoms from the incident particles. Figure 2-6, reproduced from [64], compares the measured energy distribution for Al sputtered by 500eV Xe ions at an incidence angle of 70° with respect to the surface normal. Forward-sputtered (at +50°) at backward-sputtered (at -50°) energy distributions are compared (closed and open symbols respectively), and plotted along with the TRIM.SP modeled energy distributions (solid and dotted lines).

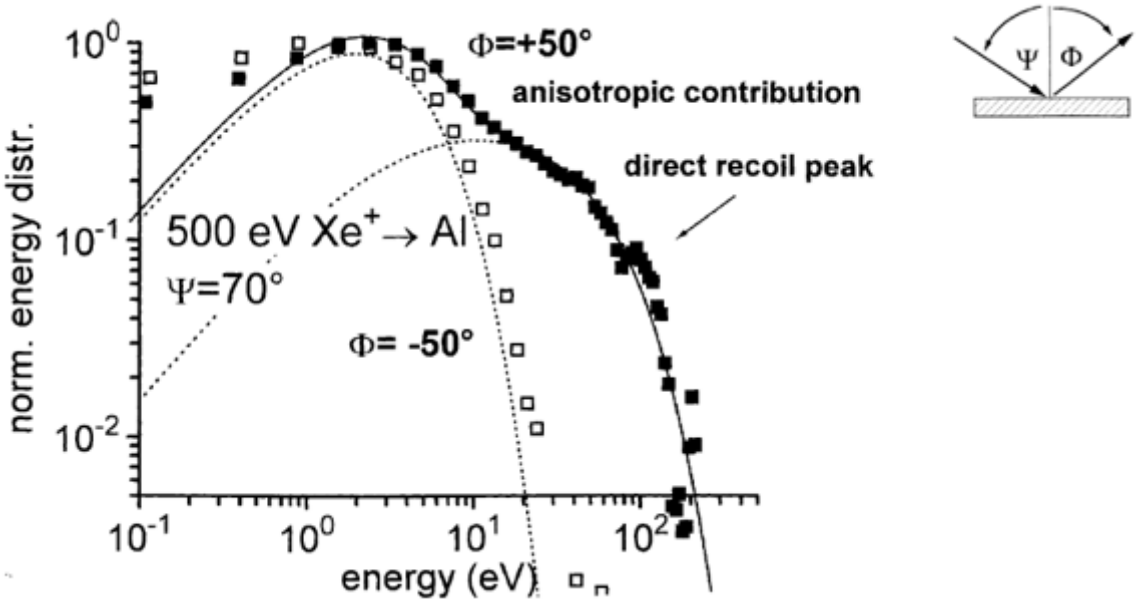

Figure 2-6. Reproduced with permission from [64].Energy distribution for 500eV xenon bombardment of aluminum at oblique incidence (PSI=70deg). The distributions detected in the forward direction (phi=50deg, solid squares) and in the backward direction (phi = -50deg, open squares) are plotted on a a double logarithmic scale. Both summands of the energy distribution are plotted as dotted lines

2.2.2 **Chemical Sputtering**

Chemical sputtering refers to the removal of surface material by the formation of volatile compounds after chemical interaction with background plasma species. Unlike physical sputtering, chemical sputtering is highly sensitive to surface temperature and surface/ion species combinations. Carbon, in the form of graphite or carbon fiber composites, can be a very capable material with excellent thermal properties and good plasma compatibility but readily forms hydrogenic compounds at low temperatures that are easily released from the surface at low temperatures. Chemical sputtering of carbon has been widely studied in the fusion community as a significant cause of material erosion, even at low ion bombarding energies [67–70]. Another form of chemical sputtering, often called chemically enhanced erosion or swift chemical sputtering [71–

73], occurs when chemical reactions between incident ions and the surface restructure of the surface bonds in a way that can reduce surface binding energy and enhance physical sputtering of the material. Carbon materials can also form amorphous hydrogenic compounds after bombardment by hydrogen that can react with background oxygen release volatile compounds [74]. Tungsten can also be chemically eroded at high temperatures in the presence of oxygen impurities, through the formation of volatile oxides WO2 and WO3 [75]. Beryllium has been shown to form hydrides, and in several experiments has been found to have enhanced erosion rates in hydrogen plasmas [73,76].

2.2.3 **Surface roughness effects**

Surface roughness is an important parameter relevant to practical plasma facing component design because it can affect the rates of erosion and prompt redeposition for all materials. The geometry of the surface roughness can prevent some sputtered particles from escaping the surface due to line-of-sight redeposition to the surface, as is depicted in Figure 2-7. Such dependence of the total sputtering yield on ion impact angle and surface roughness has been studied extensively in several past works for fusion relevant PFC materials [77–80]. As Haasz and others have shown, in addition to reducing the sputtering yield, the presence of surface roughness can reduce the angular dependence by randomizing the local ion-surface impact angle and enhancing prompt recapture of sputtered material.

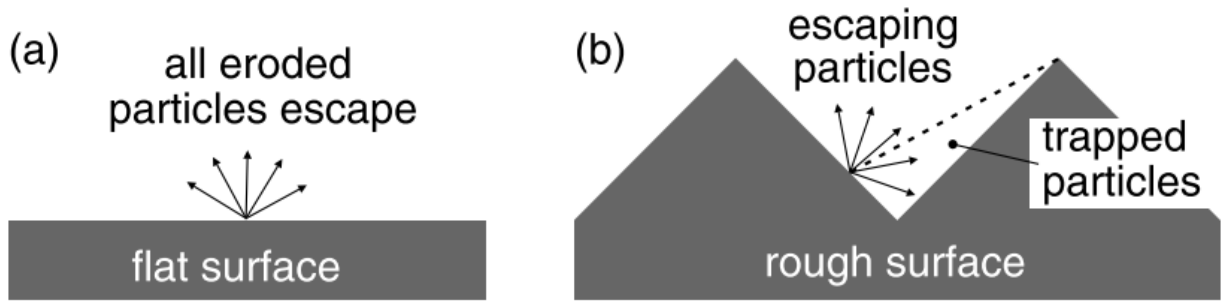

Figure 2-7. Reproduced with permission from [81]. Illustration of enhanced prompt recapture of sputtered particles on rough surfaces.

Most surfaces develop some form of ion-induced morphology change with enough ion fluence. These changes can case surface roughness to develop on initially smooth surfaces, in the form of ripples, islands, blisters, or tendrils. Alternately, pre-existing surface roughness can be modified, even eroded or polished away. Sputtering, can exacerbate roughness when the existing features have variations on the order of the atomic collision cascade. The so-called curvature-dependent sputtering instability [82] occurs because of local variations of the erosion rate that amplify the surface curvature with enhanced erosion of troughs compared to local peaks. Additional roughness promoters can exist in the surface such as seeding contaminants, preferential sputtering along certain crystal facets [83]. These processes are often enhanced at particular ion energies, ion incidence angles, and at higher ion flux.

Sputtering can also reduce surface roughness by tailoring the incident ion flux, energies, and angles. Recent studies have developed methods for both shaping and polishing surfaces to sub-nm precision for the semiconductor, magnetic storage technology, and sophisticated extreme ultraviolet (EUV) optics industries. An extensive review ion induced smoothening processes can be found in [84]. A few smoothening mechanisms relevant to this study involve direct ion sputtering with grazing angle ions (ion incidence angles <10° with respect to the surface plane) whereby surface roughness

decreases due to combination of shadowing and enhanced erosion of surface protrusions or step edges [85–87]. This mechanism, illustrated in Figure 2-8, has been used by Hirata et al. [88] to produce atomically smooth diamond films. There are also relaxation mechanisms which can counter the growth of surface roughness, such as thermally activated surface diffusion and recrystallization, or ballistic transport and reorganization of surface atoms due to the incident ion flux [89].

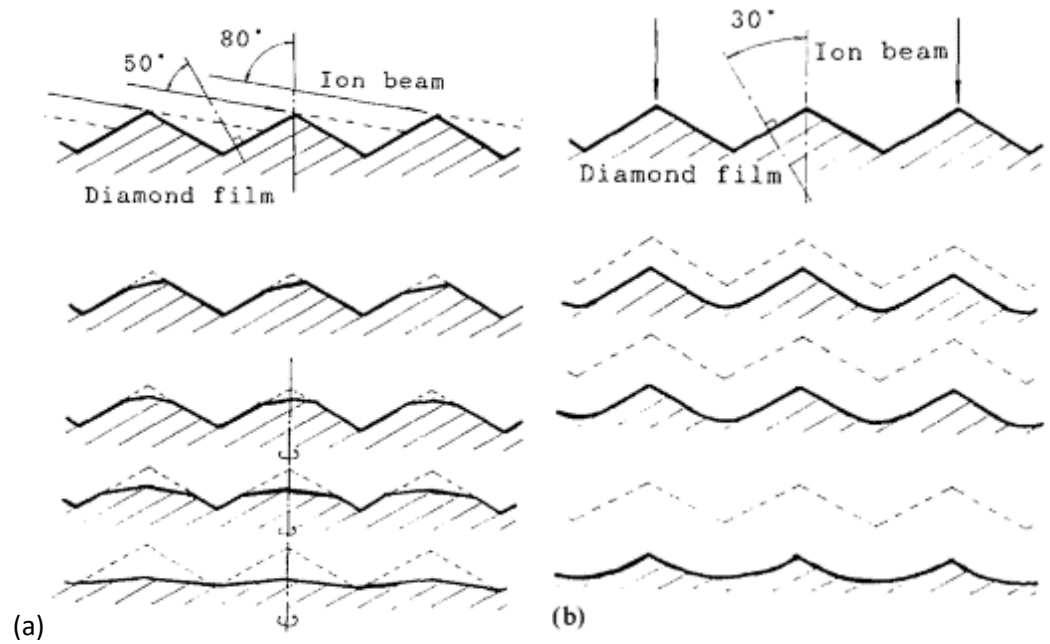

Figure 2-8. Reproduces with permission from [88]. Evolution of surface roughness under glancing angle ion bombardment leading to surface smoothening (a) compared to ripple formation under near normal incidence bombardment (b).

Some extreme examples of ion induced morphology development have been shown for fusion-relevant PFC exposure conditions. The most notable of which is nano-scale fuzz growth on tungsten and other metals under high fluences of He ions [90]. Although not entirely understood, it has been characterized to occur in a narrow temperature window and at high ion flux. Beryllium surfaces have also shown the growth of dense patterns of steep angled cones or whiskers on Be surfaces under high flux He

and D bombardment [91]. Surface roughness development may also be different on operating tokamak surfaces in the presence of a deposition source continually replenishing material. Rough surfaces of tungsten in the AUG tokamak divertor [92] and carbon in TEXTOR tokamak limiters [81] have shown surface morphology and composition changes resulting from enhanced erosion near surface peaks and increased deposition in surface troughs.

2.2.4 **Ionization**

When atoms are emitted from a surface into a plasma of sufficient temperature, collisions with background electrons can excite and ionize the atoms, a process known as electron impact ionization. The process of ionization can be described according to the methods described in [93]. For a neutral traveling at a velocity v along s, the probability of ionizing within a differential length ds is proportional to the product of the local electron density $n_e(s)$ and ionization rate coefficient $\langle \sigma v \rangle$:

$$dW = n_e(s)\frac{\langle \sigma v \rangle}{v} ds \tag{2.15}$$

Let us define $P(s)$ as the probability that a particle has ionized after traveling a distance s, and $Q(s) = [1 - P(s)]$ as the probability that it has not. Thus, the probability of ionizing within a distance ds after traveling a distance s satisfies the differential equation:

$$dP(s) = [1 - P(s)]dW \tag{2.16}$$

In this equation, $P(s)$ is the cumulative density function (CDF) for ionization along a path length s. This function can be used to sample an ionization length using numerical

Monte-Carlo methods. For plasma with uniform density $n_e(s) = n_0$ the solution to Eq. 2.16 with boundary condition $P(0) = 0$ is

$$P(s) = 1 - \exp\left(-s\, n_0 \frac{\langle \sigma v \rangle}{v}\right) \tag{2.17}$$

This function can be used to numerically sample an ionization length λ_i using Monte-Carlo methods by solving for s. Given a random number ξ from 0 to 1, the ionization length will be:

$$\lambda_i = -\frac{v}{n_0 \langle \sigma v \rangle} \ln(\xi) = -\lambda_i \ln(\xi) \tag{2.18}$$

Often, it is useful to calculate the average distance to ionization, also known as the ionization mean free path. We can determine an analytical expression for the ionization mean free path $\langle \lambda_i \rangle$ by first finding the probability density function $F(s)$:

$$F(s) = \frac{dP(s)}{ds} = [1 - P(s)] \frac{dW}{ds} \tag{2.19}$$

The expectation value of this function is most probable distance before ionization, also known as the ionization mean free path $\langle \lambda_i \rangle$. For a uniform background electron density, it can be shown that the most probable distance for a neutral atom to travel before ionizing (the ionization mean free path) is

$$\langle \lambda_i \rangle = \int_0^\infty s\, F(s)\, ds = \frac{v}{n_e \langle \sigma v \rangle} \tag{2.20}$$

2.3 Erosion/Redeposition Experiments

When the plasma-material interaction at a plasma-facing surface leads to the removal of material, either due to physical sputtering, chemical sputtering, sublimation, or other process, it is generally referred to as erosion. In cases where atoms or molecules in the plasma deposit onto the surface, either through ion implantation or physical or chemical adsorbtion, it is generally referred to as deposition. Plasma-facing surfaces always exist in a balance of erosion and deposition, and the sum of the *gross* erosion and *gross* deposition rates results in the surface experiencing a *net* erosion or a *net* deposition rate.

When material is eroded from a tokamak plasma facing component and becomes ionized, it can be transported by the plasma back to the surface in a process called redeposition. The cycle of erosion, ionization, and redeposition repeats indefinitely and leads to a gradual migration of material from regions of net erosion to regions of net deposition. For atoms ionized outside of the sheath, transport along field lines can result in remote redeposition, that is redeposition onto separate surfaces e.g. from the first wall to the divertor or short range redeposition, that is redeposition back to the same surface from which the atom was sputtered e.g. from one part of the divertor to another. In some cases, if the ionization length is short compared to the gyro-radius (as is typical for many high-Z materials), redeposition can occurs within one ion gyro-radius. This process, known as prompt redeposition, can effectively reduce the net erosion rate of that surface.

Some of the first DiMES experiments conducted on DIII-D were used to measure the net erosion rates and redeposition profiles of various metals of interest to the fusion community [94–96]. The exposure of these samples was at the outer strike point of

attached, ELM-free H mode plasmas. Density measurements were reduced by a factor of 3 in the modeling to account for the expectation that ionization occurs within the sheath and not at the upstream plasma density. The specific modeling in this study accounted for large area erosion and redeposition with sub-gyro-orbit resolution of impurity transport, and calculated sputtering yields and energies using both analytical and numerical models for pure surfaces. The effects of surface roughness were included in the sputtering codes using a fractal surface geometry model [80], although it is not clear from the manuscript what fractal dimension was used or what its effects were on the results. Absolute sputtering yields (and therefore redeposition fluxes) were not properly calculated since material mixing effects (such as the reduction of surface concentration by deposition of carbon) was not included. The main goal was to compare the shape of the computed redeposition profiles, so instead the redeposition profiles were normalized to the measurement at -7mm. In the study, the authors assumed that the measured metal coverage was proportional to the redepositing metal flux at that location. The fact that no re-erosion of deposited metals was included (nor the erosion of the carbon on which the metals were redepositing) makes the apparent agreement between model and data seem fortuitous. For two of the elements, Mo and V (Figure 2-9 a and b, respectively), the shape of the redeposition profile that was modeled did not match the measured shape, an issue that was left un-answered by the study.

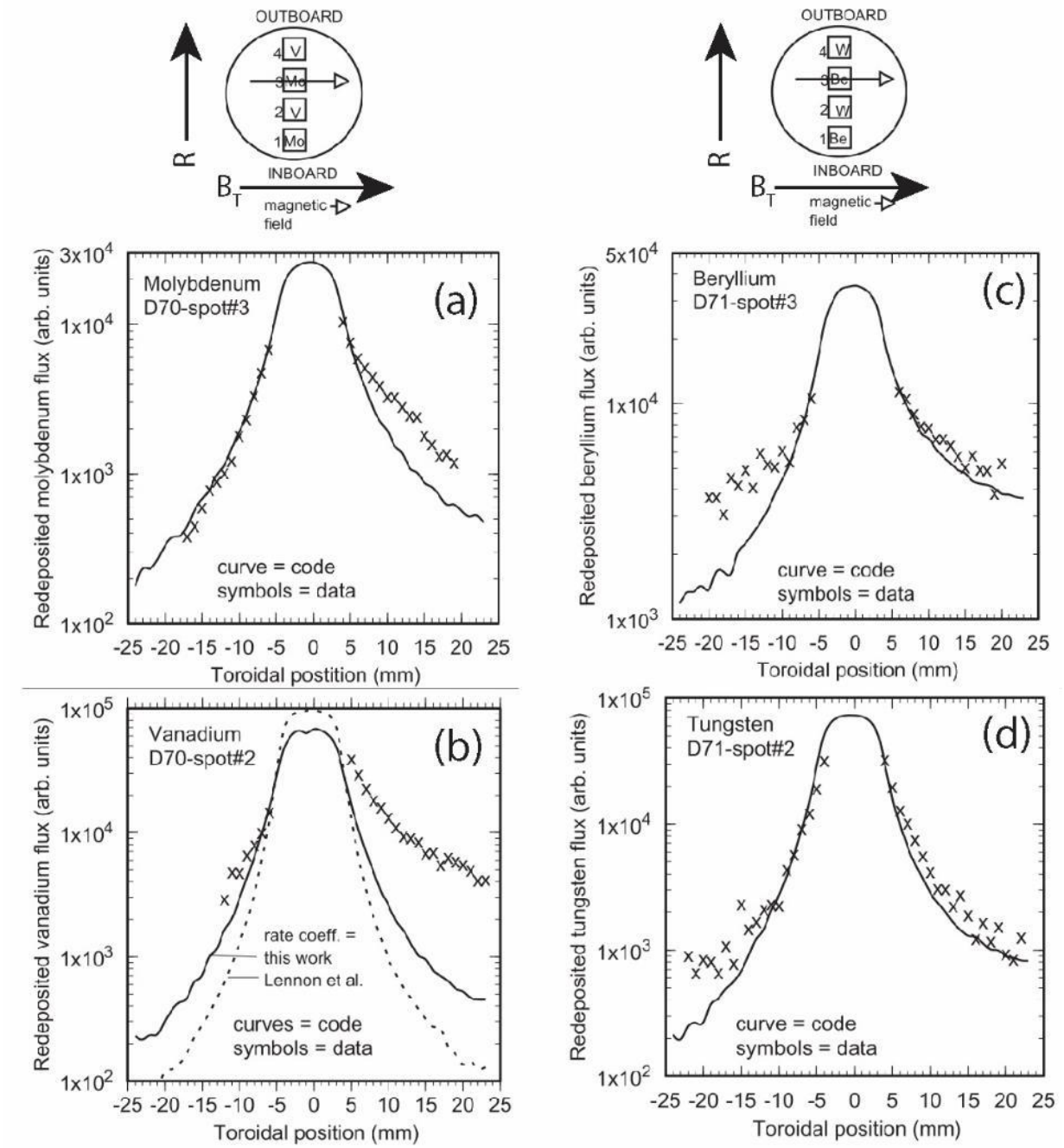

Figure 2-9. Reproduced with permission from [94]. Toroidal profiles of redeposited material measured for different materials (crosses) compared to models normalized to the data (lines). The diagrams at the top describe the sample geometry and show the scan direction with a white arrow.

More recent experiments have attempted to directly measure the net and gross erosion rate of Mo in lower single null L-mode plasmas [15] for comparison with existing models of erosion/redeposition. A 1cm diameter Mo-coated Si button was exposed

~2cm radially outboard of the outer strike point for a total of 28 seconds using the DiMES sample probe (shown in Figure 2-10 (a)). The average film thickness change was 11.6nm of net erosion, and the distribution of Mo redeposited on the graphite holder (shown in Figure 2-10 (b)) was a factor of 8-10 times larger on the downstream side of the sample compared to the upstream side. An initially surprising result was that only 19% of the Mo removed from the 1cm sample was found on the 5cm DiMES graphite head despite the fact that prompt redeposition was expected to be dominant for the eroded Mo, and the average deposition e-folding length was ~2mm. Later, modeling suggested that the low coverage was due to multiple re-erosion steps, and predicted a single-step redeposition fraction of 57%. The modeling also showed that without the MPS E-field, redeposition fraction would have been only 20% due to prompt redeposition within one gyro-radius. Although the gross erosion and redeposition rates were well matched by the modeling, the upstream/downstream distribution asymmetry was not well reproduced, as shown in the measured and modeled toroidal line profile of Mo coverage, Figure 2-10 (c). A similar discrepancy remained in the earlier models of Mo and V redeposition, as shown earlier in Figure 2-9 (a) and (b).

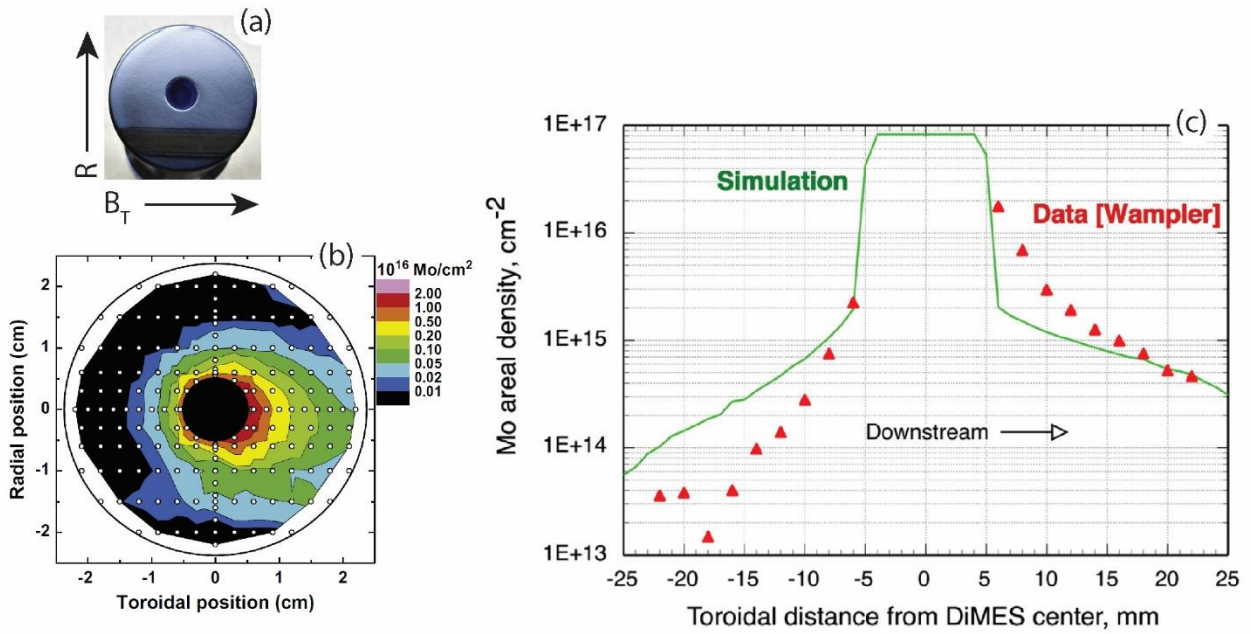

Figure 2-10. Previously measured [15] redeposition distribution from a DiMES exposure of molybdenum surface surrounded by graphite probe (a). 2D map of Mo areal density deposited on surrounding graphite (b). Mo areal density profile (c) shows data-simulation comparison using WBC-REDEP modeling of the Mo erosion/redeposition process [97].

Recent modeling [98] of the effects that the MPS E-field can have on redeposition suggest that prompt redeposition can also occur for materials with smaller gyro radii than ionization mean free path, if they are ionized within a region of MPS electric field. The model considered sputtered W which, despite its high-Z character, ionizes multiple times before completing a single orbit. It was shown that the MPS E-field dramatically increases the prompt redeposition fraction for W ionized within the MPS, despite the fact that the wide region of depleted electron density that occurs in the MPS has the effect of extending and broadening the ionization front away from the surface. An example of the calculated orbits for sputtered W are shown in Figure 2-11. Two landmark distances normal to the surface are shown in dashed lines: 10 deuterium gyro-radii signifying the end of the MPS and 1 deuterium gyro-radius signifying the region of strongest E-field. In the absence of the MPS E-field, W ions undergo multiple ionizations to higher charge

states, reducing the gyro-orbit and decreasing the prompt re-deposition fraction. When including the E-field, W redeposits at a distance much shorter than a singly charged gyro orbit radius. For low-Z ions which have much longer ionization lengths and can undergo multiple gyro-orbits within the region of weaker sheath electric field, the effect of the MPS E-field on redeposition is less obvious. The smaller radius orbits further out from the surface may lead to greater $\vec{E} \times \vec{B}$ drifts to drive the direction of material migration perpendicular to the field lines, and lower ionization states will mean atoms are driven toward the surface with less force.

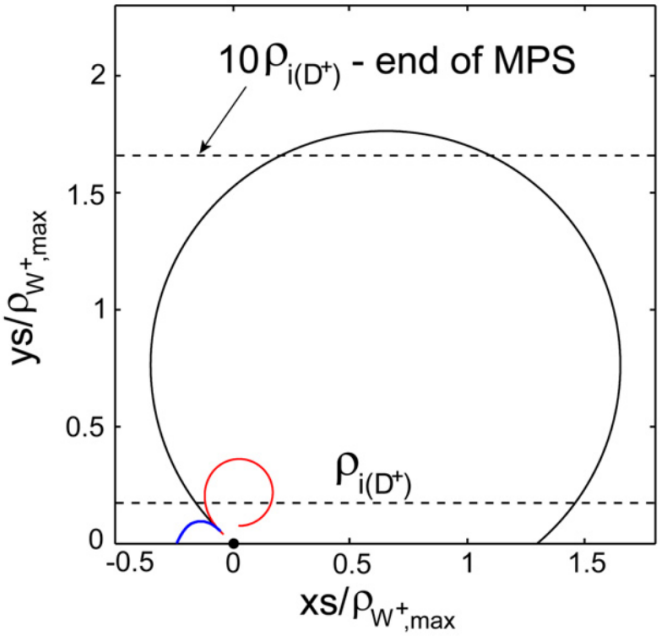

Figure 2-11. Adapted from [98]. Examples of individual orbits for W atom emitted from a surface at 135° at the point indicated on the horizontal axis. The B-field is parallel to the surface. The largest orbit (black, redeposited) is calculated with no electric field and no multiple ionizations. The medium orbit (red) is for the case with no E, but with multiple ionizations (to W^{7+}), and the smallest orbit (blue, redeposited) is for the case with both E and multiple ionizations.

2.4 Organization

The structure of this dissertation is organized as follows. In Chapter 3 we describe the experiment and basic principles of the measurements conducted. In Chapter 4 we present the first spectroscopic measurements of neutral emission anisotropy from sputtering of a controlled, localized eroding surface in a tokamak divertor plasma. The quantitative spectroscopic measurements are described and spectroscopic emission efficiencies are presented. In Chapter 5, we present an ionization-emission model that reproduced the observed anisotropy by assuming full angular sputtering yield distributions expected for grazing angle sputtering. The direction of presumed sputtering anisotropy was consistent with directional deposition patterns found within pores of the rough surface samples. The observations were an experimental validation of the predicted effects of the MPS on incident ion trajectories and subsequent sputtering distributions. In Chapter 6 we describe the physical measurements of erosion (film thickness change) and spatial distribution of Al redeposition. Changes to film composition and morphology caused by the plasma exposure are discussed, and the effective erosion yields are compared against expected sputtering yield values. In Chapter 7 we present a model of the multi-step migration (erosion, redeposition, and re-erosion) of Al which accounts for material mixing and the effect of surface roughness. The model is used to reproduces the measurements and determine the single-step redeposition efficiency in each plasma exposure case. In Chapter 8 we summarize our conclusions and propose possibilities for future experimentation and analysis based on our findings.

Chapter 3
Experimental Methods

3.1 The DIII-D Tokamak

DIII-D is a moderate-sized tokamak (vessel volume 39.6 m^3, major radius R=1.7m, minor radius a=0.68m, height 2.72 m) operated by General Atomics for the US Department of Energy, first commissioned in 1986 [99]. A cross-section of the vessel labeling individual components for reference is shown in Figure 3-1. The tokamak is controlled using a state of the art digital plasma control system (PCS) [100] that enables feedback control of the various tokamak actuators such as magnetic field coil power supplies, gas valves, and auxiliary heating sources. A set of 18 independently controlled, close-fitting plasma shaping coils enable a wide variety of poloidal cross-sections to be generated. Typical operating plasma currents are limited to 1.8-2.2 MA, at toroidal fields of up to 2.1 T. Auxiliary heating is achieved through a set of eight neutral beam (NB) sources (total injected power of about 20 MW), seven steerable 110 GHz gyrotrons (total injected power of about 3.2 MW), and two 60-120 MHz fast wave systems (injected power of about 2 MW). The typical full current plasma shot durations is 5-7 seconds. Internal plasma facing structures include dual (upper and lower) cryo-pumped divertor targets and three outer midplane radial bumper limiters.

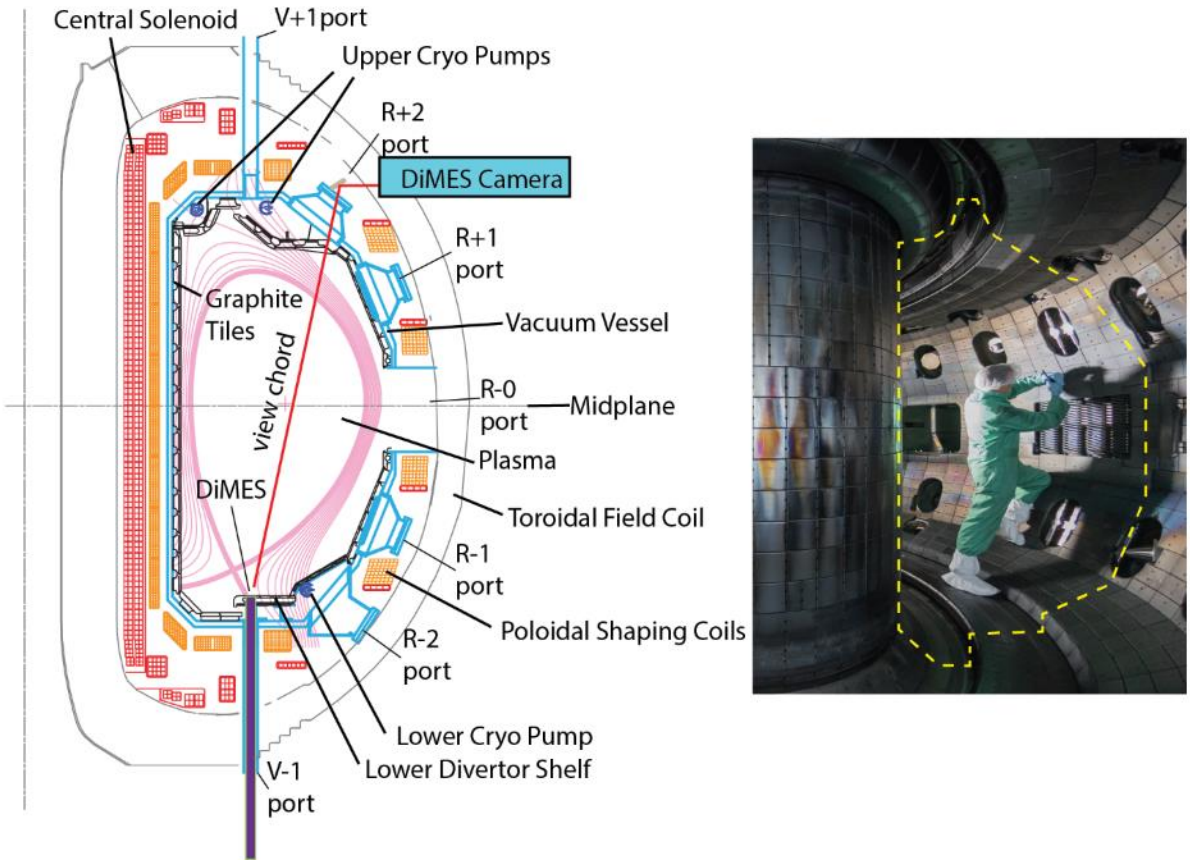

Figure 3-1. DIII-D tokamak cross section diagram, shown with lower single null plasma equilibrium, strike point positioned over DiMES with location of DiMES viewing camera diagnostic shown. Right: Interior photo of the vessel, showing worker and armor tiles, with dashed outline of poloidal section.

The DIII-D first wall consists of graphite armor tiles bolted to the water-cooled Inconel vacuum vessel or internal divertor support structures. Over 3200 tiles are used, each roughly 15x15x5cm in size, to cover a surface area of ~67m^2 (~90% of the outer wall and divertor area, limited only by openings for ports). All tiles are made from ATJ grade graphite manufactured by Union Carbide, except for limiter tiles which are made from Fiber Materials, Inc. 4D carbon fiber woven carbon matrix composite. Graphite was chosen as a wall material because of its high temperature capability, good thermal conductivity, and thermal shock toughness. The use of graphite (carbon) also reduces influx of metallic impurities from the vacuum vessel wall into the plasma which can cause

radiative cooling of the core. Typical maximum tile surface temperatures are at divertor strike point areas. During low power ohmic L-mode operation, peak tile surface temperature is typically ~150°C with peak strike point heat flux of ~30 W/cm^2, while during high power H-mode operation peak temperatures of ~1200°C are possible with average peak heat flux ~800 W/cm^2 [7].

Plasma fueling and density control is accomplished using piezoelectric gas puff valves [101] with control feedback from various plasma density and temperature measurements to achieve an average core density target programmed in the PCS. There are three toroidally symmetric cryogenic pumps, with plenums located behind the armor tiles at three locations: a lower cryo-pump underneath the lower outer baffle plate, and two upper cryo-pumps above the upper outer baffle plate and behind the upper inner corner dome tiles. An uncontrolled source of pumping and fueling also comes from deuterium adsorption and desorbed from the wall during plasma discharges. A number of wall conditioning techniques [102] are employed to maintain wall conditions as consistent as possible during each day and run period: Helium glow discharge cleaning between shots removes loosely bound D from surfaces; vessel baking up to 320-380°C between run campaigns to remove water and air (as in after a vent or long down period); and boronization (chemical deposition of ~90nm boron coating) of the vessel wall applied as needed between experimental campaigns to coat any unwanted surface impurities and provide an oxygen gettering layer for higher plasma purity.

3.1.1 **DiMES**

In the lower divertor of DIII-D, centered in an array of diagnostics described in Section 3.2, is the Divertor Materials Evaluation System (DiMES). DiMES is sample exposure station that uses a vacuum lock equipped linear transport mechanism designed to insert

a sample flush with the lower divertor shelf surface and later retract it for *ex-situ* analysis [40]. The system extends from a transfer lock chamber located underneath the DIII-D vessel up through a V-1 port at R=1.486 m and 150° toroidally, inserting the sample as a plug from behind the lower outer divertor shelf nose tile. The linear actuator is a telescoping hydraulic piston drive equipped with a 13 pin electrical feed-through (including two Type-E thermocouple pairs) to allow instrumenting of sample assemblies. This system allows for the execution of practical plasma material interaction experiments in a tokamak without requiring the shutdown and venting of the entire device to access the samples. The maximum sample or probe head diameter is 48mm, and typical sample assembly height is 95mm in height. Probe head assemblies contain a wider, chamfered base that presses against a hard stop inside the vessel when fully inserted, allowing for excellent repeatability of vertical alignment.

3.2 Sample Exposure Cases

We will discuss three different sample exposures in this dissertation, each exposed to a dedicated set of repeat plasma discharge conditions in the DIII-D tokamak and with different substrate characteristics. The sample exposure case naming convention is derived from the combined description of the substrate and plasma exposure species: a Smooth substrate sample exposed to D plasmas (case S-D), a Rough sample exposed to D plasmas (case R-D), and a Rough sample exposed to He plasmas (case R-He).

Al films were deposited using vacuum evaporative deposition coating system at Sandia Albuquerque. Films were made to an initial thickness of 80-130nm onto different carbon substrates. Substrates were masked to create uncoated regions for measuring

redeposition and migration of Al away from the coated areas. The initial coating geometry for each case was as described in Figure 3-2. Each sample included a large area for measuring net erosion and spectroscopic emission, and a small area on the toroidally upstream side where prompt redeposition would be low for measuring the gross erosion rate using only post-mortem measurements of film thickness change with He beam Rutherford Back-Scattering Spectroscopy (RBS). This method for using small area samples for post-mortem non-spectroscopic gross erosion measurement was previously developed [15] and applied to other materials (W [107], Mo [108]). In case S-D, 1mm and 10mm diameter circular coatings were used for the different eroding area sizes. For cases R-D and R-He, rectangular coatings were made, with the small area consisting of a 1x20mm stripe parallel to the radial direction and located 7mm toroidally upstream of the 15x20mm large area. The case R-He sample included additional 1mm and 6mm diameter W coating spots that were expected to be eroded primarily by C impurity ions, and were used in this study only for the purpose of estimating the C ion flux to the sample (as discussed in Section 3.5.1).

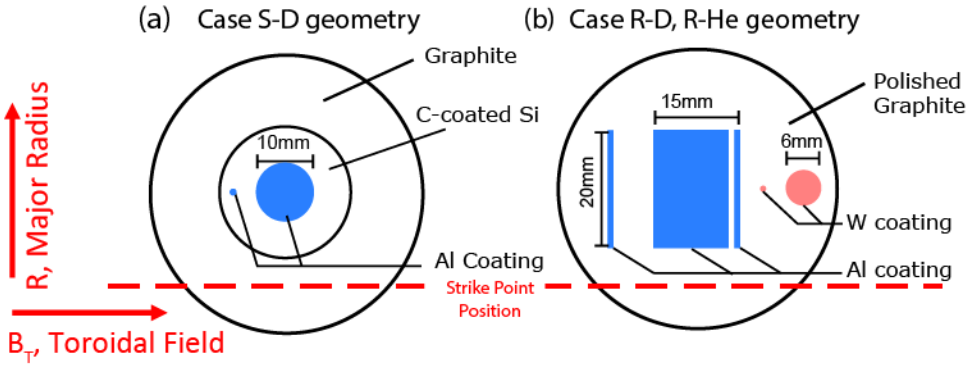

Figure 3-2. Sample coating geometries used in cases S-D (c) and R-D and R-He (d) are shown, with toroidal field directions and approximate strike point location during exposures. Note, the W coatings shown were only used in case R-He.

The smooth sample, Case S-D, used a 20mm diameter Si disk as the substrate, coated with 500nm CVD carbon layer to enable Al and C erosion rate measurements using Rutherford Back-scattering Spectroscopy (RBS). The sample had a mirror finish, with roughness negligible compared to the film thickness (~100nm). The carbon coating was included to allow the Al film thickness to be easily resolved in the RBS spectra, and to provide a measure of the local carbon erosion rate.

For cases R-D and R-He, the substrate was changed to utilize the entire DiMES probe head surface for better heat dissipation and to enable a larger measurable erosion and deposition area. The probe head was made of ATJ graphite like the surrounding tiles, polished using SiC and diamond polishing compounds and ultrasonically cleaned before applying the Al coating. The substrate roughness in these cases was minimized by polishing, but still significantly greater than the Al coating film thickness and surface roughness effects on the film measurement and the erosion behavior had to be considered in analysis. In addition, a fraction of the surface was pitted with pores intrinsic to the graphite that were irregularly shaped and were later shown to alter the local redeposition rate during exposures.

3.3 Divertor Diagnostic Suite

The DIII-D divertor has one of the most extensive sets of divertor diagnostics of any tokamak. We will describe here a limited set used in the experiments conducted for this thesis. Shown schematically below in Figure 3-3, these include the Divertor Material Evaluation System (DiMES), surface Langmuir probes, divertor Thomson scattering, a visible light divertor spectrometer, and a visible light CCD camera.

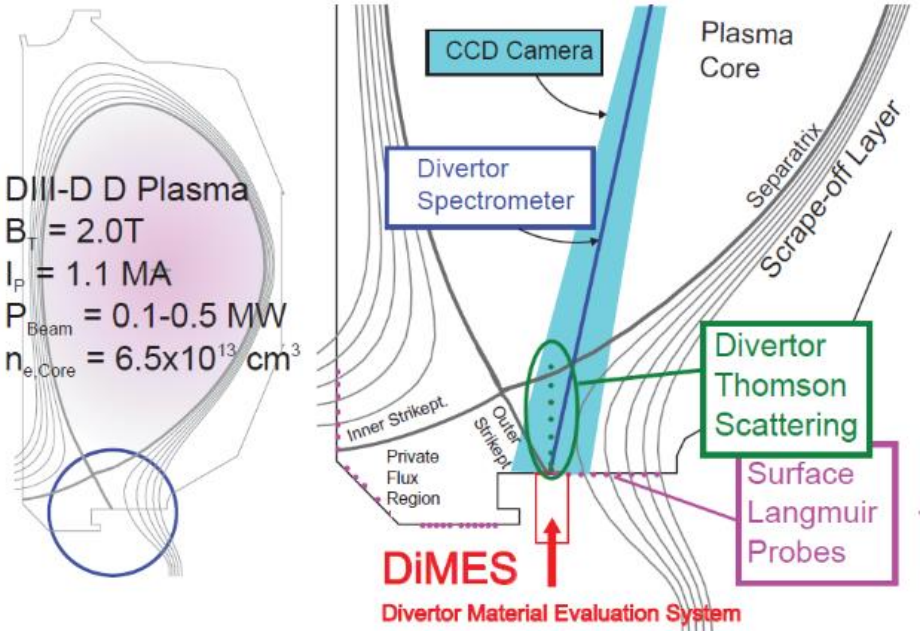

Figure 3-3. Layout of key divertor diagnostics including surface mount langmuir probes (pink dots), divertor Thomson scattering chords (green dots), multi-chord divertor spectrometer and CCD camera.

3.3.1 **Langmuir Probes**

Langmuir probes embedded in the divertor floor and shelf tiles were used for measuring localized floating potential, electron temperature, particle flux, and electron density. These probes consist 4x12mm, 12.5° sloped rooftop shaped pyrolytic graphite electrodes protruding ~1mm into the plasma and driven with an oscillating potential, arranged in a radial array as described in [103]. The current flowing through the electrode versus applied bias potential (the I-V characteristic) is analyzed to estimate the plasma parameters. The I-V characteristic is fitted to the standard Langmuir probe function

$$I = A_{coll} J_{sat} \left[1 - \exp\left(\frac{V - V_f}{\frac{kT_e}{e}} \right) \right] \quad \text{for } V < V_p \qquad (3.1)$$

where the electric potential of the electrode, V, and the current flowing into the electrode, I, are measured experimentally. The fitted parameters are the electron temperature T_e (eV), the ion saturation current density J_{sat} (A/m^2), and the floating potential V_f (V). The effective collection area is determined from the probe tip area projected through the magnetic field angle, and V_p is the plasma potential.

3.3.2 **Thomson Scattering**

The Thomson scattering system on DIII-D provides time resolved measurements of the electron temperature T_e and density n_e at multiple discrete points within the divertor and core plasma regions [104]. This is accomplished by measuring the wavelength shift and broadening of Nd:YAG (1064nm) laser light elastically scattered from plasma electrons. The volume of plasma measured is approximately 3.5x5x10mm. A total of eight divertor Thomson scattering view chords extend from Z = -1.246mm to -1.022mm, with radial location 1.48m (directly above DiMES poloidal location), and toroidal location of 120 degrees. The lowermost view chord 4mm above the floor and is used to measure the plasma conditions near the DiMES samples.

3.3.3 **Multichord Divertor Spectrometer**

The high resolution Multichord Divertor Spectrometer (MDS) [105] system on DIII-D is used for quantitative spectroscopy of the upper and lower DIII-D divertor regions. The spectrometer is often used to determine atomic influx rates from the wall by measuring the absolute intensity of a particular atomic emission line. It can be also used to determine ion temperature from Doppler line broadening, rotational and drift velocity measurements from the Dopper shift, and n_e and T_e from line intensity ratios. The system uses a McPherson model 209, 1.33mm focal length, Czerny Turner spectrometer with a

20μm wide entrance slit. It is coupled to a 16-channel Princeton Instruments VersArray back-lit CCD camera with a dispersion of 0.013nm/pixel at 400nm and 0.011nm/pixel at 910nm. A total of 16 simultaneous view chords are acquired, with 6 viewing the lower divertor at 150° toroidally including one directly over the DiMES probe. Each view chord has approximately a 1" spot size. Typical integration times are 100–200 ms, providing ~40-50 frames of data collection during a plasma shot on DIII-D. Examples of emission spectra measured during plasma exposures can be found in [106] and are discussed in Chapter 4.

3.3.4 **DiMES Camera**

Absolute spectroscopic measurements of Al erosion were also made using cameras with narrow band-pass filters centered on the 396.1 nm and 394.4 nm Al-I emission lines. In case S-D we used a Pt Grey CMOS camera (model FFMV-03M2M-CS) with a 50mm focal length lens. For the later cases R-D and R-He we used a PCO CCD camera (model PCO.PIXELFLY VGA) with a 75mm focal length lens, which provided a higher sensitivity, resolution, and bit depth. The camera and spectrometer view chords are visible in Figure 3-3. Details of the camera sensitivity and filter transmission calibrations are discussed in Sections 3.4.2 and 3.4.3, respectively. The viewing area for the spectrometer covered a ~45 mm diameter spot centered on the DiMES head, while the camera provided a view of roughly 100x100mm in area with 0.3 pixels/mm resolution. A schematic of the imaging setup is shown below in Figure 3-4.

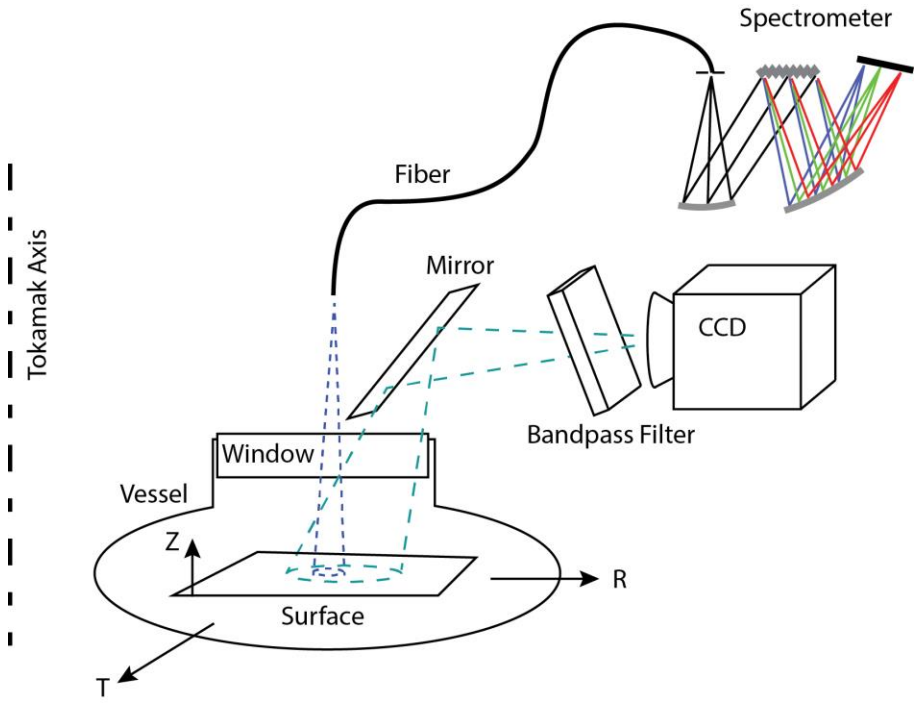

Figure 3-4. DiMES viewing camera and MDS spectrometer imaging setup on DIII-D.

The bandpass filter used for the Al-I imaging was tilted by 5.45 degrees in order to blue-shift the stock Andover filter transmission curve and avoid nearby D and C emission lines. The filter was located in front of the field imaging lens, centered on the axis of the lens, with the axis of the tilt was parallel to the toroidal field direction. The direction of the tilt was with the top of the filter tilted toward the vessel. The imaging field of view was approximately +-50mm in radial and toroidal direction, with the sample centered in the view of the camera. This resulted in a variation of light transmission angle through the filter of between 4.9 and 5.9 degrees across the radial direction, and from 5.45 to 5.53 from the center to toroidal upstream or downstream directions. Because of the light angle variation, the blue shift of the transmission curve varied across the field of view of the image somewhat. The cumulative effect of this variation was greatest in the radial direction, where we estimated it would result in a ~20% decrease in total Al-I transmission from the radially inboard edge of the image to the radially outboard edge. The effect

in the toroidal direction was relatively minor, with a symmetrical variation of +- 1.5% from center of the image to either upstream or downstream toroidal edge of the field of view. Detailed measurements of the blue-shifted transmission spectrum is described in Section 3.4.3.

3.4 Diagnostic Calibrations

3.4.1 **MDS Alignment and Spatial Calibration**

A check of the spatial alignment of the MDS spots were done in vessel, during a vent between S-D and R-D experiments. The chord was back-lit and a sheet of paper covered half of the DiMES port, while the DiMES TV camera snapped a photo (shown in Figure 3-5). A mis-alignment of ~14mm was estimated, but no alignment adjustments were made. The measurement was used as a back-calibration for the spectroscopic intensity measurements. After the R-D experiment, a check of the spatial calibration found that it had shifted. The bolts holding down the fiber optic mount to the port were loose, so there was some uncertainty in the alignment of the MDS view chord to the DiMES sample for the R-D and S-D experiments. For this reason, the CCD camera intensity calibration was relied upon and a geometric coupling factor was defined to capture the misalignment effects. The system was re-aligned and tightened, and a geometric coupling factor was measured before the R-He experiments.

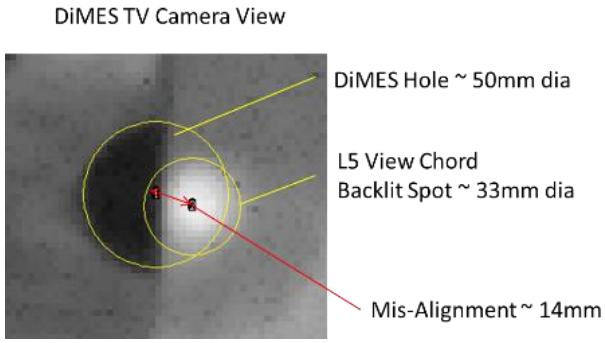

Figure 3-5. Alignment check of MDS view chord

Absolute calibration of the MDS spectrometer intensity involves using a quantitative lab sphere with a 3" aperture, much larger than the ~1" diameter collection area of the view chord. For DiMES samples with smaller emission areas or irregularly shaped areas, a geometric coupling factor has to be determined to quantify the total emitted photon flux (photons/cm^2) emitted from the sample area. An empirically determined geometric coupling factor was measured by placing a uniformly lit surface behind variable diameter apertures centered on the DiMES port. The correction factor, shown in Figure 3-6, is defined as the ratio of total counts measured for the apertured area to counts measured for the large (un-apertured) area, and is roughly equal to the ratio of the 1" diameter collection area to the emission area.

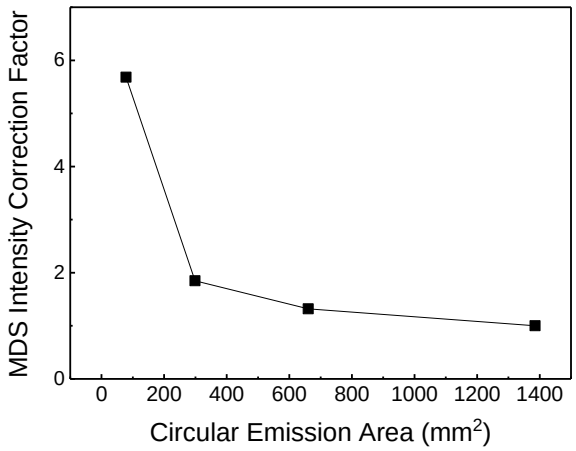

Figure 3-6. Geometric coupling correction factor for scaling MDS data to absolute intensity

3.4.2 **Camera Sensitivity Calibration**

The camera with all filters, lenses, and windows in place was calibrated with an Optronics integrating lab sphere placed inside the vessel, 3m from the camera. The reciprocal sensitivity of the camera and filter assembly was measured for each integration time (τ) and gain setting of the camera used during the experiment. The reciprocal sensitivity, S^{-1}, has units of [photons/(s-cm2-ster)]/[counts/sec].

For the Al-I 396.1nm emission range, we used a dielectric bandpass filter, Andover 010FC06-50/396.0-D, which had a 50% bandwidth of 1.03nm, center wavelength of 396.08nm, and a maximum transmission of 20%. To maximize the measurement of Al emission signal and minimize the background interference from nearby C and D emission lines, the filter was tilted roughly 2 degrees to shift its peak wavelength to 395.5nm. Additional colored glass filters Schott FG039 and FG025 were used in parallel to block continuum long wavelength emission and to increase the optical density to D-alpha emission during plasmas. For Al-II 623nnm emission range, we used a dielectric bandpass filter, Andover 010FC12-50/623.0-D, which had a center wavelength of 623.19nm, a 50% bandwidth of 1.06nm, and a peak transmission of 72%.

3.4.3 **Bandpass Filter wavelength calibration and measurement**

Filter transmission curves were measured at nominal incidence angle with a collimated light source coupled to the MDS spectrometer. Filter transmissions were also measured with a setup designed to mimic the experimental exposure measurements: by using an extended area light source 50mm in diameter positioned 3m away from the 75mm imaging lens, focused on a fiber optic link to the spectrometer, with the filter

located just in front of the imaging lens. In this arrangement the variation of the angle of light transmitted through the filter is taken into account and leads to a broadening of the bandpass region. A schematic of the filter transmission imaging setup is shown below in Figure 3-7.

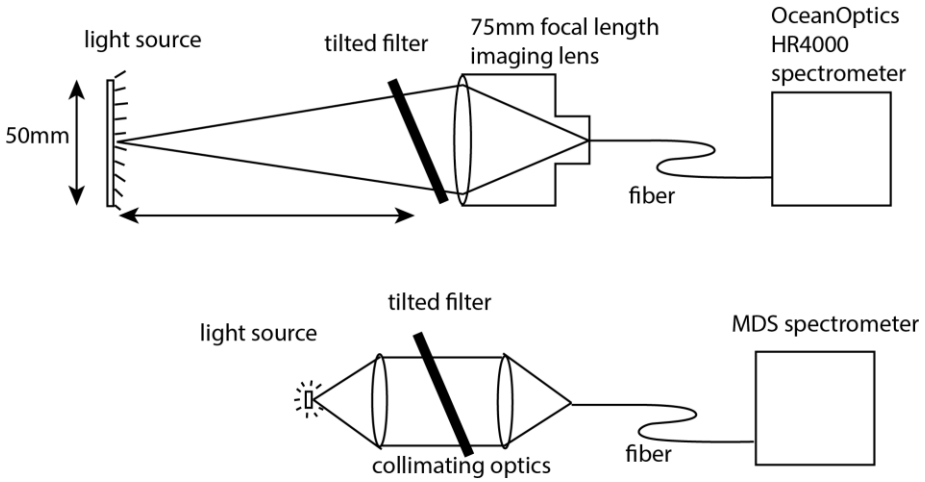

Figure 3-7. Filter transmission measurement setup.

The Al-I bandpass filter, Andover part number 010FC06-50/3960-D had a central transmission wavelength of 396.08nm, peak transmission of 20%, and a 50% bandwidth of 1.03nm. The filter was tilted 5.5 degrees during the experiment in order to blue-shift the central transmission wavelength to 395.2nm so as to avoid nearby carbon and deuterium emission lines and thereby minimize interference with background emission sources. The amount of blue-shift can be estimated using the formula $\lambda_{Blue}/\lambda_0 = \sqrt{1 - \sin^2(\theta/n)}$, where λ_{Blue} is the blue-shifted wavelength, λ_0 is the nominal center wavelength, θ is the tilt angle of the filter, and n is the effective refractive index of the filter (1.4 in this case). The filter was located in front of the field imaging lens. The centerline of the filter was aligned with the centerline of the lens, the emission area was centered in the imaging field of the camera, and the filter tilt axis was parallel to the toroidal direction. Normalized transmission spectra shown in Figure 3-8 are for the filter at 0° tilt, nominal 5.5° tilt.

However, the amount of blue-shift of the transmission curve is expected to change across the radial direction of the image field of view due to the change in the angle of the light passing through the filter. Because of the direction of the tilt, the blue-shift is expected to be greatest in greatest in the radially outboard edge of the view and smallest in the radially inboard edge. The symmetrical angle variation in the toroidal direction leads to a symmetrical blue-shift when imaging the toroidally upstream and downstream direction. Also shown in Figure 3-8 is the measured filter transmission curve when using an extended area light source (50mm in diameter) and the calculated blue-shifted transmission curves at high and low range extents of the expected variation of light angle through the filter assuming a radial field of view of 100mm at 3m distance (5.9° and 4.9°). The cumulative effect of the blue-shift variation is small, since the two Al-I emission lines (at 394.4nm and 396.1nm) are inversely affected by the shift. The calculated variation of transmission is less than +- 10% across the radial field of view, and +-1.5% across the toroidal field of view.

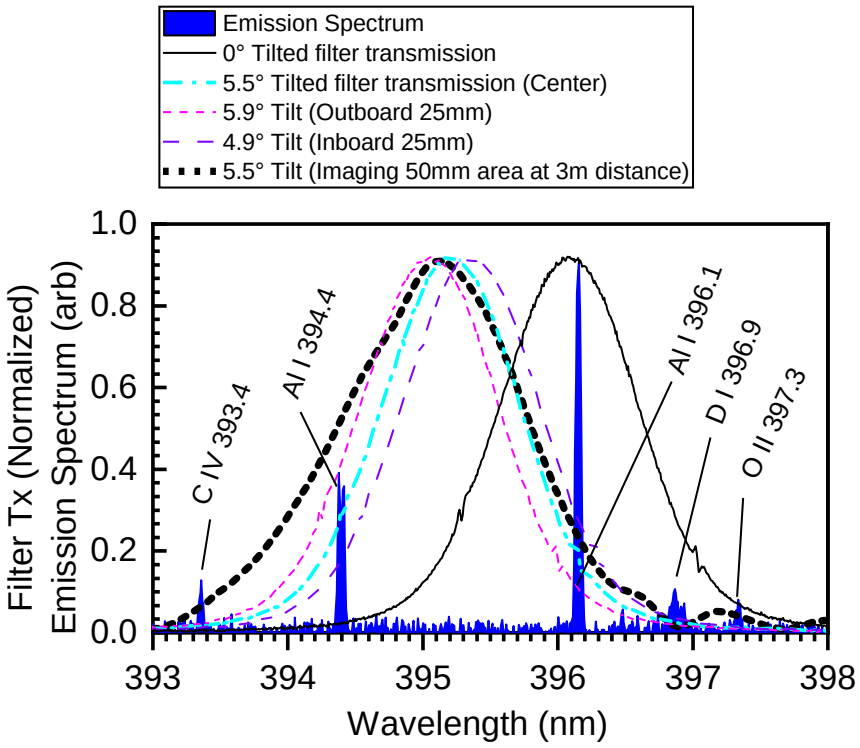

Figure 3-8. Al-I Bandpass filter transmission spectrum measured at zero tilt angle (solid black line) and at nominal tilt angle viewing a 50mm diameter light source (dashed black line). Colored dashed lines show blue shifted nominal transmission curve at radial inboard and outboard extents of the field of view.

3.5 Plasma Exposure Conditions

Plasma exposures of Al samples were carried out using the Divertor Material Evaluation System (DiMES) facility at DIII-D [40]. The DiMES system uses a retractable drive mechanism which allows for samples to be loaded in a vacuum transfer chamber and inserted into the DIII-D tokamak to be mounted mounted flush with the surrounding graphite divertor tiles near the outer strike point (OSP). These samples were exposed to a series of repeated tokamak discharges to achieve measurable levels of erosion and redeposition. Plasma conditions were well-characterized using the suite of DIII-D divertor and plasma edge diagnostics.

Three different sample exposure cases are compared to determine how different background plasma conditions (either He or D) and surface morphologies (initially smooth vs. initially rough substrate) affect the near-surface material migration cycle. We will refer to the three sample exposure cases as: Case S-D, a Smooth sample exposed to T_e ~27eV D plasma; Case R-D, a Rough substrate sample exposed to T_e ~17eV D plasma; and case R-He, a Rough sample exposed to T_e ~15eV He plasma.

The goal of each exposure was to determine the net and gross erosion rates of Al and to determine the whether redeposition is significant for Al. Al coating geometry for each case included two areas: a large area onto which significant re-deposition is likely to occur; and an area smaller than the ionization mean free path and located on the *upstream* side of the larger area, thus minimizing any redeposition. This combination enabled measurement of both the net erosion (i.e. erosion reduced by redeposition) and gross erosion (i.e. erosion without redeposition) rates using pre and post-mortem helium film thickness measurements using He beam Rutherford back-scattering spectroscopy (RBS) of the large and small areas, respectively.

Target plasma conditions were based on previously well characterized and modeled low power (P_{total} ~ 1 MW), low density (n_e ~ 2-4x10^{19} m^{-3} in the core, n_e ~ 1-3x10^{19} m^{-3} at the divertor strike point) attached lower single-null divertor L-mode plasmas [112]. Plasma conditions were measured near the sample either directly during exposure using a Thomson scattering view chord ~ 1cm above the surface or during a characterization shot where the strike point was swept gradually across an array of surface Langmuir probes. Conditions at the sample were uniform in the toroidal direction, with an approximately flat plasma density radial profile over a ~1cm span (several ionization MFP's) of the sample in the radial direction. The local plasma conditions, averaged over

the sample size for each exposure case, are listed in Table 3-1. The toroidal field strength was 2.0 T, and the magnetic field vector was inclined ~2.2° to the surface tangent at the sample. Steady exposure conditions were achieved by controlling the strike point position and keeping the sample in the private flux region until the steady phase of the discharge. Each sample accumulated between 6 and 25 seconds of steady-state plasma exposure over 2-4 tokamak discharges, achieved by using repeat steady plasmas and maintaining the OSP position 7-20mm inboard of the sample during the steady phase of the discharge. The radial profiles of plasma conditions are plotted in Figure 3-9, along with points indicating the average value of the Al coating and radial extent of the coating area. These profiles show good uniformity of density within a few mm of the radial extent of the sample area, with a slightly varying plasma temperature.

Average incident ion energies were estimated using the sum of the average ion thermal energy (which scales with plasma temperature) and sheath potential drop (which is fixed to $3T_e$ according to the Bohm criterion and scales with ion charge state): $E_{Impact} \approx 3Z_iT_e + 2T_i$ [42]. Main ion $T_i > T_e$ is possible, even likely in such low-density plasmas [42]. We assume all incident D is fully ionized to D^+, and all incident He is singly ionized to He^+. If we assume $T_i \sim T_e$, the impact energies for D^+ and He^+ ions is on average at least $5T_e$.

Table 3-1. Averaged local plasma parameters and total exposure (Exp.) time for each sample case measured as shown below. Local magnetic field strength (B_T) and pitch angle above the surface plane (α) are listed. Sample R-D parameters varied by ~30% during exposure time due to strike point position shifts, as described in more detail in [106].

Case	Plasma Species	T_e [eV]	n_e [x10^{13} cm^{-3}]	Exp. Time [s]	Perp. Ion Flux [x10^{18} $cm^{-2}s^{-1}$]	Local B_T [T]	α (deg)	DIII-D Shot Range
S-D	D	29.6[a] 25.1[b]	1.16[a] 1.34[b]	14	1.88	2.3	1.7°	148673-148677
R-D	D	16.0[a] 18.4[b]	0.96[a] 2.79[b]	12.6	0.89	2.2	1.3°	153860-153864
R-He	He	14.8[a] 14.8[b]	1.1[a] 1.7[b]	6.2	1.08	2.18	1.4°	158446-158448

a. From Langmuir probes; b. From Thomson scattering chord 10mm above surface

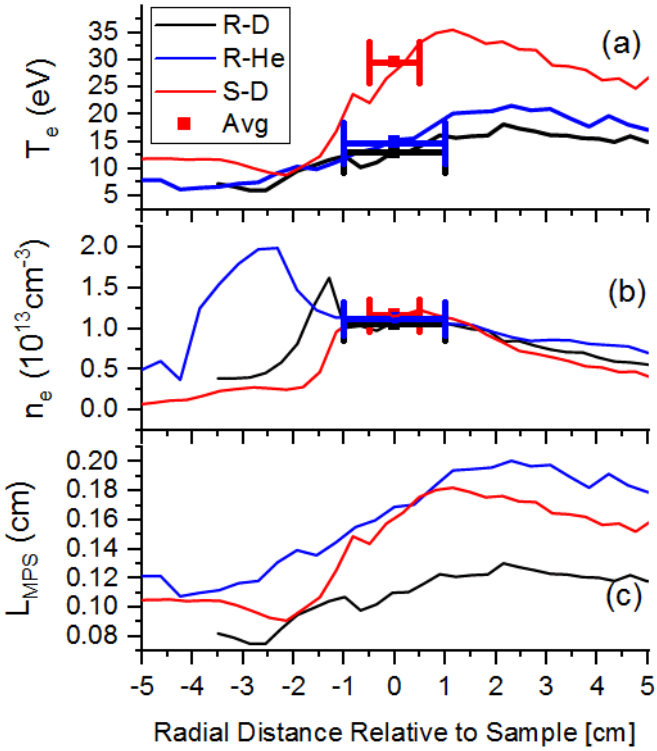

Figure 3-9. Radial profiles of electron temperature Te (a), density ne (b), and magnetic pre-sheath gradient scale length LMPS (c) for each case plotted relative to sample radial location (Rsample). Horizontal bars indicate the radial extent of the Al coating area, and are plotted at the dwell-averaged values for each case.

3.5.1 **Carbon Impurity Characterization**

Since the DIII-D tokamak is a fully graphite clad machine, the primary background impurity in the plasma is carbon. It is estimated at between 1% and 3% of the incident main ion flux to the surface, with an average charge state of +3 [3]. Carbon causes both sputtering and implantation, creating an evolving surface composition that can either increase or decrease the Al erosion rate. It has been shown that (for inter-ELM conditions) carbon ions in DIII-D are the main driver of sputtering of high-Z materials like W and Mo, but C can also reduce the erosion rate due to near-surface material mixing and carbon coating [113]. Unlike high Z materials, Al *is* sputtered by the D and He main ions in these low power plasmas (for ELMS, they also significantly sputter W [114]). In fact, the yields for D and He physical sputtering of Al are about double the yield for D and He physical sputtering of C due to the lower Al surface binding energy (3.4eV for Al, and 7.4eV for C). In addition, implantation and dilution of the Al surface by incident C likely overpowers any enhancement of erosion by C ion sputtering, as discussed in earlier work [115]. In order to consider the effects of carbon impurities on the expected erosion behavior of Al, we need some estimate of the incident C ion flux fraction, impact energy, and incidence angle.

For the D plasmas in exposure cases S-D and R-D, an estimate for the upstream carbon impurity fraction was made using Charge Exchange Recombination (CER) measurements [116]. Those measurements report C impurity fractions of below 1% measured near the outside midplane pedestal region. The carbon ion fraction actually incident on the target can be higher due to the local source of carbon sputtering near the target. In order to achieve the ~1.2×10^{15} W atoms/cm^2-s of W erosion measured in case R-He (note the addition of W coating near the Al coating in that case), we

estimated that ~3% of the incident ion flux would need to be C^{3+} ions (the He^{+} ion impact energy was below the W sputtering threshold). ERO modeling of very similar low power, low density L-mode plasma exposures of Mo and W [113,117] found good agreement with experiment when assuming a 1.8% C ion fraction.

The estimate of impact energy for the C impurity depends in large part on the distribution of charge states, which has not been experimentally measured. WBC-REDEP modeling [97] replicated the observed Mo erosion using a distribution of charge states from C^{1+} to C^{4+}, but also found that the erosion rate could be well approximated assuming a single C^{3+} charge state. Furthermore, the C ion temperature may depend on its source (be it exhausted from the core or entrained from sputtering at the edge). In similar DIII-D plasmas, experimentally observed Doppler line emission widths were matched with modeling to find the C^{1+} and C^{2+} ion temperatures were 6.7 and 14.5eV respectively while electron temperature was between 20 and 30eV [112]. If we assume Ti ~ Te for the C ions, with an average charge state of C^{3+}, the carbon ion impact energy would be $11T_e$. Owing to their higher mass, impurity ions can also gain energy by entrainment in the background ion flow speed c_s, gaining an additional energy of up to $m_C c_s^2/2$. For C ions, the amount of actual frictional coupling to the main ion flow is unknown in these low density plasmas. At an upper limit, with $c_s = \sqrt{2kT_e/m_i}$, this can provide an additional $6T_e$ of energy in D plasmas or $3T_e$ in He plasmas.

For the purposes of this study, we will consider a single average charge state of C^{3+} , neglect frictional entrainment and assume C ion temperature $T_i^C = T_e$, so that E_{Impact} = $11T_e$. Our best estimates for the actual ion flux fraction of C impurities in each case are listed in Table 3-2. Carbon impurity fractions for cases S-D and R-D are estimated based on the work by Ding and Elder modeling very similar low power, low density L-mode

plasma exposures of Mo and W [113,117], but scaled with the expected D → C sputtering yield at the electron temperature near the sample. The C^{3+} fraction estimated for case R-He is based on the C^{3+} flux required to achieve the ~1.2×10^{15} W atoms/cm^2s measured in that case (note the additional W spots included on the R-He sample for this purpose).

Table 3-2. Estimated carbon impurity properties, as fraction of flux characterization

Case	Pedestal C impurity[a] [fraction of total ions]	DiMES C impurity[b] [fraction of incident ion flux]	DiMES incident C Energy [eV]
S-D	0.63%	1%	276-326[c] 426-504[d]
R-D	0.78%	1%	176-202[c] 272-313[d]
R-He	n/a	3%	163[c] 207[d]

a. From CER measurements
b. Estimated from observed W erosion rate in similar plasmas
c. Assuming no entrainment
d. Assuming full entrainment in background ion flow

3.5.2 **Sample heat flux**

Heating of the samples was minimized in order to avoid melting the Al samples (T_{melt} = 660°C). In cases R-D and R-He, sample temperatures were monitored during exposure using a thermocouple embedded 5mm below the surface and with an infrared camera imaging the sample surface. IR camera surface temperatures measured below 100°C in case R-D and below 250°C in case R-He, consistent with thermocouple measurements after each shot. Some hot spots were observed on the samples that may have been due to dust or larger pores, but even these were estimated to be 400-650°C based on extrapolating the IR camera calibration curve.

For the S-D case, thermal modeling was conducted using a SolidWorks model of the cap and Si wafer assembly (Figure 3-10). Full temperature dependent properties of

graphite and silicon material were used, and the conservative assumption was made that there was no thermal contact between silicon wafer and graphite cap. Heat flux was inferred from Langmuir probe data of electron temperature and ion flux. A stepped heat flux profile of between 0.4MW/m^2 and 0.7MW/m^2 was used for a 5 second exposure. A worst case mis-alignment of 0.5mm was assumed at the leading edge of the cap (resulting in up to 14MW/m^2 parallel heat flux on the leading edge). Maximum surface temperatures on the Si wafer were between 150°C and 300°C, still well below the Al melting point. No clear signs of melting were observed on any samples in post-mortem inspection.

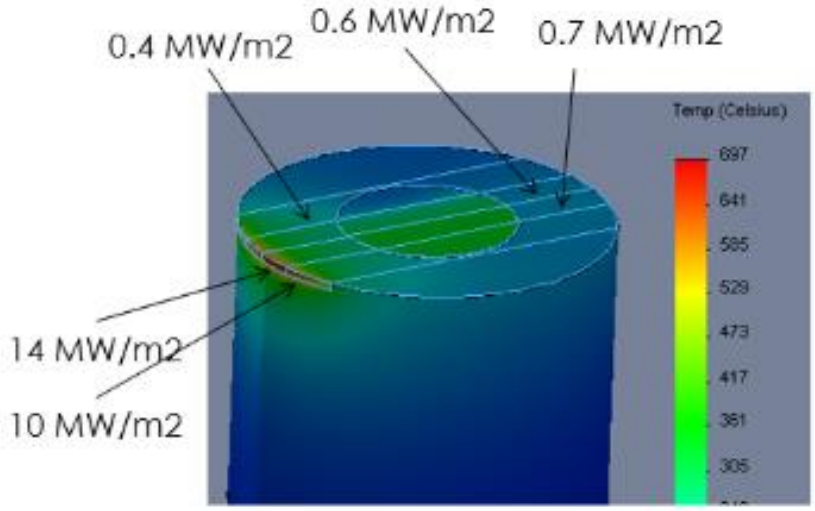

Figure 3-10. Example heat flux simulations for Si disk holder sample (circle in the center) and solid graphite head (outer cylindrical annulus).

3.6 Measurements of Aluminum Film Thickness

Before and after plasma exposure, the thickness and composition of the Al films was measured using Rutherford Back-Scattering Spectroscopy (RBS). RBS is a highly sensitive technique optimized for measuring thin films on the order of 100's of nm. It is a practical technique for measuring the sputtering and redeposition rates of materials in

tokamaks, since the exposure times allotted for measurement of such quantities are limited and often only tens of seconds of plasma exposure are available for a particular experiment.

RBS measurements presented in this thesis were conducted at two different ion beam analysis facilities. Samples S-D and R-He were measured at the Sandia Ion Beam Laboratory (IBL) by William Wampler. RBS was done using 2 MeV He4. Absolute calibration of the RBS was done using a thin gold film reference standard with known Au coverage (57.3 microgram/cm^2 or 17.52 x10^{16} atoms/cm^2, ±4.0% 2-sigma uncertainty) from the Joint Research Center Institute for Reference Materials and Measurements in Geel, Belgium. Sample R-D had RBS measurements done at the MIT Plasma Science and Fusion Center by Graham Wright and Ethan Peterson. Detailed analysis of the RBS spectra using SimNRA software to determine compositional depth profiles and film roughness effects were done by the author.

Absolute calibration of the RBS film thickness was done using a thin Al film reference standard (thickness measured by confocal profilometry step height analysis by Dean Buchenauer at Sandia Albuquerque). The author also cross-calibrated measurements at MIT with the Sandia IBL measurements thanks to a duplicate measurement of the R-He sample at both facilities.

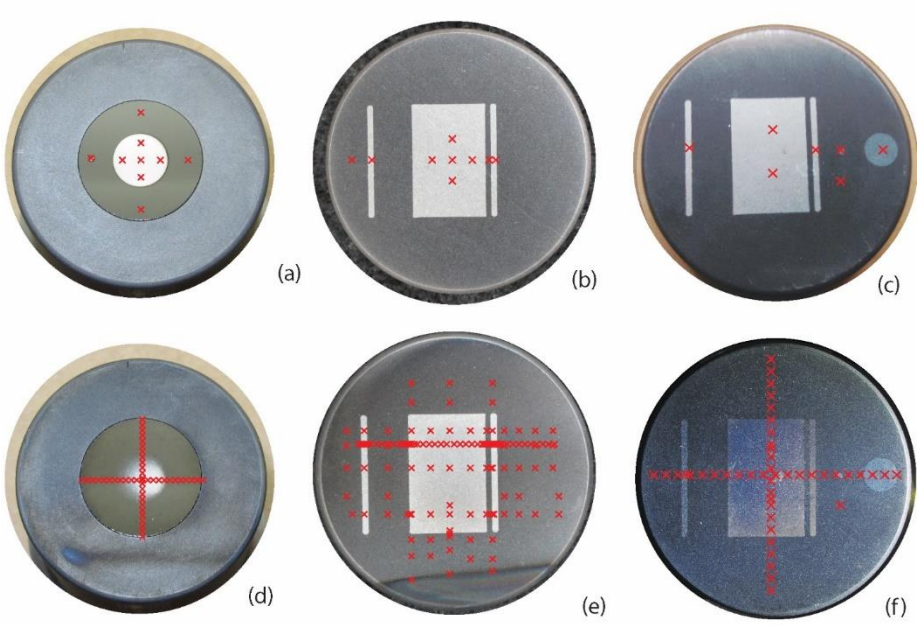

Figure 3-11. RBS measurement locations indicated with red crosses. Showing pre-exposure images and measurement points for exposure samples S-D (a), R-D (b), and R-He (c), along with post exposure images and measurement points for S-D (d), R-D (e), and R-He (f).

Measurements were made on the samples at the locations indicated by red crosses in Figure 3-11. Measurements were repeated again after plasma exposure. The analysis beam spot size was 1x1 mm for most measurements, but for spots on the 1 mm aluminum stripes the analysis beam spot size was reduced to about 0.2x0.2 mm and centered on the film by scanning in 0.1mm steps to locate the center.

RBS spectra from the pre & post measurements are shown in Figure 3-12 for the Al films. Peaks due to Al, O, and substrate C (or Si) are indicated in the figures. In cases R-D and R-He, oxygen peaks before exposure can be separated into a surface oxide, oxygen in the film, and a film-substrate interfacial oxide. Fits using the SIMNRA software [109] show the oxygen content is about 15 atomic % in the Al film as deposited, presumably due to reaction with residual gas during film deposition.

For measurements low levels of Al found on areas outside the original coating, as well as inside regions of high erosion or carbon co-deposition, careful analysis and fitting

of the RBS spectra in using SimNRA code was required to adequately account for background impurities which offset the count rate near the Al energy scattering peak and would otherwise lead to an over-estimation of Al coverage.

The shape of the Al peak in cases R-D and R-He after plasma exposure indicates a non-uniform film thickness developed after plasma exposure. The peak height decreased, but the width of the base did not. This is probably due to the roughness of the graphite substrate leading to inhomogeneous rates of erosion and deposition across the film, i.e. greater erosion near the peaks and lower erosion near the valleys will develop a non-uniform film thickness within the 0.2-1mm measurement spot. Regardless of roughness or peak shape, the integrated counts in the RBS Al peak gives a mean film thickness along the direction of the analysis beam, i.e. normal to the surface, averaged over the area of the analysis beam spot.

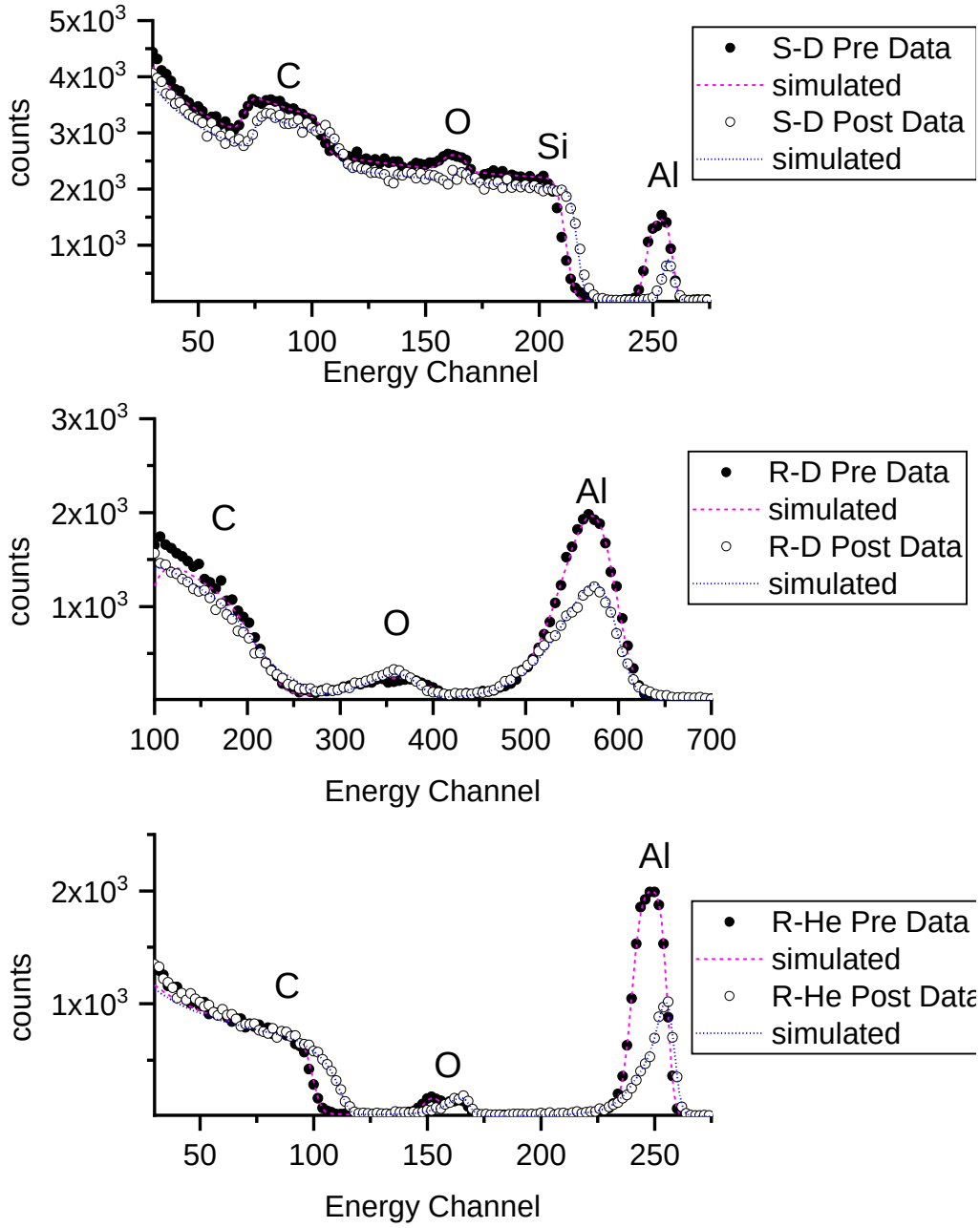

Figure 3-12. RBS Spectra on the aluminum on samples S-D, R-D, and R-He measured before (solid points) and after (hollow points) plasma exposure. SimNRA simulated spectra shown with dashed lines.

In terms of physical thickness, Al coverage from RBS values was converted to nm using the standard density of aluminum 2.70 gram/cm^3 or 0.602x10^{23} atoms/cm^3. The net erosion of Al was taken from the center of film, before plasma exposure minus the

thickness after exposure. The thickness of the net and gross erosion regions, and the net and gross erosion rates are summarized for each sample in Table 3-3.

Table 3-3. RBS Measured Al film thickness before and after plasma exposure. Typical measurement error was +- 5% of the measured thickness

Case	Thickness Before (nm)		Thickness After (nm)		Exposure Time (s)	Gross Erosion nm/s	Net Erosion nm/s
	Gross	Net	Gross	Net			
S-D	71.3	92.7	0*	21.3	14	>5.7	5.1
R-D	88.3	88.3	63.1	66.5	12.6	2.5	2.0
R-He	131.5	131.1	44.7	56.7	6.2	14	12

* not detected

3.6.1 **Rutherford Backscattering Theory**

RBS uses low intensity, high energy beams of light ions (typically a few MeV helium ions) to probe the surfaces of materials and measure their composition, quantitative depth profile, or coating areal concentration (atoms/cm^2). Mono-energetic ion beams are directed at a target surface and scattered into an energy resolving detector. A diagram of the scattering and detector geometry is shown in Figure 3-13.

The scattering cross-sections of the target material determine the sensitivity of the RBS measurement, and the scattering kinematics determine the energy of the scattered ion. Target composition is then determined by analyzing the energies and quantities of scattered ions. The scattering cross section is roughly proportional to the square of the atomic number of the target element, meaning that RBS has a greater sensitivity for detecting heavy elements than light elements. For most light elements (Z<~20), scattering cross sections are sufficient to detect sub-monolayer atomic coverages for thin films, or roughly 1x10^{15} atoms/cm2. For heavy elements such as W, sensitivities can be 100x higher.

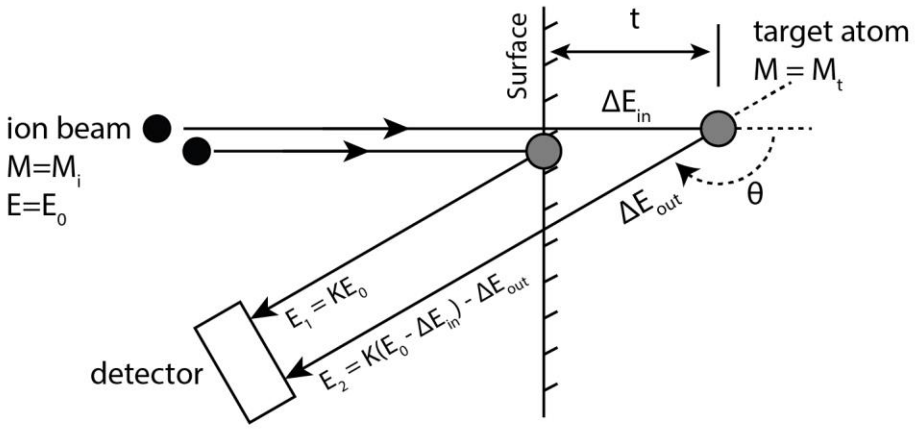

Figure 3-13. Diagram of Rutherford back-scattering spectroscopy measurement, adapted from [110].

The energy of each back-scattered ion is a fraction of the incident energy determined from classical collision physics based on the mass of the scattering and target atoms, the angle at which the ion is scattered. There is an additional energy loss when scattering from beneath the target surface due to electronic interactions with the target material. The kinematic factor, or ratio of incident ion energy before and after the back-scattering collision is

$$K = E_1/E_0 = \left(\frac{\left({M_2}^2 - {\mathrm{M}_1}^2 \sin^2\theta \right)^{\frac{1}{2}} + M_1 \cos\theta}{M_1 + M_2} \right)^2 \qquad (3.2)$$

Where E_1 and E_0 are the scattered and incident energies, respectively. The incident ion and target atom masses are M_1 and M_2, respectively. The angle between the incident ion before and after scattering is θ (typically 150°-170° in practice).

The energy loss of the incident ion is greatest for target atoms of similar mass, meaning scattering energies are higher for heavier target elements and lower for lighter target elements. The separation between energies for different target elements is greater

for lighter elements than for heavier elements, meaning that RBS is better suited for distinguishing between two light elements than two heavy elements. It should also be noted that elements as light or lighter than the incident ion will scatter at forward trajectories, thus will not be detected using classical RBS.

The rate of energy loss per unit of depth of ion penetration into the target is known as the stopping power dE/dx. Stopping power determines the depth resolution of the experimental RBS measurement. This rate of energy loss is due to both electronic stopping which behaves like friction between the incident ion and electron clouds, and nuclear stopping which occurs due to the large number of glancing angle collisions with target nuclei. Theoretical predictions of the stopping power are complicated, therefore empirical stopping powers from tabulated experimental data are often used.

3.6.2 **Thin film analysis method**

When measuring a heavy film deposited on a light substrate, the back-scattered energy spectrum will have a low energy plateau corresponding to the substrate and well separated high energy peak corresponding to the film. The total integrated area of this peak A is proportional to the backscattering yield from the film, which is equal to the product of beam fluence Γ, the target layer number density N [at/cm3] and thickness t [cm], scattering cross-section σ according to

$$A \propto \Gamma N t \sigma \qquad (3.3)$$

This is valid, as long as the energy loss in the target film is negligible such that the scattering cross-section does not vary through the layer, and other impurities contributing to the peak area are either negligible or accounted for. In practice, the peak area is

also proportional to detector sensitivity, detector solid angle. These factors can be eliminated by comparing the measured peak area to that of a well-known reference sample while maintaining all other measurement parameters constant.

3.6.3 **Characterization of surface roughness**

A detailed examination of the surface morphology for the polished graphite samples was made using both optical profilometry and SEM imaging techniques. Surface profilometry analysis results for a ~1x1mm region of polished, uncoated graphite are shown Figure 3-14. Aside from the brightness of the coating, the surface morphology of the Al-coated regions was indistinguishable from the uncoated regions. A line out (a) of the surface profilometry data (b) is shown, with the thickness of the Al film (100nm) indicated in red. Internal pore structure was out of the range of profilometer and shows up as gaps in the profile data and white areas in the profilometry image. Surface height distribution (c) excluding the pore areas indicates an RMS surface roughness of 600nm. The local surface flatness (measured as the angle slope between two measurement points) was on average ~0.4 degrees from the overall surface plane. Distribution of pore sizes determined by image analysis (e) shows a range of average diameters from 1 to 75 um was found. On average, pores were 40 microns in size and covered between 10% and 15% of the surface area. The pores were randomly distributed and irregularly shaped, as visible in the inclined SEM image and profilometry reconstruction in Figure 3-15. Their steep edges prevented optical profilometry measurements of their internal structure, but it was assumed that the pores were isotropic within the graphite, thus had a random distribution of depths approximately equal to their widths.

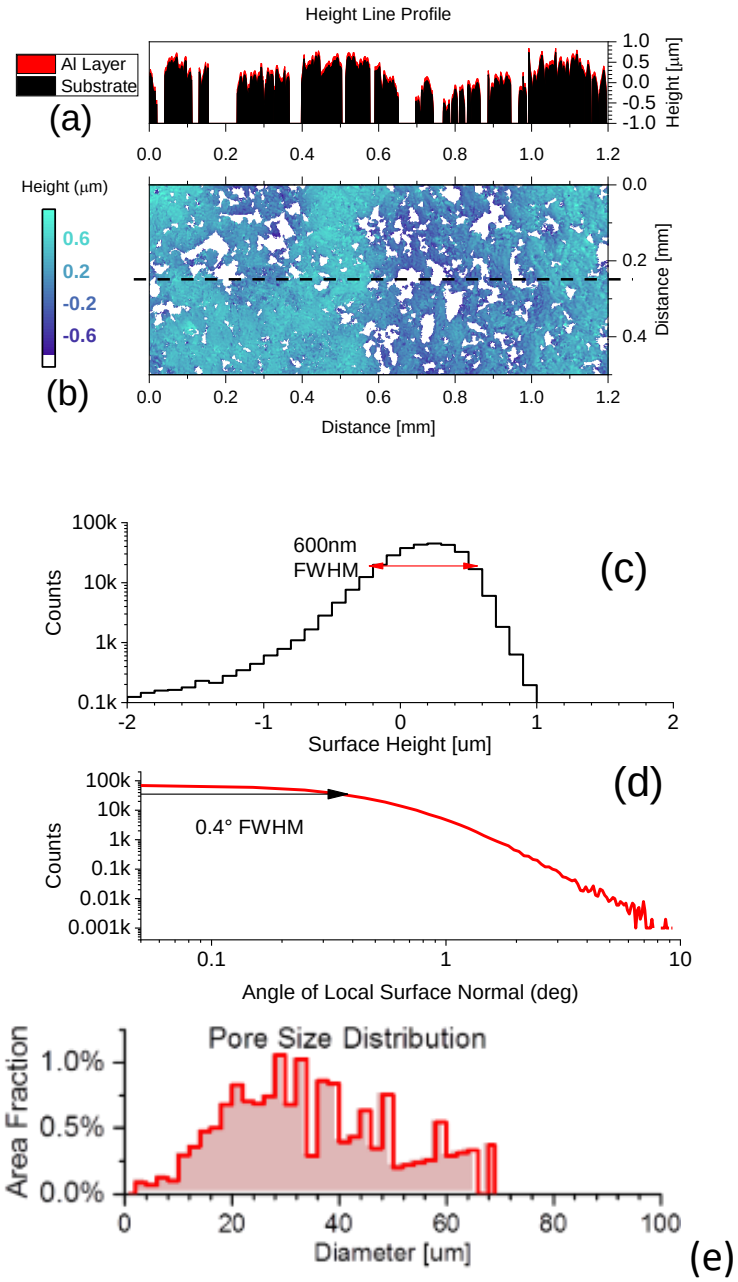

Figure 3-14. Confocal microscopy profilometry analysis of a ~1mm^2 region of polished, uncoated ATJ graphite. Line profile of surface height (a) taken from topographic image (b). The surface height distribution excluding pores (c) shows average roughness was ~600nm. Local surface angle distribution (d). Pore size distribution (e).

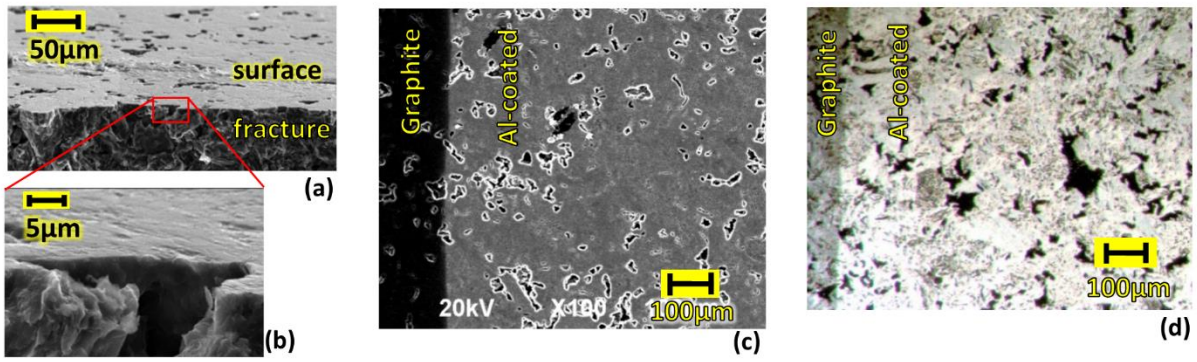

Figure 3-15. Example of the surface morphology of a polished graphite substrate similar to that used in cases R-D and R-He. Inclined SEM image (a) shows a fractured sample in cross-section, with detail of a pore inset (b). Secondary electron microscopy image of the surface near a coating boundary (c). Optical migrograph of a ~1mm^2 area near the an Al coating boundary (d).

3.6.4 **Effects of roughness on film thickness measurement**

RBS measurements on rough surfaces can be complicated by the fact that particles may pass through the film at different angles, resulting in a broadening of the scattering energy peak. In order to determine the effect of the surface roughness on the resolution of the RBS measurement technique, smooth vitreous (glassy) carbon samples were coated simultaneously with the polished graphite (rough) substrate samples and were analyzed with the same RBS instruments. The average roughness of the vitreous carbon was 25nm (RMS surface height) measured with confocal optical microscopy, which is roughly 25% of the deposited Al film thickness and has a negligible effect on the measured spectrum. The measured RBS spectra and fits comparing of the Al-coated vitreous carbon and pre-exposure polished graphite substrate are shown in Figure 3-16. In both spectra, we see distinct peaks corresponding to the Al film, surface and Al-C interfacial O, and surface and substrate C. The spectrum from the rough sample has a broader peak shape with longer low-energy tails as expected due to the surface roughness effects. We also found a slight increase in the noise floor which was likely due to presence of medium and high-Z impurities in the graphite that were not present in the

glassy carbon. Excellent fits to the data were achieved using SimNRA (solid lines) which includes two methods for simulating film roughness.

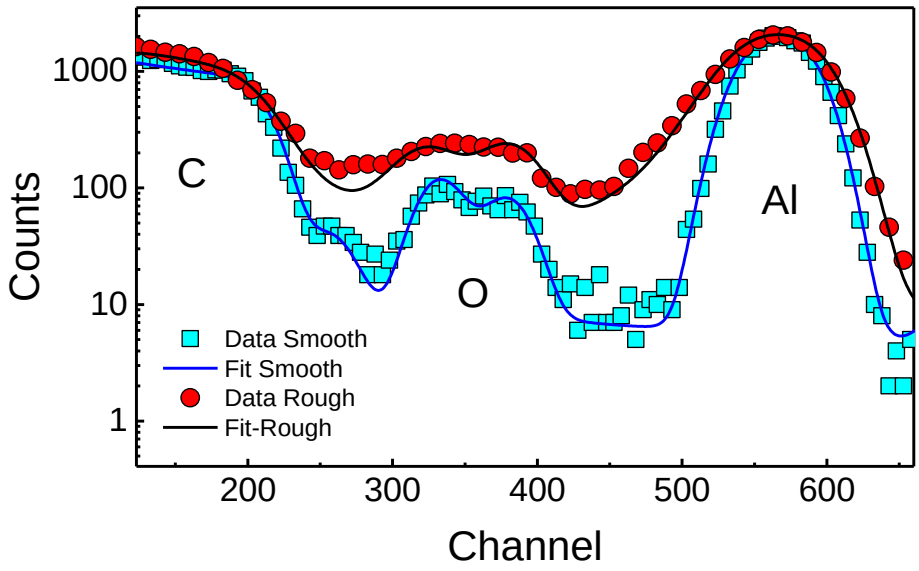

Figure 3-16. Comparison of initial RBS measured spectra on a rough and smooth C substrate. Here we compare a vitreous carbon and polished graphite samples that were coated simultaneously, so film composition and thickness is expected to be identical in each.

The cartoon in Figure 3-17 describes two different types of roughness that can be simulated for thin films in SimNRA: a) either film roughness, defined as a film with a distribution of thicknesses; and b) substrate roughness, defined as a uniform thickness film deposited on a substrate with a distribution of surface angles [111]. The effect of each type of roughness on the measured RBS spectrum is similar. The effect of each kind of roughness can be separately simulated in SimNRA. A rough film on a smooth surface is simulated in the software by treating the film as if it had a distribution of film thicknesses parameterized according to the Gamma distribution, Eq. 3.4:

$$p(d) = \frac{\beta^{\alpha}}{\Gamma(\alpha)} d^{\alpha-1} e^{-\beta d}, \;\; d > 0 \qquad (3.4)$$

With $\alpha = \bar{d}^2/\sigma^2$ and $\beta = \bar{d}/\sigma^2$. Here $\bar{d}$ is the average film thickness (center of the distribution), σ is the standard deviation, and Γ is the Gamma function. The effect of a rough substrate is simulated by considering a distribution of tilt anglesφdefined by a standard Lorentz distribution with a full-width-half-max $\delta\varphi$. The resulting RBS energy spectra for a thin Al film on a carbon substrate with different degrees of each roughness are shown in an example in Figure 3-18. A rough film on a smooth substrate is simulated in (a) and smooth film on rough substrate is simulated in (b). The area under the measured peak is proportional to the average film coverage under the measurement spot. As the simulations show, increasing film roughness produces peaks with increasing width, but decreasing height, and the total integrated counts under the peak remains roughly constant (to within 5%). The addition of substrate roughness produces peaks of slightly increasing width, but constant height. For the Al films measured in this study, we used variable film roughness, not substrate roughness, to fit the measured spectra in SimNRA. The red curve in Figure 3-18 (a) indicates the best fit achieved using a film thickness distribution **σ** equal to the film thickness **d**.

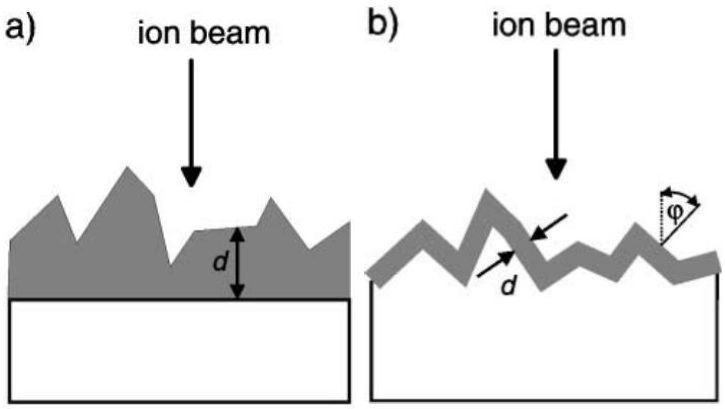

Figure 3-17. Reprinted with permission from [111]. Schematic representation of a rough film on a smooth substrate (a), and smooth film on a rough substrate (b). Grey: film; white: substrate.

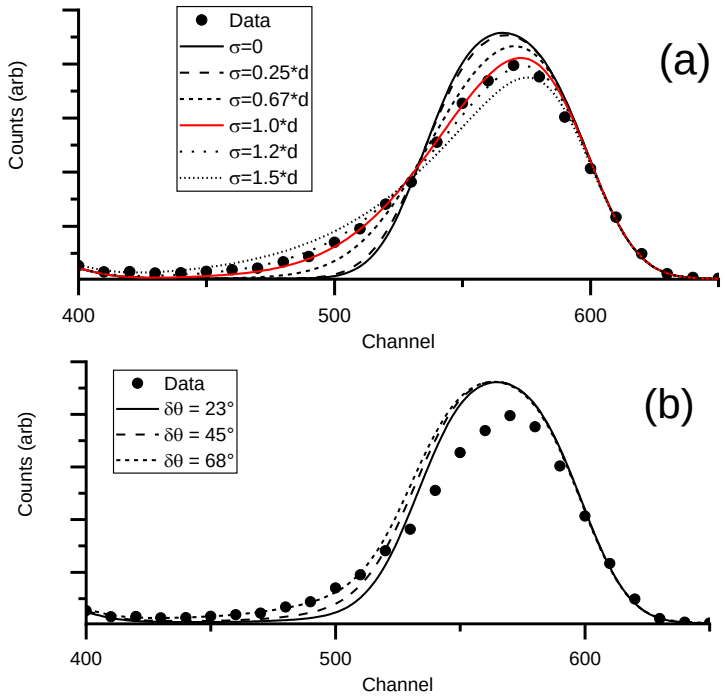

Figure 3-18. Example 1MeV He^+ RBS measured peak corresponding to a ~100nm thick Al layer deposited on a polished graphite substrate (points). Solid and dashed lines are peak shapes calculated using SimNRA [109] with either (a) varying film roughness (defined by film thickness distribution width σ) or (b) varying substrate roughness angle distribution width $d\theta$.

3.7 Measurement of net vs gross erosion

The non-spectroscopic measurements of erosion are made by post-mortem analysis of the physical removal of atoms from a surface, in this case by Al coverage measurements using RBS. In order to make a non-spectroscopic measurement of *gross* erosion, redeposition to the eroding surface must be negligible. For most materials this condition is satisfied as long as the eroding area is smaller than the ionization length of the eroding atom, and that the eroding species is unique from nearby surfaces. The eroding species being measured is Al, which is unique from the background sources so any erosion and redeposition of material can be assumed to originate only from the samples themselves. In this study we used different sized sample areas to vary the fraction of local redeposition and thus determine the net and gross erosion rate of Al. The larger coating areas approximated the measurement of net erosion (i.e. erosion reduced by local redeposition). The smaller coating areas enabled the measurement of gross erosion (erosion in the absence of redeposition). This measurement relies on the assumption that the amount of erosion from the small area is much larger than the amount of deposition to the same area. When prompt redeposition (redeposition within one ion gyro-radius) is the primary mechanism for redeposition, this condition is roughly satisfied for spot sized samples smaller than the ion gyro-radius. This method for using small area samples for post-mortem non-spectroscopic gross erosion measurement was previously developed [15] and applied to other high-Z materials with significant prompt redeposition fractions (W [107], Mo [108]).

3.7.1 **Spectroscopic Method of Gross Erosion Measurement**

In many tokamak experiments measuring erosion rates of surfaces, it is not practical to access the surfaces for detailed inspection or measurement. Instead, information about the material eroded from surfaces is inferred from passive measurements of the photo-emission spectrum associated with atomic emission from the surface. The emitted light intensity is a measure of the local electron density and flux of emitted particles, and line shifts and widths can provide information on the velocity and temperature of radiating ions. One quantitative emission spectroscopy technique that is used in this thesis to determine the material erosion rates is called the S/XB method. In this technique, excitation of the eroded material occurs via local plasma processes, primarily electron impact excitation. Spontaneous photon emission occurs as a result, emitting a photon with a wavelength and intensity determined by the radiation rate and emission line branching ratio. If the material emitted from a surface can be assumed to be fully ionized within the view of a spectroscopic diagnostic, the photo-emission intensity will be proportional to the total emitted flux of atoms. The absolute emission line intensity Ψ_a [photons/cm^2-Steradian] is proportional to the total emitted neutral Al flux Γ_{Al} [atoms/cm^2] by the S/XB coefficient for that line as:

$$\Gamma_{Al} = 4\pi\Psi_a \, {}^{S}/_{XB} \qquad (3.5)$$

When using a filtered camera passing a blend of emission lines, a similar relationship can be found where the total emitted neutral Al flux Γ_{Al} can be determined from the total transmitted Al emission line intensities Ψ_{tx} and an equivalent total S/XB_{tx} coefficient:

$$\Gamma_{Al} = 4\pi\Psi_{tx}\, {}^{S}/_{XB_{tx}} \qquad (3.6)$$

Determining the value of the S/XB coefficient requires knowledge of the local plasma parameters and modeling of the atomic excitation and de-excitation reactions, and ionization and radiation rates. In lieu of this detailed knowledge, the emission rate can be calibrated against a known gross erosion rate (net erosion may be lower due to redeposition of material) in order to determine the S/XB coefficient.

3.7.2 **Non-spectroscopic Net and Gross Erosion Measurement**

When redeposition occurs over a large distance compared to the area being eroded, the effect of redeposition to that sample may be negligible such that its net erosion rate is equivalent to its gross erosion rate. For the sample exposures in this study, small coating areas were included for this purpose. However, because of the relatively long ionization length of Al and limited sample size, some calculation of the expected redeposition fractions was necessary to determine whether the measurements would be valid.

We can consider a simple geometric study here, assuming ionization occurs after traveling a straight line distance from the point of emission, the gyro-radius is shorter than the ionization length, and redeposition occurs after the gyrating ion follows the pitch of the magnetic field line back to the surface. In this estimate, the redeposition length L becomes a function of the ionization distance λ_{ioniz}, and sputtered angle β. We assume atoms have an orbit with a gyro-radius ρ_z determined by the sputtered velocity component perpendicular to the magnetic field. We will assume ions following simple orbit trajectories along magnetic field line angle (α) toward the surface, as shown in

Figure 3-19. This simple estimate does not include any effects of the sheath electric field, which shorten the deposition length due to the deflection the ion toward the surface. Thus, the redeposition length can be estimated as:

$$L = (\lambda_{ioniz} - \rho_z)\cos(\beta) / \tan(\alpha) + \lambda_{ioniz}\sin(\beta) \qquad (3.7)$$

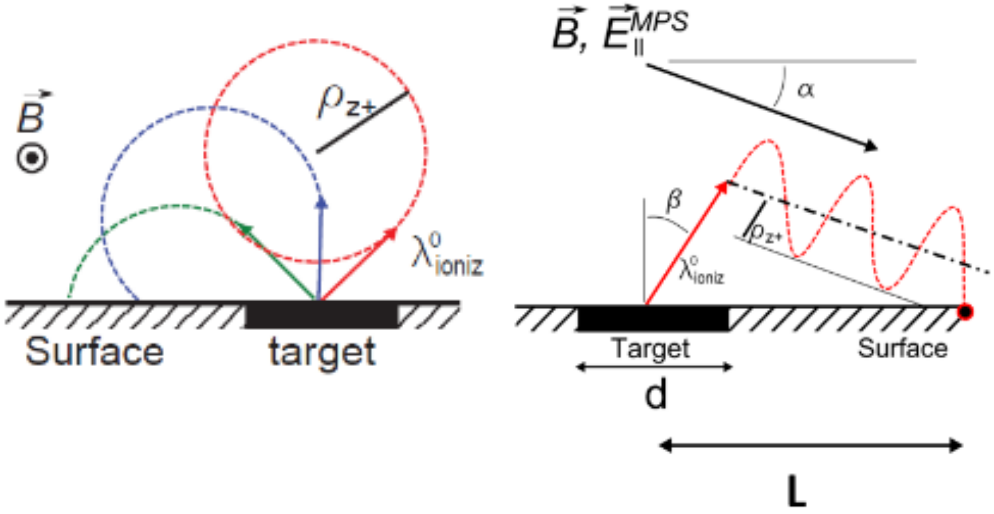

Figure 3-19. Simplified redeposition schematic showing sputtered Al atom straight line trajectory, followed by ionization and gyration along magnetic field line to the surface in the direction of the electric field E_{MPS}. Since ion gyro radius is shorter than the ionization length λ_{ioniz}, at small magnetic field angles α the redeposition length (L) can be many times the ionization length.

We find that with small magnetic field pitch angle of ~1-2 degrees, the redeposition length can be many times longer than the ionization length. Furthermore, at long ionization lengths the sputtering angle becomes important. In Figure 3-20 we show the estimated dependence of redeposition length on ionization length and sputtered angle assuming a magnetic field pitch angle of 2 degrees. The region of ionization lengths and sputtered angles expected for Al in this study is shown, indicating that in the absence of any electric field acceleration by the MPS, a range of redeposition lengths from 10-70 mm can be expected.

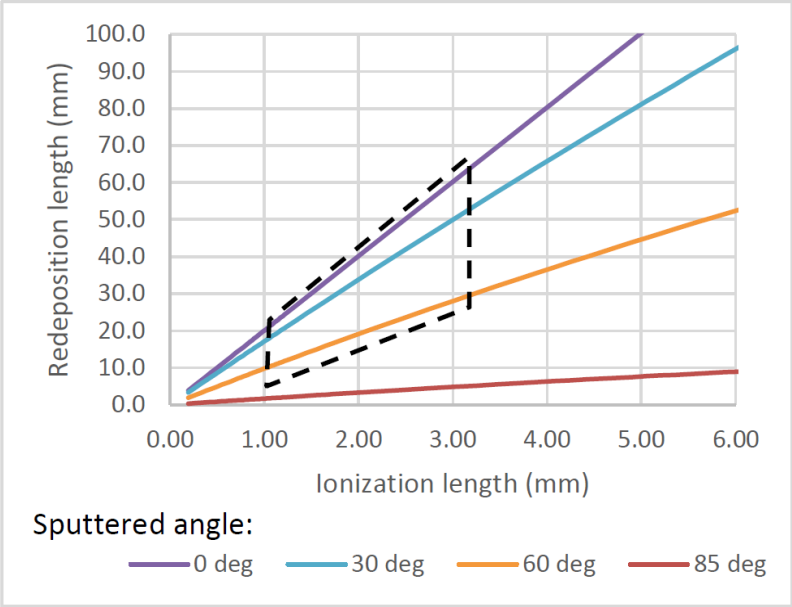

Figure 3-20. The estimated redeposition length for ions redepositing along magnetic field line, as a function of ionization length and at different emitted angles with respect to the surface normal. Calculations assume a fixed magnetic field pitch angle of 2° above the surface plane.

The redeposition fraction, defined as the fraction of material eroded from a given area that redeposits on that area, can be estimated using simple ratio of the erosion area and redeposition areas by assuming erosion from the center of a sample area. For circular sample areas, we assume redeposition is uniformly distributed within a circular area that includes the sample area. The radius of the redeposition area is defined by a redeposition length L, with sample diameter d, hence the redeposition fraction is estimated as a ratio of the sample and redeposition areas as $d^2/4L^2$. For rectangular areas, we can approximate these as infinite radial stripes of width d, and consider redeposition is uniform within a toroidal redeposition length L. Thus, the redeposition fraction can be estimated from a ratio of the lengths d/L. Shown in Figure 3-21 are the expected redeposition fractions for different sized circular and radial stripe areas dependent on redeposition length L.

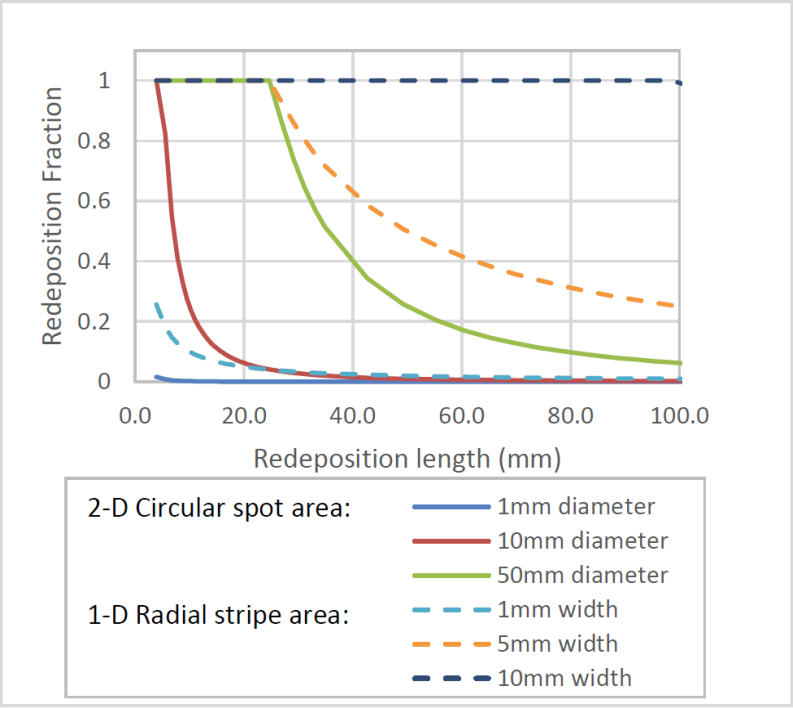

Figure 3-21. Predicted redeposition fractions for different ionization lengths and sample geometries. Circular spot geometry shown in solid lines by spot diameter, and radial line geometries shown in dashed lines by line width.

In the case of Al erosion in the DIII-D plasmas described herein, we expect sputtered energies on average of ~9 eV, with a most probable polar sputtering angle of 70° with respect to the surface normal (based on SDTRIM.SP modeling [61]). This results in Al ion gyro-radius of ~1mm, with Al ionization lengths of ~1-3mm at the average electron density of $1\text{x}10^{13}$ cm^{-3}, depending on the ionization rate coefficient [118–121]. The ionization frequency for $Al^{+} \rightarrow Al^{+2}$ is about 10-20x lower than its ion gyro frequency, meaning that an ion will orbit 10-20 times before it becomes ionized a second time. This is enough time (1.1 us) for a typical atom travelling at the plasma sound speed to travel up to 4.8cm. For this reason, multiple ionizations of sputtered Al will not be considered.

For circular spot of 1mm diameter (as used in the case S-D) the expected redeposition fraction is nearly zero. For 1mm wide stripes (as used in cases R-D and R-He), the redeposition fraction is below 10%, since redeposition lengths are estimated to be

longer than 10mm. Erosion from these areas should be a good approximation of gross erosion, provided that redeposition from the larger, downstream area is not significant. For this reason, the small areas intended for gross erosion were located toroidally upstream of the larger areas, since deposition is expected to be driven along the field lines in the downstream direction. In cases R-D and R-He, a second 1mm stripe was added just 1mm *downstream* of the large coating area to confirm this.

For net erosion measurement, the goal is to have a large enough area to capture significant redeposition, approximating the erosion of an entire divertor surface. For 10mm diameter circular spot (used in case S-D), the redeposition fraction is below 50% for L greater than ~10mm, so the area may be too small to provide a true net erosion measurement. Net erosion measurement areas were maximized to the largest practical size in cases R-D and R-He and made rectangular to cover a larger range of radial plasma positions (rectangular areas 14mm wide radially by 20mm long toroidally were used). However, for a 50mm spot (size of the DiMES head area) the redeposition fraction drops to 50% for L greater than ~50mm, so even the entire DiMES head may be too small for a true net erosion measurement for Al. Therefore, in this study we will need to estimate the redeposition length by analyzing the redeposition off the sample and may need to account for redeposition off the sample to determine the net erosion rate.

Chapter 4 Initial Spectroscopic Emission Measurements

4.1 Introduction

In tokamak based plasma-material interaction experiments, often times material erosion rates can only be measured passively based on the light emission from eroded material. In this chapter we will discuss measurements of the Al erosion rate made using spectroscopic diagnostics as samples were exposed to the plasma. These measurements will be compared to the direct (non-spectroscopic) measurements of Al erosion discussed in Chapter 4 and used to determine the ionizations per photon (S/XB) coefficients for Al-I and Al-II lines of interest. We analyze the emission plume shape and infer ionization length scales for sputtered Al. We also discuss the unexpected fluence dependence of the spectroscopic emission intensity that was observed.

4.2 Al Emission Spectrum

Absolute measurements of photon spectral emission flux (photons/cm^2-Sr-Å) were made using a high resolution calibrated visible wavelength multi-chord divertor spectrometer (MDS) [105]. The photo-emission spectrum was measured around 396nm Al-I and 623nm Al-II emission regions of interest on sequential plasma exposures of each sample. In addition, absolutely calibrated CCD cameras imaged the emission area through narrow band-pass filters centered on the Al-I and Al-II emission line groups. Transmission curves for each filter used for the emission plume imaging were also

measured with all optics in place and used to cross-calibrate the camera and spectrometer intensities. The viewing area for the spectrometer covered a ~45 mm diameter spot centered on the DiMES head, which covered most of the eroding Al area, illustrated in Figure 4-1. Camera images provided a measure of the absolute emission volume, covering a view of roughly 100x100mm in area with 0.3 mm/pixel resolution. The Al coated area was centered in the view of the camera and the CCD integration area was roughly 30mm in diameter. Between exposure shots, either camera filters or spectrometer grating alignments were changed to maximize the range of spectral coverage with limited plasma exposure time available. Plasma conditions remained constant and repeatable with each shot and were monitored using in-situ divertor Thomson scattering view chord 1cm above the sample surface, and with surface mounted Langmuir probes located 5-10cm radially outward from the sample.

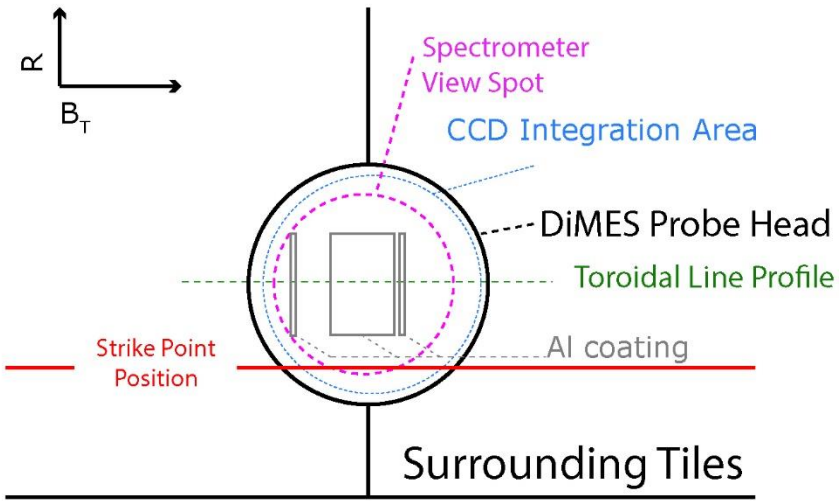

Figure 4-1. Plan view of the DiMES probe and surrounding tiles with spectroscopic emission measurement areas noted (b).

The emission spectra measured in each case, with different background plasma conditions, are shown along with camera filter transmission curves in Figure 4-2.

Transmission curves shown are as measured through the imaging optics simulating emission from the sample 3m from the lens, including the effect of blue-shift by variation of the angle of light incident on the filter, with the Al-I filter tilted 5.45 degrees. We can see that each filter passed a blend of 394.1-396.1 nm Al-I emission lines or 622.6-624.3 nm Al-II emission lines, along with a small fraction of O-II, C-II, and D-I or He-I emission lines. The main difference between R-He and R-D emission spectra shown is the roughly 10x increase in brightness of Al, O, and C lines, due to the higher erosion yield of these surface elements. Also, the presence of a He I emission line at 396.5nm in the RHe case indicates background He emission, while background D emission from the D I 396.9 emission in case R-D and S-D is blended with a nearby O II 3968.5 emission line.

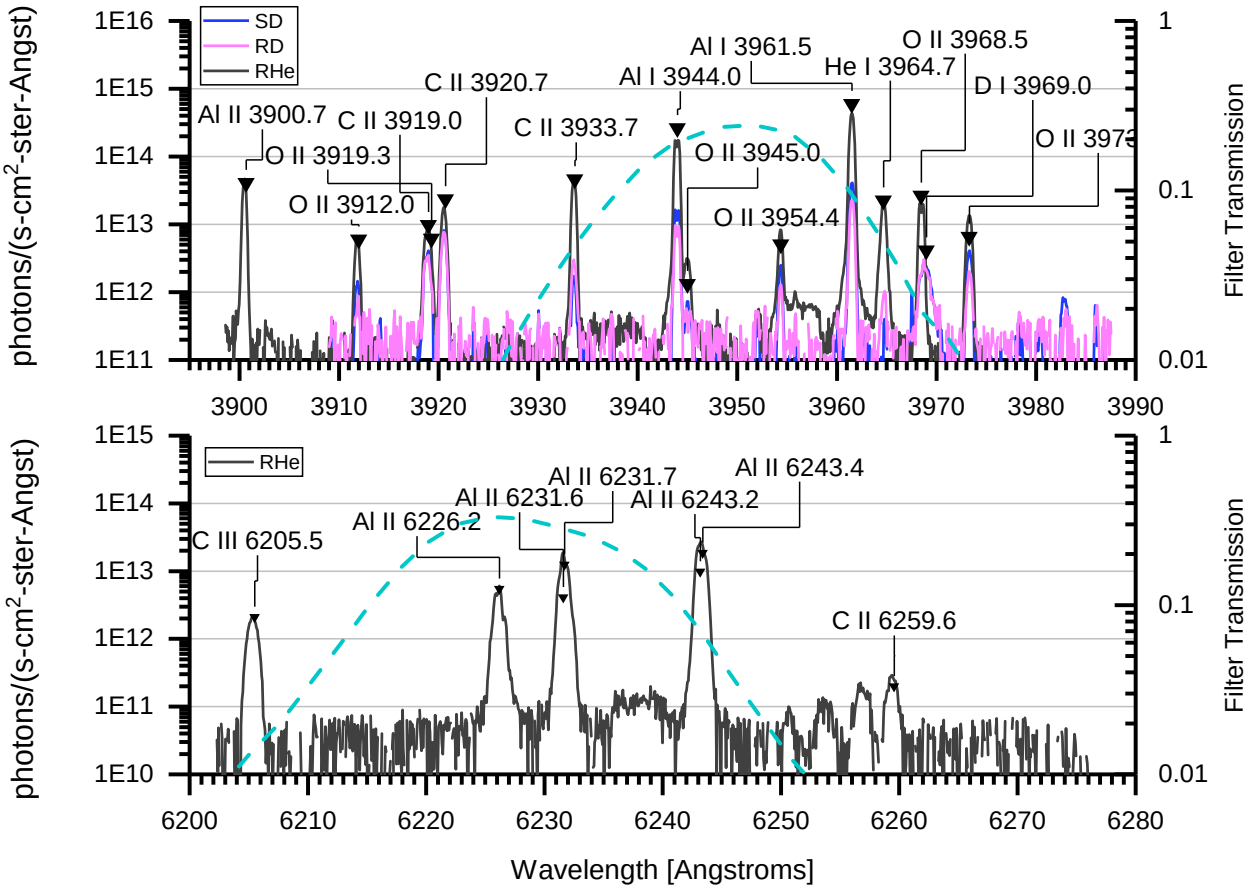

Figure 4-2. Emission spectra and camera filter transmission curves (dashed line) for the CCD camera Al I and Al II spectral regions of interest.

4.3 Emission plume imaging

For imaging in case S-D we used a Pt Grey CMOS camera (model FFMV-03M2M-CS) with a 50mm F1.3 lens, and in cases R-D and R-He we used a PCO CCD camera (model PCO.PIXELFLY VGA) with a 75mm F1.4 lens. For the Al-I emission imaging, we used an Andover 396nm/1nm bandpass filter (010FC06-50) and tilted it slightly to center the transmission region between the 394.4 and 396.1 nm Al-I emission lines. This also minimized background transmission of the two main sources of background near the Al emission line, mainly the D I 396.9 nm and C II 392.1 nm lines A pair of short-pass glass filters (Schott

FG038 and FG025) were used to reduce the background D-alpha and other out-of-band long wavelength background emission. For Al-II emission imaging, we used an Andover 624nm/1nm bandpass filter (p/n 010FC12-50) which covered a blend of Al-II emission lines between 622.6 and 624.3 nm. The primary source of background emission passed by the filter was carbon, with a C III emission line at 620.5nm.

The small amount of background emission transmitted by the filters was subtracted from the images by assuming toroidal uniformity of the background emission. This way, the intensity at a location ~50mm upstream of the sample was uniformly subtracted from the image to provide a better measurement of the absolute Al photon emission flux. Some non-symmetric emission, such as local edge effects near the gap between the DiMES head and neighboring tile were not subtracted and show up in the background-subtracted images as an arc on the downstream side of the sample. Other effects such as local O emission from the Al oxide surface are not subtracted, but represent relatively small contribution to the total imaged intensity. Example images from exposure of sample R-D of both Al-I and Al-II emission are shown in Figure 4-3, showing before and after background subtraction and annotated with camera regions of interest and spectrometer viewing regions.

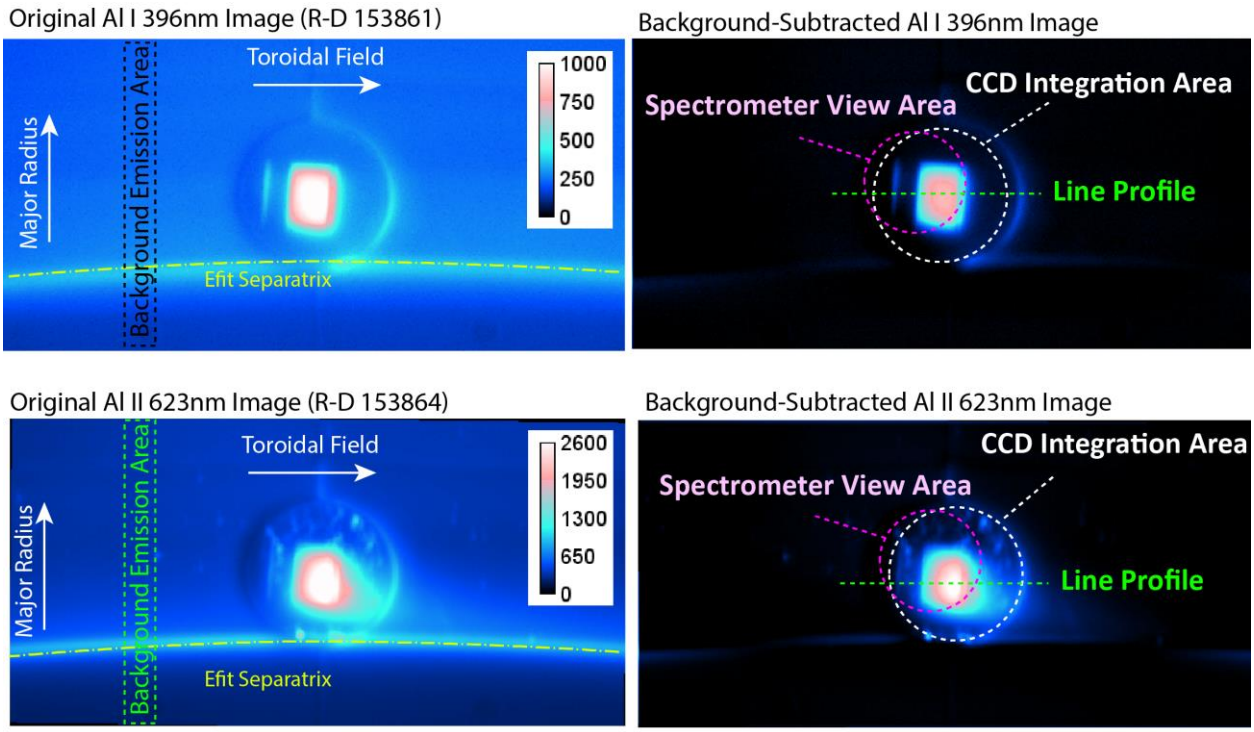

Figure 4-3. False color image CCD view of DiMES, Case R-D, through All filter. Bright Al emission is clearly visible from the rectangular Al coating area and background D I or C II light inboard of the separatrix (dash-dot line). Dashed circles indicate regions of integration for CCD data and approximate location and size of the spectrometer view spot, and area used for line emission line profiles.

The area of Al photo-emission was somewhat larger than the actual coating area, due to the ~mm range ionization lengths of the Al atoms. Therefore, the actual emitted photon flux per unit sample area (photons/cm^2-ster) was determined by normalizing the background-subtracted emission within a 30mm diameter circle to the sample area A_s. The background intensity ($I_{background}$,) value sampled 50cm toroidally upstream of the emission area was subtracted from the total intensity (I_{total}). The total photon emission was also corrected by the average sample reflectivity R_s, which was estimated from pre-exposure measurements and in-situ measurements using ambient light emission during the tokamak plasma breakdown phase to be ~20% in R-He and R-D cases, and ~90% in the S-D case. The inverse sensitivity of the camera, S^{-1} (photons/cm2-ster-count), was calibrated with all filters, windows, and optics in place using a calibrated lab sphere with

known spectral radiance. Thus, the total emitted fluence of Al emission photons Ψ_{tx}^{CCD} (ph/cm^2), which includes the blend of Al emission lines passed by the filter, was calculated as in Eq. 4.1.

$$\Psi_{tx}^{CCD} = \frac{S^{-1}\left(I_{total} - I_{background}\right)}{A_s(1 + R_s)} \qquad (4.1)$$

An asymmetry to the emission plume shape was observed for both neutral and ionized Al. Ionized Al exhibited stronger asymmetry, which was expected due to the expected Al ion motion along magnetic field toward the surface as well as entrainment in the background ion flow. However, asymmetry in the neutral Al emission plume suggests either very strong collisional interaction with background ions or some asymmetry in the emission of Al atoms from the surface. The emission intensity variation in the toroidal direction suggests possible non-uniform erosion from the sample, or some shadowing of the surface by misalignments in the upstream tile edge. However, the observed net erosion rate (as measured post mortem and described in section 1.2) appears uniform across the sample.

The shape of the emission plume depends on many factors, including the angular distribution of sputtering yield and energy and the ionization and photo-emission rates in the background plasma, as well as any gradient in the background plasma density. Sputtering modeling codes such as SDTRIM.SP can calculate angular resolved sputtered energies, but can have different results depending on assumptions about the surface and bulk binding energies for mixed materials and the incident ion angle and energy. Monte-Carlo erosion modeling codes such as ERO can simulate ionization and photo-emission of samples given a description of the background plasma.

In order to better describe the asymmetry and remove the effect of sample geometry, we will assume the resulting emission plume is a convolution of the sample geometry and an emission kernel function. The convolution can be described as an integral transformation function, essentially Green's formula:

$$F(x) = \int_0^u K(x-u)G(u)du \qquad (4.2)$$

Where $F(x)$ is the line profile of emission intensity observed above the sample, $G(x)$ is the coating geometry (equal to 1 for coated and 0 for uncoated area), and $K(x-u)$ is the emission kernel function. The true shape of the emission kernel represents the spatial distribution of Al photo-excitation originating from a single point on the coating, which we will assume is unknown. Instead, we will use a least squares fitting method to determine the best fit emission kernel that results in the imaged emission plume intensity when convolved with the coating area geometry. We will arbitrarily define a functional form for K as a lognormal distribution. This peak function is convenient in that it is similar to a normal distribution with exponentially decaying tails, but includes a parameter to induce asymmetry in the peak shape. The parameters describing it are peak area A, width σ, and asymmetry parameter μ.

$$K(x) = \frac{A}{\sqrt{2\pi\sigma}}\exp\left(-\frac{1}{2}\left(\frac{ln(x-\mu)}{\sigma}\right)^2\right) \qquad (4.3)$$

The Al I and Al II emission profiles and best fit emission kernel functions are shown side by side in Figure 4-4. A 20% reflectivity of the Al-coated areas and 0% reflectivity of the uncoated areas was included in the final calculated emission profile intensity. For both neutral and ionized emission kernel functions, the downstream tail is roughly twice the

length of the upstream tail. This suggests a common underlying cause for the asymmetry, such as a forward toroidal bias to the sputtering yield and/or sputtered energy distribution. In Chapter 5, we will present a model of photo-emission and ionization that includes angular distribution of sputtering yields to test this hypothesis.

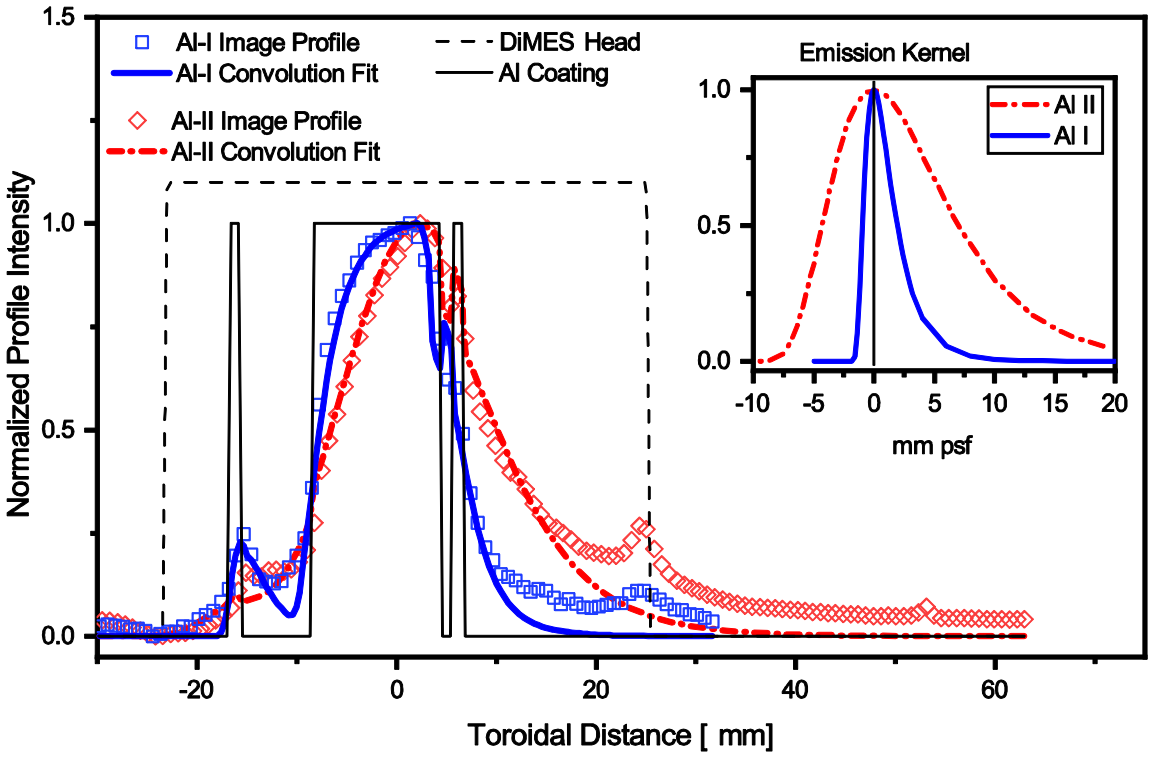

Figure 4-4. Comparison of normalized Al-I and Al-II emission toroidal profiles with deconvolution fit kernel functions. The original Al coating area is represented by a solid black line, and the DiMES head area is represented by a dashed line.

4.4 S/XB coefficient measurements

If the ratio of ionization to photo-emission for a particular line is known for the given background plasma conditions, it is possible to infer the flux of neutrals and ions into the plasma by measuring the photo-emission intensity of neutral atom and ion transitions. This

ratio, known as the S/XB coefficient, is the ratio of the atom ionization rate (S) to the photo-excitation rate (X) and line branching ratio (B). Here we can assume that all eroded atoms ionize before leaving the plasma volume (a reasonable assumption given the ionizing plasma extends several ionization mean-free-paths in each direction of the sample), thus the erosion rate measurements determine the ionization rate (S). Samples were exposed to nearly constant background plasma conditions, and thus post-mortem measurements of gross erosion (non-spectroscopic measurements) were combined with integrated absolute photo-emission measurements to determine the S/XB coefficients for various Al emission lines at these conditions.

We can assume that all eroded atoms ionize before leaving the plasma volume (a reasonable assumption here given the ionizing plasma extends several ionization mean-free-paths in each direction of the sample). Thus, the electron impact photo-excitation of neutral atoms leads to a photon emission flux that can be proportional to the gross erosion rate. The measurements of the photon emission flux for neutral and ionized Al were normalized to the post-mortem gross erosion measurements to determine the S/XB coefficients for individual lines. The S/XB ratios for a number of neutral and ionized Al emission lines were determined, and are discussed in section 4.4. Filtered light camera imaging of the samples also allowed measurement of the spatial distribution of the emission plumes, against which models of the angular and energy sputtering distribution, ionization length, and background entrainment in plasma flow can be compared.

The S/XB coefficients were determined in these plasma exposures from the ratio of the total Al photon flux for that emission line (Γ_{ph}) to the gross Al atomic erosion flux Γ_{Al} measured non-spectroscopically according to

$$S/XB = \Gamma_{Al}/\Gamma_{ph} \qquad (4.4)$$

The viewing spot size of the spectrometer was typically larger than the emitting area (as shown schematically in Figure 4-1), but absolute calibrations of the spectrometer are done with large area uniform light sources that fill the entire viewing area. For this reason, absolute line intensity measured by the spectrometer would under-estimate the actual radiance emitted from the coating area. A geometric coupling correction factor Λ_{MDS} was calculated by cross-calibrating with the area-integrated emission from filtered CCD camera measurements. The geometric coupling factor was determined by equating the total transmitted photon flux by the camera Ψ_T^{CCD} to the total flux measured by the spectrometer Ψ_{MDS} weighted by the filter transmission curve T at wavelength λ.

$$\Lambda_{MDS} = \Psi_T^{CCD} / \int \mathrm{T}(\lambda) \cdot \Psi_{MDS}\, d\lambda \qquad (4.5)$$

This geometric factor is different for emission by ionized Al and neutral Al, due to differences in the emission plume size. However, for each emitting species, we assume that relative line intensities would be constant across the emission area and throughout plasma exposure. Thus, the S/XB coefficients for a particular emission line were determined as:

$$S/XB = \Gamma_{Al} / \Lambda_{MDS} \Psi_{MDS} \qquad (4.6)$$

The resulting S/XB values for measured Al I and Al II emission lines are plotted in Figure 4-5. The measured values are compared with theoretical S/XB vs T_e curves calculated using ionization cross-sections available in ADAS [119] and Plane-Wave Born (PWB) scaling of excitation [122]. For both species, the theoretical values under-estimate the measured values by large amounts. The discrepancy is too large to be explained by any geometric coupling calibration or measurement error. In related work,

measurements of the S/XB coefficient made in the PISCES-B linear plasma facility were roughly a factor of 5 higher than the ADAS calculated values [106].

The cause of the measurement-theoretical estimate discrepancy is unclear at this point. The ADAS calculated S/XB values assume do uniform plasma density, which may not be valid given the density gradient in the magnetic pre-sheath. However, varying density by an order of magnitude resulted in no significant change in the ADAS calculated S/XB values. Experimental measurements of the ionization rate coefficients made by Freund et al [120] are higher than the ADAS modeled ionization rate coefficients by about a factor of 3. A more likely reason for the low ADAS calculated S/XB coefficients may come from the calculation of photo-emission coefficients. It appears from the data measured here that the T_e dependence of these photo-emission coefficients is not correctly captured in the ADAS atomic physics calculations.

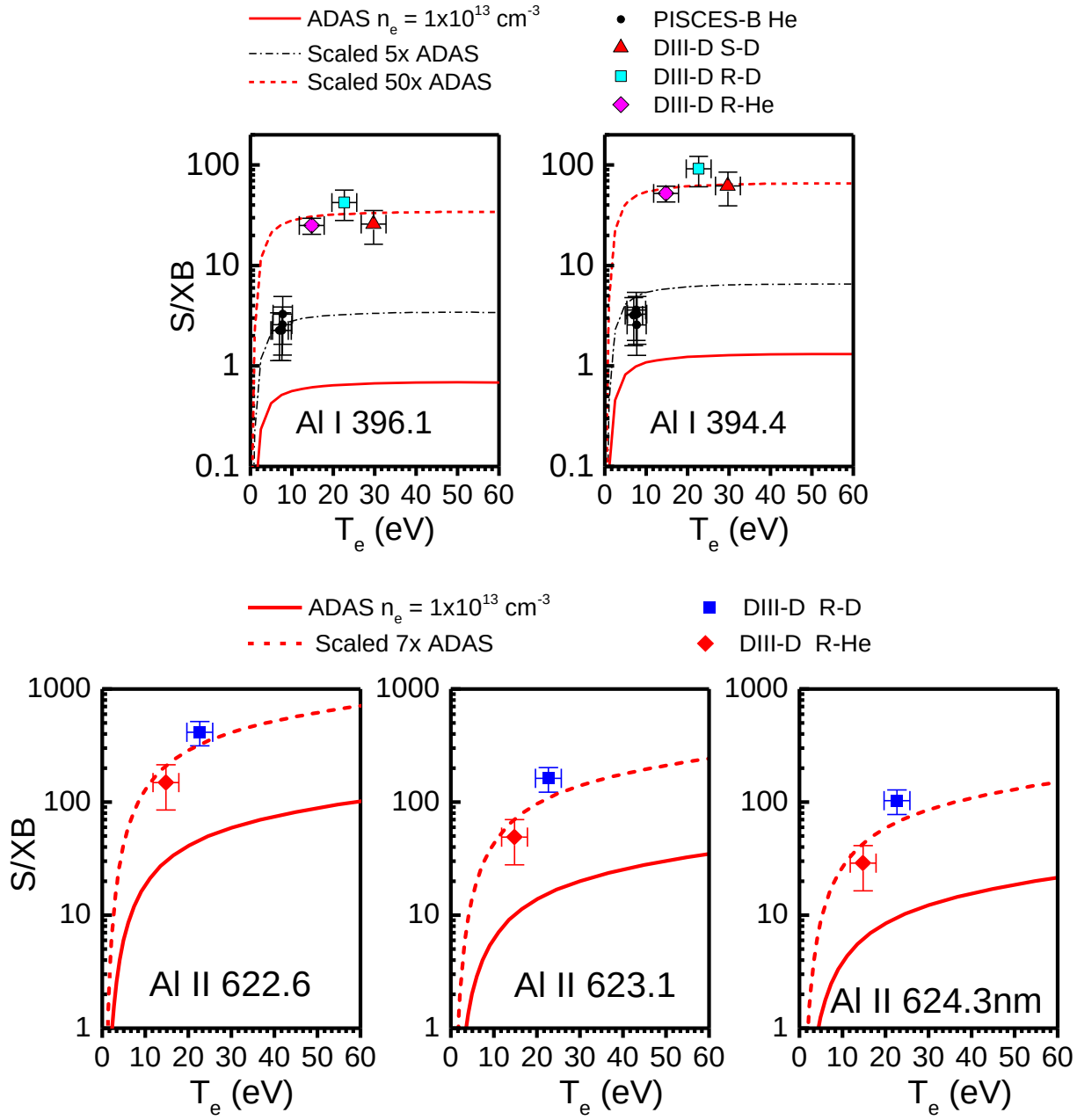

Figure 4-5. Measured S/XB values plotted for Al-I and Al-II emission lines (points) compared to ADAS calculated S/XB values (solid lines). Dashed lines are the ADAS calculated values scaled linearly to match the measurements. For the Al I plots, PISCES-B measured values are reproduced from [106].

4.5 Fluence Dependence of Al-I Emission Intensity

The MDS spectrometer and camera imaged intensities both recorded changes in individual Al emission intensity during exposure that suggest some changes in the surface erosion rate or composition occurred. The cause of the emission increase is not well understood at this point, and in fact erosion was expected to decrease with fluence due to surface dilution by carbon deposition and implantation [97] or due to ion induced surface roughening as has been observed in linear plasma devices [123]. The increase in the Al emission intensity came along with changes in the emission of O and C, the two main impurities found in the Al sample surface after plasma exposure.

One of the drivers of the increase may be evolution of the surface composition, although here there are two competing effects: erosion of the native oxide exposes more Al for erosion, while implantation of C should lead to a reduction in Al available at the surface. We see evidence of both oxide removal and carbon increase when tracking the emission intensities of Al, O, and C lines with exposure time in cases R-D (Figure 4-6) and R-He (Figure 4-7). The brightest emission lines in the 380-400nm spectral range were selected. S-D sample is not compared, since the size of its Al sample area was small compared to the total spectrometer detection area and trends may be skewed by the surrounding C surface. The window of uniform condition exposure for each plasma shot was ~1.5-4.5 seconds. D and He emission remained constant during this window, or proportional to the small changes in plasma temperature and density, (as measured by Thomson scattering view chord 1cm above the sample). The total exposure time shown for each case represents similar total net Al erosion: ~25 nm of Al for the 12.6 seconds of exposure in R-D and ~31nm in the first 3.8 seconds of plasma exposure in R-He.

In both cases, the observed Al-I emission intensity increases by a factor of four. O I and O II emission stay relatively constant in R-D case, but shows a strong decrease in the R-He case. The Al erosion rate increase may be partly attributed to oxide removal, since total initial oxide thickness was roughly 10nm. The oxygen emission lines near the sample did appear to decrease for the first R-He exposure, indicating oxide removal, but this was not observed in case R-D. There, either background O emission dominated the signal or the surface oxide was replenished between shots.

In both R-D and R-He cases we see the C II emission increases during the exposure which points to evidence of carbon surface concentration increase. However, Al I emission also increased rather than decreasing as would be expected with a decrease in Al concentration. It is possible that a mixed Al:C material may have a higher average Al sputtering yield than pure Al, via reduction in bulk Al binding energy, although this is inconsistent with the fact that the measured erosion yield under-estimates expected yields for pure Al.

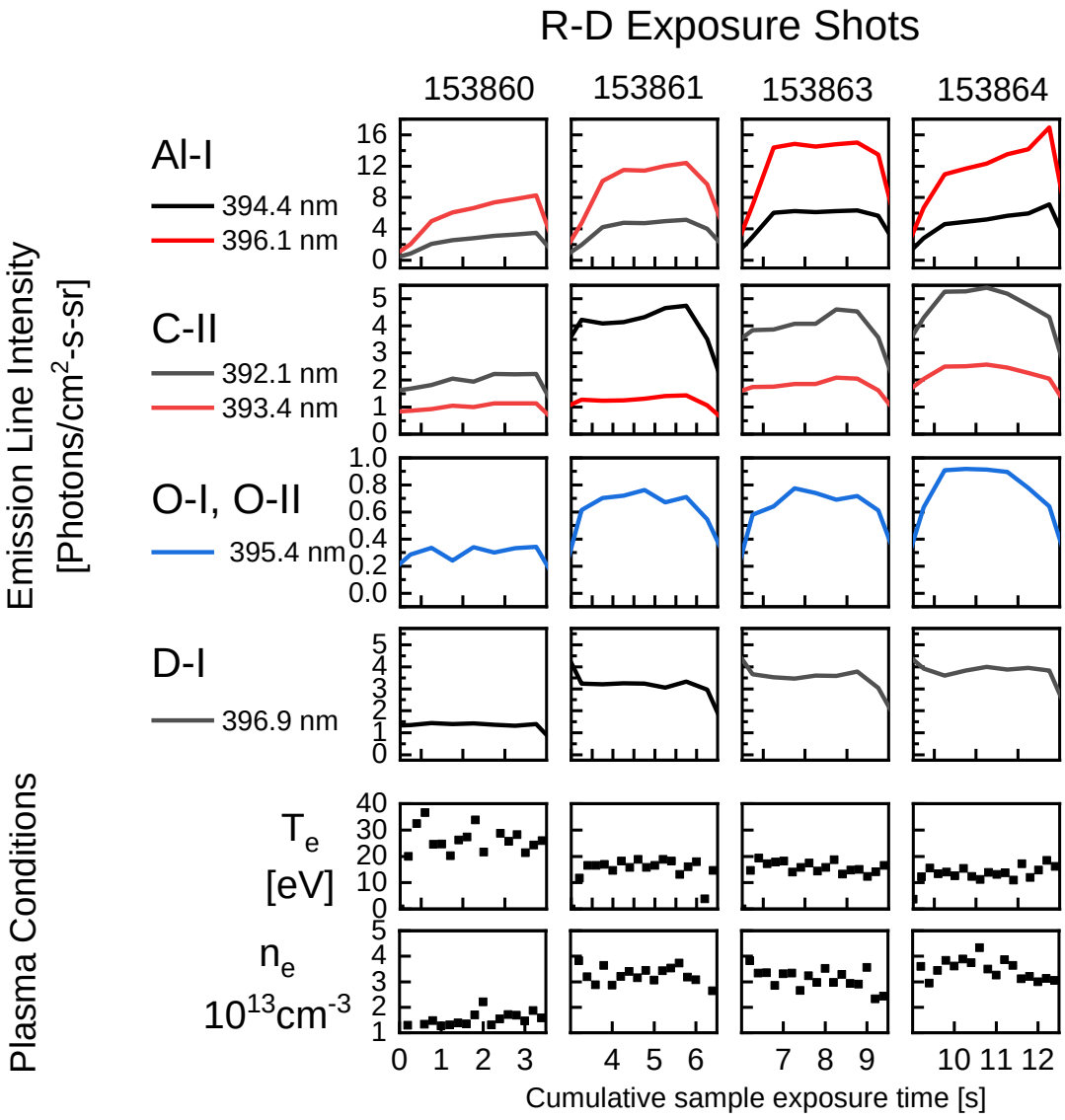

Figure 4-6. Emission line intensities for Al-I, C-II, O-I, and D-I vs time for each consecutive exposure shot in case R-D. Plasma temperature and density during each exposure shot shown in the scatter plots at the bottom.

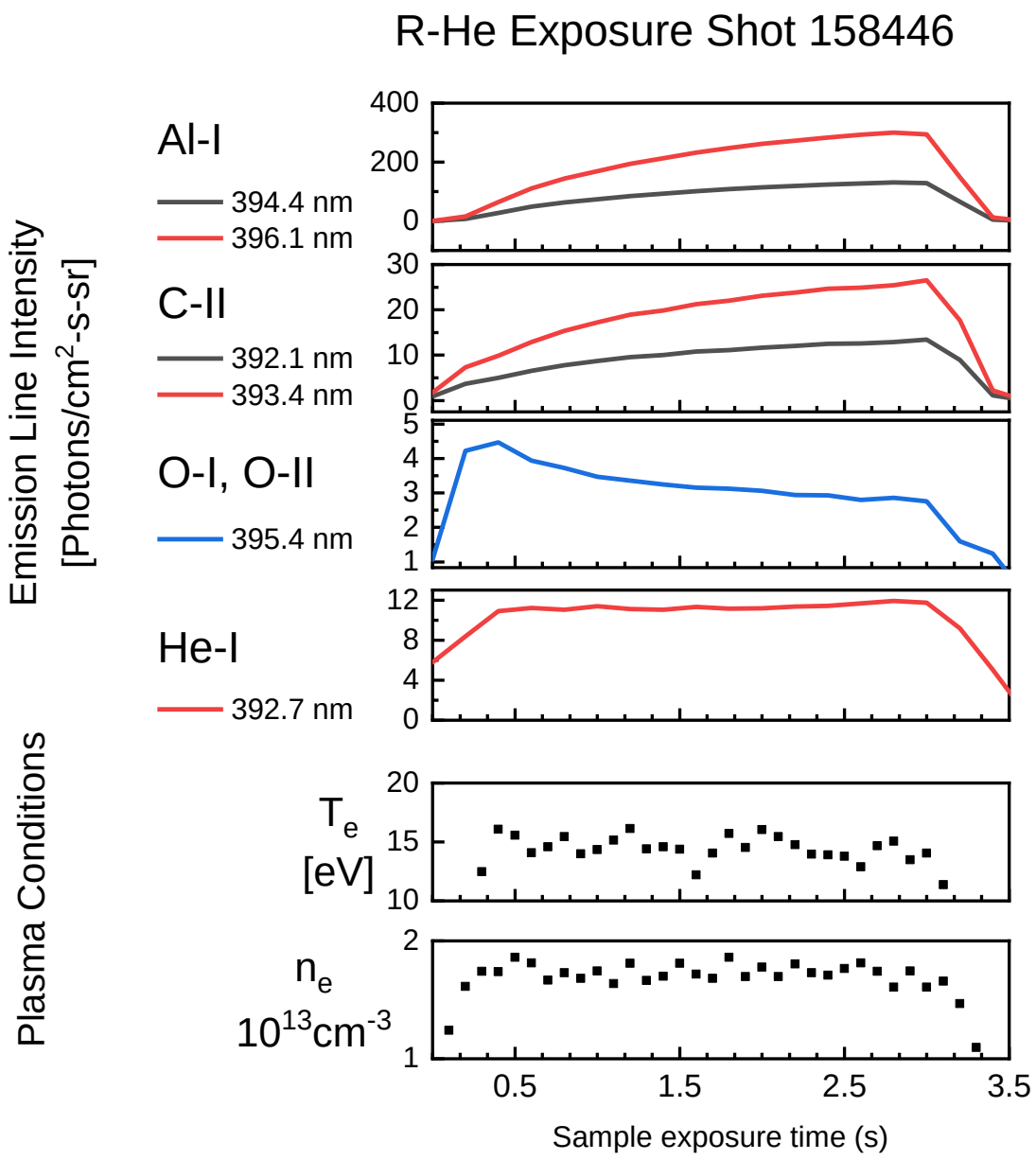

Figure 4-7. Emission line intensities for Al-I, C-II, O-I, and He-I vs. time for the first exposure shot of case R-He. Plasma temperature and density during each exposure shot shown in the scatter plots at the bottom.

Another cause of the Al emission increase may be due to an increase in the effective area of the eroding surface during the plasma exposure. The emission as seen

through the spectrometer view chord may appear brighter because more of the view chord area is filled by eroding Al surface. One cause would be redeposition and re-erosion from a wider area of the sample. However, the total fraction of redeposition is low, and it is not realistic to expect a 4x increase in the intensity by a relatively small increase in sample area. Another cause can be due to microstructure smoothening, since a reduction in surface roughness can lead to less microscopic shadowing and larger effective eroding area. Typically surfaces experience a micro or nano-scopic roughening or other morphology development during ion erosion [82]. However, some degree of surface smoothening may occur with ions that are incident with a small enough angle (relative to the overall surface plane). If small protrusions that lead to shadowing are eroded away, more of the surface can be exposed and the total area of Al erosion and thus emission can increase. There are some examples of this type of surface smoothening in the literature [84]. Smoothening can also increase the surface reflectivity and thus the detected emission flux. The samples did visibly appear shinier after exposure than before exposure, although no controlled pre-exposure measure of the specular reflectivity were made.

The Al I emission increase suggests higher Al erosion rate, although if that is not the case it would suggest higher Al I emission coefficient. A variation in the local photo-emission coefficient in an otherwise uniform plasma may suggest that the average sputtered energy of Al atoms is changing. The higher sputtered energies may result in deeper penetration of Al through the plasma sheath, to areas of higher electron density and thus brighter emission. Average sputtered energies may increase if the Al surface binding energy is decreasing, which may occur as a result of formation of a mixed Al:C

material, or for Al redepositing on an active surface in a high ion flux environment (as suggested for C in JET [124], Mo in DIII-D [15], and Be in PISCES-B [125].

The brightness increase was not uniform over the entire sample area. Shown in Figure 4-8 are the emission images for sample R-D at (a) 100ms into plasma exposure, (b) 6 seconds into plasma exposure. The time evolution of the toroidal profile of emission (c) shows how the increase in brightness occurs more strongly over the 15mm Al stripe area and downstream of the Al coating area than over the 1mm stripe area. The most significant increase in Al brightness occurs over the wide stripe region and on the downstream side of the sample. Some of the Al-I light emission may be due to re-erosion of Al deposited downstream of the original coating, and this appears as a slight increase in the baseline of the profile on the downstream side compared to the upstream side (An increase is also observed around the edge of the tile downstream of the DiMES head, where there may be some leading edge effects). This is a small increase and constant, which indicates that the redepositing flux is rapidly re-eroded and moved far from the sample. The emission increase occurs more strongly over the 15mm stripe region than over the 1mm region, and this suggests that the size of the emission plume (and thus the sputtering yield or energy) is increasing in the downstream more than in the upstream direction.

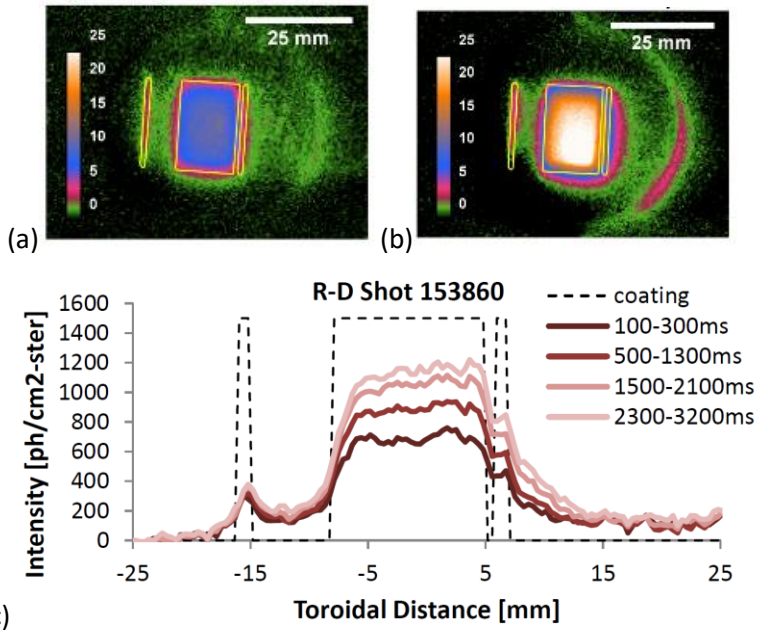

Figure 4-8. Al I emission image during first 100ms (a) and after 6 seconds (b) of uniform plasma exposure. Original Al coating area highlighted in yellow. The emission intensity line profile taken through the sample center at different times during plasma exposure (c). Initial Al coating areas indicated with dashed lines.

4.6 Conclusions

We present the first spectroscopic measurements of Al erosion in DIII-D tokamak. Al is expected to behave as a low-Z material in erosion-redeposition, having an ionization mean free path that is long compared to its ion gyro radius. For this reason, Al can be a useful proxy for Be erosion-redeposition studies, where Be is otherwise restricted due to its toxicity.

Al emission spectra in divertor plasmas find bright and useful Al emission lines distinct from background C, O, D, and He lines. Imaging of the Al-I and Al-II emission plumes were made using narrow bandpass filtered cameras. We presented

measurements of the S/XB coefficients for Al-I and Al-II emission lines and suggest that the ADAS S/XB calculations for Al be revisited.

In these initial observations we have found a number of unexpected observations that warrant further research. Emission plume shapes were analyzed and found to have an asymmetry along the toroidal direction for both neutral and ionized Al emission lines. The plume length scales were within the expected range of ionization lengths data for Al neutral atoms, but the asymmetry suggests a toroidally forward-bias to the sputtering yield and/or sputtered energy for Al. Furthermore, the emission plume length was seen to increase with ion fluence primarily in the toroidally downstream direction. This is thought to be partly due to material migration behavior (re-erosion of Al in the primary redeposition direction), but may also be due to surface morphology or composition evolution leading to higher average sputtered energies in the initial asymmetry direction. Redeposition length scale appears similar to the ionization length, which was surprising given the simple picture of redeposition along field lines. More sophisticated models of the erosion, ionization and redeposition cycle are needed to address these discrepancies. Models should include the role of the sheath electric field, surface morphology, and a dynamic evolution of surface composition. Full angular distributions of sputtering and ionization, along with estimates of neutral and ion entrainment in background plasma flow should be included to compare with the measured emission plume asymmetry.

4.7 Acknowledgements

This work was supported in part by the US Department of Energy under DE-FC02-04ER54698, DE-FG02-07ER54917, DE-AC52-07NA27344, DE-SC00-02060, and DE-AC04-

94AL85000. Sandia National Laboratories is a multi-mission laboratory managed and operated by National Technology and Engineering Solutions of Sandia LLC, a wholly owned subsidiary of Honeywell International Inc. for the U.S. Department of Energy's National Nuclear Security Administration under contract DE-NA0003525. DIII-D data shown in this paper can be obtained in digital format by following the links at https://fusion.gat.com/global/D3D_DMP.

This chapter includes text and data that is a reprint of the material as it appears in C. Chrobak, P. C. Stangeby, A. W. Leonard, D.L. Rudakov, C.P.C. Wong, A.G. McLean, G.M. Wright, D. A. Buchenauer, J.G. Watkins, W.R. Wampler, J.D. Elder, R.P. Doerner, D. Nishijima, G.R. Tynan, "Measurements of Gross Erosion of Al in the DIII-D Divertor." Journal of Nuclear Materials, vol. 463, 2015, Pages 810–813. The dissertation author was the primary investigator and author of this paper.

Chapter 5

Measurement and Modeling of Aluminum Sputtering and Ionization in the DIII-D Divertor Including Magnetic Pre-Sheath Effects

5.1 Introduction

Recent analysis of Al (a proxy for Be) erosion in different attached L-mode divertor plasmas in the DIII-D tokamak has found that asymmetries in the Al I photo-emission plume and Al redeposition patterns are consistent with an anisotropy in the angular sputtering distributions expected due to sputtering by near grazing incidence angle ions. In this chapter we calculate the expected incident angle distributions (IADs) for ions accelerated through the magnetic pre-sheath and Debye sheath potential gradients using a numerical particle tracking model. The full incident ion angle and energy distributions for main and impurity ions were calculated using particle tracking model including full gyro-motion and drifts due to potential gradients of the magnetic pre-sheath (MPS), also known as the Chodura sheath [43]. Next, we will present the resulting angular distributions of sputtering yield and energy due to ions with the aforementioned IADs. Angular resolved sputtering distributions were calculated using the SDTRIM.SP binary collision sputtering modeling code. Lastly, we will model the resulting spatial distribution of ionizations and photo-emission due to the sputtering distributions and compare the result to experimental observations of the emission plumes. Our model uses numerical Monte-Carlo methods to simulate electron-impact ionization and photo-

emission of sputtered neutrals in the MPS electron density gradient. Synthetic diagnostic images of the eroding surface are generated from the output of the model and used to compare with experimental observations.

5.2 Magnetic Pre-Sheath Effects on Incident Ions

For tokamak plasma material interactions, in particular for divertor plasmas where a grazing incidence angle between the magnetic field and material surfaces is required to reduce the projected heat flux onto the target, the sheath potential drop is likely dominated by the magnetic pre-sheath (MPS), with an essentially non-existent Debye sheath (DS) [45]. The broad region of weak electric field in the MPS (compared to the DS) can produce very different near-surface ion flows and incident ion directions than the DS. Stangeby [45] and Ahedo [52] fluid models show that ion fluid drifts in the $\vec{E} \times \vec{B}$ direction within the MPS can be comparable to c_s, which alters the boundary conditions for tokamak plasma flows. Recent modeling of incident ion trajectories in magnetized plasmas [92,126,127] has shown that the average incident ion pitch angles become smaller with increasingly narrow distributions as magnetic field pitch angle decreases. Additionally, a deflection of the ion trajectories perpendicular to the field direction occurs as ions approach the surface due to $\vec{E} \times \vec{B}$ drifts within the sheath. Here we present calculations of the ion impact angle distributions (IAD) using similar Monte-Carlo particle tracking methods for each of the exposure cases in this study.

The coordinate systems used in this chapter are either orthogonal (X,Y,Z) or spherical (r, φ, θ) where appropriate and are aligned to tokamak oriented directions (toroidal, radial) relevant to the DiMES exposures in this thesis (Figure 5-1). The ion impact angles distributions (IADs) are described here in terms of the polar angle θ (angle relative

to surface normal) and azimuthal angle φ (angle relative to toroidal direction). The toroidal field pitch angle $\alpha = 90^{\circ} - \theta$ is in degrees above the surface plane. The sputtered material emission or scattering angle β is referenced to the surface plane and spans 180° from the forward-scattering to backward-scattering direction (relative to the incident ions).

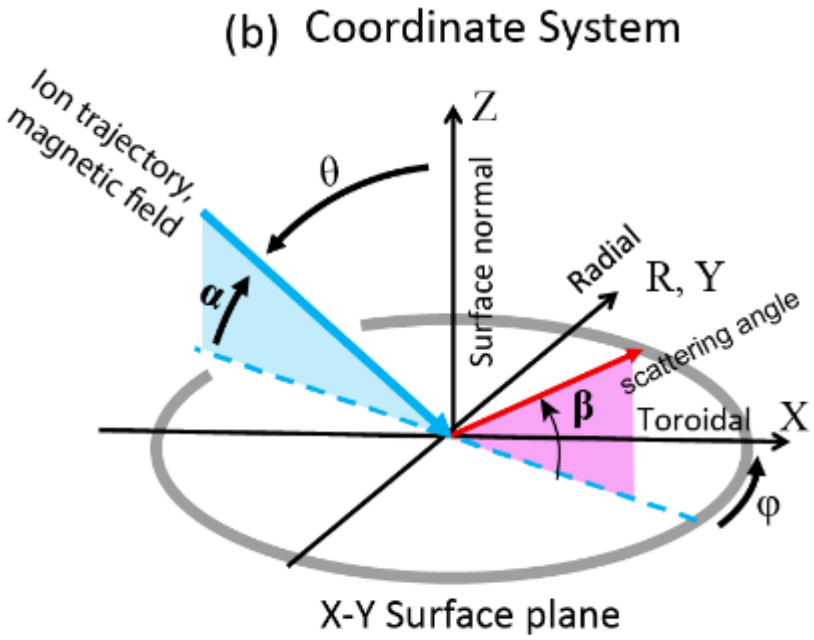

Figure 5-1. Coordinate system used for incidence ion angle distribution and emission plume modeling

Khaziev and Currelli [126] have previously used both Monte-Carlo and Particle-In-Cell type kinetic modeling codes to model the sheath and full 3D ion velocity distributions at different magnetic field pitch angles. Their results show that as the magnetic field pitch angle approaches grazing angle, ions are less deflected by the E-field and incident angles more closely approach the field incidence angle. Following similar methods as described in [92] we have calculated the expected ion incidence angle distributions (IADs) using a Monte Carlo particle tracking model for the plasma conditions expected

in DIII-D. The sheath density and potential gradients were calculated according to the convenient expressions derived by Borodkina [127] which are summarized in section 2.1. Particles were launched from the edge of the sheath , a location defined as where the normalized sheath electric field gradient is 1% of the maximum value near the surface. Particles were started at the top of their orbits ($v_\perp = +v_x$) so that they would enter the MPS on their first gyration. Particle trajectories were calculated using a Runge-Kutta numerical solution to the single particle differential equation of motion (Eq. 5.1). Here, the +y direction is normal to the surface. $\vec{\boldsymbol{E}} = \boldsymbol{E_y}$ and is negative, directed toward the surface. Toroidal field $\vec{\boldsymbol{B}}$ points in the +z direction with minor components in the –y and –x directions.

$$\frac{d\vec{\boldsymbol{v}}}{dt} = \left(\frac{q_i}{m_i}\right)\left(\vec{\boldsymbol{E}} + \vec{\boldsymbol{v}} \times \vec{\boldsymbol{B}}\right) \qquad (5.1)$$

Initial particle velocity distributions were defined in the parallel ($v_\parallel$) and perpendicular ($v_\perp$) to $\vec{\boldsymbol{B}}$ directions. For the initial velocity in the parallel to **B** direction, we assumed a shifted top-hat velocity distribution with a width of the ion thermal speed $c_i = \sqrt{kT_i/m_i}$ and a maximum at the plasma sound speed $c_s = \sqrt{(kT_e + kT_i)/m_i}$. A finite ion temperature $T_i = T_e$ is assumed. This simple ion velocity distribution satisfies the generalized Bohm criterion constraint [42] and ensures all ions at the sheath edge are travelling toward the surface. For the velocities perpendicular to the **B** direction, we assumed a Maxwellian distribution for the specified ion temperature. Some example particle trajectories are shown in Figure 5-2 (a), for particles with parallel and perpendicular velocity components chosen from the distributions as shown in Figure 5-2 (b).

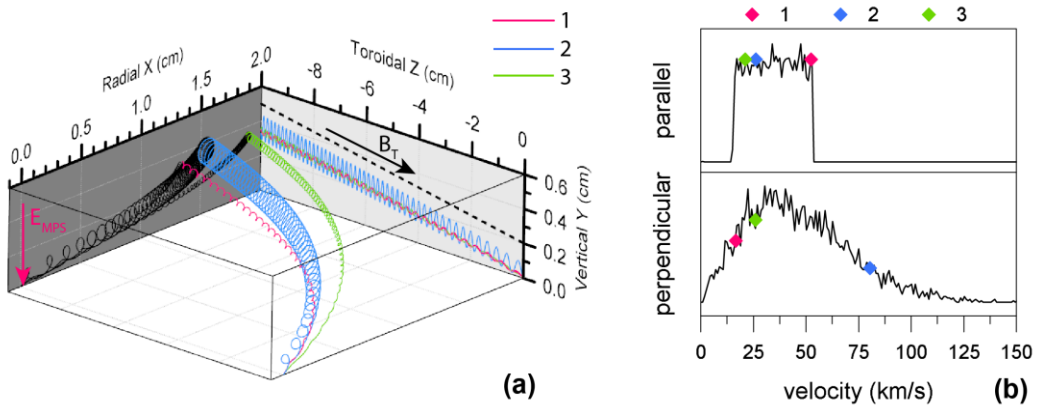

Figure 5-2. Computed ion trajectories (a) for three D^+ ions 1, 2, and 3 travelling through a collisionless deuterium plasma MPS. The toroidal coordinate is compressed to highlight the extent of the radial ExB drift. Perpendicular and parallel velocity distributions at the sheath edge are shown (b), with points indicating the initial launch velocities of each of the particles.

Some examples of sheath potential gradients and the resulting IADs for different magnetic field pitch angles are shown in Figure 5-3. In these examples we use the plasma parameters of T_e = 29eV, n_e = 1.1x10^{13} cm^{-3}, and toroidal field pitch angle α = 1.7 - 40 degrees above the surface plane to calculate the sheath gradients using the equations described in Chapter 2. The MPS region of the sheath potential gradient is shown plotted in a dashed line, with the DS region shown calculated in solid line. The resulting distributions of ion impact angles are described here in terms of the polar angle $\boldsymbol{\theta}$ (angle relative to surface normal) and azimuthal angle $\boldsymbol{\varphi}$ (angle relative to toroidal direction). At α = 40° magnetic field pitch angle (50° from surface normal), 80% of the sheath potential drop occurs over the DS, and the peak polar impact angle occurs at 15° from surface normal. At α = 1.7° magnetic field pitch angle (88.3° from surface normal), the entire potential drop occurs over the MPS and peak polar ion impact angle occurs around 82° from surface normal.

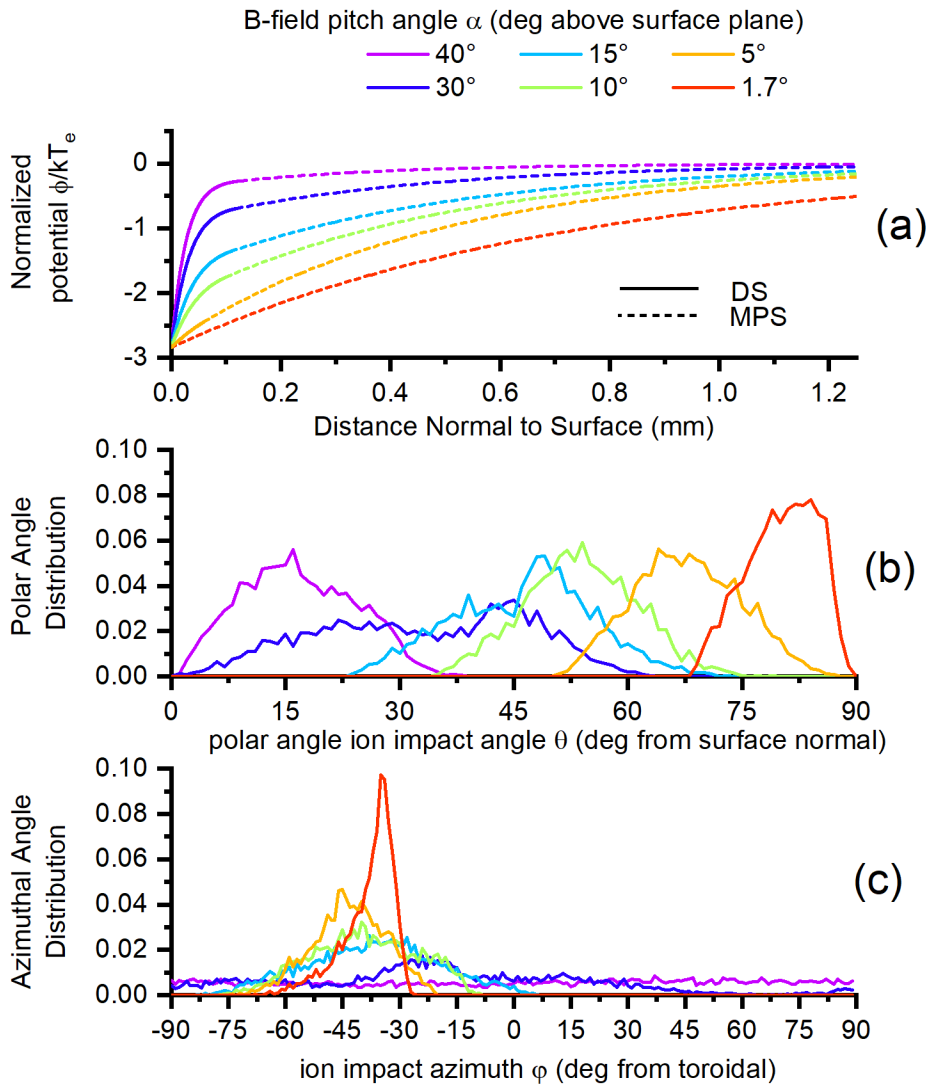

Figure 5-3. Sheath potential drops for each pitch angle shown in (a) with solid or dashed lines indicating Debye sheath (DS) or magnetic pre-sheath (MPS) regions. Impact angle distributions for the polar (b) and azimuthal (c) angles shown (see also Figure 5-1.

Next we examine the IAD dependence on sheath potential gradient with fixed magnetic field pitch angle. The potential gradients shown in Figure 5-4, were calculated using plasma parameters from the R-He exposure case with a fixed magnetic field pitch angle (α = 1.4°), but we have imposed different sheath solutions by artificially specifying the size of the DS potential drop to be a fraction of the total floating potential. The DS and MPS potential gradients were calculated according to the expressions for the

sheath [128]. Also, MPS length scale factors of k= 2 and 3 main-ion gyro radii are compared (where MPS gradient length $L_{MPS} = k\rho_i \cos(\alpha)$). While these potential gradients may be artificial, they illustrate that the absence of the DS is responsible for the near surface potential gradient (and thus E-field strength) decrease, shifting the most probable polar ion impact angle from ~45 degrees to ~80 degrees with respect to surface normal. The azimuthal E×B deflection angle decreases with vanishing DS, and a large change in azimuthal impact angle shows up when assuming the MPS length factor k=3 ion gyro radii. Experimental measurement of the azimuthal impact angle may be a useful for estimating the MPS potential gradient scale length.

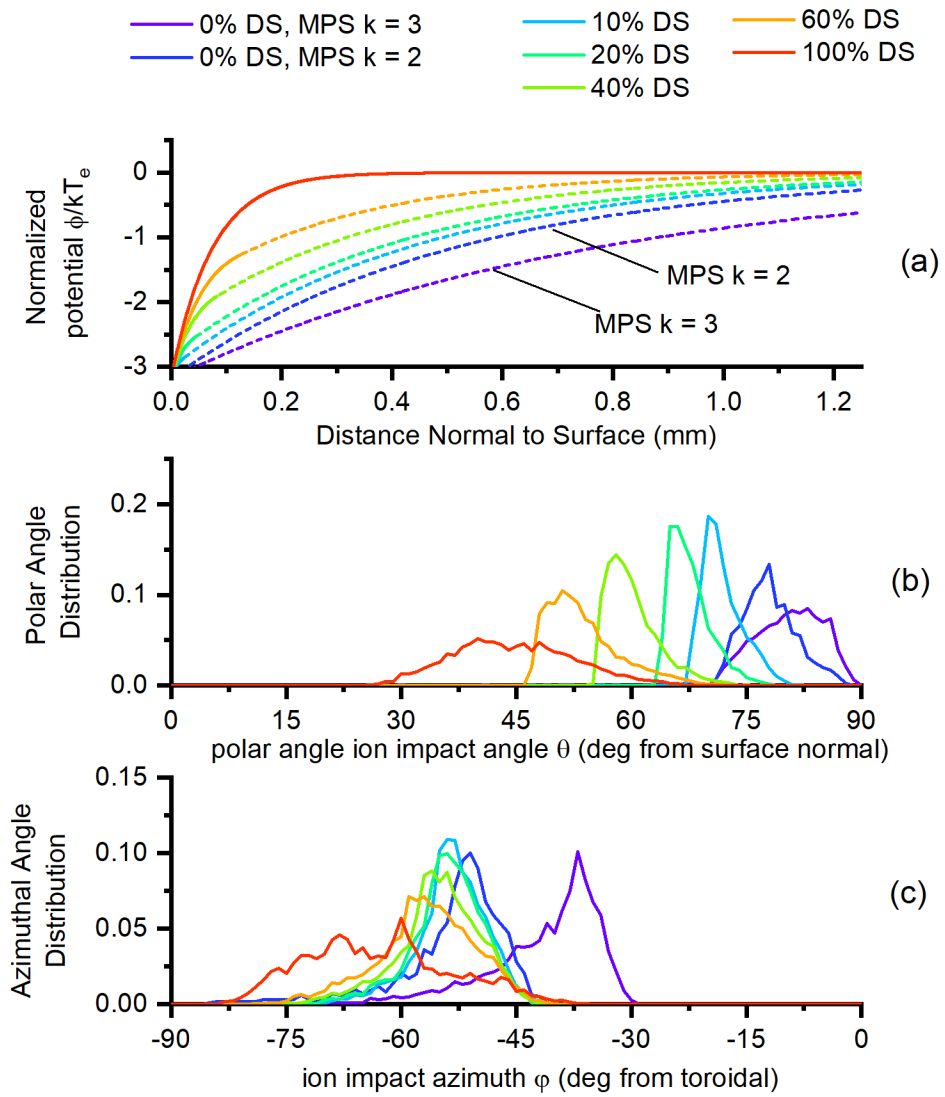

Figure 5-4. Sheath potential drops (a) calculated using R-He plasma conditions, fixed magnetic field pitch angle of 1.4°, and with potential drop artificially divided between DS and MPS solutions as shown. Also MPS gradient lengths factors k=2 or 3 compared (see eq 2.7). Resulting ion impact distributions in the polar (b) and azimuthal (c) angle.

To describe the MPS structure in these experiments we used the measured plasma parameters and calculated the sheath electric field and density gradient. We assumed $T_e = T_i$ and singly ionized main ions. The resulting sheath electric field and density gradient vs. distance normal to the surface for each exposure case are compared in Figure 5-5. The sheath is thinnest for the R-D case, and thickest for the R-He case, although roughly

~2 mm in all cases. This is much longer than the classical Debye sheath thickness, which is on the order of 50 μm in these plasmas, and more on the order of the ion gyro radius (average main-ion ρ_i = 487, 371, and 508 μm in case S-D, R-D, and R-He, respectively, indicated with scale bars in Figure 5-5). The gradually diminishing potential extending several times the incident main-ion gyro radius weakens the near-surface (Debye Sheath) electric field that would otherwise deflect ions toward the surface, as will be discussed in the following sections. Furthermore, the low near-surface electron density region can increase the ionization length and enlarge the spectroscopic emission area, which will also be discussed in following sections.

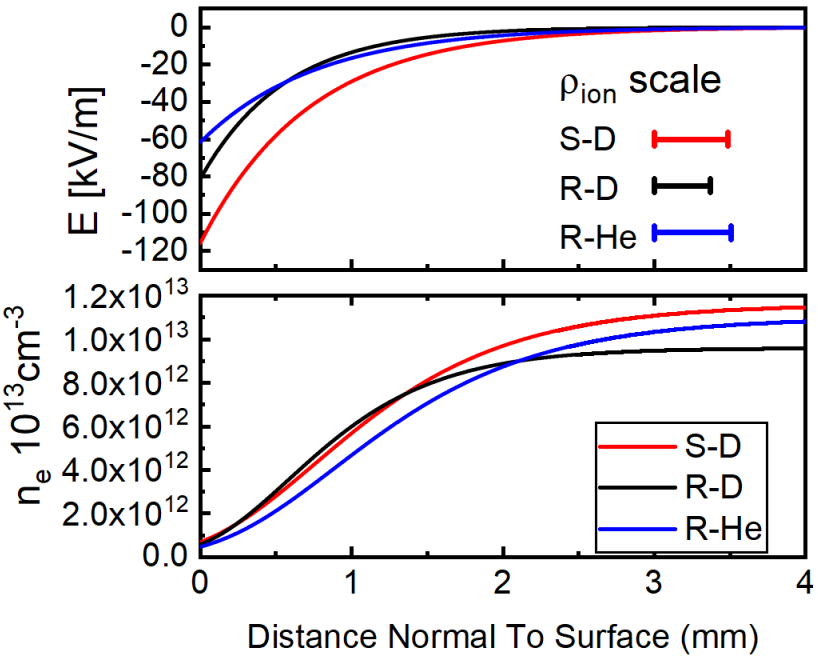

Figure 5-5. The sheath density (n_e) and electric potential (V) calculated for each exposure case at the average plasma n_e, T_e conditions vs distance normal to the surface. Average ion gyro radius in each case shown as scale bars.

Both main ion and carbon impurity IADs were calculated for each exposure case in this study. We treated C impurity ions as fully thermalized and entrained in the

background plasma flow. That is, C ion velocity perpendicular to **B** followed a Maxwellian with the same specified temperature T_i, and C ion velocity parallel to **B** followed the same shifted top-hat velocity distribution as the main ions. The main ion IADs are shown in Figure 5-6. The IADs for impurity ion C^{3+} in each case were similar, to within 5 degrees of the main ion distributions, and are not shown here. In Figure 5-6 we show the fraction of the IAD corresponding to different ranges of the initial parallel ion flow speed. In solid black line we show the impact angle distribution resulting from initial top-hat parallel velocity distribution of parallel Mach number $M_{\|}$ = 0.3-1.0, and in dashed lines sub-sets above and below $M_{\|}$ = 0.5. Overall, we find that the impact angle distributions were similar in all three cases and not terribly sensitive to the parallel flow speed assumptions. Higher parallel flow speeds resulted in somewhat smaller polar impact angles and broader azimuthal angle distributions. The distribution of polar impact angles in case R-D was overall slightly higher than in S-D, mainly due to the smaller gyro-orbits and perpendicular/parallel velocity ratios resulting from the lower ion temperature (16eV vs 30eV, respectively). For the R-D and R-He cases, plasma temperatures were similar the larger He gyro-radius led to lower impact angles. As a check, we also calculated the impact angle distributions assuming $T_i = 2T_e$, which is often assumed for low density SOL conditions. The results were only slightly broader than the distributions shown in Figure 5-6, indicating ion temperature was not a sensitive parameter in determining the impact angle.

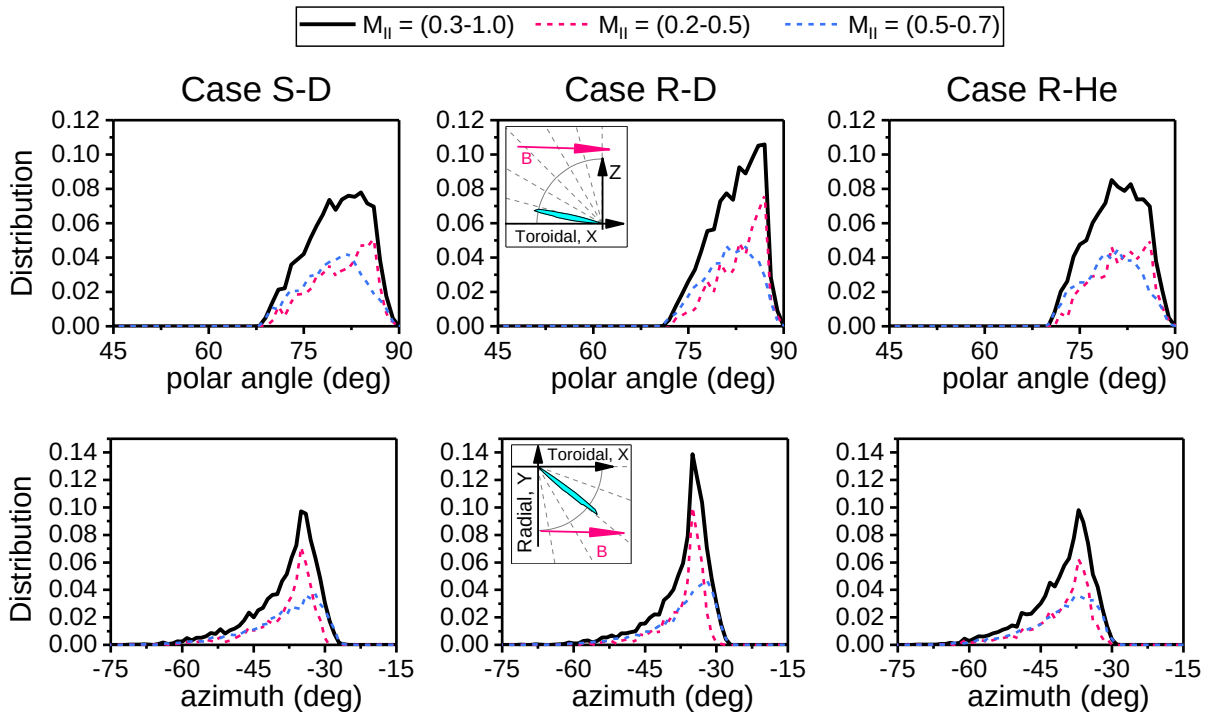

Figure 5-6. Incident ion angle distributions (IADs) calculated for each sample exposure case, shown for polar angle θ (in the Y-Z plane) and azimuthal angle φ (in the X-Y plane) relative to the toroidal field direction. Dashed lines shown in pink and blue indicate the IADs for high and low initial parallel flow speed assumptions. The inset plots show the distributions represented in polar coordinates to aid in visualization.

5.2.1 **Experimental evidence of sputtering by oblique incident ions**

Microscopic post-mortem observations of the eroded samples reveal features that may be indicative of directional, grazing angle ion bombardment. It is well known that under continuous ion bombardment the roughness of a surface either increase or decrease due to a number of competing processes that are dependent on surface temperature, ion flux, and incidence angle. Smooth surfaces can develop roughness due to a curvature dependent sputtering instability [82], faceting or ripple formation [83,89]. Rough surfaces can undergo smoothening under conditions of low energy grazing angle ion bombardment due to enhanced erosion of surface protrusions or step edges [84–88]. While a detailed analysis of such effects is beyond the scope of this study,

a short discussion on the observations of surface morphology development and surface roughness effects in the presence of grazing angle ion bombardment is presented here.

Post-exposure SEM imaging of the plasma-exposed Al surface in case S-D showed some microstructure development that may be evidence of directional ion impact angles. No pre-exposure SEM image was available, but it is reasonable to assume the vapor deposition process formed an initially featureless smooth surface. The eroded Al surface, shown in Figure 5-7, shows a uniform pattern of sub-micrometer sized Al-rich islands with a somewhat elongated shape. The direction of island elongation appears to be roughly 60° relative to the toroidal field toward the E×B direction, a somewhat larger angle than the 37° average predicted by the azimuthal IAD discussed in section 5.1. The islands may or may not be evidence of a minor ion induced surface morphology change. They appear to be very different than the ion-induced 'cone' morphology seen to grow on Be and other metals in the PISCES-B linear plasma device with ~normal incidence ions [91], and also different in scale than the tungsten 'nano-tendrils' observed to grow in the C-mod tokamak on a biased tungsten Langmuir probe surface that was inclined to the field at ~11 degrees [129].

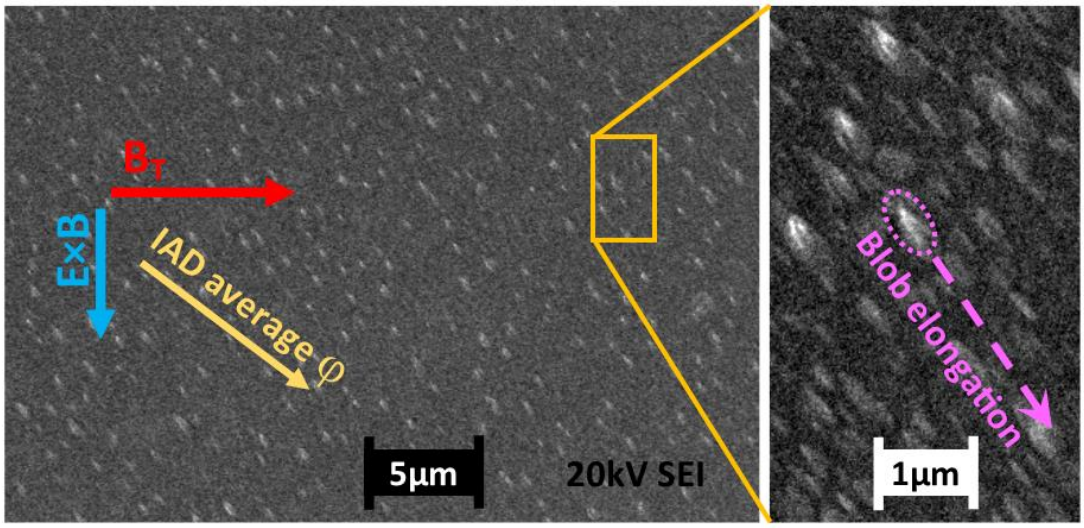

Figure 5-7. Post-mortem imaging of the surface shown at two magnifications. The expected 37° IAD average azimuthal angle φ is shown in yellow, and the inferred 60° elongation direction of the blobs is shown in pink.

In cases R-D and R-He, we had reported in earlier work [115] that the amount of Al found redeposited outside the coating area was much higher than expected. In that study, this increased deposition was attributed to accumulation of redeposited Al in shadowed areas of these pores. We proposed that enhanced erosion at pore leading edges led to line of sight deposition on the opposite pore surface that was shadowed from direct ion flux and protected from subsequent re-erosion, although this type of shadowing would require near grazing incidence ion angles. We have since found direct evidence of such accumulation by mapping the surface Al concentration on the microscopic scale with a scanning Auger microscopy technique. In this technique, a qualitative map of Al coverage is obtained at SEM level resolution by mapping the count rate of surface-emitted Al KL1 Auger electrons at 1388.9 eV and subtracting the neighboring background at 1368 eV. The mean-free path of the Auger electron in the surface is ~5nm. This sets the depth resolution of this technique to be on the order of the expected surface Al:C mixing layer thickness (expected to be roughly ~1-2nm based on

the implantation depth of 200-400eV C in Al). Measurement results are shown in Figure 5-8, with SEM image showing pore structure and AES image showing Al surface concentration through relative 1382eV peak brightness. Al appears clearly concentrated in the pores (brighter AES image = higher Al concentration). In general, pores appear to have more strongly concentrated Al on the side of the pore most shadowed from direct ion impact (upper left corner of the pores). There was no Al present before plasma exposure in these pores, and its accumulation there is consistent with the anticipated shadowing due to the expected grazing incidence angle ions.

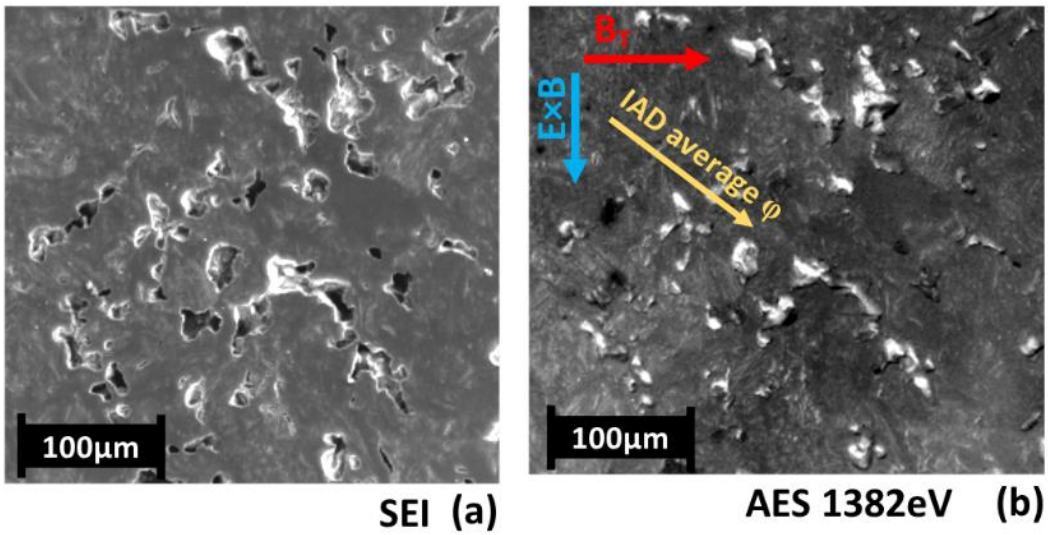

Figure 5-8. Sample surface 5mm toroidally downstream of the Al coating in case R-He made using (a) SEM imaging and (b) AES imaging. The SEM image illustrates the pore structure, and the AES map of the same area maps the concentration of Al on the surface (brighter = more Al). Note the average azimuthal angle of the incident ion angle distribution shown with yellow arrow.

5.2.2 **Angular dependence of the sputtering yield**

It is well known that the sputtering yield is dependent on the incidence angle [130], typically increasing with incidence angle up to a point then decreasing to zero as the angle approaches surface tangency. The effect of carbon implantation and dynamic

surface composition evolution can be dependent on the incident ion angle as well. We compare the measured total erosion yield in each case against the total sputtering yield vs incident ion polar angle as calculated using the SDTRIM.SP [61] binary collision sputtering modeling code in Figure 5-9. The calculated sputtering yield curves cover a range representing the low estimate of incident ion energy ($E_i = 5T_e$, for $T_i = T_e$) and high range of incident ion energy ($E_i = 7T_e$, for $T_i = 2T_e$). Dashed line curves were calculated with the addition of a C^{3+} impurity flux fraction with incident energy of $11T_e$, and dynamic evolution of the surface composition due to C implantation. We see that the addition of C decreases the calculated erosion yield for normal incidence as expected due to surface C enrichment and Al dilution. At incident angles above ~75 degrees, the surface C enrichment effect diminishes and yield approaches that of pure He or D sputtering.

The measured erosion yields in each case [106] are plotted at the average incidence angle from the IAD calculated earlier. Horizontal error bars represent the width of the IAD, and vertical error bars represent the combined uncertainty in ion flux and film thickness change measurements. In both the D plasma cases, the measured yield falls below the predicted yield at this angle, but perhaps serendipitously matches with the expected yield at 0-45 degree incidence angles. It is commonly expected that for practical surfaces of tokamak plasma facing components, surface roughness can reduce such incident angle dependence on yield due to line-of-sight redeposition of sputtered material [92]. However, even in the smooth substrate case we observed similarly lower than modeled erosion rates and find good agreement with the modeled yield for the rough substrate He plasma case R-He. This may suggest that some other yield-reducing effects such as flux-dependent near-surface dynamic retention of D may

be playing a role in reducing the observed sputtering yield in both D plasma cases [123], and that sputtering yield reduction due to surface roughness is small in these cases.

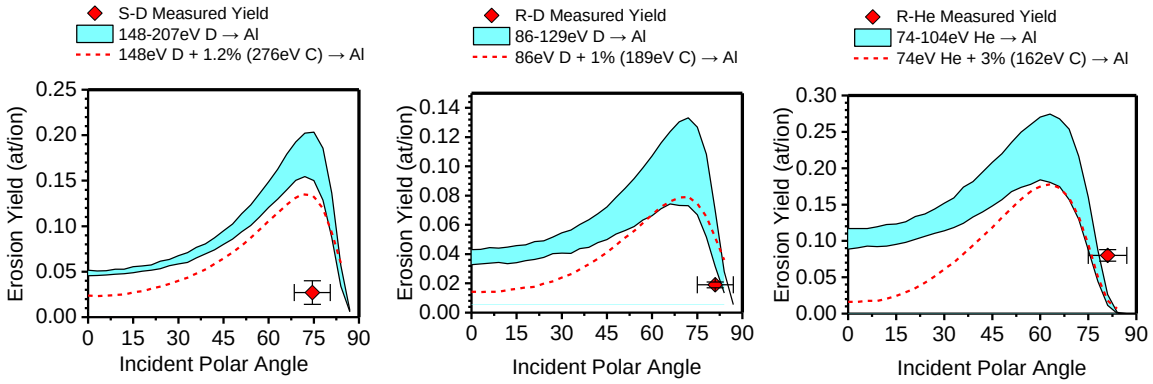

Figure 5-9. Measured erosion yields (points) compared to effective yield calculated by SDTRIM.SP (lines) as a function of incident ion angle and range of ion energies for each case. The wide bands represent the low and high range of sputtering yields due to pure D or He ions with incident energies from $5T_e$ assuming $T_e = T_i$ to $7T_e$ assuming $Ti = 2T_e$). The red dashed line represents the erosion yield due to $5T_e$ incident energy main ions with the addition of a C^{3+} ion impurity with energy $E_i = 11T_e$, including dynamic evolution of the surface carbon concentration.

5.3 Angular Distributions of Sputtering Yield and Sputtered Particle Energy

As the angle between the incident ion and the surface tangent becomes smaller, the sub-surface collision cascade occurs closer to the surface and as a result the sputtering yield and in particular the average sputtered energy tends to increase [82]. The angular distribution of sputtered material distribution is expected to become increasingly skewed in the forward-scattering direction. This effect has been measured experimentally by Goehlic, et al. where thin, atomically smooth evaporated Al films were bombarded by Ar and Xe ions at various incidence angles [64,65]. The measured

distributions of yield and energy were also well reproduced by the binary collision modeling code SDTRIM.SP. While the surfaces in our study have more roughness than those measured by Goehlic, it is plausible that a significant part of a rough surface would be shadowed due to the expected small angles between incident ions and the global surface plane (~5-15 degrees). The observed angular distribution of erosion would thus be dominated by a narrow range of surface-ion angles at the non-shadowed high points on the surface. For this reason, we will assume that the angular differential sputtering yields and energies calculated by SDTRIM.SP for ideally smooth surfaces can be applied to these cases.

An example of the calculated angular distributions of sputtering yield and average sputtered energy for 100eV D sputtering of Al at different incident ion angles is shown in Figure 5-10. The angular distributions are plotted as functions of the scattering angle β, that is the angle of the sputtered atom relative to the surface plane as noted in Figure 5-1. Distribution curves are colored corresponding to the incident ion directions shown with arrows, where the incidence angle θ is measured from the surface normal ($\theta = \beta - 90°$). This example shows that for normal incidence ions (in blue), the sputtering yield distribution follows a cosine distribution which is symmetrical about the surface normal, with uniform average sputtered energy in each direction. However, as the angle between the incident ion and the surface tangent becomes smaller, the sputtering yields and average sputtering energies increase in the forward-scattering direction, with average sputtered energies making a dramatic increase at incident angles of 60° and larger. Average sputtered energies nearly double, with highest average sputtered energy occurring for atoms sputtered at angles near the surface plane. When sputtering into a plasma, this forward-scattering bias can be significant in driving the redeposition

material migration direction, and the higher average sputtered energy can increase penetration of sputtered material into the plasma.

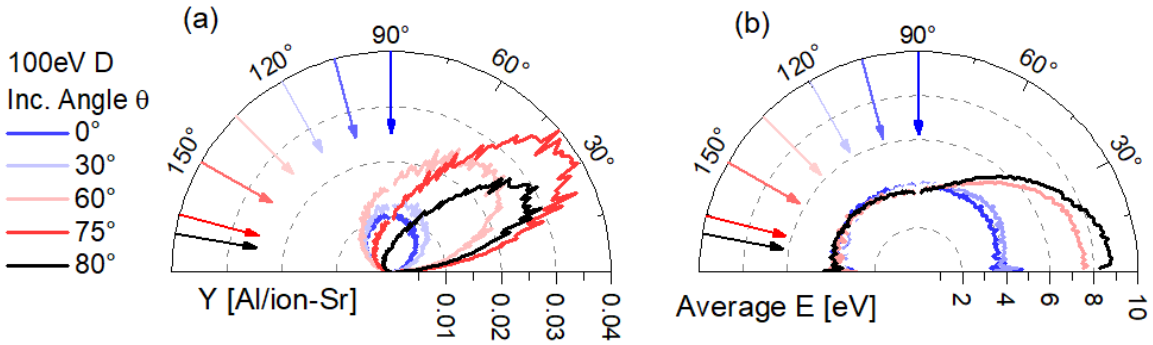

Figure 5-10. Example of Al sputtering yield Y per steradian (a) and average sputtered energy E (b) versus scattering angle β for 100eV D ions at different incident polar angles θ. Incident ion angles with respect to the surface normal are listed and plotted with arrows, and are color coded to the resulting distribution curves.

The angular distributions of yield and energy were calculated with SDTRIM.SP for each of the cases S-D, R-D, and R-He, shown in Figure 5-11. Either D^+ or He^+ incident ions with incident angle distributions from Section 3.1 were provided as inputs to the SDTRIM.SP code. To illustrate the effect of the carbon impurity, the same cases with and without the estimated carbon ion flux fraction (as discussed in Section 2.2) are compared. Incident ion energies were based on the average ion thermal energy and sheath potential drop at the measured exposure conditions in each case, with $T_i = T_e$, such that $E_i = 11T_e$ for C^{3+} and $E_i = 5T_e$ for D^+ or He^+ ions. Dynamic evolution of the surface composition due to incident carbon was suppressed, so that surfaces were pure Al and pure Al surface binding energy (3.4eV) was used. The summary of input energies and carbon ion flux fractions used are listed in Table 5-1. The effect of the added carbon ion flux in these cases resulted in a small increase in sputtering yield and significant increase

in sputtered neutral energy over pure main ion sputtering. These angular sputtering and energy distributions including carbon impurity sputtering shown in Figure 5-11 were used as input parameters to the ionization and photo-emission plume modeling to be discussed in the next section.

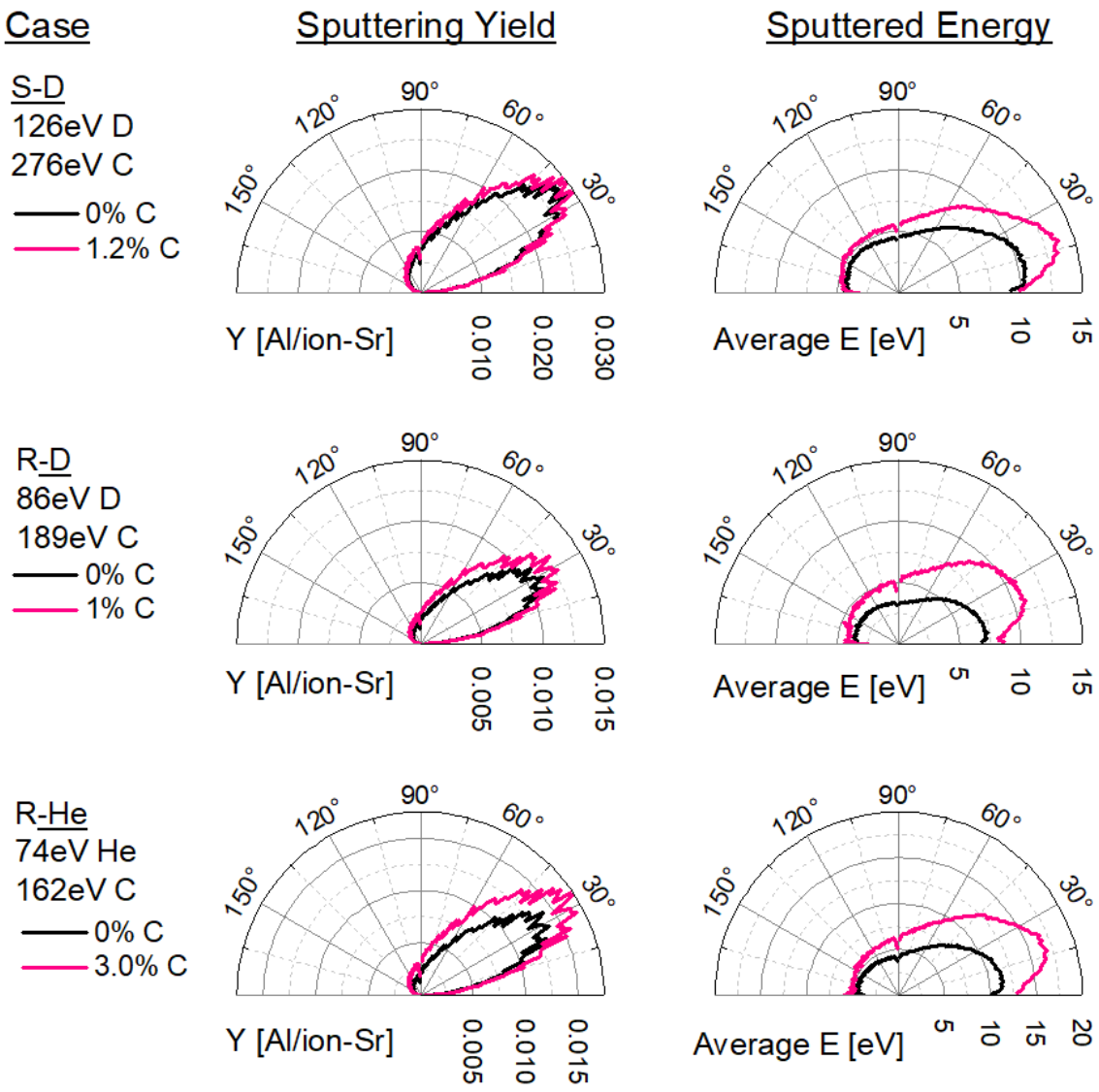

Figure 5-11. Angular distributions of yield and energy calculated by SDTRIM.SP for cases SD, RD, and RHe, shown for different carbon impurity assumptions. Varying carbon impurity has a larger effect on sputtered energy than sputtering yield.

Table 5-1. Input parameters for SDTrim.SP sputtering code and summary of calculated results. IAD total sputtering yields and average sputtered energy are calculated using the ion incidence angle distributions (IADs) shown in Figure 5-11. Average sputtered energy and sputtering yield for normal incidence ions at otherwise identical conditions are listed for context.

Case	Incident Ion species	Incident Energy eV	Incident Ion Fraction	IAD Total Sputtering yield [at/ion]	Average Sputtered energy [eV]	Normal Inc. Sput. Yield [at/ion]	Normal Inc. Sput. Energy [eV]
S-D	D^+	126	99%	0.1	9.0	0.048	4.9
	C^{3+}	276	1%				
R-D	D^+	86	99%	0.04	8.4	0.039	3.9
	C^{3+}	189	1%				
R-He	He^+	74	97%	0.05	11.6	0.10	4.5
	C^{3+}	162	3%				

5.4 Measurement and modeling of photo-emission plume

5.4.1 **Imaging of the Al I photo-emission plumes**

The background-subtracted images obtained for each of the exposure cases are shown in Figure 5-12. The original coating geometry in each case is outlined in white, and against this the asymmetry of the emission plume is clearly visible. Cases R-D and R-He had identical sample geometries and imaging conditions. In case R-D the boundary between the DiMES sample and downstream tile (highlighted with a dashed red line) appears brighter most likely because of some background D I emission that was likely more intense near the gap where some leading edge plasma interaction may be occurring. The image in case S-D was slightly out of focus, so the emission plume shape is blurred but a weak band of emission downstream of the sample is indicative of re-erosion of migrating Al.

The asymmetry in each case is in the toroidally downstream and radially inward direction in an otherwise toroidally uniform divertor plasma. In particular, we find that the direction of the observed neutral Al emission plume asymmetry in each case is similar to the expected direction of incident ions accelerated through the sheath as discussed in the following section. One possible explanation for the asymmetry is frictional entrainment of neutrals in the background plasma flow. However, estimates of the deuterium and helium to Al ion-neutral cross-sections using hard sphere approximation finds that the rate of ion-neutral collisions is ~10x lower than the rate of electron impact ionization, meaning that ionization was much more likely to occur before any ion collision affecting the neutral trajectory. Thus, it is reasonable to assume that the sputtered neutral atoms move in straight line trajectories up to the point of ionization, and any asymmetry in their distribution is due to an asymmetry in the angular sputtering distribution.

We also note that the intensity of the emission increases toroidally across the sample and shows a longer decay length on the downstream side of the sample than on the upstream side. It is not likely that the gross erosion rate varied toroidally across the sample significantly, in fact analysis of the post-mortem measurements of the Al erosion presented in [115] confirm a nearly uniform net erosion rate toroidally across the sample with only slight variations due to dilution of the surface elemental composition by incident carbon ions. As we will discuss in section 5.4, this asymmetric emission gradient can be caused by directional asymmetry in the ionization lengths for Al, which can be on the order of a few mm in these plasmas.

Such ionization length asymmetries were unexpected, as it has usually been assumed that surface roughness inherent to practical surfaces in tokamaks homogenizes surface-ion impact angles and results in symmetric angular distributions [78,81]. Similar

asymmetries in the upstream/downstream material migration patterns have also been observed in post-mortem analysis of the redeposited material distribution for W, Mo, V, and Be [94,96,107,108], although these were asymmetries in redeposited material and were attributed to increased transport of ions along toroidal field lines toward the surface. Models of the redeposition in these earlier experiments assumed cosine angular distributions of yield and directionally uniform Thompson sputtered energy distributions and consistently under-estimated the extent of the upstream/downstream asymmetry observed.

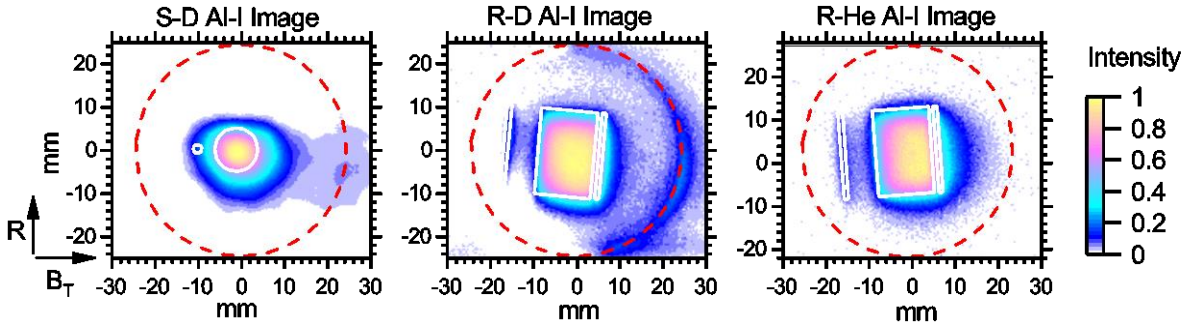

Figure 5-12. Filtered light images of the Al-I emission with background emission subtracted. Coating areas indicated with thin white outline, and the boundary between the DiMES head and surrounding tiles is indicated with a dashed red line. The S-D image was slightly out of focus so some of the plume broadening is exaggerated. In the S-D and R-D image, some emission localized around the downstream edge of the DiMES head may be background D-I emission passed by the filter or Al-I re-erosion from outside the coating area.

5.4.2 **Modeling of the Ionization and Photo-Emission Plumes**

The asymmetrical angular sputtering yield and energy distributions arising from sputtering by grazing angle ions can be expected to produce a directional asymmetry in ionization lengths. This asymmetry is evident in images of the photo-emission plume above the sample. In this section, we will present modeled three-dimensional distribution of ionization and photo-emission originating from a point source of sputtered neutrals into

a specified sheath density gradient. We will consider both uniform density and a MPS density gradient [45,46], and will use the angular sputtering yield distributions calculated by SDTRIM.SP as described in section 5.2.1 as inputs to define the initial neutral velocities and directions.

The model uses Monte-Carlo sampling of an ionization length cumulative distribution function (ICDF) for each sputtered atom trajectory. The ICDFs were defined in terms of the sputtered atom's polar angle θ, velocity v_i, and ionization rate coefficient $\langle \sigma v \rangle$ assuming electron impact ionization. Derivations of the ICDFs for both uniform and varying background plasma density can be found in the Appendix. A number of data sources for the electron impact ionization cross-sections or rate coefficients for Al are available in the literature and published databases [118,119,121]. In general the ADAS [119] calculated ionization rate coefficients were on the low end of the uncertainty range for measured or modeled ionization rate coefficients published elsewhere [118,120,121]. For comparison, the available rate coefficients are plotted vs. electron temperature in Figure 5-13. In this study we chose to use the rate coefficients published by Lennon et.al., which have a quoted uncertainty of ±60% that covers the full range other published values as denoted by the gray band in Figure 5-13.

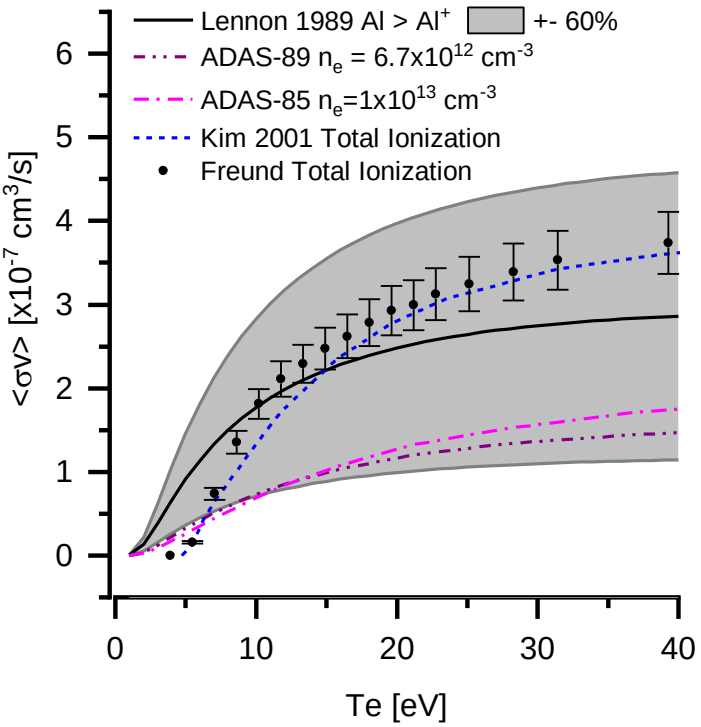

Figure 5-13. Ionization rate coefficients for Al compiled from several sources.

In this model, each sputtered neutral was considered to move in a straight line trajectory with velocity and direction determined by the average sputtered energy angular distribution. The photo-emission from each atom was treated as a line source made up of discrete emission segments along the atom's path up to the point of ionization. The brightness of each emission segment was proportional to the local electron density and a constant photo-emission coefficient (PEC). Each of the discrete emission points was binned into a three dimensional cloud about the sputtering point, thus producing the three dimensional distribution of photo-emission.

5.4.2.1 3D ionization and photo-emission distributions

Examples of the three-dimensional ionization and emission clouds (point source functions), is displayed along with peak-normalized radial and toroidal profiles below in Figure 5-14. These were calculated using parameters from the R-He exposure case with

MPS density gradient model scale length k=2. The figures show 2D contour maps of the top-down view (Toroidal-Radial plane) and side-on view (Toroidal-Vertical plane) of the distributions. The toroidal, radial, and vertical profiles of the distributions are shown above and to the right of the contour plots. The green arrows indicate the average direction of the incident ions that generate the sputtering plume. From these figures we can see the cloud of ions generated from the point source of neutral emissions has an asymmetric shape consistent with the incident ion direction. The asymmetry is due to the strong forward-scattering component of the sputtering distribution. The e-folding lengths of the distribution are about 3.2mm in the positive toroidal direction and 1.5mm in the negative toroidal direction. In the direction normal to the surface, the peak ion density occurs about 1.4mm above the surface followed by an e-folding length of about 2.2mm.

The distribution of emission, shown here on the same scale, appears narrower since photo-emission occurs from the point of atomic emission up to the point of ionization. The width of the distribution in toroidal and radial directions is still about 3.4mm with a similar asymmetry as in the ion distribution. These lengths are larger than the scale length of some of the coating features and are easily resolvable with the visible imaging camera.

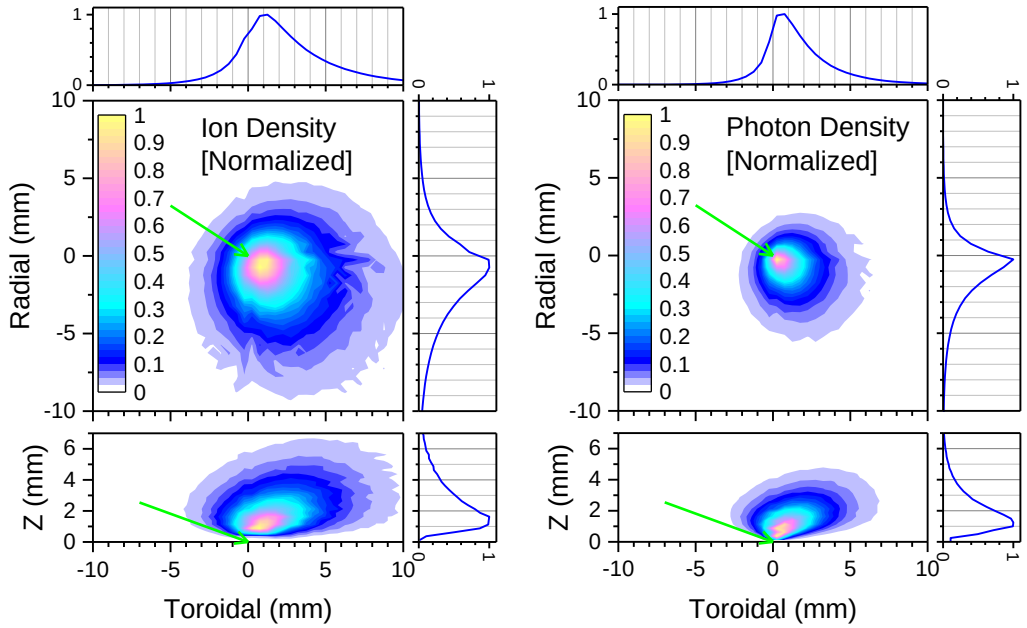

Figure 5-14. Example point source ionization and photo-emission distributions shown for R-He case. Other cases were similar.

5.4.3 **Simulated Photo-emission plumes**

A simulated emission plume for each sample's coating area was then constructed by convolving the point source emission function with the coating geometry. The Al erosion rate at each point on the coating was explicitly uniform in the simulations, and no Al erosion from outside the coating area was included. An average Al coating surface reflectivity of 20% in the R-D and R-He cases, and 90% in the S-D case was included. The simulated emission plumes are shown below in Figure 5-15 and are shown normalized to the peak emission intensity similar to the actual imaged emission plumes in Figure 5-12. The MPS density gradient structure assumed in these simulations was prescribed as shown in Figure 5-5 according to the sheath analytic expression from [127] with scale length k=2.0 and sheath-entrance plasma density equal to the density measured by the Langmuir probes.

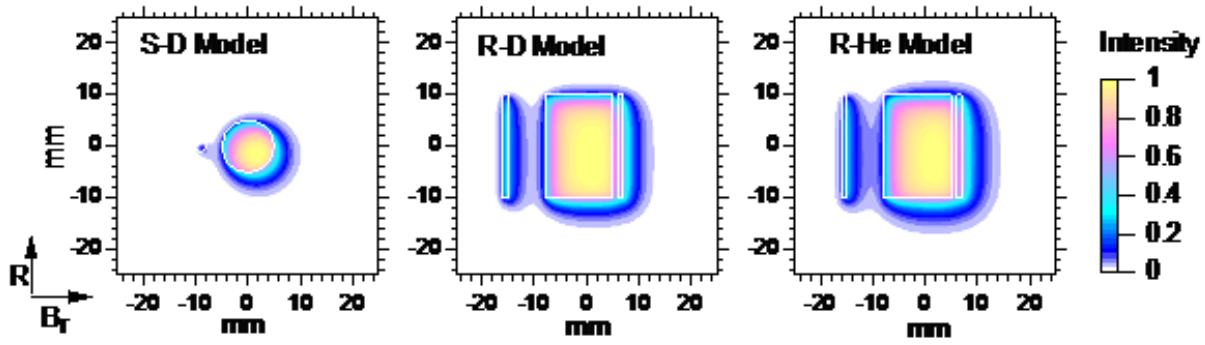

Figure 5-15. Modeled photo-emission plumes for three sample exposure cases, using ion impact angle distributions, SDTRIM.SP calculated angular sputtering distributions, and ionization/emission in MPS density gradient. Coating area boundaries are shown outlined in white. The photo-emission model includes reflectivity of the coating which was 20% in cases R-D and R-He and 90% in S-D.

We are able to make useful comparisons between the calculated and imaged emission plume in cases R-He and R-D, while the S-D case is somewhat inconclusive since the image was unfortunately out of focus. We show in Figure 5-16 toroidal and radial line profiles of the R-D and R-He emission plume image data (dots) compared with three different emission plume models (lines). The line profiles go through the center of the R-D and R-He emission plume. A remarkable match is found between image data (points) and the first model (red line), which used the anisotropic angular sputtering distributions calculated in Section 5.3, and the ionization in a MPS density gradient (Eq. A5, Appendix). The model reproduces the width, asymmetry, and overall shape of the imaged profile. For comparison, we also modeled the commonly assumed symmetric (cosine) sputtering distribution (resulting from normal incidence ions) with a MPS density gradient, but the result (green line) did not have the width or asymmetry present in the toroidal or radial profile data. A third model case assumed the anisotropic sputtering distribution with ionization in a uniform density (Eq. A5, Appendix), but the result (blue line) was a narrower plume shape than the measurement.

The largest discrepancy we find between the data and Model 1 is in the radially inward direction (negative direction in Figure 5-16 c, d). While our model assumes radially uniform plasma parameters and erosion rates, in reality there are likely radial variations. Of the known variations, such as the radial ne and Te profiles shown in Figure 3-9, the drop in electron temperature (and presumably the ion temperature) across the sample radially may be the most significant in explaining this discrepancy. Other expected radial variations which are not well known but may be responsible, include varying impurity fraction or charge state distribution (carbon deposition in these types of discharges is often strongest near or just inboard of the magnetic separatrix), or variation in the bandpass filter transmission (estimated to vary linearly by 4% across the 20mm radial field of view). Some measured emission >10mm toroidally beyond the coating area not reproduced since the extra emission due to re-erosion of migrated Al or localized D emission at the edge of the downstream tile was included in the model. The additional Al emission by re-erosion is expected to be a small effect since the flux of eroding Al is proportional to the surface concentration of Al, which is much lower for migrated deposits than the original coated-sample area.

The close agreement between the observed emission plumes and these simulations suggests that the anisotropic sputtering distribution and reduced density near the surface due to the MPS are the two most important factors controlling distribution of ionization of sputtered Al in these experiments. Our models did not need to account for ion-neutral collisions or modification of the sputtering distribution by surface roughness, so these appear to have been small factors.

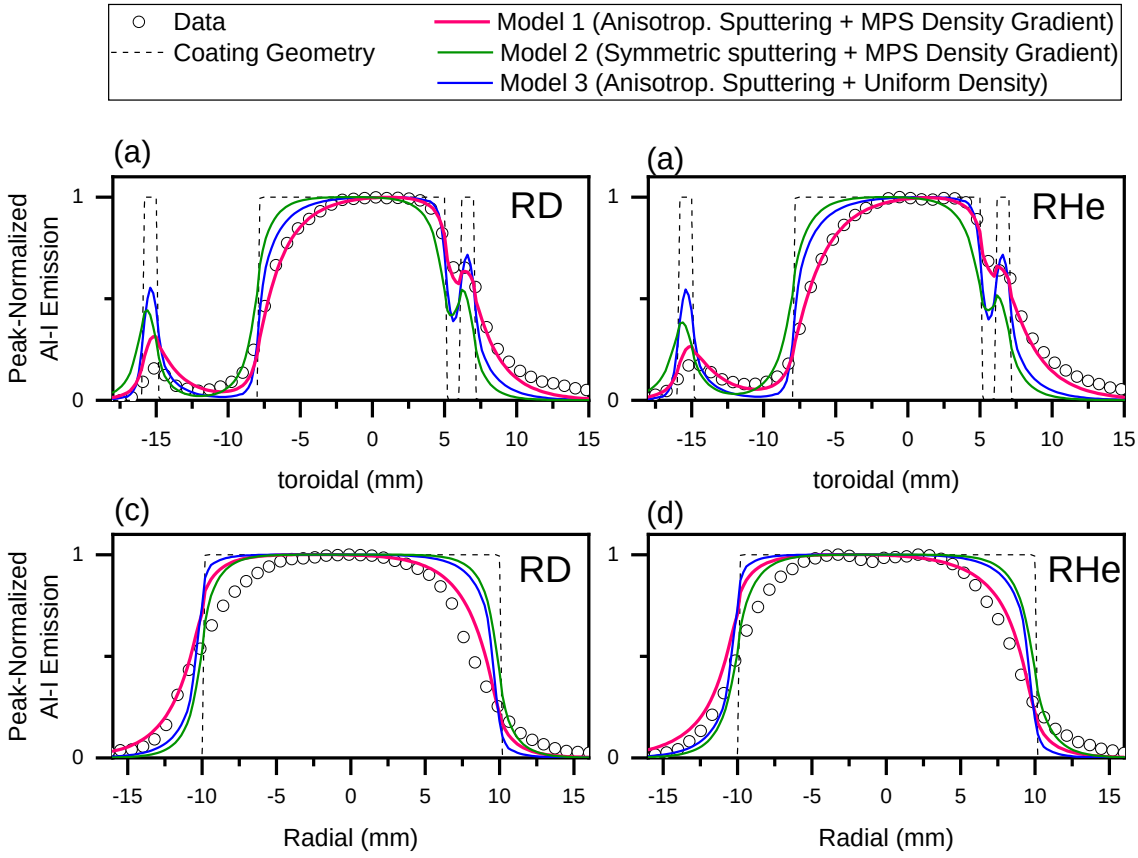

Figure 5-16. Comparison of imaged and modeled toroidal and radial profiles of photo-emission data (circles) with three different models (solid lines). Dashed lines indicate the initial coating area.

5.4.4 **Material redeposition implications**

In an analysis of the distribution of Al redeposition measured on these same samples presented in [115] (and also in Chapter 7), we found clear evidence of increased redeposition in the downstream toroidal direction, with redeposition length scales on the order of a few mm. In that study, the spatial distribution of redeposition was described by a point source toroidal redeposition distribution function that was fitted to the post-mortem measurements of Al net erosion and redeposition. What we find here is that the toroidal profiles of the ionization distribution calculated in this study closely match the scale length, shape, and asymmetry of those redeposition distribution functions. The

two distributions are compared in Figure 5-17 for case R-D (a) and R-He (b). The match between these distributions, each arrived at independently from different aspects of the material migration cycle, is remarkable and suggests that indeed the angular sputtering asymmetry may be the driver of the redeposition asymmetry. It also suggests Al ions are driven to the surface rapidly by the MPS E-field, rather than moving further along the magnetic field lines, since the spatial distribution of measured redeposition profile is similar to the spatial distribution of ionization. This agrees with the simulations by Chankin et al. [98] that the MPS E-field is largely responsible for the prompt redeposition of tungsten. Also shown in Figure 5-17 is the ERO modeled redeposition distribution function for case R-D using the same ionization rate coefficients (no R-He case was modeled by ERO due to a lack of a plasma background solution for He plasmas). What we find is that the ERO code, which includes the MPS E-field and collisions with the background plasma flows, but assumes a symmetric cosine distribution for sputtered atoms, qualitatively reproduces the redeposition scale lengths but not the forward-backward asymmetry. The inclusion of angular sputtering distributions to the ERO model should be considered for a future study and may result in improved agreement with measurement.

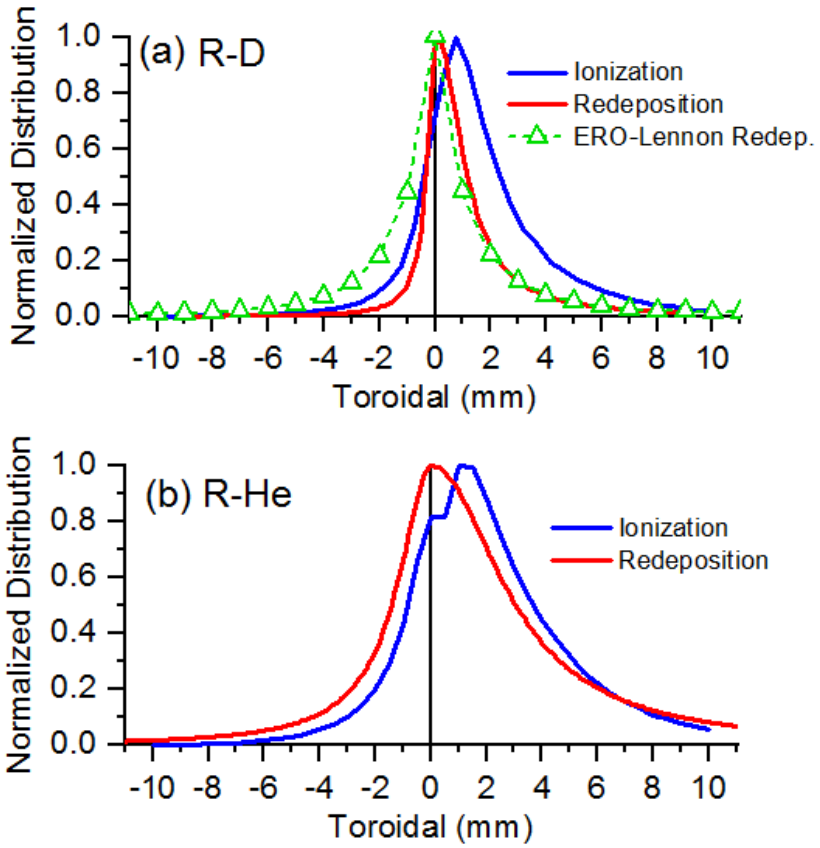

Figure 5-17. Toroidal profiles of the calculated ionization distribution along with toroidal profiles of measured redeposition taken from [115] for case R-D (a) and R-He (b). For case R-D we also compare the calculated redeposition distributions from an ERO simulation (green, triangles) which assumed a symmetrical cosine distribution of sputtered Al.

5.5 Conclusions

Al was used in this study as a proxy for studying Be erosion in tokamak divertor plasmas. Detailed measurements and analysis of the ionization and emission plumes were made to provide insight into the sputtering and ionization phase of the material migration cycle. Our comparison of Al erosion in similar He and D plasmas finds that in He plasmas, the photo-emission plume length and thus the Al ionization lengths are longer due to the higher average sputtering energy and a longer sheath density gradient for He compared

to D plasmas. The longer sheath gradient length also reduces the near-surface electric field strength, leading to reduced local redeposition rates. This is consistent with observations in previous work [115] where longer Al redeposition lengths and lower redeposition rates were found in the He plasma case.

We have calculated that the distribution of ion incidence angles for small magnetic field pitch angles is strongly affected by the presence or absence of a Debye Sheath, DS. For small angles between the surface plane and magnetic field, the disappearance of the DS weakens the near-surface electric field that would otherwise deflect ions toward the surface. Post-mortem microscopic imaging and compositional mapping of exposed surfaces finds directional erosion and deposition patterns consistent with the calculated polar and E×B incidence angles caused by the MPS electric field. This has implications for impurity migration in divertors since it can drive 'cross-field' material migration in a direction controllable by the toroidal field polarity.

These results are to the author's knowledge the first to measure an asymmetry in the neutral photo-emission flux as well as in the redeposited material direction. Models of the redeposition in these and other similar experiments had previously assumed cosine angular distributions of yield and directionally uniform sputtered energy distributions and consistently under-estimated the extent of the upstream/downstream redeposition asymmetry observed. The forward-scattering asymmetry is evident on both smooth and porous graphite surfaces studied here, which is counter to the common assumption that practical surfaces with roughness would approximately randomize the local impact and sputtered angles, creating a more symmetrical cosine-distribution of sputtered material

These results would indicate that material migration models should not necessarily assume cosine sputtering distributions, but rather include the full angular distributions of

sputtering yield and sputtered energy that can be readily calculated using the sputtering modeling code SDTRIM.SP for specified incidence ion angle distribution. The angle dependence of sputtering yield and sputtered energy distributions can vary with incident angle, especially for low-Z materials like Be. When interpreting material migration as a multi-step process, the sputtering yield distribution can drive the material migration direction. It may also be important to include the effects of grazing incidence ions on sputtering yield and sputtered energy distributions in models of fuel recycling and near-surface ion or neutral flows.

The extreme grazing incidence of the incident ions expected here (greater than 70 degrees with respect to the surface normal) may actually lead to a decrease of surface roughness over time for two reasons: protrusions and leading edges preferentially erode away due to concentration of ion flux (a plasma-machining process), and ion-shadowed regions may fill-in by accumulation of redeposited material. We do see some μm-scale island-like structures developed on the initially smooth Al surface with a coherent directionality near the expected azimuthal angle of incident ions. At this point the mechanism of the island growth is unknown, and no other micro-roughening of the surface was observed. We see no such morphology growth on the polished graphite surfaces, but there is evidence of increased Al deposition inside surface pores.

These findings also point to a potential benefit whereby surfaces can be intentionally biased or textured to control a preferential direction of material migration and co-deposit accumulation. Biasing can alter the sheath potential gradient and incident ion angles. On surfaces with tailored roughness, the relative surface-ion incidence angle can be controlled to form microscopic leading edges and shadowed areas to control erosion deposit accumulation locations. Further experimentation is

needed to study the role of different roughness scale lengths compared to scale lengths of the plasma sheath and incident ion gyro radii (~mm-scale) and scale lengths of the ion implantation depth and ion-solid collision cascade (~nm-scale). To date, direct measurement of the electric potentials and particle densities within the MPS have not been practically possible. The sheath structure during plasma detachment, edge localized mode (ELM) interactions, during RF heating, or on non-floating surfaces may be very different and may have profound effects on the net erosion rate and local material migration directions. Future work in this area ought to make attempts to measure the near surface density gradients using e.g. high resolution spectroscopic techniques or to design samples that enable measurements of the incident ion direction by careful post-mortem analysis.

5.6 Acknowledgements

This material is based upon work supported by the U.S. Department of Energy, Office of Science, Office of Fusion Energy Sciences, using the DIII-D National Fusion Facility, a DOE Office of Science user facility under awards DE-FC02-04ER54698, DE-SC0001961, DE-AC04-94AL85000, DE-AC52-07NA27344, DE-AC02-09CH11466, DE-NA0003525, and DE-FG02-94ER52435. Sandia National Laboratories is a multi-mission laboratory managed and operated by National Technology and Engineering Solutions of Sandia LLC, a wholly owned subsidiary of Honeywell International Inc. for the U.S. Department of Energy's National Nuclear Security Administration under contract DE-NA0003525.

DISCLAIMER: This report was prepared as an account of work sponsored by an agency of the United States Government. Neither the United States Government nor any

agency thereof, nor any of their employees, makes any warranty, express or implied, or assumes any legal liability or responsibility for the accuracy, completeness, or usefulness of any information, apparatus, product, or process disclosed, or represents that its use would not infringe privately owned rights. Reference herein to any specific commercial product, process, or service by trade name, trademark, manufacturer, or otherwise, does not necessarily constitute or imply its endorsement, recommendation, or favoring by the United States Government or any agency thereof. The views and opinions of authors expressed herein do not necessarily state or reflect those of the United States Government or any agency thereof.

DIII-D data shown in this paper can be obtained in digital format by following the links at https://fusion.gat.com/global/D3D_DMP.

This chapter includes text and data that is a reprint of the material as it appears in C. P. Chrobak, P.C. Stangeby, E. Hollmann, D.L. Rudakov, T. Abrams, R. Ding, J.D. Elder, J. Guterl, E. Hinson, H.Y. Guo, D.M. Thomas, C. H. Skinner, A.G. McLean, W.R. Wampler, D.A. Buchenauer, R.P. Doerner, G.R. Tynan "Measurement and Modeling of Aluminum Sputtering and Ionization in the DIII-D Divertor Including Magnetic Pre-Sheath Effects", submitted for publication in Nuclear Fusion. The dissertation author was the primary investigator and author of this paper.

Chapter 6
Initial Measurements of Erosion and Redeposition of Al in the DIII-D Divertor

6.1 Introduction

In this chapter we compare the measured net and gross erosion rates of Al samples exposed to different plasma conditions in the DIII-D divertor and discuss the method used for measuring the net and gross erosion rates non-spectroscopically.

The erosion of the low-Z element aluminum (Al) is being studied as a proxy for beryllium (Be), which will be the primary plasma facing material in the ITER first wall and secondary (upper) divertor plasma-facing components. Al is a useful proxy for Be since it shares similar sputtering and chemical characteristics [41] without having the severe chemical toxicity restrictions of Be, and is easily distinguishable from background sources in DIII-D. We compare the surface morphology before and after exposure for both initially smooth and initially rough surfaces. We analyze RBS spectra to infer the pre and post exposure depth profile of the coating and note changes to the surface and film carbon and oxygen content after plasma exposure.

Samples contained Al coatings of an initial thickness of 80-130nm on different carbon substrates. We consider three exposure cases here: a Smooth sample exposed to D plasmas (case S-D), a Rough sample exposed to D plasmas (case R-D), and a Rough sample exposed to He plasmas (case R-He). Case S-D used a Si substrate coated with 500nm of C on which to deposit a smooth Al film with a negligible (<20nm) surface roughness housed in a graphite probe. Cases R-D and R-He used the entire graphite

probe surface as the substrate. The effect of surface roughness on the erosion rate will be discussed.

All samples were exposed near the outer strike point (OSP) of a series of repeated lower single null, ohmic low density attached L-mode plasmas. These plasmas were similar to those previously modeled [112] and used in net and gross erosion measurements of other materials (W [107], Mo [108]). Each sample accumulated between 6.2 and 14 seconds of steady-state plasma exposure over 2-4 tokamak discharges, achieved by maintaining the OSP position 7-20mm inboard of the sample during the steady phase of repeat discharges and 50mm outboard of the sample during the ramp-up and ramp-down phases. Erosion rates in each case were on the order of 10 nm per second. The ionization mean free path for sputtered Al in the cases presented here is ~1.6 ± 1 mm, which is on the same order as its ion gyro radius, ~0.4mm. The toroidal field strength (B_T) and shallow inclination angle (B_{incl}) are such that we expect the entire sheath potential drop occurs across the magnetic pre-sheath (also known as the Chodura sheath) [45], which is also expected to have a thickness on the order of a few mm. Heat flux calculated from surface Langmuir probe measurements of particle flux, plasma temperature and density, using a sheath heat transmission factor of 7 [42] agrees with divertor tile thermocouple measurements to within a factor of 2. Based on these measurements and infrared camera images of the sample, we estimate the Al surface temperature remained below the Al melting point, reaching ~300-500°C in each exposure for case S-D, and below 100°C for cases R-D and R-He. The lower temperatures were in part due to 2-3x lower heat flux and in part due to using a solid graphite substrate as opposed to a 3mm thick silicon wafer.

Pictures of the coatings, before and after plasma exposure, are shown in Figure 6-1. The coating geometry for each sample included both large (10-20mm) sized area for measuring net erosion, and a small (~1mm) sized area for measuring the gross erosion rate non-spectroscopically by post-mortem RBS analysis. In case S-D, circular spots were used for the different sized areas. For cases R-D and R-He, rectangular areas were used, with the small area consisting of a 1x20mm stripe parallel to the radial direction. The **R-He** sample included additional 1mm and 6mm diameter W coatings, for the purpose of estimating gross erosion by C impurity ions.

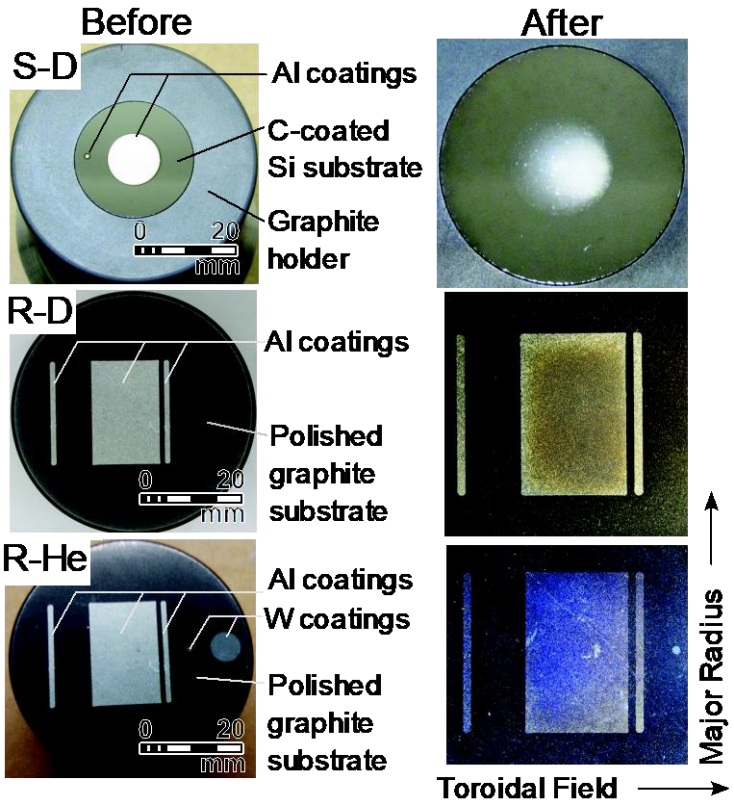

Figure 6-1. Pre and post-exposure images of S-D, R-D, and R-He coating samples. Sample S-D used 1mm and 10mm diameter Al spots. Samples R-D and R-He used 1x20 and 15x20mm Al rectangles, with a 1x20mm uncoated (masked) region on the larger area. Sample R-He included additional 1mm and 6mm diameter spots coated with W. For sample S-D, the 1mm spot and portions of the 10mm spot were completely eroded after plasma exposure. R-D and R-He coatings were partially eroded, and developed a non-isotropic darkening or discoloration as visible in the images above.

6.2 Measurement of Al Erosion and Redeposition

The erosion and redeposition rates of Al were determined by measuring the change in Al coverage and film thickness at multiple locations across the sample before and after plasma exposure, and dividing by the plasma exposure time. Measurements of Al coverage on the samples were made using 1-2MeV He Rutherford Back-Scattering (RBS). Multiple measurements along toroidal and radial directions through the center of the sample were made in order to map the toroidal and radial variation in erosion and deposition rate. We expected that if prompt redeposition were to be significant, we would find that the large coating areas would have a reduced net erosion rate compared to the small coating areas. We also expected to find Al redeposited around the original coating area, in decreasing amounts with distance from the coating edge. The decay length is related to the redeposition length, i.e. the length an atom travels from the point of erosion to the point of redeposition.

The toroidal and radial profiles of net erosion and deposition rate are shown in Figure 6-2. The black symbols are direct measurements of the rate of Al coverage change, and the coating area boundaries are indicated with the vertical gray bands. As expected, we find net deposition rate outside the Al coating and net Al erosion rate inside the Al coating areas. Note that the vertical scale range is about 10x smaller in the redeposition rate (positive) than the erosion rate (negative) direction, since the rates of redeposition were much less than the rates of erosion. The highest measured erosion rate in each case here is assumed to be the gross erosion rate, which is indicated with a dashed blue line. The hollow symbols represent the gross deposition rate on the Al

coating, i.e. the net erosion rate less the expected gross erosion rate (assumed uniform across the sample).

As expected, the erosion rate of small areas was higher than the large areas, and a good estimate for gross erosion rate was measured. In case S-D the small area was completely eroded after plasma exposure (it was initially thinner than the large area), thus the measured -4.5x10^{17} at/cm^2-s provided only a lower limit measurement of the gross erosion rate. Erosion rate measured on the upstream edge of the round 10mm spot provided a better estimate of the gross erosion rate in that case. In case R-D and R-He, the highest erosion rate was measured within the upstream 1mm stripe region.

The difference between the erosion rate the 1mm and 15mm stripes was only slightly greater than the measurement error. This means that the amount of redeposition received by the larger area coatings was low. The net erosion rate was higher within a few mm of the edge of the large area spots (most evident in case S-D and R-D). This suggests that the length scale for redeposition was a non-negligible fraction of the sample size, i.e. that the net erosion rate measured on the large areas may have been even lower with larger sized samples.

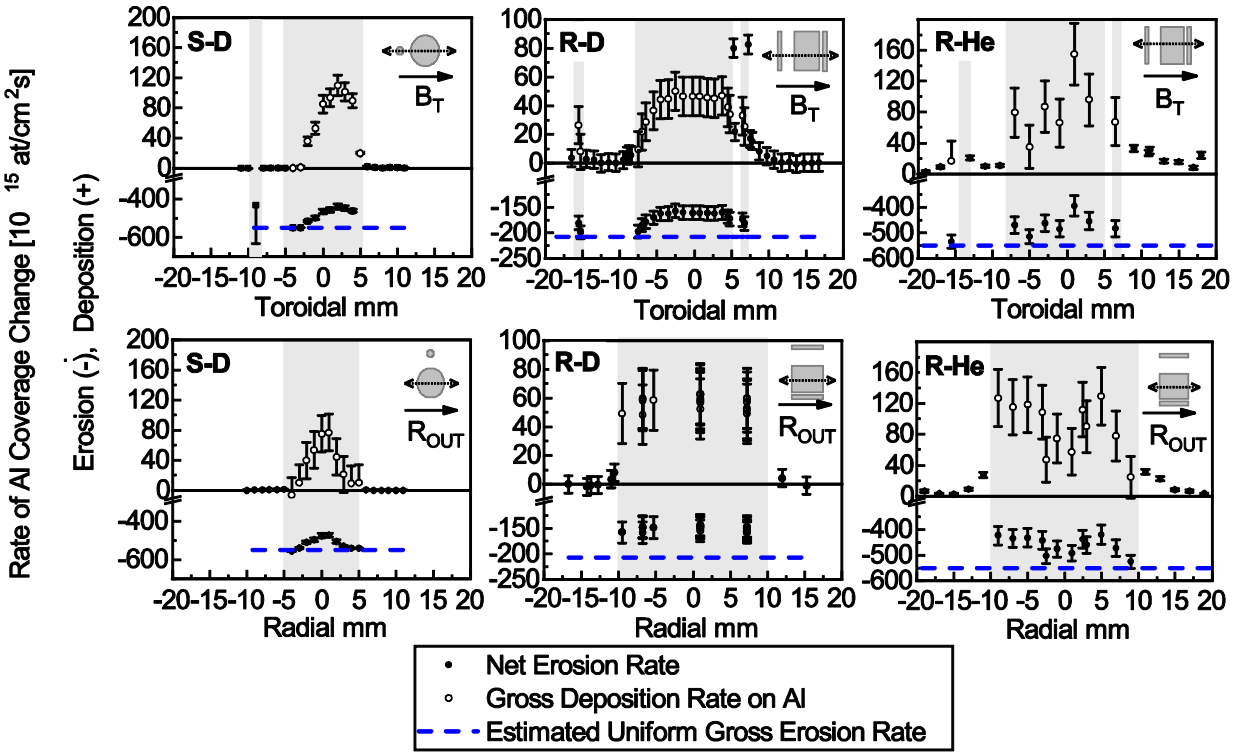

Figure 6-2. Toroidal and radial profiles of erosion and deposition rate determined from Al coverage change measurements. Vertical axes contain different scales for positive values (deposition) and negative values (erosion). Gross deposition on Al (hollow symbols) represents the difference between net deposition and gross erosion rate.

The total amount of redeposited material in each case was much less than the net amount of eroded material from each coating. This suggests that in each case, the majority of the eroded Al was transported away from the DiMES sample completely either because redeposition was negligible or because multiple re-erosion cycles migrated the Al away from the DiMES probe. A 2D map of the gross Al redeposition rate (i.e. the net erosion rate less the expected gross erosion rate) was made for case R-D, shown in Figure 6-3. We can estimate the total redeposition fraction by integrating gross redeposition across the entire sample, divided by the coating area-integrated gross erosion. For estimating the total redeposition fraction in cases S-D and R-He, the toroidal and radial profile data was used. We find redeposition fractions on the order of 30-40% for cases R-D or R-He, but only 6.2% for S-D. The large difference in redeposition fractions despite

relatively small differences in plasma conditions is surprising, and suggests that the substrate morphology plays an important role in reducing net erosion and thus increasing the apparent redeposition fraction.

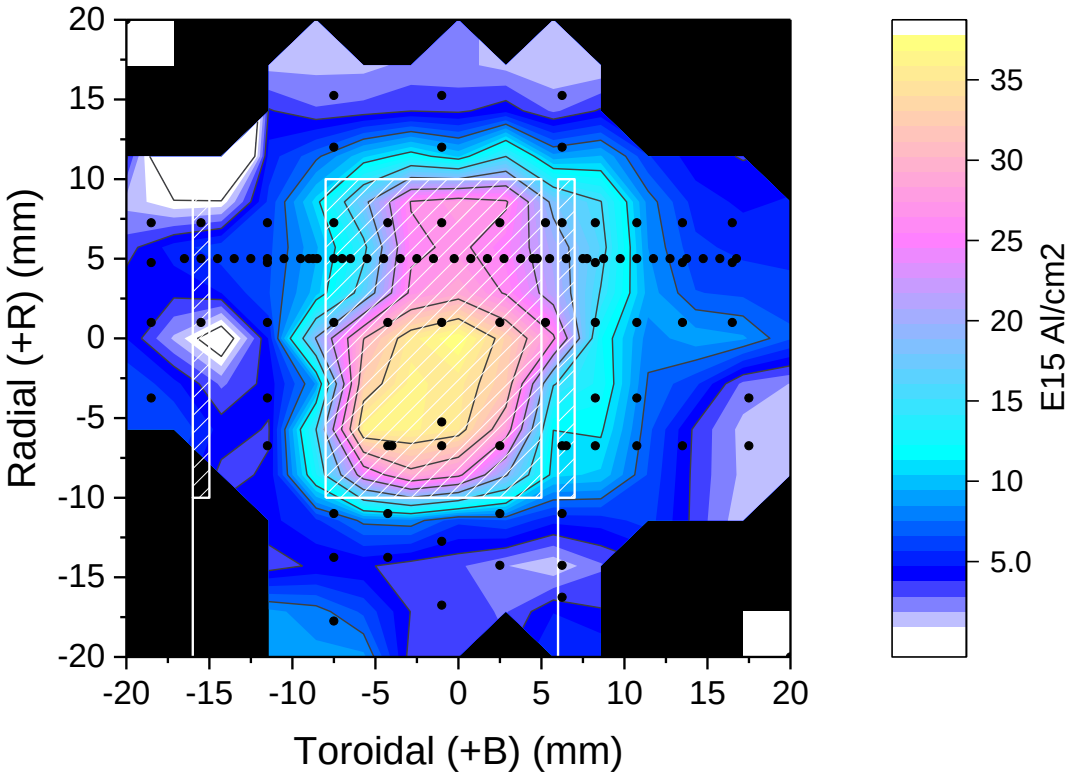

Figure 6-3: Two-dimensional (R,Z) contour plot of gross redeposited Al coverage around the sample from case R-D. Within the coating area (cross-hatched) the amount of gross redeposited Al is shown, which is equal to the difference between measured net and gross erosion rate across the coating.

6.2.1 **Redeposition length scale**

An estimate of the redeposition length scale was made by fitting the profiles of redeposited material outside the coating area to an exponential decay. Toroidal and radial line profiles of Al coverage before and after exposure are shown for each case in Figure 6-4, plotted on a semi-log scale. The short (few mm) decay length fits are indicated with straight lines through the data on either side of the large coating. The redeposition scale length listed in Table 6-1 was determined from the slope of these fits.

The redeposition scale lengths were between 1.5 and 7mm, and varied with plasma conditions, suggesting that prompt redeposition (within one gyro-radius) is not playing a role. The length scale for prompt redeposition in Al would be on the order of the Al ion gyro radius, roughly 0.5mm in these plasmas assuming sputtered energy of 3.5eV. The lengths observed are on the order of the expected ionization mean free path of sputtered Al in these plasmas. Still, the lengths were surprisingly short, since simple geometry of redeposition along the magnetic field lines (inclined 1-2 degrees above the surface) would suggest that redeposition lengths on the order of 10's of mm would have been expected.

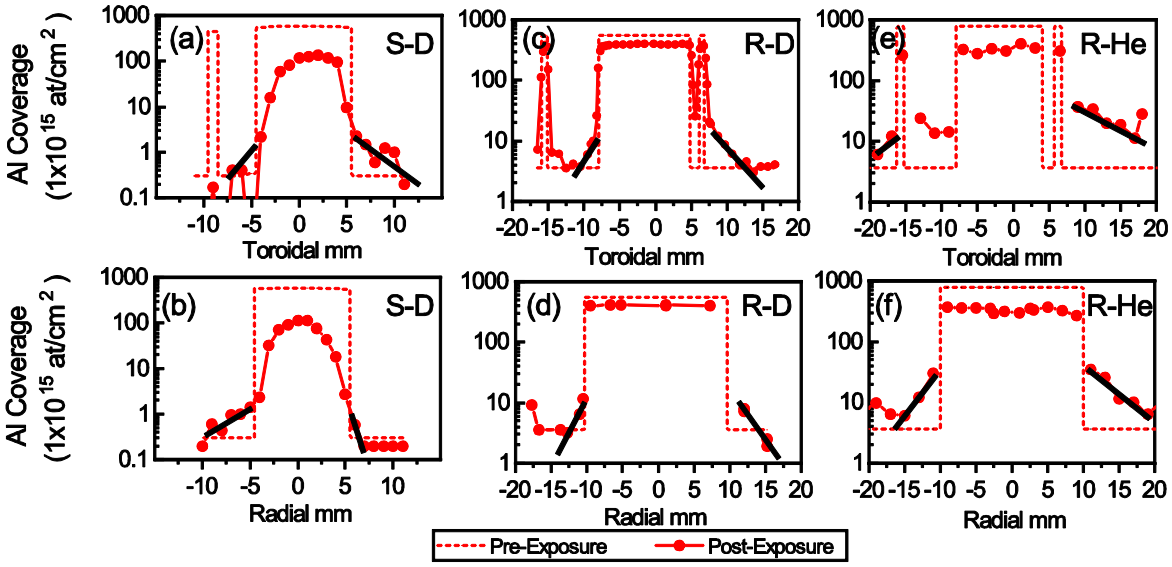

Figure 6-4. Toroidal and radial profiles of Al coverage measured across all three sample exposure cases. Highest net erosion amount was measured in case S-D, while highest amounts of redeposition outside the original coating was measured in cases R-D and R-He.

Table 6-1. Summary of RBS-measured effective net and gross erosion as measured from large and small area coatings.

Case	Te Ev	Gross Yield At/ion	Gross Erosion nm/s	Net Erosion nm/s	Total Gross Dep %	1/e redeposition lengths, mm			
						Toroidal -	Toroidal +	Radial -	Radial +
S-D	25	>.018	>5.7	5.1	6.2%	1.7	2.8	3.5	0.7
R-D	15	.017	2.5	2.0	40%	2.4	3.3	1.9	2.6
R-He	14	.080	14	12	31%	4.6	7.1	2.9	4.7

Since the redeposition length scales vary from case to case, the factors determining the redeposition length are likely more due to the different ionization lengths and sheath electric field strengths in each case. Bulk plasma density was roughly constant across the three cases, but sheath density gradient may vary depending on the plasma species and temperature. Redeposition occurs after ionization, and for ionization within the magnetic pre-sheath, the main driver for redeposition is the pre-sheath electric field [98]. In R-D, redeposition lengths are longer than in S-D, where plasma temperatures were higher and thus sheath electric field was stronger. Also, redeposition lengths were longest in case R-He, where the magnetic pre-sheath gradient lengths (which are proportional to the main ion gyro radius) would be longer and sheath electric field strengths weaker.

Across all three cases, there is a clear and consistent asymmetry in the toroidal direction redeposition lengths. Since plasma conditions in these exposures were uniform in the toroidal direction, the asymmetry indicates a preferential redeposition direction in the downstream toroidal field direction. Similar deposition toroidal asymmetry has been observed for other materials exposed using DiMES: namely Mo, W, V, Be with the effect being more pronounced for medium-Z materials [95].

Radial profiles of redeposition rate were expected to show inboard redeposition preference due to redepositing ion ExB drift within the pre-sheath E-field. However, the radial variation of plasma parameters n_e, T_e, ion flux, and possibly carbon impurity fraction complicates the interpretation in the radial direction profiles and requires a more comprehensive two-dimensional model including material mixing and deposition by Al and C ions. Cases R-D and R-He both showed roughly symmetric inboard/outboard radial redeposition length scales, but a few points near the far radially inboard edge of the R-D and R-He samples did show higher redeposition that didn't follow the exponential redeposition trend line. We believe these outliers are due to radial variations in the carbon net deposition rate across the sample. In these low density L-mode discharges, often a visibly dark region of heavy carbon-rich deposits forms near or just inboard of the separatrix, and the increase in Al there may be due to some co-deposition of Al with C there.

One inconsistency we found was that despite the shorter redeposition length scales in the highest T_e case S-D, the total fraction of material found deposited on the surface was much lower than the other two cases. The Al coverage on the carbon surrounding the original coating area was ~25x lower in case S-D than in either R-D or R-He cases. One explanation for the low fraction of net eroded material found in case S-D is that re-erosion of redeposited material occurred more rapidly than in the other cases, possibly an effect of the rougher substrate in cases R-D and R-He. The rough surface may have created some shadowed areas suppressing some of the re-erosion rate thus leading to a higher apparent redeposition rate [81]. Another possibility is that the erosion of Al from the initially smooth CVD C surface may occur at a higher rate than either the

Al coated or the rougher, graphitic C surface. Further analysis is planned to simulate these different scenarios with multi-step erosion/redeposition modeling code.

6.3 Effective Al Sputtering Yield

One of the goals of this experiment was to determine the effective sputtering yield of Al in the DIII-D tokamak divertor. Estimates of the sputtering yield cover a wide range, depending on assumptions about the ion impact energies, ion impact angles, and the properties of the carbon impurity ions. Some estimates of the expected sputtering yield were calculated using the SDTRIM.SP [61] sputtering modeling code, to simulate different ion impact angles and carbon impurity ion assumptions. Calculated sputtering yield curves vs incident energy are shown compared to measured erosion yields in Figure 6-5. Simulations were run in both static (no surface composition change) and dynamic modes (including surface composition evolution by carbon ion implantation). Sputtering yields were calculated assuming normal incidence, 45-degree incidence, and 75 degree incidence angles. Calculations assumed mono-energetic impact energies, calculated based on acceleration through a sheath potential drop of $3T_e$. The total impact energy is thus the sum of the average ion thermal energy and sheath potential drop, $E_{Impact} \approx 3Z_iT_e + 2T_e$ [42]. For the R-He case, an average He charge state of +1 was assumed (such that $E_{i,He} = 5T_e$), and for all cases an average carbon ion charge state of +3 was used (such that $E_{i,C} = 11T_e$). The estimated fraction of C in the incident ion flux was 1-3% of the background ion flux.

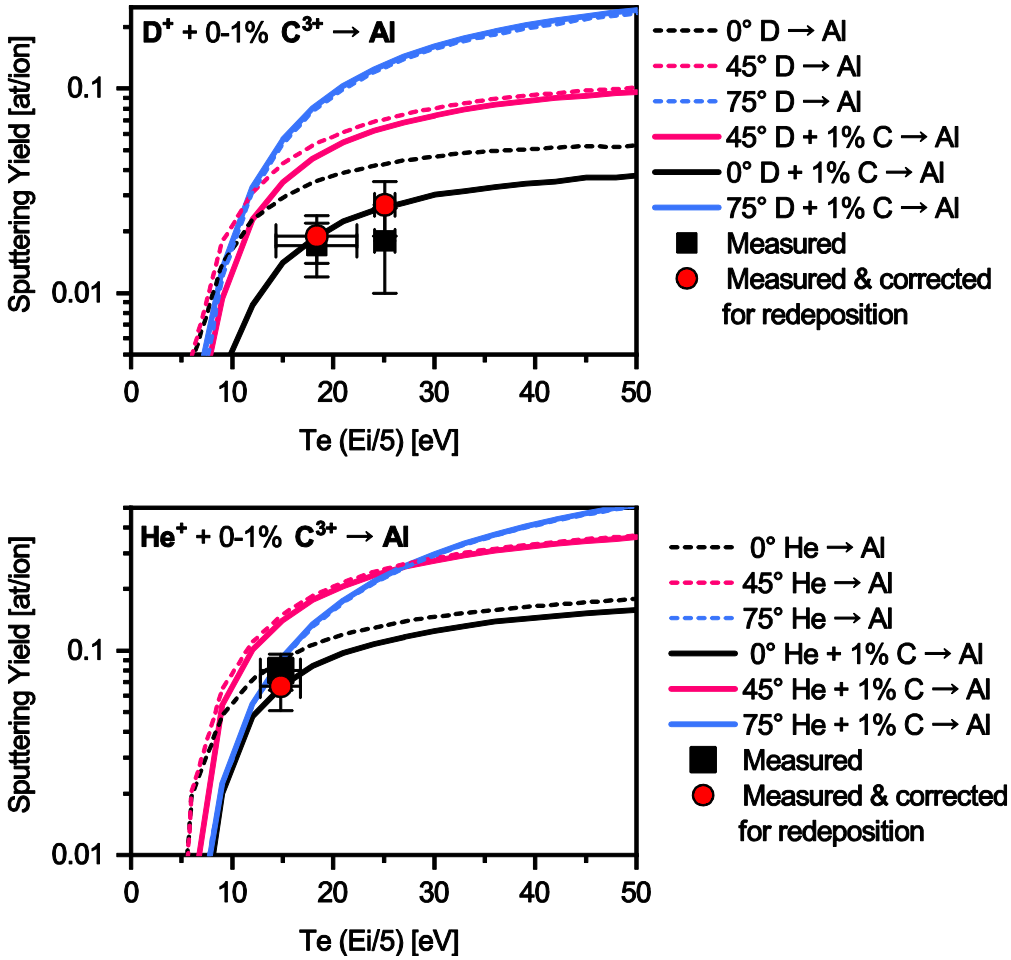

Figure 6-5. SDTRIM.SP calculated sputtering yield curves for Al with different ion incidence angles and different C impurity fractions. The experimental gross erosion measurements from post-mortem RBS small spot analysis is shown, along with values based on the large area coating, corrected for redeposition.

The experimentally measured sputtering yields were derived from the gross erosion rate measurements using RBS film thickness change of the small sized samples, assuming erosion by physical sputtering with ion flux from by surface Langmuir probe measurements. The measured erosion yields in each case are consistently lower than sputtering yield models. The discrepancy with sputtering models was roughly a factor of 2, which is not unreasonable given the uncertainties in the ion flux, energy, and incident angle estimates used in calculating the sputtering yield. Some complicating real-world

factors not included in the calculated yields are the effect of surface roughness, surface saturation by incident ions, or a shielding effect of a low-energy carbon coating or surface oxide. These factors may vary with flux or fluence and are not understood well enough to accurately model.

6.4 Surface morphology changes

Inspection of the S-D sample was made before and after plasma exposure (Figure 6-6). The sample initially had a mirror finish, with roughness negligible compared to the film thickness (~100nm). After plasma exposure, the coating was completely eroded in some areas down to the carbon substrate layer beneath. Where Al remained, SEM imaging showed blob like features that were rich in Al and O. No pre-exposure SEI imaging was made, so the cause of the formation is unknown. Thermal effects such as melting were unlikely, since the surface temperature in the S-D case was estimated to be between 100-300°C based on measurements of heat flux in the divertor and 1-D thermal modelling of the Si substrate. Assuming the surface was initially featureless, these Al-rich blobs may have developed during plasma exposure by some sputtering instability or due to shielding by distributed surface impurities. Similar but more severe microstructure development under plasma bombardment has been observed on bulk Al and Be samples exposed in PISCES-B [131] after 4000 sec at $4x10^{18}$ cm^{-2} s^{-1} ,100eV D-plasma ion flux at 45° C.

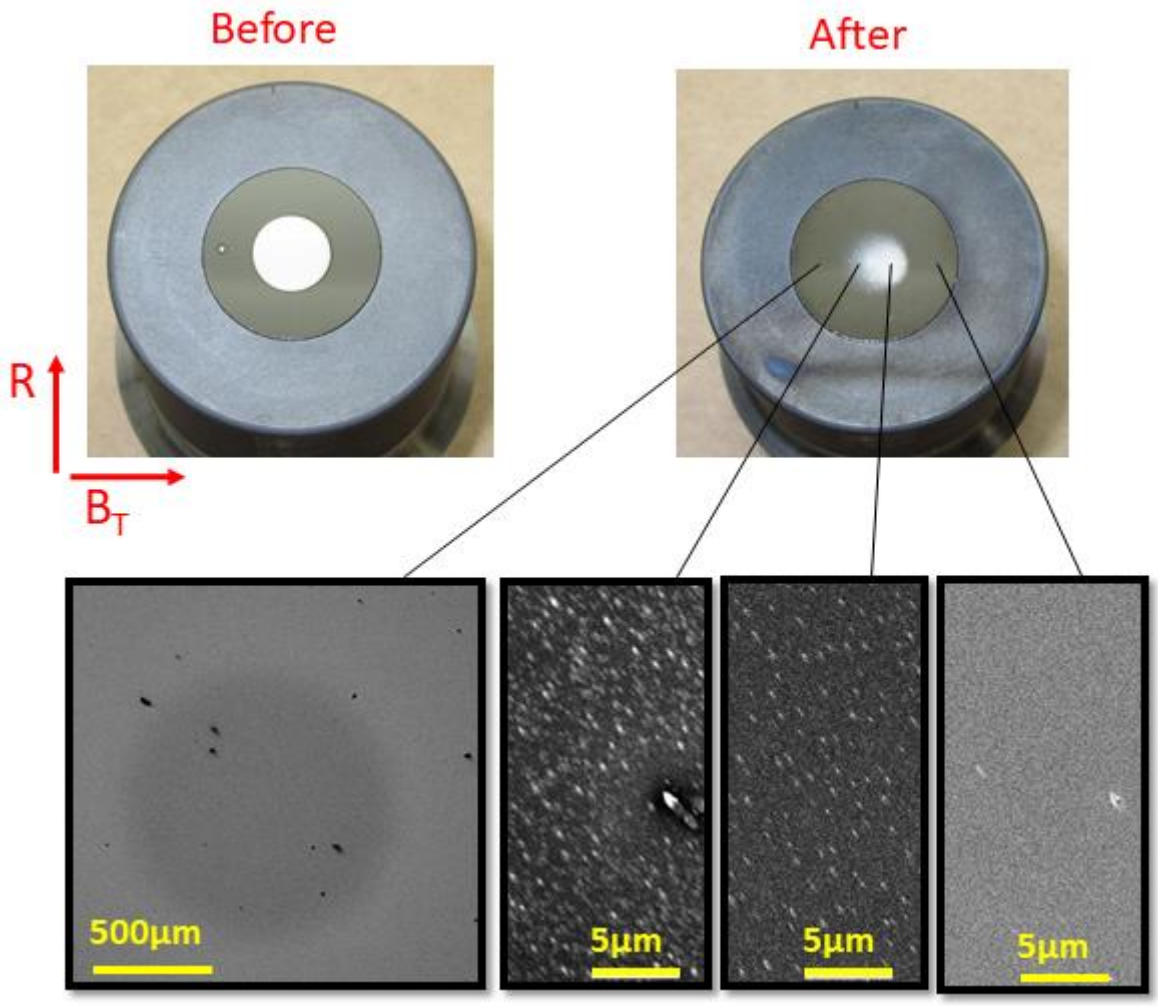

Figure 6-6. Before and after exposure images for case S-D. No pre-exposure SEI images were made, but surface had mirror finish and is expected to be mostly featureless.

The rough substrate samples, cases R-D and R-He, used similarly polished graphite as the coating substrate. The graphite was polished to a roughness of ~600 nm, excluding 10-15% of the surface area that was pitted with 5-50 µm sized pores. The surface roughness and presence of pores is expected to have a small effect on the measured erosion, since the total affected area is relatively small (~10% of the total area) and the amount of total erosion was small compared to the scale of the surface roughness (~20-50 nm net Al eroded from the surface). The pore sizes in the samples in this study is on the order of the plasma Debye length (~50 µm), so surface roughness is not expected to

affect the sheath or ion trajectories. The expected ion gyro-radius for Al ions is ~700 μm at 3.5eV sputtered energy, and for D, He, and C^{3+} ions is 350 μm, 500 μm, and 300 μm at 25eV ion temperature – all roughly 10x the size of the surface pore dimensions – so we expect that pore edges may act as leading edges with enhanced erosion while inner pore structure will be shadowed from erosion.

Secondary electron imaging (SEI) of the R-D and R-He surfaces before and after plasma exposure shows no significant change to the morphology appearance. An example of the before and after R-D images is shown in Figure 6-7. After exposure, the contrast between Al-coated and uncoated areas decreased, which is consistent with Al:C material mixing in the near surface layer. Energy dispersive X-ray (EDX) measurements in areas on and off the coating showed an increase in Al off the coating and an increase in C on the coating area after plasma exposure, with higher amounts of Al and O detected inside the pores than between them. Quantifying the EDX measurements was difficult due to the long interaction range of electrons compared to the coating thickness. More detailed coating thickness and composition change measurements were made using Rutherford Back-scattering Spectroscopy (RBS), discussed in the following section.

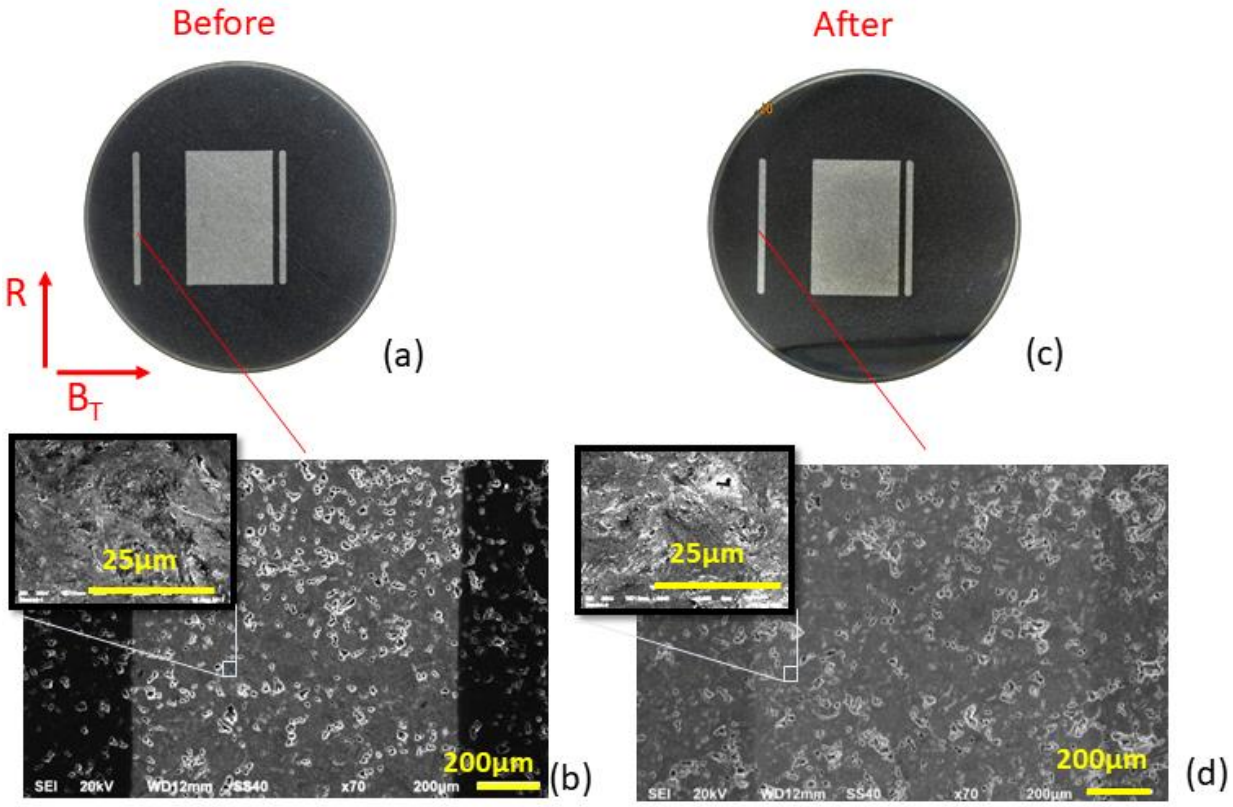

Figure 6-7. Before and after plasma exposure images for case R-D. Before and after photos (a,c) corresponding to before and after SEI images of 1mm Al stripe region (b,d).

A microscopic mapping of the surface composition, made using a scanning Auger microscopy technique, shows a similar effect. In this technique, a qualitative map of Al coverage is obtained at SEM level resolution by mapping the count rate of surface-emitted Al KL1 Auger electrons at 1388.9 eV and subtracting the neighboring background at 1368 eV. A map of the relative Al AES electron peak count rate (~proportional to surface Al concentration) was made around one of the pores in the R-He sample, shown in Figure 6-8 (b) alongside an SEM image of the same pore (a). The mean-free path of the Auger electron in the surface is ~5nm, which sets the depth resolution of this technique. AES estimated average Al concentration with the ~5nm sampling depth indicated to be ~30% inside the pore, while only 6% outside the pore. This pore was located ~ 5mm toroidally downstream of the original Al coating, and thus had

no Al present before exposure. The resulting composition map reveals a lower concentration of Al on the pore edge at ~ -35degrees with respect to the toroidal field direction, and a higher concentration on the opposite surface. This is consistent with the line-of-sight deposition from the erosion of the opposite leading edge, as illustrated in Figure 6-9. Similar effects have been observed on rough surfaces in contact with tokamak plasmas previously for tungsten in the AUG divertor [92] and carbon in TEXTOR limiters [81].

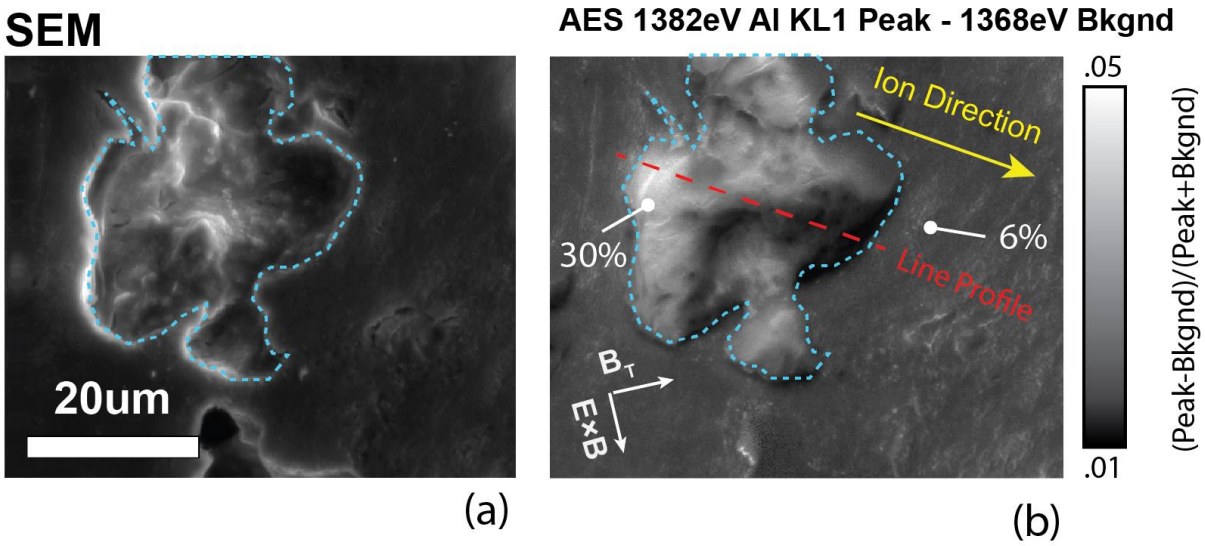

Figure 6-8. Secondary electron microscopy image (a) and Auger electron spectroscopy surface area map (b) of the same pore from the R-He sample graphite surface, outlined with blue dashed line. AES composition map brightness shown in terms of relative Al 1382eV peak height above background (a few percent full scale). Al composition measured by local AES emission indicated inside (30%) and outside (6%) of the pore.

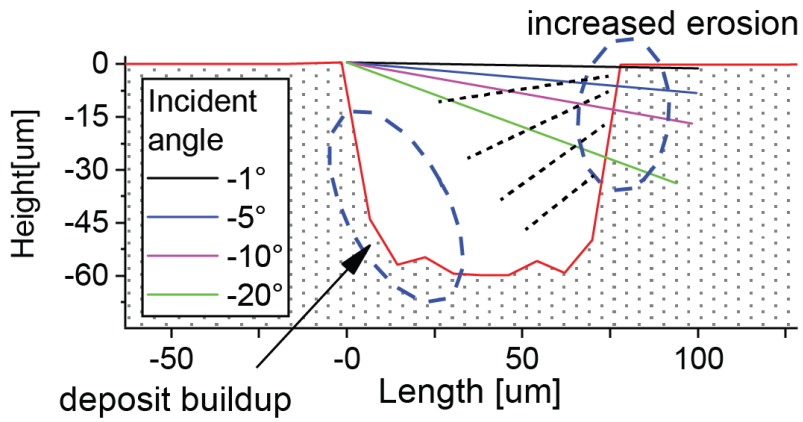

Figure 6-9. Synthetic surface height line profile of a typical pore, likely representative of the pore along the 'line profile' indicated in Figure 6-8. Incident ion trajectories indicating expected increased erosion rate and areas of expected increase in direct line of sight deposition on the opposite surface.

6.5 Film composition and depth profile measurement

In addition to measuring Al coverage, the RBS technique used here enabled investigation into the film composition and depth profile before and after exposure. Film composition and depth profile was determined by fitting the measured RBS energy spectra using the SimNRA [109] code. SimNRA is a code for simulating several ion beam analysis techniques such as Rutherford Backscattering (RBS), Elastic Recoil Detection (ERD), and nuclear reaction analysis (NRA). The code allows for simulation of different target-beam geometries, and can treat targets of any composition and multiple layers.

The RBS spectra measured here used a 1MeV He4 beam with 0.5mm diameter beam spot size (for Case R-D), or a 2MeV He4 beam with between 0.2 and 1mm spot size (for cases S-D and R-He). Some example measured RBS spectra from the R-D sample are shown plotted as points in Figure 6-10. The spectra have distinct peaks or ledges corresponding to the Al film, surface O, interfacial O between the Al layer and C substrate, and substrate C. The roughness of the surface created some broadening of the peaks and loss of resolution, as was expected. RBS energy peak broadening on rough

surfaces is well known and occurs as RBS probing beam particles, scattering from peaks and valleys in the sample, lose varying amounts of energy on their trajectory out of the surface proportional to the amount of surface height variation (or roughness) present in the sample.

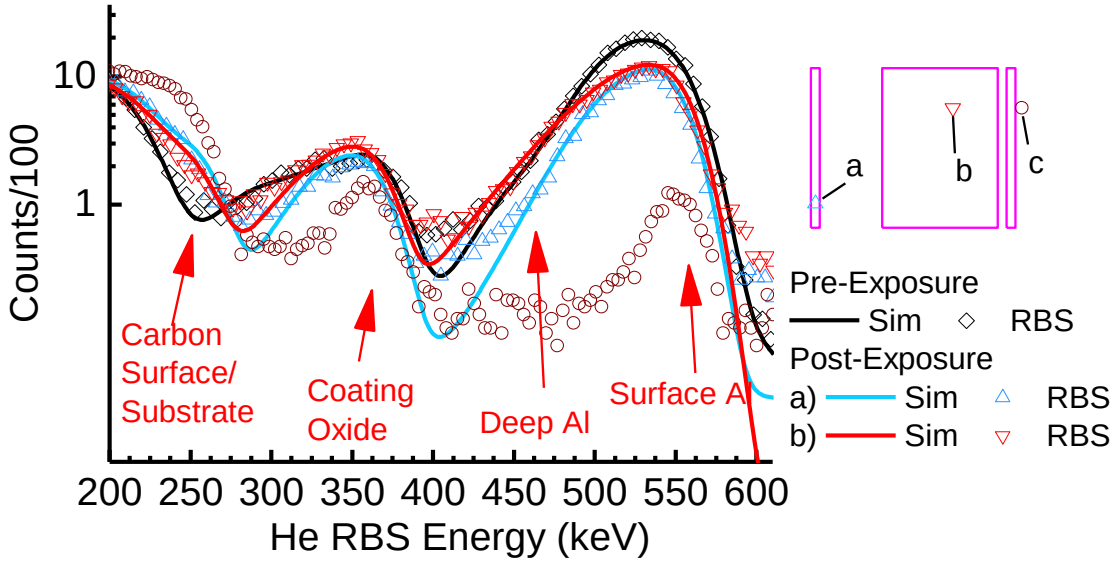

Figure 6-10. RBS measured data and simulated spectra on rough (case R-D) samples before and after plasma exposure. Post-exposure spectra taken at three locations as shown with inset.

The SimNRA code was able to reproduce the observed spectra and quantify the film thickness, composition, and depth profile. SimNRA target simulation fits are shown in solid lines for case R-D in Figure 6-10. Depth profiles were obtained by fitting the spectra with a four-layered target: 1) a thin-surface layer ~15nm thick with an initial surface oxide and a post-exposure mixed Al/C/O composition; 2) a partially oxidized Al film layer where thickness and Al/O concentration were used as fitting parameters; 3) an interfacial layer between the film and substrate with mixed Al/C/O composition; and 4) a substrate primarily of C with small fractions of impurities Fe, Si, and Ca adjusted based on the 'noise floor' in the spectrum. Layer thickness and composition was manually iterated to fit the

observed RBS spectrum. The depth profiles resulting from fitting the spectra for case R-D in Figure 6-10 are shown in Figure 6-11 (a). Depth profiles for case R-He before and after exposure are shown in Figure 6-11 (b). Average initial oxygen content in the Al films in each case was found to be ~10%, with a ~20nm oxygen-rich surface layer. After plasma exposure we noticed a reduction in the Al film thickness, accompanied by an increase in the average oxygen fraction and a near surface carbon fraction.

The peak broadening was reproduced by assigning an average roughness (film thickness distribution width) to the Al layer (layer 2). The relative width of the thickness distribution provides information on the uniformity of the Al layer coverage on the sample. Before plasma exposure, the thickness distribution width was 75-90% of the original film thickness, suggesting that some surfaces (presumably inside of the pores) were not adequately coated by Al. After plasma exposure, the layer thickness decreased due to erosion while the relative thickness distribution width increased to ~200% of the film thickness. This increase in relative distribution width indicates an increase in the fraction of areas with little or no coating compared to the areas with Al coating. The cause was likely due to inhomogeneous erosion and deposition on the surface on a scale smaller than the measurement area of the beam (~0.5mm diameter).

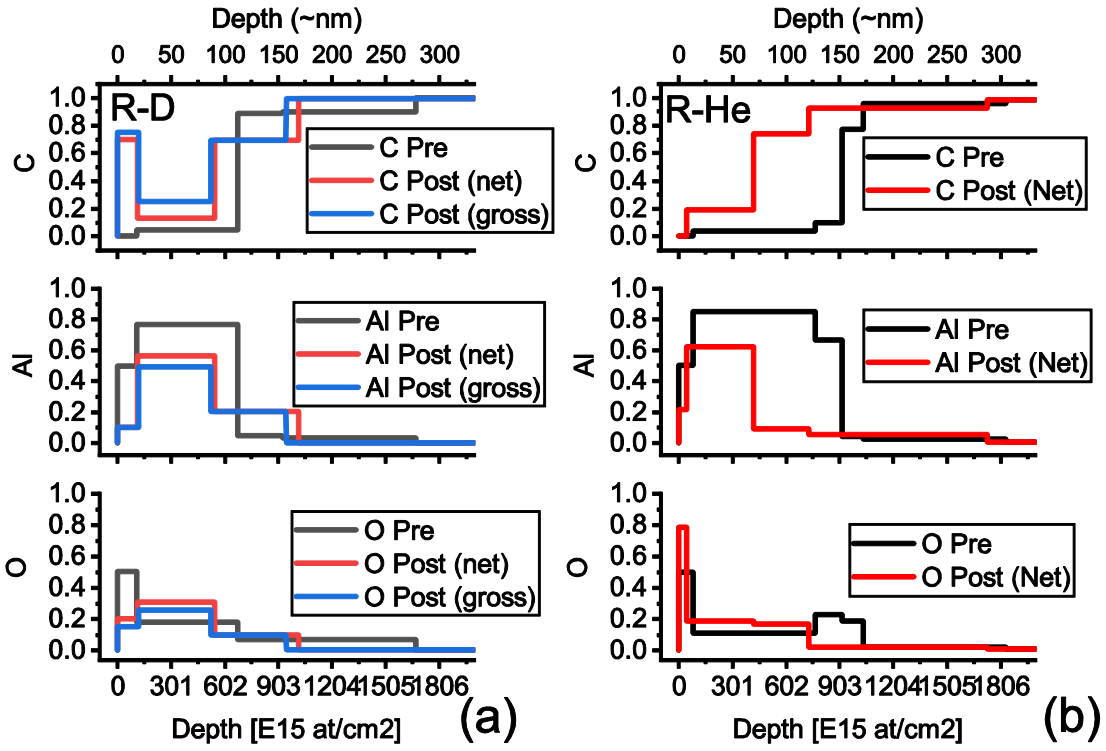

Figure 6-11. Depth profiles for Al, C, and O fitted for case R-D (a) case R-He (b) before and after plasma exposure. For case R-D, depth profiles fitted in the net erosion spot (large coating area) and gross erosion spot (small coating area) are shown.

6.6 Conclusions

We have presented the first measurements of Al erosion in the DIII-D tokamak divertor strike point region. The average gross Al erosion rate measured in DIII-D using non-spectroscopic measurements is estimated to be ~2x lower than the range of expected sputtering yields. The low erosion rate may be due to some transient effects, such as the removal of a surface oxide, or a shielding effect whereby the amount of Al present for sputtering from the surface is reduced by implantation of carbon or dynamic retention of D or He ions in the near-surface Al layer. Resolving this will require a more detailed model of the dynamic evolution of the surface composition throughout the plasma exposure.

An apparent contradiction is posed by the increased redeposition fraction accompanied by longer redeposition length scales on samples R-D and R-He compared to S-D. It is thought that increased redeposition fraction should be accompanied by shorter redeposition length scales. More detailed model of redeposition that includes energy and angle resolved distributions of sputtering energy may resolve this contradiction. Also, surface roughness may cause the higher than expected redeposition fractions in the rough surface cases, if microscopic pits and valleys on the surface cause localized net deposition regions that can accumulate redepositing material linearly fluence. More detailed measurement of composition on the scale of the surface roughness may be required.

In these initial observations we have found that the redeposition length scale appears similar to the ionization length, which was surprising given the simple picture of Al redeposition along field lines. This is evidence of the role of the sheath electric field in accelerating the redepositing ions and driving redeposition motivated the detailed measurement and modeling of erosion, ionization discussed in Chapters 4 and 5. It is not clear whether the net or gross erosion rate measured using the small and large area film thickness change is sufficient given the long redeposition length scales involved. More careful analysis of the redeposition in the context of material mixing and re-erosion is needed, which will be presented in Chapter 7. In Chapter 7, we will present a numerical model of material migration that includes material mixing and re-erosion effects. The model will be used to fit the observed erosion rate data and determine the single-step redeposition fraction for Al, rather than the fraction of material remaining on DiMES. Furthermore, this model will provide a more accurate measurement of gross erosion by

estimating and accounting for the fraction of material redepositing on the small area coatings.

6.7 Acknowledgements

This work was supported in part by the US Department of Energy under DE-FC02-04ER54698, DE-FG02-07ER54917, DE-AC52-07NA27344, DE-SC00-02060, DE-AC02-09CH11466, DE-NA0003525, and DE-AC04-94AL85000. Sandia National Laboratories is a multi-mission laboratory managed and operated by National Technology and Engineering Solutions of Sandia LLC, a wholly owned subsidiary of Honeywell International Inc. for the U.S. Department of Energy's National Nuclear Security Administration under contract DE-NA0003525. DIII-D data shown in this paper can be obtained in digital format by following the links at https://fusion.gat.com/global/D3D_DMP.

This chapter includes text and data that is a reprint of the material as it appears in C. Chrobak, P. C. Stangeby, A. W. Leonard, D.L. Rudakov, C.P.C. Wong, A.G. McLean, G.M. Wright, D. A. Buchenauer, J.G. Watkins, W.R. Wampler, J.D. Elder, R.P. Doerner, D. Nishijima, G.R. Tynan, "Measurements of Gross Erosion of Al in the DIII-D Divertor." Journal of Nuclear Materials, vol. 463, 2015, Pages 810–813. The dissertation author was the primary investigator and author of this paper.

Chapter 7
Modeling of Multi-Step Material Migration and Mixing

7.1 Introduction

The intense plasma conditions and high ion fluxes possible at the divertor strike point can lead to lifetime limiting surface erosion rates. A fraction of this eroded material is expected to return to the divertor and redeposit, thereby reducing the net erosion rate. However, the divertor strike point can also act as a sink, receiving an influx of impurities sputtered from other first wall surfaces. For ITER, it is expected that the Be main wall will primarily be in a net erosion state, and that the eroded material will be transported to the divertor where it may undergo multiple deposition and re-deposition cycles. Possible surface modification by material mixing can lead to degraded thermal and mechanical properties of the tungsten divertor [132] [133]. Material accumulation in regions of net deposition will lead to tritium retention by co-deposition.

In Chapter 6 we presented measurements of Al erosion and deposition on samples exposed at the outer divertor of DIII-D. The measurements were intended to provide a benchmark dataset for codes modeling low-Z materials in divertor plasma contact. One of the unexpected results was a significantly (25x) higher redeposition rate found on samples that experienced similar erosion rates but had different surface morphologies. One possible explanation for this result would be if the surface were accumulating some redeposited material in microscopic, distributed shadowed surfaces in the surface

roughness. Another difficulty with the experimental measurement was uncertainty in the actual redeposition fraction measured. Due to the presence of multiple erosion-redeposition cycles with high erosion rates, and the fact that each redeposition cycle had a length scale on the order of or possibly longer than the coating area, direct measurement of the redeposition fraction was difficult on the limited sample size. We will focus on the differences observed between smooth and rough surfaces, and propose a multi-step migration model that qualitatively accounts for the observed effects of surface roughness.

In this chapter we will describe a model of multi-step erosion-deposition and migration that is designed to test the material accumulation hypothesis and account for multiple erosion/redepositon cycles to determine the single-step redeposition fraction for Al in each of the experiments. At the core of the model is a redeposition probability distribution function defined by a total redeposition probability and an asymmetrical peak-shaped spatial distribution (width, asymmetry factor) which was adjusted to fit the measured net erosion data. We hope that this will help simplify the material migration problem by enabling separate testing of material-oriented parameters such as assumptions on the material mixing and surface roughness effects without requiring a full model of the ionization and plasma transport processes. The fitting of an arbitrary redeposition distribution function to measured data will be the result of the multi-step material erosion/redeposition model and will distill true redeposition fraction and redeposition length scales from the radial and toroidal profiles of Al coverage change.

7.2 Material Migration Model

7.2.1 **Overview**

A model of the dynamic erosion and deposition process that includes surface composition evolution due to impurity ion implantation and multiple erosion-deposition cycles has been developed to interpret and reproduce the erosion measurements in [115] and Chapter 4 of this thesis. The model starts from an initial target composition and layout description, then with each subsequent erosion, redeposition steps the material is distributed and migrates across the sample, with a fraction being lost to the plasma each time. The model is able to reproduce the effect of surface C enrichment by ion implantation, even on eroding surfaces. The composition of a thin surface interaction layer is evolved with each erosion cycle as the outgoing (i.e. sputtering) and incoming (i.e. redeposition, plasma impurity implantation) fluxes of atoms are balanced. Each cycle of erosion and redeposition occurs during a discrete time step, which is limited so that no more than 5% of the interaction layer is eroded or added to in each step. In order to account for the hypothesized accumulative effect of surface roughness, we will assume the redepositing flux of material is split between the mixed material eroding surface and a hidden inventory of non-eroding, or 'trapped' deposits. This type of a trapped deposition is intended to simulate the effect of the pores or valleys on rough surfaces that are shadowed from incident ion flux and thus accumulate in the absence of erosion.

The model does not simulate any plasma or ion bombarding effects. Instead, the sputtering yields for each ion-target combination is explicitly defined at the outset based on SDTRIM.SP modeled single component sputtering yields. Redeposition is calculated

as a pre-set fraction of the eroded material (with some spatial distribution, as will be discussed). Other sources of deposition include a pre-defined flux of depositing ions, to simulate the effect of depositing plasma impurities.

A conceptual visualization of the model is shown in Figure 7-1, and details of each part of the model are described in equations 7.1 - 7.6 in the following sections. Incoming and outgoing fluxes of a target material *T*, in this case C and *Al* are denoted as φ_C and φ_{Al} (or generally φ_T). The composition of each target species in the mixed material surface layer is denoted as a concentration $X_T(x)$. A previous version of this model, presented by Wampler [134], was developed to understand how a Mo surface in the DIII-D divertor developed a high concentration of carbon on the Mo surface despite the net erosion of C and Mo from the sample [108,134]. We have added to the original model the effect of trapping to test the effect of deposit accumulation in shadowed areas of rough surfaces.

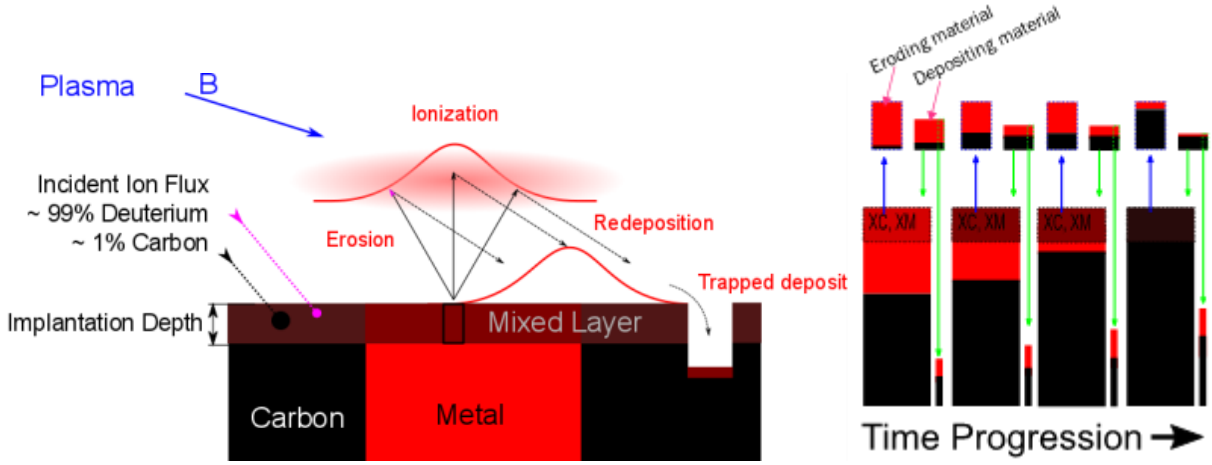

Figure 7-1. Schematic of the erosion/deposition model. This shows the Al layer on top of a carbon substrate, and a mixed material layer forming on the surface due to incident carbon impurities. The time progression series illustrates the evolution of surface carbon and metal concentrations (XC and XM, respectively) while total layer thickness decreases due to net erosion. Redeposition into a hidden inventory of surface traps accumulates throughout the simulation.

7.2.2 **Surface Erosion**

Sputtering and implantation typically occur within the first few nm of a surface. For sputtering of mixed material surfaces, or when sputtering by multiple ion species (such as D and C impurities), the composition of this surface layer can change dramatically from the bulk material. In this model, we define a thin interaction layer whose composition is allowed to change based on the balance of incoming and outgoing atoms. A deficit in the atomic balance to the interaction layer in each time step is treated as net erosion, while a surplus is treated as net deposition. The thickness of the mixing layer remains constant at the beginning of each time step, with eroded material replenished by the material species below the interaction layer. Time steps are limited such that at most 10% of the layer is eroded or deposited within each step. A similar model is employed by SDTRIM.SP, where dynamic evolution of the target can be tracked, due to competing processes of sputtering, reflection, and implantation. The erosion rate of a particular atomic species can be reduced by diluting the surface concentration of that particular species, reducing the available number of atoms to erode from that surface. Furthermore, species with higher sputtering yields will be depleted from a mixed surface, while the lower sputtering yield component will become enriched.

The outgoing flux of target atoms φ_T^{out} (Eq. 7.1) was calculated at each surface position $\mathbf{x}$. Theoretical sputtering yields ($\boldsymbol{S_{i\rightarrow T}}$) for each ion $\boldsymbol{i}$ onto pure element targets $\boldsymbol{T}$ were weighted by the concentration $\boldsymbol{X_T}$ of the target element in the mixed surface layer. Sputtering yields $\boldsymbol{S_{i\rightarrow T}}$ for all incident ions (i) and targets (T) were calculated from SDTRIM.SP [61] using the ion impact energy estimated as discussed earlier using $E_{Impact} \approx 3Z_iT_e + 2T_e$ [42], pure component targets, and a single average 45-degree angle of incidence. The actual angular sputtering dependence and other secondary effects

such as flux-dependent surface saturation with the main sputtering ion [123] or surface temperature effects are not included at this point. Instead, all calculated sputtering yields were scaled by single free parameter factor, $\mathbf{F_Y}$, to fit the experimentally measured *gross* erosion rate.

$$\varphi_T^{out}(x) = \boldsymbol{F_Y} X_T(x) \sum_i S_{i\to T}\varphi_{ion} \qquad (7.1)$$

7.2.3 **Deposition, Mixing and Trapping**

The total incident flux of target species ($\boldsymbol{\varphi_T^{in}(x)}$, Eq. 7.2) is split into two parts: a component due to the background plasma impurity level of that species which is proportional to the incident ion flux ($\boldsymbol{F_T^{ion}}\varphi_{ion}$), and a component due to the redeposition of the outgoing flux of that species. The redepositing flux is calculated by integrating the outgoing ion flux of that species from each relative location on the sample (*x*+*u*) scaled by the probability $\mathbf{R_T}$ of redepositing to that position. The redeposition probability distribution function is an important feature of this model and will be discussed in more detail in the next section.

$$\varphi_T^{in}(x) = \boldsymbol{F_T^{ion}}\varphi_{ion} + \int_u \varphi_T^{out}(x+u) R_{PDF}(x+u)du \qquad (7.2)$$

The factors determining the composition of the mixed material surface layer in this model are the sputtering yields of the components, the incident fluxes of those components from the background plasma, and the depth over which the mixing occurs. The depth of this mixed layer was set in this model by the average range of C ions in Al in each case (~1-2nm for 200-400eV C ions). We calculate the rate of change of atoms of

target species T ($\boldsymbol{dN_T^{surf}/dt}$, Eq. 7.3) by balancing the particle fluxes into ($\boldsymbol{\varphi_T^{in}}$) and out of ($\boldsymbol{\varphi_T^{out}}$) the inventory of atoms in the surface layer.

The effect of deposit trapping in pores was included here by assuming a fraction of the redepositing flux of particles lands in shadowed surface areas and is counted in a separate 'trapped' inventory that does not become part of the eroding mixed material inventory. Re-erosion from this inventory is suppressed, so the traps are forced to be in net deposition and material accumulates. Another cause for deposit accumulation would be cases where the trapped target species is buried by a high flux of a non-eroding impurity species (in the case of D co-deposition, for example). The rate of accumulation in the trapped surface inventory, ($\boldsymbol{dN_T^{trap}/dt}$, Eq. 7.4) is set by the fraction ($\boldsymbol{F_{trap}}$) of incident material flux.

$$dN_T^{surf}/dt = \left(1 - \boldsymbol{F_{trap}}\right)\varphi_T^{in} - \varphi_T^{out} \quad (7.3)$$

$$dN_T^{trap}/dt = \boldsymbol{F_{trap}}\varphi_T^{in} \quad (7.4)$$

The total flux of atoms into the surface interaction layer is reduced by the trapping fraction for conservation. The model assumes homogeneous mixing and adjusts the composition with each time step, maintaining a fixed total inventory of atoms. When the net balance of particles to this layer was negative, the surface is determined to be in net erosion and the composition is adjusted to include replenishment of net eroded material by the material beneath the mixed layer. Time steps are limited so that the total erosion is less than15% of the total mixing layer particle inventory in each step. In this way, total erosion through finite film thicknesses can be modeled (as was seen in the S-D case). When the net balance was positive, the surface was determined to be in net deposition

and the mixed layer thickness is grown. Layer growth, or net deposition, only becomes important for low sputtering yields or high deposition rates. The composition of the trapped material was equal to the composition of the eroded material in each time step, therefore no difference in the individual atomic redeposition fractions were included. This is reasonable, since both Al and C may have similar redeposition fractions, and surface trapping is likely due to line of sight deposition from nearby eroding surfaces. The total measured inventory of Al in the surface using RBS cannot easily separate between the Al in traps and near surface mixing layer.

By balancing the rate equations so that $dN_T^{surf}/dt = 0$, we find that the time at which this surface reaches its steady state concentration depends on the mixing layer thickness and rates of incident deposition (or implantation) and erosion. The surface concentration as a function of time becomes

$$X_T(t) = \frac{\varphi_T^{in}}{\varphi_T^{out}}\left\{1 - \exp\left(\frac{t}{\tau}\right)\right\} \qquad (7.5)$$

with $\tau = N/\varphi_T^{in}$, or on the order of 1 second in the sample exposures in this study. In the absence of significant redeposition (such as in the case of carbon on the metal surface) the equilibrium concentration reduces to the ratio of impurity fraction to total sputtering yield: $X_T^{ion}/\sum_{ion} \boldsymbol{S_{ion \to T}}$.

7.2.4 **Redeposition Probability Distribution Function**

Each time an atom is sputtered from the surface, there is a probability that it will redeposit to another location on that surface. This probability distribution function represents the spatial distribution of ionization and redeposition trajectories that a single eroding atom may take back to the surface. This probability is defined by the complex

interactions of the sputtered atom energy and angular distribution, ionization mean free path, collisions and entrainment by background plasma, thermal forces, diffusion, drifts, and acceleration through the sheath. For Al, the predicted ionization mean free path in the cases presented was ~1.6 ± 1 mm, which is on the same order as its ion gyro radius, ~0.4mm. The ionization mean free path estimate is based on available electron impact ionization cross section data from IAEA database [118], and ADAS [119] collisional radiative modeling database. For this reason, prompt redeposition is expected to be low. Redeposition is expected to be primarily driven by forces within the magnetic pre-sheath, including electric field and entrainment in background plasma flow. The widely used Monte-Carlo erosion-deposition modeling code ERO[135] [135] can account for these forces and simulate such a distribution for a particular set of plasma parameters, although comparing to experimentally observed data can be difficult since ERO does not include multi-step material migration and re-erosion that is needed to compare to the observed data. Furthermore, when comparing between model and experiment it can be difficult to determine which parts of the ERO model are responsible for any discrepancies with the actual observation. The redeposition distribution for a 1mm sized Al area in a uniform background D plasma with T_e = 17 eV and n_e=2x10^{-13} cm^{-3}, and 2.1T magnetic field in the toroidal (x) direction was simulated using the ERO modeling code. Three different sets of ERO simulations were run, each using a different data set for Al Ionization rate coefficients (ERO, ADAS [119], and IAEA [118]). The resulting distributions are shown in Figure 7-2a, with ionization rate coefficient data sets used in the simulations in Figure 7-2b. The lower ionization rate coefficient resulted in lower broader tails to the distribution, although with a reduction in the total redeposition fraction (i.e. the total fraction of Al returning to the surface, the rest is assumed lost outside the plasma

simulation volume). The total redeposition fraction was 77% for ADAS, 90% for ERO, and 92% for ERO-IAEA ionization rate coefficient data sets.

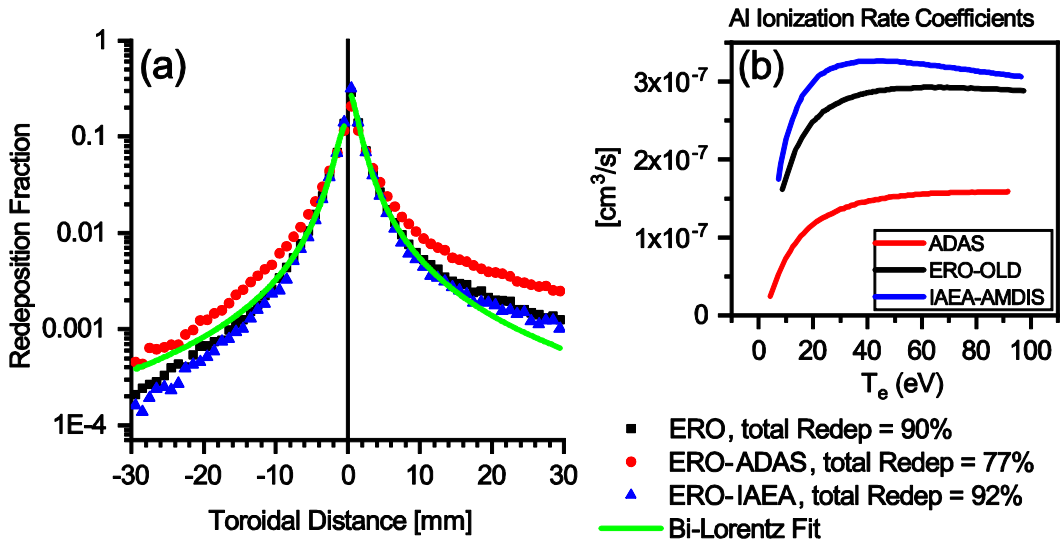

Figure 7-2. ERO simulated redeposition distributions and Bi-Lorentz peak fit for 1mm Al spot centered at 0mm (a). Ionization rate coefficients used in the simulations shown inset (b).

For uniform plasma conditions and sputtering conditions this distribution should be identical for each atom sputtered from the surface. By using a fixed redeposition probability for each erosion step, we can simulate the multi-step erosion, redeposition and migration of material across a surface using the surface mixing and trapping model described earlier. To help identify possible discrepancies between the ERO model and observed redeposition distribution, we chose to use an analytic function for the redeposition distribution that reasonably approximates the ERO calculated distribution but allows for fitting to the observed data. We found that an asymmetric Lorentzian peak function centered at $\boldsymbol{x_o}$ reasonably approximated the ERO modeled results, as shown plotted in Figure 7-2. The left/right asymmetry in the distribution is approximated with a skew term $\boldsymbol{\gamma}$, which scales the left and right half peak widths $\boldsymbol{w}$ using a piecewise definition where $1 > \gamma > 0$ for $x > x_o$, and $-1 < \gamma < 0$ for $x > x_o$. The function is normalized such that

its integral represents the total redeposition fraction $\boldsymbol{F_R}$. This general function for a redeposition distribution was used, with the parameters $\boldsymbol{F_R}$, $\boldsymbol{w}$, and $\boldsymbol{\gamma}$ used as fitting parameters to match the observed post-exposure coverage. In our material migration model, the sputtered Al redeposition flux $\boldsymbol{\varphi_{Al}^{in}}$ at each location on the sample was calculated by integrating the product of the outgoing flux at each point's relative position ($\boldsymbol{x+u}$) by the same redeposition probability distribution function $\mathbf{R_{PDF}}$.

$$R_{PDF}(x) = \boldsymbol{F_R} \cdot \frac{2\boldsymbol{w}}{\pi} \cdot \frac{(1-\boldsymbol{\gamma})}{(1+\boldsymbol{\gamma})} \cdot \frac{1}{4(x-x_o)^2 + \left(\boldsymbol{w}(1-\boldsymbol{\gamma})\right)^2} \quad (7.6)$$

7.2.5 **Examples of Model Results**

The output of this model is a one dimensional map of the surface Al and C coverage, surface concentration, and trapped deposit inventory across a pre-defined sample geometry. To illustrate the effect of each of the different fitting parameters on the resulting Al coverage profiles, examples of different model results are illustrated in the figures below. Here, we compare the modeled toroidal profiles of erosion and deposition rate across a sample like R-D. The initial coating geometry (boundary shown in red) here has a 14mm wide Al stripe and two 1mm Al stripes, one on offset 6mm on the left and one offset 1mm on the right side of the wider stripe. The surface between these is initially pure C, and the coverage of Al increases with time as eroded material is redeposited there.

In Figure 7-3 (a), we show the effect of increasing the sputtering yield correction factor $\boldsymbol{F_Y}$. Increasing the correction factor increases all the sputtering yields in the model proportionally. The result is mainly to increase the gross erosion rate across the entire sample, but at the same time the Al coverage deposited outside the coating increases

as well (the increased erosion also proportionally increases the redeposition flux). The other factor that has a strong effect on the gross erosion rate is the carbon ion fraction. Shown in Figure 7-3 (b) are two nearly identical erosion results achieved with $\mathbf{F_C}$ = 1% and $\mathbf{F_C}$ = 2% carbon ion flux fractions by increasing the yield correction factor from $\mathbf{F_Y}$ = 0.4 to $\mathbf{F_Y}$ = 0.6. In these same results, a map of the surface Al concentration (Figure 7-3 (c)) shows that the increased carbon reduced the surface Al concentration, so a higher sputtering yield was needed to reach the same Al coverage change.

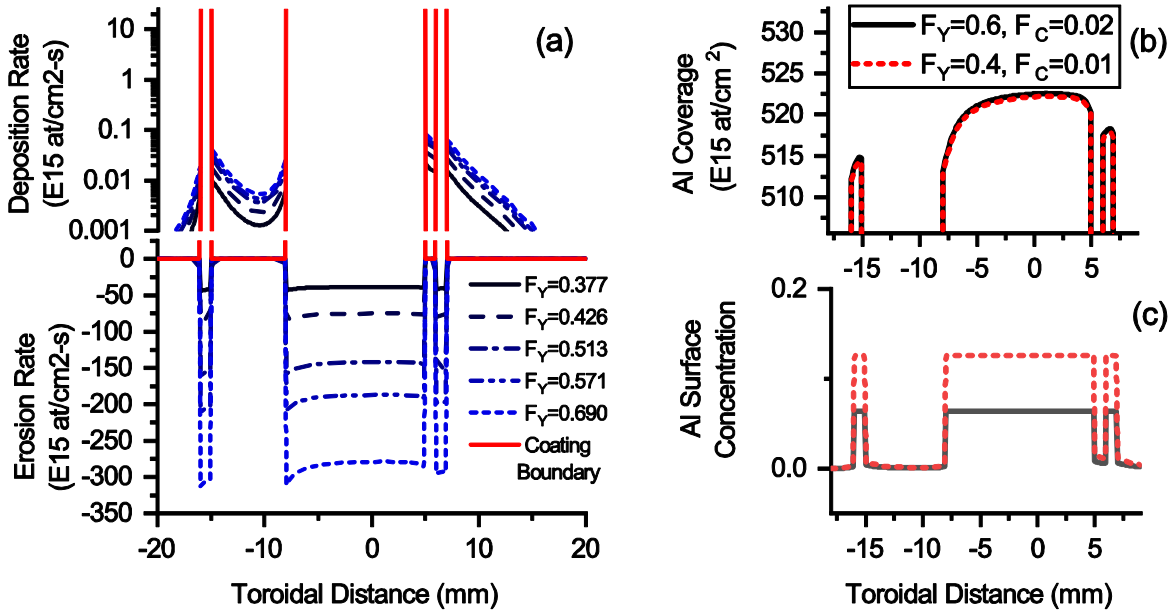

Figure 7-3. Effect of varying sputtering yield factor F_Y shown in (a) with a linear and semilog scales to highlight erosion and deposition, respectively. Similar erosion rates resulting from two different carbon flux fractions F_C were matched by adjusting the sputtering yield factor F_Y (b). The effect of the increased carbon flux was mainly to reduce the surface Al concentration (c).

In Figure 7-4 we compare the effect of independently varying the redeposition fraction $\boldsymbol{F_R}$ (a) and the trapping fraction $\boldsymbol{F_T}$ (b), while holding all other factors constant. Varying the redeposition fraction has a strong effect on changing the relative erosion

rate of the narrow (1mm) stripe compared to the wider (14mm) stripe. While the amount of redeposited material varies as well, the total redeposited amount is still small even with 100% redeposition fraction since the re-erosion rate is high. Varying the trapping fraction (while keeping redeposition fraction fixed at 30%) has little effect on changing the relative net erosion rate of the Al coating, but instead it has a large effect on changing the amount of redeposited material found outside the initial coating boundaries.

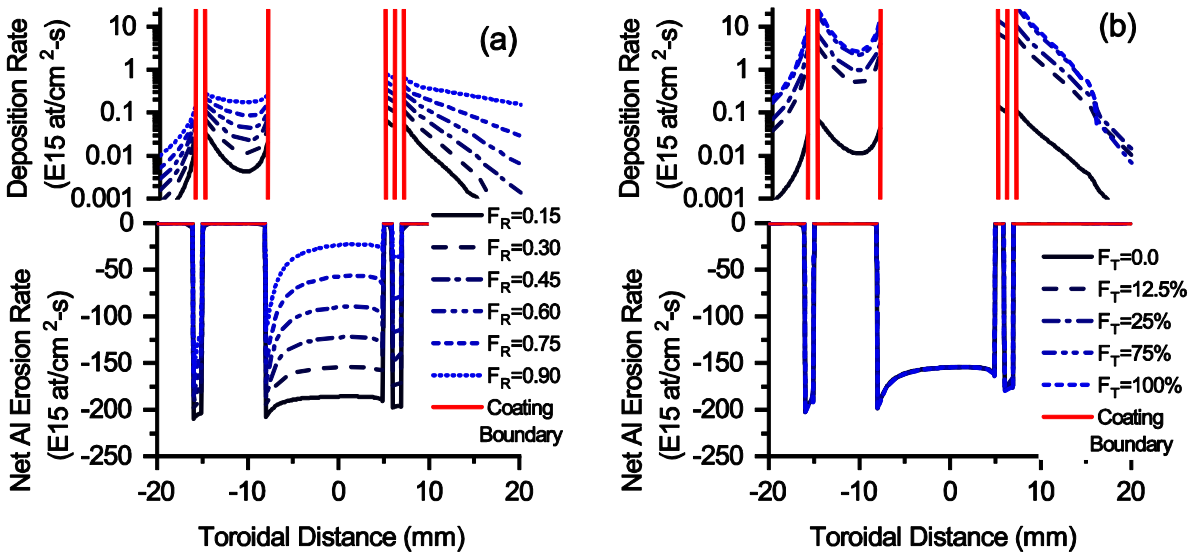

Figure 7-4. Examples of different simulation results showing the effect of varying redeposition fraction (a) with zero trapping fraction and varying trapping fraction (b) with 30% redeposition fraction.

Changing the value of the width ($\boldsymbol{w}$) without adding any skew changes the erosion profile shape as shown in Figure 7-5 (a). The skew ($\boldsymbol{\gamma}$) of the redeposition function changes the asymmetry of the redeposition and erosion shown in Figure 7-5(b).

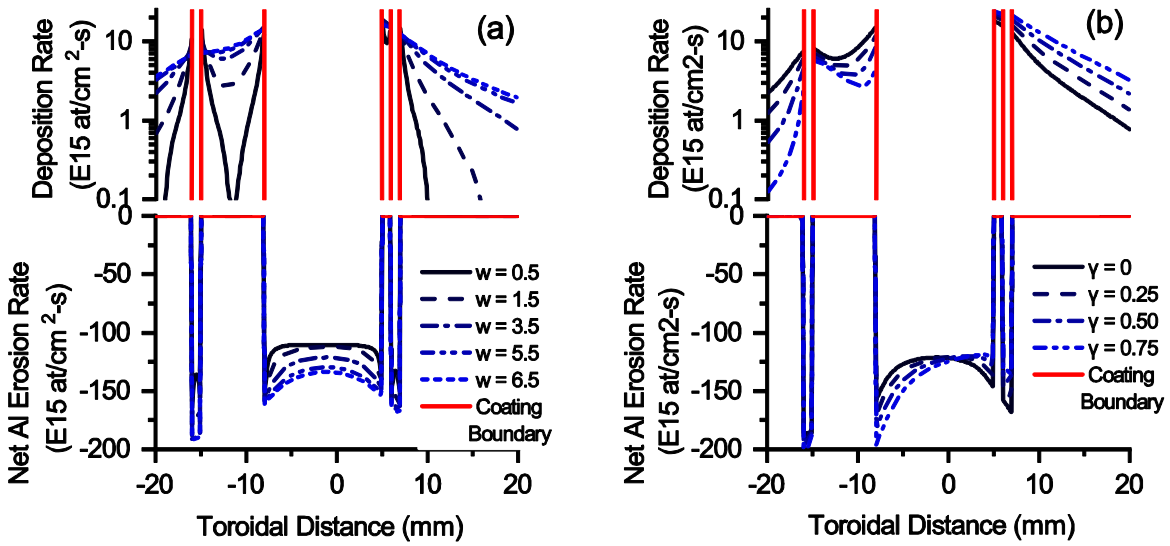

Figure 7-5. Erosion and deposition rate profiles resulting from different values of the redeposition function width parameter (a) and skew parameter (b).

7.3 Fits to measured erosion-deposition profiles

Each of the exposure cases was simulated in this model, and erosion rates and the Al redeposition profile parameters were adjusted to fit the measured erosion-deposition profiles. Targets representing each of the initial coating geometries were specified as initial conditions for the model, with coating surfaces of pure Al surrounded by pure C. Gross erosion of the target Al and C was calculated based on the expected sputtering yields for D or He, C, and Al self-sputtering. Sputtering yields for each case were determined from SDTRIM.SP calculations using a fixed incident ion energy (Set by initial thermal energy plus acceleration through the $3T_e$ sheath potential gradient) and single 45-degree incidence angle. The carbon impurity fraction (typically 1-3% of the incident D or He ion flux) in the plasma was pre-set based on the best estimate experimentally determined as discussed in Chapter 3, Section 3.5.1. No spatial variation of C redeposition was considered, since the component of incident carbon due to local

redeposition was likely a small fraction of the incident impurity flux. No other plasma impurity elements were considered.

A total of five fitting parameters were used in each case: three factors describing the redeposition probability distribution function, a trapping fraction, and an erosion rate scaling fraction. These were manually iterated until the model was able to satisfactorily reproduce the observed erosion and deposition rates (toroidal and radial) from each measurement. The complete input parameters are listed in Table 7-1, showing both the fitting parameters and fixed parameters used for each case.

Table 7-1. Model input parameters for each case

Fitting Parameters	**Name**	**S-D**	**R-D**	**R-He**
Total Redeposition Fraction	Fml	0.76	0.3	0.3
Redeposition Distribution Width Toroidal	Width	1.0	1.5	3.2
Redeposition Distribution Skew Toroidal	Skew	0.50	0.5	0.65
Surface Trapping Fraction	fmtrap	0	0.5	0.5
Sputtering yield correction factor	trimcor	1.4	0.588	0.909
Fixed Parameters				
Redeposition Distribution Offset	Xoff	0	0.05	0.00
Ion flux (ions/cm2-sec)	Fid	1.80E+18	8.90E+17	1.08E+17
C flux fraction	cp	0.01	0.01	0.03
Mixing Layer thickness (atoms/cm2)	d	1.20E+16	1.33E+15	1.00E+15
Time step (sec)	dt0	5.00E-03	5.00E-03	5.00E-03
Initial metal layer thickness	m0	5.80E+17	5.54E+17	7.48E+17
Sputtering Yields				
D>C	scd	3.36E-02	2.70E-02	5.28E-02
C>C	scc	4.10E-01	3.32E-01	2.20E-01
Al>C	scm	9.10E-01	4.00E-03	0
D>Al	smd	5.36E-02	6.10E-02	1.45E-01
C>Al	smc	1.00E+00	1.11E+00	1.11E+00
Al>Al	smm	5.00E-02	1.50E-01	3.00E-02

The five main parameters of the redeposition distribution function (listed in Table 7-2) were individually varied sequentially to fit different parts of the erosion/deposition

profile. The sputtering yield correction factor was the main parameter used for adjusting the gross erosion rate. With the other parameters initialized at Initial guesses of 2mm for redeposition length and 0% for redeposition fraction, the yield correction factor was fitted first to match the observed gross erosion rate (typically near the coating edges or 1mm spot). The redeposition fraction was fitted second, and had the effect of reducing the erosion rate on the large coating area. The width and skew parameters were fitted third, which had the effect of changing the shape of the net erosion profile and slope of the net deposition profiles upstream and downstream of the coating. The trapping fraction parameter was fitted last, and had the effect of increasing the amount of redeposited material found surrounding the coating. Finally, the process was iterated until a match to the observed total erosion and redeposition was achieved.

The fit results for each experimental case are compared in Figure 7-6, with final fit parameters listed in Table 7-2. The total integrated fraction of eroded material returning to the surface ($\boldsymbol{F_R}$) increases for higher plasma temperature and density, consistent with the shorter expected ionization mean-free-paths for sputtered Al in those cases. Both D plasma cases have similar spatial, although slightly higher redeposition fractions for the higher density case S-D. The key difference that led to the large difference in total post-mortem measured deposition outside the coating area is primarily due to the deposit trapping effect in the rough substrate. The longer redeposition length scales and lower redeposition fractions in the R-He case are consistent with the thinner MPS and longer ionization mean free paths expected in those plasmas.

Comparing the fit parameters across exposure cases reveals that the total probability of eroded material redepositing on the sample ($\boldsymbol{F_R}$) increase while the redeposition length scales ($\boldsymbol{w}$, $\boldsymbol{\gamma}$) decrease for higher plasma temperature and density,

which is consistent with expectations. Sputter yield correction factors ($\boldsymbol{F_Y}$) for all cases were ~40-70%, which is reasonable given the uncertainties in carbon impurity fraction, ion impact energies, and theoretical sputtering yields. Furthermore, the model reconciled the redeposition discrepancy mentioned earlier by requiring that 50% of the redeposited material became trapped and accumulated in pores for rough substrate cases R-D and R-He. Only surface mixing (and no trapping) was required to account for the redeposited material found on the smooth substrate S-D case.

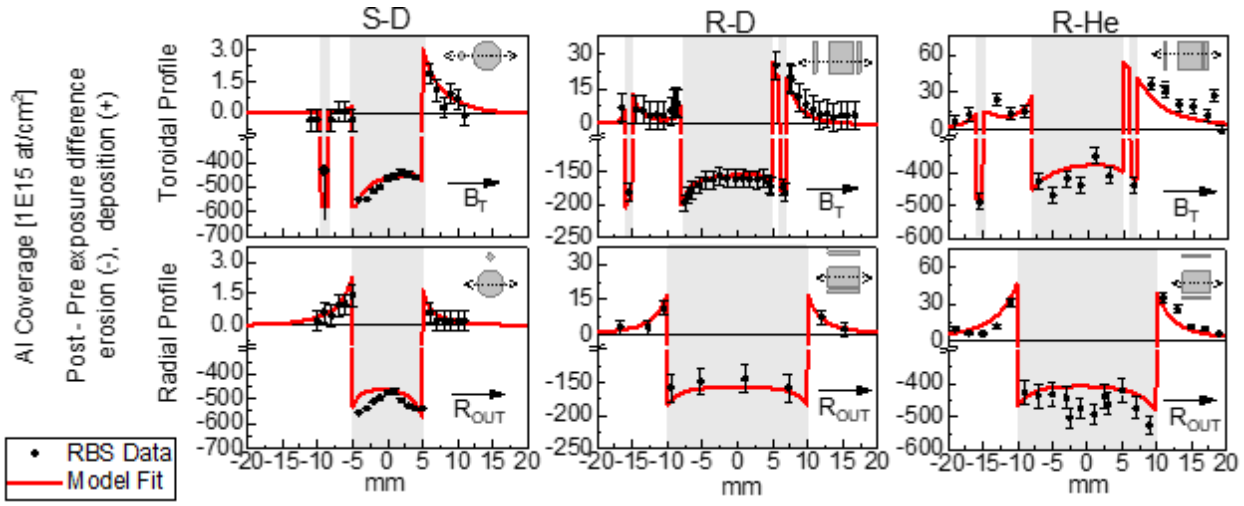

Figure 7-6. Toroidal and radial profiles of Al coverage change after exposure cases S-D , R-D, and R-He as measured by RBS (black points) and simulated with a model (red lines). Profile locations across coatings are shown with inset diagrams in each case, and shaded region indicates the initial Al coating region. Vertical axes have split scales to emphasize both erosion (negative change) and deposition (positive change).

The close match between both the spatial variation of erosion measured *within* the Al coatings and deposition *outside* the coating area, shown in Figure 7-6, suggest the material migration process is well reproduced with the model assumptions. Comparing the fit parameters across exposure cases reveals that the total probability of eroded material redepositing on the sample ($\boldsymbol{F_R}$) increases while the redeposition length scales ($\boldsymbol{w}$, $\boldsymbol{\gamma}$) decrease for higher plasma temperature and density, which is consistent with expectations. The model reconciled the redeposition discrepancy mentioned earlier by

requiring that 50% of the redeposited material became trapped and accumulated in pores for rough substrate cases R-D and R-He. This may seem high since only about 10% of the surface was covered with pores, but it is reasonable since our measurements of Al concentration inside the pores (see Figure 6-8) was ~6x higher than on the surface between pores. Only surface mixing (and no trapping) was required to account for the redeposited material found on the smooth substrate S-D case. For the R-He case, the redeposition lengths were approaching 50% of the sample size. This was long enough such that a significant fraction of the local redeposition occurred outside the original coating area and led to an initial over-estimate of the net erosion rate using just the film thickness change measurements.

The sputter yield correction factors ($\boldsymbol{F_Y}$) for all cases were ~40-70%, which is reasonable given the uncertainties in carbon impurity fraction, ion impact energies, and theoretical sputtering yields. However, since the erosion rate predicted by the model is reduced by high carbon flux diluting the surface, these correction factors to the sputtering yields are affected by the assumption of carbon impurity. A higher carbon impurity fraction, therefore, would also reduce the erosion yield much like the yield correction factor $\mathbf{F_Y}$ would. Using the carbon impurity fractions that were determined from experiments as discussed earlier, all cases these indicate that the resulting theoretical sputtering yields would over-estimate the actual erosion yield. The correction factor was larger for the rougher surfaces, suggesting that the effect of the surface roughness decreases the sputtering yield below theoretical sputtering rate.

Table 7-2. Summary of RBS-measured effective net and gross erosion as measured from large and small area coatings, along with model fit values of ideal net and gross Al erosion corrected for long range redeposition and deposit accumulation. The fraction of Al eroded from the coating found redeposited outside the coating shown as Off-Coating Dep %. Model fit parameters for the total redeposition fraction, trapping fraction, sputtering yield correction factor, and redeposition function shape parameters are shown.

Case	Perp. Ion Flux $x10^{18}cm^{-2}s^{-1}$	Gross Erosion nm/s	Gross Yield At/ion	Net Erosion nm/s	Off-Coating Dep %	SAP model fit parameters				
						F(Dep) %	F(Trap) %	F(Yield) %	**w**	**γ**
S-D	1.88	>5.7[a] 8.6[b]	>.018[a] .027[b]	5.1[a] 5.2[b]	0.2%	76%	0%	1.2%	1.0	0.5
R-D	0.89	2.5[a] 2.9[b]	.017[a] .019[b]	2.0[a] 2.0[b]	5%	30%	50%	59%	1.5	0.5
R-He	1.08	14[a] 12.4[b]	.080[a] .067[b]	12[a] 8.7[b]	6%	30%	50%	91%	3.2	0.65

a. RBS Measured effective erosion rate from small (gross) and large (net) coating areas. b. Model fit corrected ideal values.

The separation of deposit trapping, mixing, and re-erosion effects in the model allows for a direct comparison of the single-step redeposition probability in each plasma case. Shown below in Figure 7-7 are the final redeposition probability distribution functions used to fit the observed net erosion data in each of the exposure cases. What is apparent from this comparison is that the increased redeposition fraction in case S-D over R-D and R-He (76% compared to 30% in the other cases) occurs within 1-2mm of the eroding source. The increased redeposition fraction is consistent with the higher near-surface electric field in the magnetic pre-sheath in case S-D expected because of the higher background plasma electron temperature (~30eV in case S-D compared to ~15eV in cases R-D and R-He). Also, while the redeposition fraction was similar in cases R-D and R-He, the spatial distribution of redeposition was much broader in R-He. This increase in redeposition distribution width is likely due to the longer density gradient lengths in the magnetic pre-sheath in the R-He case compared to the R-D case because of the larger ion gyro radius of the He ion.

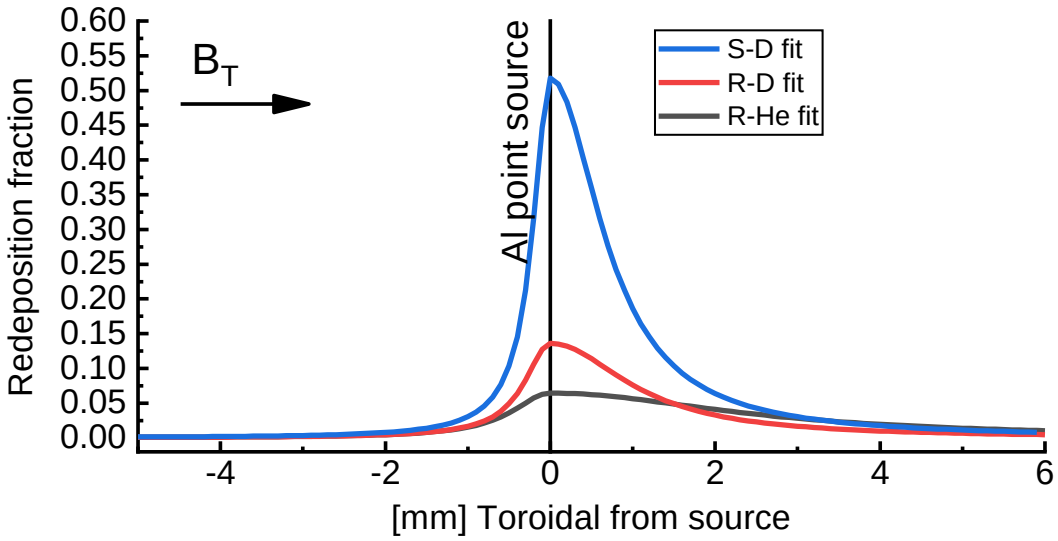

Figure 7-7. Redeposition distribution functions R_{PDF} required to match the observed toroidal erosion profile for all three cases.

7.3.1 **Comparison with ERO Model**

The arbitrary fit approach taken by this model produces a redeposition distribution function solution that can reproduce the measured erosion/deposition pattern. Assuming our simple model of multi-step migration, material mixing and trapping is sufficient to describe the surface composition evolution, the fitted redeposition distribution should be an accurate portrayal of the actual redeposition distribution produced by the plasma. The complex atomic and plasma redeposition physics can be modeled separately by the 3D Monte-Carlo impurity transport code ERO and compared with the fitted redeposition distribution. The ERO code has been widely used for simulating the processes of sputtering, ionization and redeposition in fusion plasma material interaction experiments.

We can now compare the results of our redeposition distribution fit for case R-D to the ERO simulation with background plasma parameters matched to the exposure conditions, shown in Figure 7-8. The ERO simulation assumed homogeneous background

plasma conditions (set to match the measured conditions in case R-D) with a constant n_e, and T_e. The plasma flow was assumed to be sonic along the toroidal field direction. Ionization rate coefficients from the ADAS database were used. Sputtered Al is assumed to follow a symmetric cosine type sputtered angular distribution with a Thompson sputtered energy distribution. The ERO redistribution model predicts slightly higher overall redeposition fraction, with a more symmetric distribution about the source than the redeposition fit to the measurement. ERO does include the friction of impurity with background plasma, but based on the small asymmetry generated in the redeposition distribution, it seems that this effect is not that significant. It is possible that such effects are under estimated in the code. Another more likely possibility is that the angular sputtering distribution is far from symmetrical, due to the oblique incidence of sputtering ions, where in the ERO simulations shown here it was assumed to be a symmetrical cosine distribution. This hypothesis was addressed in Chapter 5, where we showed that angular sputtering distributions resulting from grazing angle ion bombardment have nearly all sputtered material emitted in the forward-scattered direction, with average energies greater than would be expected for normal incidence bombardment.

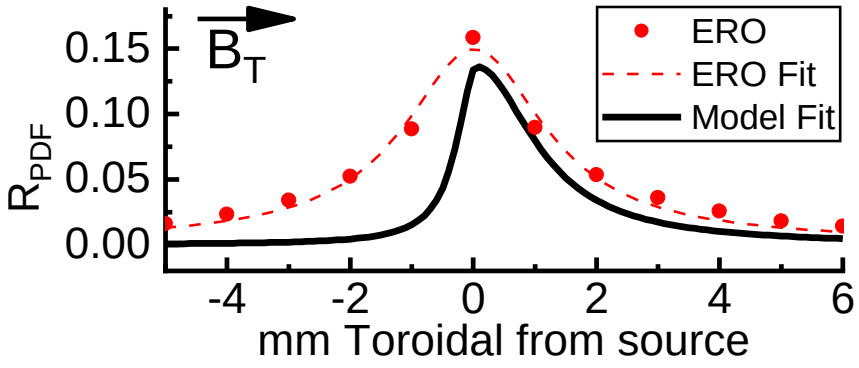

Figure 7-8. Comparison of ERO modeled redeposition function (points) with a and Lorentz peak fit to the ERO data (dashed line) and the point source redeposition distribution function fit to the measurement for case R-D.

7.4 Conclusions

We have measured erosion and deposition of Al in divertor plasma contact using post-mortem surface analysis techniques, and developed a time-dependent model that reproduces the spatial profiles of redeposition and net erosion rates for both smooth and rough surfaces. On rough surfaces, we have found an unusually high amount of Al deposited outside the original coating area that is inconsistent with the amount of redeposition inferred from the large/small area erosion measurements. We have determined this to be due to material accumulation in areas shadowed from incident ion flux. The type of material accumulation seen on rough surfaces in this study has implications for the predictions of material migration and material mixing for real fusion devices, particularly for those with grazing incidence magnetic field geometries. Even for initially smooth surfaces, with sufficient plasma fluence the surface is likely to develop some micro-scale surface roughness. The effect of flux shadowing is likely to result in a spatially inhomogeneous surface composition, with an enrichment of low sputtering yield material in high areas and accumulation of migrating material in low areas. The suppression of re-erosion of these trapped materials is expected to decrease the rate of multi-step material migration across the surface, but also increase mixing and retention of deposited material in the surface.

The redeposition distribution fits to the data suggest that between 30-76% of the eroded Al atoms return to the surface and are redeposited within 1cm of the original location, with longer redeposition lengths and lower probability of local redeposition occurring at lower plasma temperature. This implies that although lowering the plasma temperature may decrease the gross erosion rate for plasma facing components, the

material that is eroded will be transported farther, potentially increasing the rate of material migration. The amount of Al found redeposited outside the coating was in fact proportional to the amount eroded from the coating, suggesting an accumulation or trapping of redeposited Al in surface pores and other areas shadowed from re-erosion. The effect of deposit trapping in pores was included here by assuming a fraction of the redepositing flux of particles lands in shadowed surface areas and is counted in a separate 'trapped' inventory that does not become part of the eroding mixed material inventory. Re-erosion from this inventory is suppressed, so the traps are forced to be in net deposition and material accumulates. In our results, a 10% surface porosity fraction led to a trapping of half of the redepositing atomic flux. The results of the model fits reveal that the probability of local redeposition increases with higher plasma temperature (~30% for 15-18eV plasmas, and ~76% for 25-30eV plasmas). The observed probability of redeposition was more strongly skewed in the downstream toroidal direction, with much less redeposition in the upstream direction than otherwise predicted by the ERO modeling code. This discrepancy motivated the detailed sputtering and ionization analysis of Chapter 5, and suggests that the anisotropic sputtering which is not included in the ERO code can influence the direction and amount of local redeposition.

These results show that material migration models should include corrections for sputtering angle distributions, especially for Be which has a strong angular dependence on sputtering yield and energy. Estimates of fuel retention should consider codeposit accumulation by trapping in gaps, cracks, and surface porosity, which is can be more difficult to recover fuel from than thin layer codeposit coatings. Full vessel material migration patterns may also be affected by both of these factors.

Future improvements are planned to extend the model to allow simultaneous two-dimensional calculations (currently only 1-D radial or toroidal profiles are modeled), include more realistic depth dependent surface mixing effects, and allow for spatially or temporally varying redeposition functions. Two-dimensional redeposition distribution (Simultaneous R,X migration) may help resolve disagreement between model and data near the sample edges and offer insight into redeposition in the ExB direction. At this point our model includes only a single layer thickness which is prescribed based on the average implantation depth of the incident carbon ions. A more rigorous model could use a multi-layer approach to simulate the actual concentration gradient that would occur with a range of implantation depths. Further experimentation is needed to study the role of different roughness scale lengths compared to plasma scale lengths (sheath lengths and ion gyro radii). Large gaps and cracks may behave differently than small scale surface roughness.

7.5 Acknowledgements

This material is based upon work supported by the U.S. Department of Energy, Office of Science, Office of Fusion Energy Sciences, using the DIII-D National Fusion Facility, a DOE Office of Science user facility under awards DE-FC02-04ER54698, DE-SC0001961, DE-AC04-94AL85000, DE-AC52-07NA27344, and DE-FG02-94ER52435. Sandia National Laboratories is a multi-mission laboratory managed and operated by National Technology and Engineering Solutions of Sandia LLC, a wholly owned subsidiary of Honeywell International Inc. for the U.S. Department of Energy's National Nuclear Security Administration under contract DE-NA0003525. Special thanks go to Bill Wampler for his development of the initial model, Dean Buchenauer and Bernice Mills for sample

preparation and surface analysis, Graham Wright for the detailed RBS measurements, and the DIII-D operations team for their support.

This chapter includes text and data that is a reprint of the material as it appears in C. Chrobak, R. P. Doerner, P. C. Stangeby, W. R. Wampler, D. L. Rudakov, G. M. Wright, T. Abrams, R. Ding, J. D. Elder, J. Guterl, H. Y. Guo, C. Lasnier, D. M. Thomas, A. W. Leonard, D. A. Buchenauer, A. G. McLean, J. G. Watkins, and G. R. Tynan. "Characterizing Low-Z Erosion and Deposition in the DIII-D Divertor Using Aluminum." Nuclear Materials and Energy, vol. 12, 2017, Pages 441–446. The dissertation author was the primary investigator and author of this paper.

Chapter 8
Conclusions and Vision for Future Work

The design of first wall and divertor plasma facing components (PFCs) represents one of the greatest challenges facing the successful operation of a tokamak fusion power reactor. Material erosion by impact of energetic ions and neutrals can limit the lifetime of the eroding PFC, contribute to cooling of the plasma core, lead to fuel dilution and can trigger disruptions. Higher density plasmas, such as those expected in the divertor region, can promote local redeposition of the wall material thereby reducing the net erosion rate. However, long range migration from the first wall and other low-density plasma regions to the divertor can lead to uncontrolled deposition and failure due to formation of thick layers of mixed composition and poor thermal shock resistance. In addition, accumulation of radioactive tritium in these layers poses both a safety risk and a tritium fuel cycle problem. Subsequent multi-step cycle of balanced erosion and redeposition can also lead to changes in the surface morphology and composition that can alter the PFC performance. Managing the balance of between erosion and deposition in the divertor will require an understanding of redeposition on different scale lengths, from local redeposition (on the scale of ionization length of the sputtered atom) to long range plasma transport such as material migration from the first wall to the divertor.

We proceeded to conduct experiments of local erosion/redeposition of Al in attached L-mode divertor plasmas, in order to characterize the balance of erosion and deposition for a Be-like material. Gross Al erosion rates were measured directly and through spectroscopic methods, and enabled the quantification of emission efficiencies.

Net erosion of Al proved to be difficult to measure directly, since multi-step erosion quickly removed Al from the small localized samples. We developed a simple model of material migration that used multiple erosion/redeposition steps to simulate the coverage evolution using a spatially defined redeposition probability distribution. A larger sample with migration measurement along multiple tiles around the divertor would be needed to verify the rate of migration experimentally, although the effort required to dedicate tile removal and end of an operational campaign is often prohibitively expensive. Future work is still needed to address this, especially in H-mode and more ITER-relevant plasma configurations.

We found a spatial asymmetry in the emission plume that was not previously measured for sputtered neutral atoms localized in the divertor plasma. Our modeling reproduced the asymmetry using an angular sputtering anisotropy that may be caused by grazing incidence angle ions produced by acceleration through the magnetic pre-sheath. Existing models have typically written off such anisotropy as insignificant due to the surface-ion angle randomization by surface roughness. However, these models consistently under-estimated the extent of the upstream/downstream redeposition asymmetry observed. The redeposition asymmetry in our measurements was congruent with the scale and direction of the measured sputtered emission asymmetry. Some of the redeposition asymmetry may be due to ion-neutral collisions and ion-ion collisions along the sputtered particle's path back to the surface. Our initial calculations suggest that these collisions are insignificant compared to initial sputtered directions and sheath ExB drifts, but future work expanding the scope of our model to include these collisions and track the ionized Al back to the surface would be needed to confirm this.

Our calculations of the ion incident angle distribution find that the majority of ions are predicted to strike the horizontal DiMES surface at <15 degrees with respect to the surface plane, in a direction 30-60 degrees away from the toroidal field (when projected on the horizontal surface plane). Modeling also shows that the relatively thick region of the MPS creates a region of strong E×B drift flow which can drive cross-field migration of incident fuel ions and sputtered and ionized material. As the ions travel through the MPS, a strong ExB drift velocity approaching the ion sound speed creates a significant near surface poloidal flow approaching the ion sound speed and will likely drive migration of the re-ionized sputtered atoms. Incident ions drift 1-3cm radially in the E×B direction over a 2mm distance normal to the surface.

Our measurements show that surface roughness in the presence of oblique ion bombardment results in increased single-step redeposition rates due to distributed microscopic areas shadowed from incident sputtering ions. This observation should not be overlooked as a potential diagnostic capability. The use of microscopic deposition distribution measurements like imaging AES on rough surfaces can be used to infer more about the angular distributions of incident ions and redepositing particles. In future long pulse and high duty cycle tokamaks this could lead to the formation of inhomogeneous surface compositions with pockets of heavy deposits that may not be well accounted for in existing material migration models. The effects of such mixed material deposits on the co-deposited tritium retention and release rates should be investigated. Furthermore, since Al has known chemical oxide and hydride similarities with Be, more work should be done to measure the hydrogen retention behavior of Al compared to Be.

More work needs to be done to investigate the extent of sputtering anisotropy for other elements and its sensitivity to different practical surface roughness parameters and

scale lengths. It may be possible that future divertor designs can reduce erosion by increasing the incidence angle further so that ions reflect from rather than sputter material from surfaces. However, the engineering constraints required on achieving component alignment increase with increasing incidence angle. For practical erosion models, the effects of gaps between components on the sheath, incidence angle and sputtered material distributions should be included. It is the author's opinion that by designing surfaces with tailored micro-textured facets, it may be possible to exploit the sputtering anisotropy to direct the sputtered material into the desired material migration direction. Such a design may be a step towards designing a self-protecting surface where a thin layer of material is continually eroded and re-deposited locally so that net erosion is balanced out to zero. An alternate possibility would be to use the directional sputtering to drive the re-erosion of first wall material towards a dedicated catcher system that can be emptied, cleaned, or replaced.

We identified useful and bright Al-I and Al-II emission lines distinct from background C, O, D, and He lines and quantified their S/XB values. Imaging of the Al-I and Al-II emission plumes was possible with narrow bandpass filtered cameras, and provided insight into the direction of material sputtering and ion transport. While Al may not be a practical plasma facing material, its high erosion rate and easily measurable emission spectrum make it a good candidate for use as a material for quantitative emission spectroscopy in tokamaks. Furthermore, its medium range ionization length (~1-3mm) makes it useful for testing theories of the pre-sheath structure, since the transport of Al-II ions should be sensitive to changes in the pre-sheath structure during ELMs or upon approaching detachment. Sputtered Al may be a useful probe material to study the sheath flows and low-Z erosion/deposition balance in other divertor configurations with

expanded magnetic field flux, near grazing incidence angles, and higher neutral densities achieved with detachment.

References

[1] Kikuchi M, Lackner K and Quang M 2012 Fusion Physics *Iaea* 24–6

[2] Lawson J D 1957 Some Criteria for a Power Producing Thermonuclear Reactor *Proc. Phys. Soc. Sect. B* **70** 6–10

[3] EUROfusion 2005 Tokamak Principle

[4] Federici G, Skinner C ., Brooks J ., Coad J ., Grisolia C, Haasz A ., Hassanein A, Philipps V, Pitcher C ., Roth J, Wampler W . and Whyte D . 2001 Plasma-material interactions in current tokamaks and their implications for next step fusion reactors *Nucl. Fusion* **41** 1967–2137

[5] Organization I The ITER Tokamak

[6] Atomics G The DIII-D Tokamak

[7] Lasnier C J, Makowski M A, Boedo J A, Allen S L, Brooks N H, Hill D N, Leonard A W, Watkins J G and West W P 2011 Scaling of divertor heat flux profile widths in DIII-D *J. Nucl. Mater.* **415** S353–6

[8] Petrie T W, Maingi R, Allen S L, Buchenauer D A, Hill D N and Lasnier C J 1997 Partially detached radiative divertor with active divertor pumping *Nucl. Fusion* **37** 643–55

[9] Kotschenreuther M, Valanju P, Covele B and Mahajan S 2013 Magnetic geometry and physics of advanced divertors: The X-divertor and the snowflake *Phys. Plasmas* **20**

[10] Wesson J 2011 *Tokamaks* (New York, NY: Oxford University Press)

[11] Roth J, Tsitrone E, Loarte A, Loarer T, Counsell G, Neu R, Philipps V, Brezinsek S, Lehnen M, Coad P, Grisolia C, Schmid K, Krieger K, Kallenbach A, Lipschultz B, Doerner R, Causey R, Alimov V, Shu W, Ogorodnikova O, Kirschner A, Federici G and Kukushkin A 2009 Recent analysis of key plasma wall interactions issues for ITER *J. Nucl. Mater.* **390–391** 1–9

[12] Zinkle S J and Busby J T 2009 Structural materials for fission & fusion energy *Mater. Today* **12** 12–9

[13] Hatano Y, Shimada M, Otsuka T, Oya Y, Alimov V K, Hara M, Shi J, Kobayashi M, Oda T, Cao G, Okuno K, Tanaka T, Sugiyama K, Roth J, Tyburska-Püschel B, Dorner J, Yoshida N, Futagami N, Watanabe H, Hatakeyama M, Kurishita H, Sokolov M and Katoh Y 2013 Deuterium trapping at defects created with neutron and ion irradiations in tungsten *Nucl. Fusion* **53**

[14] Stangeby P C 2011 Assessing material migration through 13C injection experiments

J. Nucl. Mater. **415** S278–83

[15] Stangeby P C, Rudakov D L, Wampler W R, Brooks J N, Brooks N H, Buchenauer D a., Elder J D, Hassanein A, Leonard A W, McLean A G, Okamoto A, Sizyuk T, Watkins J G and Wong C P C 2013 An experimental comparison of gross and net erosion of Mo in the DIII-D divertor *J. Nucl. Mater.* **438** S309–12

[16] Kreter A, Brezinsek S, Coad J P, Esser H G, Fundamenski W, Philipps V, Pitts R A, Rohde V, Tanabe T and Widdowson A 2009 Dynamics of erosion and deposition in tokamaks *J. Nucl. Mater.* **390–391** 38–43

[17] Pégourié B, Brosset C, Tsitrone E, Beauté A, Brémond S, Bucalossi J, Carpentier S, Corre Y, Delchambre E, Desgranges C, Devynck P, Douai D, Dunand G, Ekedahl A, Escarguel A, Gauthier E, Gunn J P, Hertout P, Hong S H, Kazarian F, Kočan M, Linez F, Marandet Y, Martinez A, Mayer M, Meyer O, Monier-Garbet P, Moreau P, Oddon P, Pascal J Y, Rimini F, Roth J, Saint-Laurent F, Samaille F, Vartanian S, Arnas C, Aréou E, Gil C, Lasalle J, Manenc L, Martin C, Richou M, Roubin P and Sabot R 2009 Overview of the deuterium inventory campaign in Tore Supra: Operational conditions and particle balance *J. Nucl. Mater.* **390–391** 550–5

[18] Widdowson A, Coad J P, Temmerman G De, Farcage D, Hole D, Ivanova D, Leontyev A, Rubel M, Semerok A, Schmidt A and Thro P Y 2011 Removal of beryllium-containing films deposited in JET from mirror surfaces by laser cleaning *J. Nucl. Mater.* **415** S1199–202

[19] Strachan J D, Corrigan G, Kallenbach A, Matthews G F, Meister H, Neu R, Rohde V and Spence J 2004 Diverted tokamak carbon screening: scaling with machine size and consequences for core contamination *Nucl. Fusion* **44** 772

[20] Brezinsek S, Widdowson A, Mayer M, Philipps V, Coenen J W W, Heinola K, Huber A, Likonen J, Petersson P, Rubel M, Stamp M F F, Borodin D, Coad J P P, Carrasco A G G, Kirschner A, Krat S, Krieger K, Lipschultz B, Linsmeier C, Matthews G F F, Schmid K, Baron-Wiechec P, Coenen J W W, Heinola K, Huber A, Likonen J, Petersson P, Rubel M, Stamp M F F, Borodin D, Coad J P P, Carrasco A G G, Kirschner A, Krat S, Krieger K, Lipschultz B, Linsmeier C, Matthews G F F and Schmid K 2015 Beryllium migration in JET ITER-like wall plasmas *Nucl. Fusion* **55** 63021

[21] Krat S, Mayer M, von Toussaint U, Coad P, Widdowson A, Gasparyan Y and Pisarev A 2016 Beryllium film deposition in cavity samples in remote areas of the JET divertor during the 2011-2012 ITER-like wall campaign *Nucl. Mater. Energy* **0** 1–5

[22] Zhou Y, Bergsåker H, Bykov I, Petersson P, Possnert G, Likonen J, Pettersson J, Koivuranta S and Widdowson A M 2017 Microanalysis of deposited layers in the inner divertor of JET with ITER-like wall *Nucl. Mater. Energy* **12** 412–7

[23] Lagoyannis A, Tsavalas P, Mergia K, Provatas G, Triantou K, Tsompopoulou E, Rubel M, Petersson P, Widdowson A, Harissopulos S, Mertzimekis T and JET contributors 2017 Surface composition and structure of divertor tiles following the JET tokamak operation with the ITER-like wall *Nucl. Fusion* **57** 76027

[24] Catarino N, Barradas N P, Corregidor V, Widdowson A, Baron-Wiechec A, Coad J P, Heinola K, Rubel M and Alves E 2016 Assessment of erosion, deposition and fuel retention in the JET-ILW divertor from ion beam analysis data *Nucl. Mater. Energy* **0** 1–5

[25] Causey R A 2002 Hydrogen isotope retention and recycling in fusion reactor plasma-facing components *J. Nucl. Mater.* **300** 91–117

[26] Abdou M A, Vold E L, Gung C Y, Youssef M Z and Shin K 1986 Deuterium-Tritium Fuel Self-Sufficiency in Fusion Reactors *Fusion Technol.* **9** 250–85

[27] Sawan M E and Abdou M A 2006 Physics and technology conditions for attaining tritium self-sufficiency for the DT fuel cycle *Fusion Eng. Des.* **81** 1131–44

[28] Wampler W R, Pitts R A, Carpentier-Chouchana S, Stangeby P C, Ding F, Mao H M, Wang W Z, Qian J P, Gong X and Luo G-N 2014 Experimental Advanced Superconducting Tokamak/material and plasma evaluation system material migration experiment *Phys. Scr.* **T159** 14069

[29] Ding R, Pitts R A, Borodin D, Carpentier S, Ding F, Gong X Z, Guo H Y, Kirschner A, Kocan M, Li J G, Luo G-N, Mao H M, Qian J P, Stangeby P C, Wampler W R, Wang H Q and Wang W Z 2015 Material migration studies with an ITER first wall panel proxy on EAST *Nucl. Fusion* **55** 23013

[30] Borodin D, Kirschner A, Carpentier-Chouchana S, Pitts R A, Lisgo S, Björkas C, Stangeby P C, Elder J D, Galonska A, Matveev D, Philipps V and Samm U 2011 ERO code benchmarking of ITER first wall beryllium erosion/re-deposition against LIM predictions *Phys. Scr.* **T145** 14008

[31] Borodin D, Brezinsek S, Miettunen J, Stamp M, Kirschner A, Björkas C, Groth M, Marsen S, Silva C, Lisgo S W, Matveev D, Airila M and Philipps V 2014 Determination of Be sputtering yields from spectroscopic observations at the JET ITER-like wall based on three-dimensional ERO modelling *Phys. Scr.* **T159** 14057

[32] Carpentier S, Pitts R A, Stangeby P C, Elder J D, Kukushkin A S, Lisgo S, Fundamenski W and Moulton D 2011 Modelling of beryllium erosion–redeposition on ITER first wall panels *J. Nucl. Mater.* **415** S165–9

[33] Allen S L, Wampler W R, McLean A G, Whyte D G, West W P, Stangeby P C, Brooks N H, Rudakov D L, Phillips V, Rubel M, Matthews G F, Nagy a., Ellis R and Bozek a. S 2005 13C transport studies in L-mode divertor plasmas on DIII-D *J. Nucl. Mater.* **337–339** 30–4

[34] Wampler W R, McLean a. G, Allen S L, Brooks N H, Elder J D, Fenstermacher M E, Groth M, Stangeby P C, West W P and Whyte D G 2007 Transport and deposition of 13C from methane injection into partially detached H-mode plasmas in DIII-D *J. Nucl. Mater.* **363–365** 72–7

[35] Kirschner a., Philipps V, Coster D P, Erents S K, Esser H G, Federici G, Kukushkin a. S,

Loarte a., Matthews G F, Roth J and Samm U 2005 Experimental observations and modelling of carbon transport in the inner divertor of JET *J. Nucl. Mater.* **337–339** 17–24

[36] Pitts R A, Carpentier S, Escourbiac F, Hirai T, Komarov V, Kukushkin A S, Lisgo S, Loarte A, Merola M, Mitteau R, Raffray A R, Shimada M and Stangeby P C 2011 Physics basis and design of the ITER plasma-facing components *J. Nucl. Mater.* **415** S957–64

[37] Schmid K, Reinelt M and Krieger K 2011 An integrated model of impurity migration and wall composition dynamics for tokamaks *J. Nucl. Mater.* **415** S284–8

[38] Schmid K, Krieger K, Lisgo S W, Meisl G and Brezinsek S 2015 Quantitative modeling of fuel retention in the JET-C and JET-ILW wall configurations by WallDYN and predictions for ITER *J. Nucl. Mater.* **463** 66–72

[39] Widdowson A, Alves E, Baron-Wiechec A, Barradas N P, Catarino N, Coad J P, Corregidor V, Garcia-Carrasco A, Heinola K, Koivuranta S, Krat S, Lahtinen A, Likonen J, Mayer M, Petersson P, Rubel M and Van Boxel S 2016 Overview of the JET ITER-like wall divertor *Nucl. Mater. Energy* **0** 1–7

[40] Wong C P C, Junge R, Phelps R D, Politzer P, Puhn F, West W P, Atomics G, Box P O, Diego S, Brooks J and Hua T 1992 Divertor materials evaluation system at DIII-D *J. Nucl. Mater.* **196–198** 871–5

[41] Marot L, Linsmeier C, Eren B, Moser L, Steiner R and Meyer E 2013 Can aluminium or magnesium be a surrogate for beryllium: A critical investigation of their chemistry *Fusion Eng. Des.* **88** 1718–21

[42] Stangeby P C 2000 *The Plasma Boundary of Magnetic Fusion Devices* (IOP Publishing Ltd)

[43] Chodura R 1982 Plasma–wall transition in an oblique magnetic field *Phys. Fluids* **25** 1628

[44] Riemann K -U 1994 Theory of the plasma–sheath transition in an oblique magnetic field *Contrib. to Plasma Phys.* **34** 127–32

[45] Stangeby P C 2012 The Chodura sheath for angles of a few degrees between the magnetic field and the surface of divertor targets and limiters *Nucl. Fusion* **52** 83012

[46] Coulette D and Manfredi G 2016 Kinetic simulations of the Chodura and Debye sheaths for magnetic fields with grazing incidence *Plasma Phys. Control. Fusion* **58** 25008

[47] Singha B, Sarma A and Chutia J 2002 Experimental observation of sheath and magnetic presheath over an oblique metallic plate in the presence of a magnetic field *Phys. Plasmas* **9** 683

[48] Kim G H, Hershkowitz N, Diebold D A and Cho M H 1995 Magnetic and collisional effects on presheaths *Phys. Plasmas* **2** 3222–33

[49] Siddiqui M U, Thompson D S, Jackson C D, Kim J F, Hershkowitz N and Scime E E 2016 Models, assumptions, and experimental tests of flows near boundaries in magnetized plasmas *Phys. Plasmas* **23** 57101

[50] Siddiqui M U, Jackson C D, Kim J F and Hershkowitz N 2014 Direct measurements of ion dynamics in collisional magnetic presheaths *Phys. Plasmas* **21**

[51] Riemann K U 1997 The influence of collisions on the plasma sheath transition *Phys. Plasmas* **4** 4158–66

[52] Ahedo E 1997 Structure of the plasma-wall interaction in an oblique magnetic field *Phys. Plasmas* **4** 4419–30

[53] R.E. H. Clark D H R 2005 *Nuclear Fusion Research* vol 78, ed R E H Clark and D H Reiter (Berlin/Heidelberg: Springer-Verlag)

[54] KENMOTSU T, YAMAMURA Y, ONO T and KAWAMURA T 2004 A New Formula for Energy Spectrum of Sputtered Atoms Due to Low-Energy Light Ions *J. Plasma Fusion Res.* **80** 406–9

[55] Bohdansky J 1984 A universal relation for the sputtering yield of monatomic solids at normal ion incidence *Nucl. Inst. Methods Phys. Res. B* **2** 587–91

[56] García-Rosales C, Eckstein W and Roth J 1995 Revised formulae for sputtering data *J. Nucl. Mater.* **218** 8–17

[57] Wilson W D, Haggmark L G and Biersack J P 1977 Calculations of nuclear stopping, ranges, and straggling in the low-energy region *Phys. Rev. B* **15** 2458–68

[58] Yamamura Y, Itikawa Y and Itoh N 1983 *Angular dependence of sputtering yields of monatomic solids* (Nagoya, Japan: Institute of Plasma Physics, Nagoya University)

[59] Roth J, Bohdansky J and Eckstein W 1983 Angular distributions and differential sputtering yields of binary compounds as a function of angle of incidence *Nucl. Instruments Methods Phys. Res.* **218** 751–6

[60] Eckstein W 2007 Sputtering Yields **187** 33–187

[61] Mutzke A, Schneider R, Eckstein W and Dohmen R 2011 *SDTrimSP Version 5.00 IPP Report 12/8* (Garching)

[62] Langley R A, Bohdansky J, Eckstein W, Mioduszewdki P, Roth J, Taglauer E, Thomas E W, Verbeek H and Wilson K L 1984 Sputtering *Nucl. Fusion Spec. Suppl.* **24** 61

[63] Falcone G 1987 Theory of collisional sputtering *Surf. Sci.* **187** 212–22

[64] Goehlich A, Gillmann D and Döbele H F 2001 An experimental investigation of angular resolved energy distributions of atoms sputtered from evaporated aluminum films *Nucl. Instruments Methods Phys. Res. Sect. B Beam Interact. with Mater. Atoms* **179** 351–63

[65] Goehlich A, Gillmann D and Döbele H F 2000 Angular resolved energy distributions of sputtered atoms at low bombarding energy *Nucl. Instruments Methods Phys. Res. Sect. B Beam Interact. with Mater. Atoms* **164** 834–9

[66] Mutzke A, Bandelow G and Schmid K 2015 News in SDTrimSP Version 5 . 05 1–46

[67] Horn A, Schenk A, Biener J, Winter B, Lutterloh C, Wittmann M and Küppers J 1994 H atom impact induced chemical erosion reaction at C:H film surfaces *Chem. Phys. Lett.* **231** 193–8

[68] Roth J and García-Rosales C 1996 Analytic description of the chemical erosion of graphite by hydrogen ions *Nucl. Fusion* **36** 1647–59

[69] Hopf C and Jacob W 2005 Bombardment of graphite with hydrogen isotopes: A model for the energy dependence of the chemical sputtering yield *J. Nucl. Mater.* **342** 141–7

[70] Haasz A A and Davis J W 1990 Comparison of the chemical erosion of carbon/carbon composites and pyrolytic graphite *J. Nucl. Mater.* **175** 84–9

[71] Nordlund K, Björkas C, Vörtler K, Meinander A, Lasa A, Mehine M and Krasheninnikov A V. 2011 Mechanism of swift chemical sputtering: Comparison of Be/C/W dimer bond breaking *Nucl. Instruments Methods Phys. Res. Sect. B Beam Interact. with Mater. Atoms* **269** 1257–61

[72] Salonen E, Nordlund K, Keinonen J and Wu C H 2001 Swift chemical sputtering of amorphous hydrogenated carbon *Phys. Rev. B - Condens. Matter Mater. Phys.* **63** 1–14

[73] Björkas C, Borodin D, Kirschner A, Janev R K, Nishijima D, Doerner R and Nordlund K 2013 Molecules can be sputtered also from pure metals: sputtering of beryllium hydride by fusion plasma–wall interactions *Plasma Phys. Control. Fusion* **55** 74004

[74] Davis J W and Haasz a. a. 2001 Overview of Thermo-oxidation of Tokamak Codeposits *Phys. Scr.* **T91** 33

[75] Landman I S and Würz H 2003 Effect of hydrogen retention on tungsten erosion by oxygen *Fusion Eng. Des.* **66–68** 231–6

[76] Brezinsek S, Stamp M F, Nishijima D, Borodin D, Devaux S, Krieger K, Marsen S, O'Mullane M, Bjoerkas C and Kirschner A 2014 Study of physical and chemical assisted physical sputtering of beryllium in the JET ITER-like wall *Nucl. Fusion* **54** 103001

[77] Eckstein W, Bohdansky J and Roth J 1991 Physical Sputtering *Atomic and Plasma-Material Interaction Data for Fusion (Suppl. to Nucl. Fusion)* vol 1(Vienna: IAEA)p 51

[78] Haasz A A, Davis J W and Wu C H 1989 Angle of incidence dependence of light ion physical sputtering of carbon *J. Nucl. Mater.* **162–164** 915–9

[79] Wu C H 1988 The angular dependence of physical sputtering of graphite by light ions in the low-energy regime *J. Nucl. Mater.* **160** 103–6

[80] Ruzic D N 1990 The effects of surface roughness characterized by fractal geometry on sputtering *Nucl. Instruments Methods Phys. Res. Sect. B Beam Interact. with Mater. Atoms* **47** 118–25

[81] Kreter A, Brezinsek S, Hirai T, Kirschner A, Krieger K, Mayer M, Philipps V, Pospieszczyk A, Samm U, Schmitz O, Schweer B, Sergienko G, Sugiyama K, Tanabe T, Ueda Y and Wienhold P 2008 Effect of surface roughness and substrate material on carbon erosion and deposition in the TEXTOR tokamak *Plasma Phys. Control. Fusion* **50** 95008

[82] Sigmund P 1973 A mechanism of surface micro-roughening by ion bombardment *J. Mater. Sci.* **8** 1545–53

[83] Carter G 2001 The physics and applications of ion beam erosion *J. Phys. D. Appl. Phys.* **34** R1–22

[84] Frost F, Fechner R, Ziberi B, Völlner J, Flamm D and Schindler A 2009 Large area smoothing of surfaces by ion bombardment: fundamentals and applications *J. Phys. Condens. Matter* **21** 224026

[85] Holzwarth M, Wissing M, Simeonova D S, Tzanev S, Snowdon K J and Yordanov O I 1995 Preparation of atomically smooth surfaces via sputtering under glancing incidence conditions *Surf. Sci.* **331–333** 1093–8

[86] Wißing M, Batzill M and Snowdon K J 1997 Preparation by glancing incidence ion irradiation of CaF2 surfaces with angstrom-scale RMS roughness *Nanotechnology* **8** 40–5

[87] Kimura K, Fukui A, Nakajima K and Mannami M 1999 Preparation of smooth Si(001) surfaces by glancing angle sputtering *Nucl. Instruments Methods Phys. Res. Sect. B Beam Interact. with Mater. Atoms* **148** 149–53

[88] Hirata A, Tokura H and Yoshikawa M 1992 Smoothing of chemically vapour deposited diamond films by ion beam irradiation *Thin Solid Films* **212** 43–8

[89] Carter G and Vishnyakov V 1996 Roughening and ripple instabilities on ion-bombarded Si *Phys. Rev. B* **54** 17647–53

[90] Baldwin M J and Doerner R P 2008 Helium induced nanoscopic morphology on tungsten under fusion relevant plasma conditions *Nucl. Fusion* **48** 35001

[91] Doerner R P, Baldwin M J and Nishijima D 2014 Plasma-induced morphology of beryllium targets exposed in PISCES-B *J. Nucl. Mater.* **455** 1–4

[92] Schmid K, Mayer M, Adelhelm C, Balden M and Lindig S 2010 Impact of gyro-motion and sheath acceleration on the flux distribution on rough surfaces *Nucl. Fusion* **50** 105004

[93] Tavernier S 2010 *Experimental Techniques in Nuclear and Particle Physics* (Berlin, Heidelberg: Springer Berlin Heidelberg)

[94] Brooks J . and Whyte D . 1999 Modelling and analysis of DIII-D/DiMES sputtered impurity transport experiments *Nucl. Fusion* **39** 525–38

[95] Wampler W R, Bastasz R, Buchenauer D, Whyte D, Wong C P C, Brooks N H and West W P 1996 Erosion and deposition of metals and carbon in the DIII-D divertor *J. Nucl. Mater.* **233–237** 791–7

[96] Whyte D G, Brooks J N, Wong C P C, West W P, Bastasz R, Wampler W R and Rubenstein J 1997 DiMES divertor erosion experiments on DIII-D *J. Nucl. Mater.* **241–243** 660–5

[97] Brooks J N, Hassanein a. and Sizyuk T 2013 Advanced simulation of mixed-material erosion/evolution and application to low and high-Z containing plasma facing components *J. Nucl. Mater.* **438** S673–6

[98] Chankin A V., Coster D P and Dux R 2014 Monte Carlo simulations of tungsten redeposition at the divertor target *Plasma Phys. Control. Fusion* **56** 25003

[99] Luxon J L 2002 A design retrospective of the DIII-D tokamak *Nucl. Fusion* **42** 313

[100] Ferron J R, Penaflor B, Walker M L, Moller J and Butner D 1995 Flexible software architecture for tokamak discharge control systems *Proc. - Symp. Fusion Eng.* **2** 870–3

[101] Burrell K H 1978 Fast hydrogen gas injection system for plasma physics experiments *Rev. Sci. Instrum.* **49** 948–54

[102] Holtrop K L, Jackson G L, Kellman A G, Lee R L and Hollerbach M A 1994 Operation of DIII-D with all-graphite walls *J. Vac. Sci. Technol. A Vacuum, Surfaces, Film.* **12** 1269–74

[103] Watkins J G, Taussig D, Boivin R L, Mahdavi M A and Nygren R E 2008 High heat flux Langmuir probe array for the DIII-D divertor plates *Rev. Sci. Instrum.* **79** 1–5

[104] Carlstrom T N, Campbell G L, DeBoo J C, Evanko R, Evans J, Greenfield C M, Haskovec J, Hsieh C L, McKee E, Snider R T, Stockdale R, Trost P K and Thomas M P 1992 Design and operation of the multipulse Thomson scattering diagnostic on DIII-D (invited) *Rev. Sci. Instrum.* **63** 4901–6

[105] Brooks N H, Howald A, Klepper K and West P 1992 Multichord spectroscopy of the DIII-D divertor region *Rev. Sci. Instrum.* **63** 5167–9

[106] Chrobak C, Stangeby P C, Leonard A W, Rudakov D L, Wong C P C, McLean A G, Wright G M, Buchenauer D A, Watkins J G, Wampler W R, Elder J D, Doerner R P, Nishijima D and Tynan G R 2015 Measurements of gross erosion of Al in the DIII-D divertor *J. Nucl. Mater.* **463** 810–3

[107] Rudakov D L, Stangeby P C, Wampler W R, Brooks J N, Brooks N H, Elder J D, Hassanein A, Leonard A W, McLean A G, Moyer R A, Sizyuk T, Watkins J G and Wong C P C 2014 Net versus gross erosion of high- Z materials in the divertor of DIII-D *Phys. Scr.* **T159** 14030

[108] Wampler W R, Stangeby P C, Watkins J G, Buchenauer D a., Rudakov D L and Wong C P C 2013 Measurements of net erosion and redeposition of molybdenum in DIII-D *J. Nucl. Mater.* **438** S822–6

[109] Mayer M 1997 *SIMNRA User's Guide, Report IPP 9/113* (Garching, Germany)

[110] Wang Y and Nastasi M 2010 *Handbook of Modern Ion Beam Materials Analysis* (Materials Research Society)

[111] Mayer M 2002 Ion beam analysis of rough thin films *Nucl. Instruments Methods Phys. Res. Sect. B Beam Interact. with Mater. Atoms* **194** 177–86

[112] Stangeby P C, Elder J D, Boedo J A, Bray B, Brooks N H, Fenstermacher M E, Groth M, Isler R C, Lao L L, Lisgo S, Porter G D, Reiter D, Rudakov D L, Watkins J G, West W P and Whyte D G 2003 Interpretive modeling of simple-as-possible-plasma discharges on DIII-D using the OEDGE code *J. Nucl. Mater.* **316** 883–7

[113] Ding R, Rudakov D L, Stangeby P C, Wampler W R, Abrams T, Brezinsek S, Briesemeister A, Bykov I, Chan V S, Chrobak C P, Elder J D, Guo H Y, Guterl J, Kirschner A, Lasnier C J, Leonard A W, Makowski M A, McLean A G, Snyder P B, Thomas D M, Tskhakaya D, Unterberg E A, Wang H Q and Watkins J G 2017 Advances in understanding of high- Z material erosion and re-deposition in low- Z wall environment in DIII-D *Nucl. Fusion* **57** 56016

[114] Abrams T, Ding R, Guo H Y, Thomas D M, Chrobak C P, Rudakov D L, McLean A G, Unterberg E A, Briesemeister A R, Stangeby P C, Elder J D, Wampler W R and Watkins J G 2017 The inter-ELM tungsten erosion profile in DIII-D H-mode discharges and benchmarking with ERO+OEDGE modeling *Nucl. Fusion* **57** 56034

[115] Chrobak C P, Doerner R P, Stangeby P C, Wampler W R, Rudakov D L, Wright G M, Abrams T, Ding R, Elder J D, Guterl J, Guo H Y, Lasnier C, Thomas D M, Leonard A W, Buchenauer D A, McLean A G, Watkins J G and Tynan G R 2017 Characterizing Low-Z erosion and deposition in the DIII-D divertor using aluminum *Nucl. Mater. Energy* **12** 441–6

[116] Chrystal C, Burrell K H, Grierson B A, Haskey S R, Groebner R J, Kaplan D H and

Briesemeister A 2016 Improved edge charge exchange recombination spectroscopy in DIII-D *Rev. Sci. Instrum.* **87** 1–4

[117] Ding R, Stangeby P C, Rudakov D L, Elder J D, Tskhakaya D, Wampler W R, Kirschner A, McLean A G, Guo H Y, Chan V S and Snyder P B 2016 Simulation of gross and net erosion of high- *Z* materials in the DIII-D divertor *Nucl. Fusion* **56** 16021

[118] Lennon M ., Bell K L, Gilbody H B, Hughes J G, Kingston A E, Murray M J and Smith F J 1988 Recommended Data on the Electron Impact Ionization of Atoms and Ions: Fluorine to Nickel *J. Phys. Chem. Ref. Data* **17** 1358

[119] Summers H P 2007 *Atomic Data and Analysis Structure User Manual*

[120] Freund R S, Wetzel R C, Shul R J and Hayes T R 1990 Cross-section measurements for electron-impact ionization of atoms *Phys. Rev. A* **41** 7

[121] Kim Y-K and Stone P M 2001 Ionization of boron, aluminum, gallium, and indium by electron impact *Phys. Rev. A* **64** 52707

[122] Kim Y-K 2001 Scaling of plane-wave Born cross sections for electron-impact excitation of neutral atoms *Phys. Rev. A* **64** 32713

[123] Doerner R P, Björkas C, Nishijima D and Schwarz-Selinger T 2013 Erosion of beryllium under high-flux plasma impact *J. Nucl. Mater.* **438** S272–5

[124] Kirschner A, Wienhold P, Philipps V, Coad J P, Huber A and Samm U 2004 Modelling of carbon transport in fusion devices: Evidence of enhanced re-erosion of in-situ re-deposited carbon *J. Nucl. Mater.* **328** 62–6

[125] Doerner R P, Jepu I, Nishijima D, Safi E, Bukonte L, Lasa A, Nordlund K and Schwarz-Selinger T 2015 The relationship between gross and net erosion of beryllium at elevated temperature *J. Nucl. Mater.* **463** 777–80

[126] Khaziev R and Curreli D 2015 Ion energy-angle distribution functions at the plasma-material interface in oblique magnetic fields *Phys. Plasmas* **22** 43503

[127] Borodkina I, Borodin D, Kirschner A, Tsvetkov I V, Kurnaev V A, Komm M, Dejarnac R and JET Contributors 2016 An Analytical Expression for the Electric Field and Particle Tracing in Modelling of Be Erosion Experiments at the JET ITER-like Wall *Contrib. to Plasma Phys.* **56** 640–5

[128] Borodkina I E, Komm M and Tsvetkov I V. 2015 Application of Analytical Model of the Electric Potential Distribution for Calculation of Charged Particle Dynamics in a Near-Wall Layer and Sputtering of the Plasma Facing Surfaces *Russ. Phys. J.* **58** 438–45

[129] Wright G M, Brunner D, Baldwin M J, Doerner R P, Labombard B, Lipschultz B, Terry J L and Whyte D G 2012 Tungsten nano-tendril growth in the Alcator C-Mod divertor *Nucl. Fusion* **52** 42003

[130] Yamamura Y, Itikawa Y and Itoh N 1983 Angular dependence of sputtering yields of monoatomic solids Rep. IPPJ-AM-26

[131] Kreter A, Dittmar T, Nishijima D, Doerner R P, Baldwin M J and Schmid K 2014 Erosion, formation of deposited layers and fuel retention for beryllium under the influence of plasma impurities *Phys. Scr.* **T159**

[132] Doerner R P, Baldwin M J and Causey R A 2005 Beryllium-tungsten mixed-material interactions *J. Nucl. Mater.* **342** 63–7

[133] Yu J H, Doerner R P, Dittmar T, Höschen T, Schwarz-Selinger T and Baldwin M J 2014 ITER-relevant transient heat loads on tungsten exposed to plasma and beryllium *Phys. Scr.* **T159** 0–5

[134] Wampler W R 2015 The influence of carbon in the plasma on metal erosion and redeposition in the DIII-D divertor *Plasma Facing Materials and Components for Fusion Applications* (Aix en Provence, France: 15th international conference on plasma-facing materials and components for fusion applications)

[135] Kirschner A, Philipps V, Winter J and Kögler U 2000 Simulation of the plasma-wall interaction in a tokamak with the Monte Carlo code ERO-TEXTOR *Nucl. Fusion* **40** 989–1001

[136] Abramowitz M, Stegun I A and Miller D 1965 Handbook of Mathematical Functions With Formulas, Graphs and Mathematical Tables (National Bureau of Standards Applied Mathematics Series No. 55) *J. Appl. Mech.* **32** 239

Appendix

Ionization probability distribution function derivation

Ionization probability distribution functions for neutral atoms traversing uniform and varying background plasma density gradients in a straight line trajectory are derived here according to the methods described in [93]. For a uniform plasma with constant density $n_e(s) = n_0$ the ionization probability, **P,** is independent of neutral direction and dependent only on the path length, ***s***, of the sputtered neutral. The ICDF constrained with boundary condition P(0) = 0 is thus:

$$P_{uniform}(s) = 1 - \exp\left(-s\, n_0 \frac{\langle\sigma v\rangle}{v_a}\right) \tag{A1}$$

Where $\langle\sigma v\rangle$ is the average ionization rate coefficient at a given plasma temperature, and v_a is the average sputtered neutral atom speed. It can be shown that the most probable distance for a neutral atom to travel before ionizing (the ionization mean free path) in this case is

$$\langle\lambda_i\rangle = \frac{v_a}{n_e\langle\sigma v\rangle} \tag{A2}$$

If we define a functional form for the density variation with distance from the surface as derived by [127] to describe the magnetic pre-sheath, we can project the density onto the trajectory of a neutral emitted at an angle θ with respect to the surface normal as being:

$$n_e(s) = n_o \exp\left(\psi_W \exp\left(\frac{-2s}{L_{MPS}/\sin(\theta)}\right)\right) \tag{A3}$$

where L_{MPS} is the sheath scale length normal to the surface, θ is the angle between the surface plane and sputtered neutral vector, and ψ_W is the floating potential at the wall. The MPS gradients simulated here use a scale length of $L_{MPS} = 2\rho_i \sin(\alpha)$, where α is the angle between the surface plane and toroidal field vector.

Next, we find the differential probability *dW* for ionization in a length *ds*:

$$dW = n_o \frac{\langle \sigma v \rangle}{v} \exp\left(\psi_W \exp\left(-\frac{2s}{L_{MPS}/\sin(\theta)}\right)\right) ds \tag{A4}$$

The probability of ionizing within a distance ds after traveling a distance s is the ICDF function P, which satisfies the differential equation $dP(s) = [1 - P(s)]dW$. Solving for P involves an indefinite integral of the type $\int e^{e^{-x}} dx$. If we denote $u = e^x$, then $dx = u^{-1}du$, and so the integral becomes the so-called exponential integral $\int u^{-1}e^u du = Ei(u)$ [136]. The resulting ICDF for a MPS-type density gradient is found to thus be:

$$\mathrm{P_{MPS}(s)} = 1 - \exp\left(n_o \frac{\langle \sigma v \rangle}{v} \frac{L_{MPS}/\sin(\theta)}{2} \left(\mathrm{Ei}\left(\psi_W \exp\left(\frac{-2s}{L_{MPS}/\sin(\theta)}\right)\right) - \mathrm{Ei}(\psi_W)\right)\right) \tag{A5}$$

Ionization length distribution for other density gradient functions

For a neutral traveling at a velocity v along *s*, the probability of ionizing within a differential length ds is proportional to the product of the local electron density $n_e(s)$ and ionization rate coefficient $\langle \sigma v \rangle$:

$$dW = n_e(s) \frac{\langle \sigma v \rangle}{v} ds \tag{A6}$$

Let us define P(s) as the probability that a particle has ionized after traveling a distance s, and $Q(s) = [1 - P(s)]$ as the probability that it has not. Thus, the probability of ionizing within a distance *ds* after traveling a distance s satisfies the differential equation:

$$dP(s) = [1 - P(s)]dW \tag{A7}$$

In this equation, P(s) is the cumulative density function (CDF) for ionization along a path length s. This function can be used to sample an ionization length using numerical Monte-Carlo methods. For plasma with uniform density $n_e(s) = n_0$ the solution to (1) with boundary condition P(0) = 0 is

$$P(s) = 1 - \exp\left(-s\, n_0 \frac{\langle \sigma v \rangle}{v}\right) \tag{A8}$$

This function can be used to numerically sample an ionization length λ_i using Monte-Carlo methods by solving for s. Given a random number ξ from 0 to 1, the ionization length will be:

$$\lambda_i = -\frac{v}{n_0 \langle \sigma v \rangle} \ln(\xi) = -\lambda_i \ln(\xi) \tag{A9}$$

Often, it is useful to calculate the average distance to ionization, also known as the ionization mean free path. We can determine an analytical expression for the ionization mean free path $\langle \lambda_i \rangle$ by first finding the probability density function F(s):

$$F(s) = \frac{dP(s)}{ds} = [1 - P(s)] \frac{dW}{ds} \tag{A10}$$

The expectation value of this function is most probable distance before ionization, also known as the ionization mean free path $\langle \lambda_i \rangle$:

$$\langle \lambda_i \rangle = \int_0^\infty s\, F(s)\, ds \tag{A11}$$

For a uniform background electron density, it can be shown that the most probable distance for a neutral atom to travel before ionizing (the ionization mean free path) is

$$\langle \lambda_i \rangle = \frac{v}{n_e \langle \sigma v \rangle} \tag{A12}$$

Linear density gradient

Next, we will consider the simple case of a uniform density gradient, such that the electron density is defined as $n_e(z) = n_0 z/L_{MPS}$. The sheath scale length L_{MPS} normal to the surface is roughly equal to 5 ion gyro radii. Thus for a particle emitted from the surface at an angle θ with respect to the surface plane the density gradient projected on its path s is

$$n(s) = n_{e,0} s \sin(\theta)/L_{MPS} \tag{A13}$$

For clarity, we will define a projected sheath scale length $L = L_{MPS}/\sin(\theta)$. The probability of ionizing within a length ds increases with distance s according to:

$$dW = n_0 \frac{\langle \sigma v \rangle}{v} \frac{s}{L} ds \tag{A14}$$

Solving eq. (A7) in this case with boundary condition P(0) = 0, we find:

$$P(s) = 1 - \exp\left(-n_0 \frac{\langle \sigma v \rangle}{v} \frac{s^2}{2L}\right) \tag{A15}$$

We can sample an ionization length using Monte-Carlo methods by solving for s. Given a random number ξ between 0 and 1, the ionization length λ_i will be:

$$\lambda_i = \sqrt{\frac{-2L}{n_0 \frac{\langle \sigma v \rangle}{v}} \ln(\xi)} \tag{A16}$$

We can analytically find the ionization mean free path $\langle \lambda_i \rangle$ from the expectation value of the probability density function F(s):

$$F(s) = n_0 \frac{\langle \sigma v \rangle}{v} \frac{s}{L} \exp\left(-n_0 \frac{\langle \sigma v \rangle}{v} \frac{s^2}{2L}\right) \tag{A17}$$

$$\langle \lambda_i \rangle = \int_0^\infty s\, F(s)\, ds = \sqrt{\frac{\pi}{2}} \sqrt{\frac{L\, v}{n_0 \langle \sigma v \rangle}} \tag{A18}$$

Exponential Density Gradient:

We can apply a similar method to determine the ionization length of particles traveling through an exponential density gradient. In this case, the density gradient is normal to the surface, and for a particle emitted at an angle θ with respect to the surface, the effective electron density gradient along its path s is described as:

$$n_e(s) = n_o\left(1 - \exp\left(-\frac{s\sin(\theta)}{L_{MPS}}\right)\right) \tag{A19}$$

Again, we can define the projected sheath scale length $L = L_{MPS}/\sin(\theta)$. The differential probability of ionizing within a distance ds:

$$dW = n_o\frac{\langle\sigma v\rangle}{v}\left(1 - \exp\left(-\frac{s}{L}\right)\right)ds \tag{A20}$$

Solving eq. (A7) in this case with boundary condition P(0) = 0, we find the cumulative probability density function:

$$P(s) = 1 - \exp\left(-n_0\,\frac{\langle\sigma v\rangle}{v}L\left(\frac{s}{L} + \exp\left(-\frac{s}{L}\right) - 1\right)\right) \tag{A21}$$

Thus, the probability density function for ionization of a particle traveling a distance s is then:

$$F(s) = n_0\frac{\langle\sigma v\rangle}{v}\left(1 - \exp\left(-\frac{s}{L}\right)\right)\exp\left(-n_0\,\frac{\langle\sigma v\rangle}{v}L\left(\frac{s}{L} + \exp\left(-\frac{s}{L}\right) - 1\right)\right) \tag{A22}$$

Finding the expectation value of this function is not straight-forward. Instead, we numerically sampled the ionization length from the cumulative probability density function using Monte-Carlo methods. Given a random number ξ from 0 to 1, the ionization length will be:

$$s = \frac{1}{a}(aL - \ln(1-\xi) + aL\,\mathbf{W}\left[\frac{-1}{e}(1-\xi)^{1/aL}\right] \tag{A23}$$

Where a = $n_0 \frac{\langle \sigma v \rangle}{v}$ and **W** is the Lambert-W or product log function.

Ionization and photo-emission distribution dependence on background density

A comparison of the resulting ionization and photo-emission PDF's for different density gradients as a function of distance from the surface is shown below in Figure A-1. The sputtering distributions and background plasma parameters from the R-He case were used in this example. We find that due to the MPS gradient, the ionization and photo-emission fronts are pushed further out from the surface than would be expected for a uniform background density. Also, the average value of the local electron density at the point of emission is roughly half that of the bulk density, but has a wide range over the emission plume.

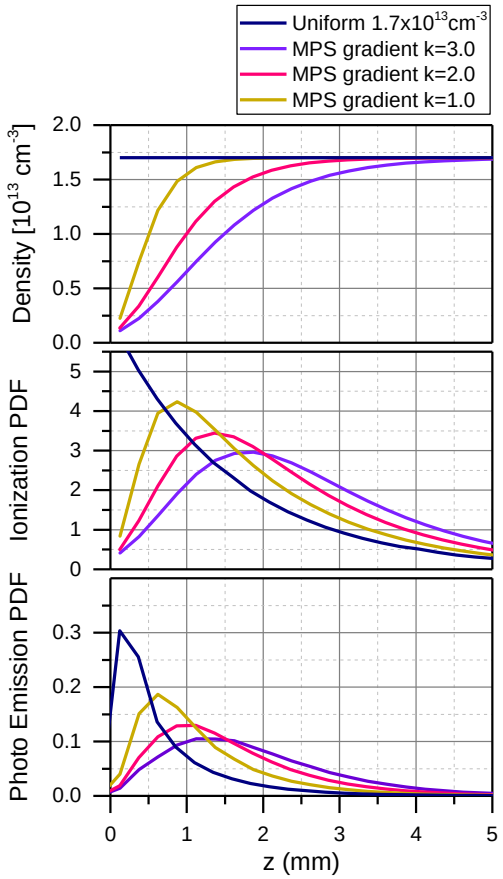

Figure A-1. Plasma density and ionization probability distribution function vs distance normal to surface shown for the R-He case comparing multiple MPS gradient scale lengths.